Normandie Université

UNIVERSITÉ DE ROUEN NORMANDIE

THÈSE

Pour obtenir le diplôme de doctorat

Spécialité **PHYSIQUE**

Préparée au sein de l'**Université de Rouen Normandie**

Terahertz-assisted Atom Probe Tomography development for the analysis of non-conductive materials.

Présentée et soutenue par

DE TULLIO MATTEO

Thèse soutenue le 05/12/2025

devant le jury composé de :

MME VELLA ANGELA	Professeur des Universités - URN - Université de Rouen Normandie	Directeur de thèse
M. PAREIGE PHILIPPE	Professeur des Universités - URN - Université de Rouen Normandie	Président du jury
M. ROPITAUX MARC	Maître de conférences - URN - Université de Rouen Normandie	Co-encadrant
M. LAMPIN JEAN-FRANÇOIS	Directeur de Recherche - Universite de Lille	Membre du jury
M. DI RUSSO ENRICO	Maître de Conférences HDR - Université de Padue, Italie	Rapporteur du jury
M. PAPARO DOMENICO	Directeur de recherche - Consiglio Nazionale delle Ricerche, Naples, Italie	Rapporteur du jury

Thèse dirigée par **VELLA ANGELA** (GROUPE DE PHYSIQUE DES MATERIAUX)

ED 591 PSIME

GPM Groupe de Physique des Matériaux

Alla mia famiglia

Acknowledgements

I wish to express my deepest gratitude to my supervisor, Angela Vella, who deserves a paragraph alone. Her talent, passion and tireless work ethic have been, for me, a constant source of inspiration. Having the chance to be her student has been a privilege, something that I especially realized and appreciated over the three years together. It's been a non-stop learning journey, that truly meant both a scientific and personal growth for me, even through dark moments, as they eventually lead to truly satisfying outcomes. She's taught me how to stay focused, sharp, and always being prepared to deliver outstanding work, hopefully one day the same way she does. I will always remember the time she has dedicated me in moments of need, and especially during this challenging period of thesis drafting, with real interest, with a degree of humbleness that few in her same position normally show. *Grazie di cuore, Angela.*

I sincerely thank my co-supervisors, Jonathan Houard and Marc Ropitaux, for their patient guidance and support throughout this journey. I am grateful to the rapporteurs, Enrico Di Russo and Domenico Paparo, for accepting to read and examine this thesis, thanks to Philippe Pareige and Jean-François Lampin for accepting to be members of my jury.

My thanks extend to the partners of the MIMOSA project for a fantastic collaboration, stimulating discussions, and friendships born along the way: Gustav Eriksson, Francesco Carnovale, Giovanni N. Inverardi, Anna Martinez, Rebeca Tudor, Tommaso Morresi... I collected so many fantastic memories with you. I am also grateful to Ammar Hideur, Simone Taioli, Gianluca Lattanzi, Martin Andersson, Mathias Thuvander, and Mats Hulander for being extraordinary co-authors and collaborators in our publications.

Special thanks go to my friends Léo Guiramand, Florant Exertier and Alexandre Fahy, indispensable sources of help and scientific exchange who helped me find the right direction during difficult experimental times, to Benjamin Klaes for his software tips, and to Ivan Blum, Emmanuel Cadel, Simona Moldovan, Laurence Chevalier, and Fabien Cuvilly for their technical and experimental support. Thank you to Lorenzo Rigutti, for inspiring conversations about music and for his precious scientific and human advice.

I am grateful to all the colleagues, who became all friends outside of the lab, who accompanied me during this PhD and made it lighter with lunches and coffees: Aidar, Ganesh, Onkar, Samba, Eric, Subodh, Nissrine, Anastasiia, Tom, JB, Arnaud, Alexandre, Christian, Luis, Aissatou, Antonella, Thomas and all those I may have unintentionally forgotten - thanks from my heart for dedicating me your time. I want to

thank the special people who made Rouen feel like home: Sindi, Luis, Raffaele, Julio, Simo, Michella, Josette, and Mohammad... I will always be grateful for your constant presence in difficult moments. Thank you for being there all along these three years. To my best friends, Francesco and Federico, thank you for always having my back since almost 25 years ago. To my family, thank you for your constant support, distance never weakened our bond.

Finally, I dedicate all of this to my partner, Jen, my *habibi*, for filling this path with joy, care and love, for believing in me in the worst times, for being my rock... I could have never done this without you.

Scientific contributions

Publications

1. K. Chen, E. Napolitani, **M. De Tullio**, C. Jiang, H. Guthrey, F. Sgarbossa, S. Theingi, W. Nemeth, M. Page, P. Stradins, S. Agarwal, D. Young. *Pulsed Laser Annealed Ga Hyperdoped Poly-Si/SiO$_x$ Passivating Contacts for High-Efficiency Monocrystalline Si Solar Cells* (Published outside PhD work). *Energy & Environmental Materials* 6 (2023): e12542.

2. **M. De Tullio**, G. Novi Inverardi, M. Karam, J. Houard, M. Ropitaux, I. Blum, F. Carnovale, G. Lattanzi, S. Taioli, G. Hulander, M. Andersson, A. Vella, T. Morresi. *Evaporation of cations from non-conductive nano-samples using single-cycle THz pulses: an experimental and theoretical study*. *Physical Review B* 111 (2025): 045428.

3. G. Eriksson, **M. De Tullio**, F. Carnovale, G. Novi Inverardi, T. Morresi, J. Houard, M. Ropitaux, I. Blum, E. Cadel, G. Lattanzi, M. Thuvander, M. Andersson, M. Hulander, S. Taioli, A. Vella. *Role of Defects in Atom Probe Analysis of Sol–Gel Silica*. *ACS Omega* 10 (30), 33741–33754 (2025).

Manuscripts in preparation

1. *Chromium- and Monolayer Graphene-Based Coating Solutions for Field Enhancement in THz-Assisted Atom Probe Tomography of Sol–Gel Silica Specimens*.
M. De Tullio, F. Exertier, I. Blum, E. Cadel, L. Chevalier, J. Houard, S. Moldovan, M. Andersson, G. Eriksson, M. Ropitaux, A. Vella.

2. *Ion Field Emission Driven by a High-Repetition-Rate Intense Single-Cycle Terahertz Source*.
L. Guiramand, F. Exertier, A. Fahy, A. Martinez, **M. De Tullio**, S. Idlahcen, J. Houard, G. Da Costa, T. Godin, X. Ropagnol, D. Paparo, F. Blanchard, A. Vella, A. Hideur.

3. *Field Evaporation of Germanium under THz Pulses: Application to Atom Probe Tomography* (submitted).
M. Karam, **M. De Tullio**, J. Houard, I. Blum, A. Vella.

Conference contributions

- **SFμ** (Rouen, 2023) — Poster presentation.
- **SFO** (Rouen, 2024) — Oral presentation.
- **EMC** (Copenhagen, 2024) — Poster presentation.
- **APT&M 2025 — Müller Award Competition Finalist** (IIT Madras, Chennai, India).
- **SFμ** (Toulouse, 2025) — Poster presentation.

Abstract

Atom Probe Tomography (APT) is an imaging technique with high spatial resolution and chemical sensitivity, initially designed for metals and alloys but recently extended to other materials through the use of pulsed lasers. However, its effectiveness is limited in low-conductive materials due to decreased resolution due to thermal effects in semiconductors, geological, and biological samples. APT can act as a complementary technique alongside other well-established nanoscale bio-imaging microscopy techniques. A recently proposed way to extend APT's applicability to biomolecules is to replace the aqueous environment with an amorphous sol–gel silica matrix. However, defects and the intrinsic porosity of this material can still degrade analysis quality. This thesis investigates the combination of APT intense two-color plasma generated, single-cycle THz pulses (1 kHz repetition rate) on sol-gel silica matrices to improve the control of ion emission and reduce thermal effects, offering an innovative solution to such limitations. Such THz-source platform offers the possibility to switch pulse polarity.

Initially, we investigate the effects of UV and Deep-UV laser pulsing on amorphous thin-film and bulk sol–gel silica matrices, focusing on how pulse wavelength and structural defects influence spectral fidelity and composition. It then explores THz-assisted evaporation, where THz pulses with negative polarity enhance electron emission and field evaporation, contrasting with the ineffectiveness of positive pulses in field amplification on insulating samples. The research introduces surface engineering strategies, *i.e.* chromium layer sputtering and graphene encapsulation to create conductive interfaces which enable the enhancement of THz field in both pulse polarities, improving peak resolution in mass spectra, and reducing background noise.

By employing a new high repetition rate THz source (100 kHz) based on optical rectification in lithium niobate crystal, the research demonstrated effective large-volume field evaporation for the first time, achieving high-quality mass-spectral data, enhanced spatial resolution, and reliable 3D reconstructions on both coated and uncoated sol–gel silica, as well as a complex Ni-based superalloy (NS8), matching the performance of commercial laser-assisted methods.

Key words: Atom Probe Tomography, Terahertz-assisted field evaporation, sol-gel silica embedding, conductive coatings, high-repetition-rate THz source

Résumé

La Sonde Atomique Tomographique (SAT) est une technique d'imagerie à haute résolution spatiale et à une forte sensibilité chimique. Initialement conçue pour les métaux et alliages, elle a été récemment étendue à d'autres matériaux grâce à l'utilisation de lasers pulsés. De nombreux travaux ont laissé entrevoir son potentiel d'être appliquée aux matériaux biologiques à l'échelle nanométrique en complément d'autres méthodes d'imagerie grâce à sa haute sensibilité chimique. Néanmoins, cela demande une préparation des échantillons adaptée à cette nouvelle approche, notamment par l'encapsulation de molécules biologiques dans une matrice de silice sol-gel amorphe. Toutefois, ce type d'échantillon entraine de nombreux défauts et la porosité intrinsèque à ce type de matériau peut dégrader la qualité des analyses. Cette étude explore la combinaison de la SAT et de l'impulsion térahertz (THz) générée par un plasma bichromatique (fréquence de répétition de 1 kHz) afin d'améliorer le contrôle de l'émission ionique et réduire les effets thermiques, tout en inversant la polarité des impulsions.

Nous avons examiné les effets du pompage UV et Deep-UV sur des matrices de silice sol-gel amorphes sous forme de couches minces et de volumes massifs en nous concentrant sur la manière dont la longueur d'onde des impulsions et les défauts structuraux influencent la fidélité spectrale et la composition. Par la suite, nous avons exploré l'évaporation assistée par THz, où des impulsions THz de polarité négative renforcent l'émission électronique et l'évaporation de champ, par contraste avec l'inefficacité des impulsions positives. Enfin, ces travaux introduisent des stratégies d'ingénierie de surface par le dépôt d'une couche de chrome et l'encapsulation par du graphène afin de créer des interfaces conductrices permettant d'amplifier le champ THz pour les deux polarités d'impulsion et ainsi améliorer la résolution des pics dans les spectres de masse tout en réduisant le bruit de fond.

En employant une nouvelle source THz à haute cadence (100 kHz) basée sur la rectification optique dans un cristal de niobate de lithium, les recherches démontrent pour la première fois une évaporation de champ à grand volume efficace, obtenant des spectres de masse de haute qualité, une résolution spatiale accrue et des reconstructions 3D fiables, tant sur la silice sol-gel, revêtue ou non d'un superalliage complexe à base de nickel (NS8), atteignant des performances comparables aux méthodes commerciales assistées par laser.

Contents

General introduction **1**

1 State of the art **5**

1.1 Introduction 5

1.2 Overview of APT 11

1.2.1 Principles of APT 13

1.3 Laser–Assisted APT 17

1.3.1 Physical mechanisms of laser-pulse–assisted field evaporation 18

1.4 Atom probe tomography of bio-materials: state of the art 21

1.5 Silica as a candidate for bio-molecules encapsulation for APT study 28

1.6 Introduction to THz-Assisted Atom Probe Tomography 29

1.6.1 THz Radiation Properties 29

1.6.2 THz evaporation mechanism 30

1.6.3 Experimental studies on Al and LaB_6 tips 34

1.7 Conclusion 37

2 Materials and Methods **39**

2.1 Introduction 39

2.2 Practical Principles of Atom Probe Operation 40

2.2.1 Ion Detection and Signal Processing 41
2.2.2 Mass spectrum construction 44
2.3 3D volume Reconstruction 48
2.3.1 Reconstruction protocols used in this thesis 50
2.4 Atom Probe Instrumentation: Laser-Assisted and Terahertz-Assisted Systems . . 50
2.4.1 Laser-Assisted Wide-Angle Tomographic Atom Probe 52
2.4.2 Local Electrode Atom Probe (LEAP) systems 54
2.4.3 Terahertz-Assisted APT Systems (Tera-SAT) 55
2.5 Samples 61
2.5.1 Synthesis of sol–gel silica: water glass method 62
2.5.2 Other materials 67
2.6 Electrochemical and Ion Beam-Based Specimen Preparation 69
2.6.1 Specimen preparation by electropolishing 69
2.6.2 Focused Ion Beam-based specimen preparation 71
2.7 Coating methods 75
2.7.1 Deposition *via* PECS – Equipment and Parameters 76
2.7.2 Graphene Coating for APT specimens 78

3 Analysis of sol-gel silica samples by UV-laser assisted Atom Probe Tomography 87

3.1 UV analyses (LAWATAP) of Thin film sol-gel silica samples embedding ferritin . 88
3.1.1 Low-field regime analysis 89
3.1.2 High-field regime analysis 93
3.2 Near-UV vs deep UV-assisted APT on “bulk” sol–gel silica specimens 97
3.2.1 Compositional analysis 101
3.2.2 Thermal response 103
3.3 Conclusion 106

4 Low repetition rate Tera-SAT - Analysis of sol-gel silica samples 109

4.1 Low repetition rate Tera-SAT: THz-assisted analysis of sol–gel silica specimens . 111
4.1.1 Negative vs. positive–polarity THz pulses 111
4.1.2 Comparative analysis: THz vs. NIR vs. UV assisted APT on sol–gel silica 115

4.1.3 Evaporation mechanisms under THz negative polarity 118
4.2 Coating Strategies for THz-field enhancement on sol-gel silica specimens 122
4.2.1 Chromium-coated sol–gel silica under THz pulsing 123
4.2.2 Graphene-coated sol–gel silica under THz pulsing 127
4.2.3 Comparative analyses under THz-Positive pulses: Graphene vs. Chromium coating 129
4.3 Preliminary results on the high–repetition–rate Tera-SAT (100 kHz) 132
4.3.1 First experiment: THz negative pulses vs IR on empty sol-gel silica sample 132
4.3.2 Second experiment: THz positive pulses analysis on Cr–coated silica . . . 134
4.4 Conclusion 137

5 High-repetition-rate Tera-SAT: Results and discussion on NS8 nickel-based superalloy 141

5.1 Introduction 141
5.2 High repetition rate Tera-SAT - analysis of the γ phase region 144
5.2.1 Negative THz pulses vs IR-assisted analyses 144
5.2.2 Positive THz pulses - impact of THz beam energy variation 146
5.3 High repetition rate Tera-SAT - analyses of the γ' phase and θ-type clusters region 151
5.3.1 Analysis 1: THz^- and IR-assisted APT in γ' phase with θ-type clusters . 151
5.3.2 Analysis 2: THz^+-assisted APT in γ' phase with θ-type clusters 157
5.4 Comparison THz-assisted APT vs LEAP 5000 XS (laser and electric mode) - γ and γ' phases 162
5.5 Conclusion 165

General conclusions 167

Appendix 171

1.1 Fourier-based estimate of spatial resolution in APT. 171
1.2 Artefacts, biases, and quality control in 3D reconstruction 172
1.3 Clusters and precipitates 173

Bibliography 177

General introduction

Cryo–electron microscopy (cryo-EM) has transformed structural biology, and cryo-(T)EM routinely yields near-atomic reconstructions of macromolecular assemblies and nano–drug carriers [1, 2]. Yet, for specimens rich in light elements, low contrast, dose limits, and sensitivity constraints complicate native-state 3D reconstructions and EDX/EELS chemistry at nanometric scales [3, 4]. These limitations motivate a shift from purely 3D structure toward the so-called 4D microscopy, *i.e.* volumetric datasets that capture composition and 3D structure simultaneously with high fidelity [5].

Biology demands nanoscale, chemically resolved analysis: protein function is shaped not only by the amino-acid sequence but also by dynamic three-dimensional conformations, ligand interactions, and environment-dependent states. Despite major advances in X-ray crystallography, NMR, cryo-EM, and machine-learning-based structure prediction, many different bio-features remain difficult to detect under native-like conditions with simultaneous 3D structural *and* chemical fidelity and, above all, at the nanoscale level.

Atom probe tomography (APT) provides sub-nanometric spatial resolution with isotopic sensitivity by analysing ions emitted *via* controlled field evaporation from nanometric-radius, needle-shaped tips [6–8]. Essentially, it is a method that operates in four dimensions: time-of-flight mass spectrometry yields chemical identity while position-sensitive detection enables three-dimensional reconstruction of atomic distributions [9–12]. Field-evaporation techniques have

evolved from high-voltage pulsing—effective on conductive materials but limited on low-free-carrier specimens, such as semiconductors and oxides, to laser assistance [13], which extended the applicability of the technique at the cost of thermal artifacts that degrade accuracy in spectral analysis and volume reconstruction [14, 15].

Previous work has shown that APT isn't limited to metals: it has been used on bio-minerals [16, 17] and on biomolecules embedded in solid matrices [18, 19], demonstrating that the approach can, in practice, be extended to biological systems. That said, moving from mineral-rich samples to truly hydrated, non-conductive specimens is challenging: water content and thermal fragility clash with laser-pulsed APT, and even cryogenic workflows risk ice crystallization that disturbs native bio-structures [20, 21].

Recent work shows that ultrafast single-cycle terahertz (THz) transients can drive *non-thermal*, field-driven emission with V/nm near-fields, extending control from electron to ion emission [22–24], and connecting to THz-driven Scanning Tunneling Microscopy and nano-tip physics [25–27]. Within APT analysis of conductive materials, THz pulsing has been demonstrated to strongly reduce or cancel thermal effects, but open issues remain: asymmetric ToF and mass spectra and ultrafast ion dynamics [28], quantitative accuracy of compositions, and the efficiency of THz-triggered evaporation in wide-band-gap semiconductors and oxides. Moreover, no THz-assisted APT analysis has ever been attempted on biological samples.

In this context, the present thesis constitutes the first systematic attempt to implement THz-assisted APT beyond conductive specimens, targeting *insulating* systems and *complex amorphous* materials such as sol–gel silica; it also reports the first ever attempts toward THz-driven evaporation of *biological* matter. Over the course of the work, the initial low-repetition-rate source (1 kHz) was replaced by a high-repetition-rate platform (100 kHz class), enabling for the first time field evaporation of *large datasets* under THz pulsing.

The objectives of this thesis are to:

- establish UV/deep-UV (DUV) and near-infrared (NIR) laser-assisted APT baselines on sol–gel silica specimens embedding biomolecules, across multiple sample preparation geometries, to serve as quantitative references for the next THz-assisted analyses;
- probe how THz pulse polarity actually changes the way insulating matrices evaporate

under the field;

- make THz coupling work better in practice by engineering the sample's surface (for example, with chromium sputtering or graphene encapsulation);
- show that the approach holds at high repetition rates, and check its performance head-to-head against standard laser-assisted APT.

These works have begun with a collaborative project between the GlycoMEV and GPM (Groupe de physique des Matériaux) laboratories (BIOTAP, RIN d'excellence 2021-2024) and the collaboration has been extended throughout the processes of sample preparation and material selection. This thesis is conducted within the EU Pathfinder project **MIMOSA** (*4D Microscopy of Biological Materials by Short Pulse Terahertz Sources*), a multi-partner consortium in which GPM laboratory, leads THz-APT development and integration; in CNRS–CORIA laboratory, together with the industrial partner AFS high-repetition-rate ultrafast fiber-laser drivers are developed, while the groups in CNR and ETS advance THz generation, characterization, and beam/pulse shaping; the group in Chalmers University develops the whole silica-embedding and specimen preparation for biological samples used for this work. The group in FBK provides multiscale theory and modelling of proteins in silica and field-evaporation, and finally, INSERM–EnVI supplies/qualifies biomedical samples.

The manuscript is organized into five chapters as follows:

- In Chapter 1, we review the fundamentals of APT—field evaporation principles, conventional methodologies, and their limitations for biological materials—and survey the first demonstrations of THz-assisted APT.

- In Chapter 2, we describe the practical operation of APT (ion detection and data-processing workflows), the laser-assisted and THz-assisted instrumentation employed, the samples, and the two surface-engineering strategies used throughout this work: chromium coating by Precision Etching and Coating System (Gatan PECS) sputtering and graphene encapsulation by wet transfer.

- In Chapter 3, we present UV and deep-UV experiments on thin-film and bulk sol–gel silica: first, we assess how field regimes affect spectral response and composition in ferritin-loaded

thin films; second, we examine how wavelength and defects influence thermal response and composition in bulk specimens.

- In Chapter 4, we report THz-assisted APT on sol–gel silica using a low-repetition-rate (1 kHz) source to probe polarity-dependent evaporation mechanisms and benchmark them against NIR and UV pulsing; we then present results on Cr-coated and graphene-encapsulated tips and introduce preliminary data obtained with a high-repetition-rate system on coated and uncoated sol–gel specimens.

- In Chapter 5, we evaluate the high-repetition-rate THz system on the Ni-based superalloy NS8 (a conductive, multiphase alloy with nanoscale features), demonstrating large-volume acquisition and strong spectral/compositional fidelity, compared against a commercial LEAP operated in both laser and high-voltage pulsing modes.

Part of the results presented in Chapter 3 and 4 have been published in the following references: [29] and [30].

CHAPTER 1

State of the art

1.1 Introduction

A rigorous understanding of materials requires knowledge about the arrangement of atoms and how these dispositions evolve over time. Properties such as mechanical strength, optical response, and thermal transport are set by defects, interfaces, and the structure at the atomic scale. Establishing structure–property relationships, therefore, calls for methods that deliver quantitative, three-dimensional reconstructions at the atomic scale.

The analysis of biological and bio–inorganic materials relies on a diverse set of methods that together span structure, chemistry, mechanics, and dynamics across multiple length scales. Electron microscopy, scanning probes, and magnetic resonance each bring their own strengths, but no single method on its own can deliver quantitative, three-dimensional chemistry at the nanoscale.

In structural biology, the advent of cryo–EM has made near–atomic structural determination of biomolecules routine; nevertheless, when the goal is to understand function in situ, one ultimately needs *4D* information: 3D structure *plus* local chemistry, at relevant length scales.

TEM and especially cryo–EM have transformed structural biology by enabling near–atomic re-

constructions of macromolecular complexes, membrane proteins, and viral assemblies in a minimally perturbed state. Advances in direct electron detection, phase plates, motion correction, and image processing have made resolutions in the 2–3 Å range routine for favourable targets, with sub–2 Å structures now reported even at 200 keV under optimised conditions [31, 32]. For compositional analysis, scanning TEM can be coupled to electron energy–loss spectroscopy (EELS) and energy–dispersive X–ray spectroscopy (EDS). EELS is especially informative for low–Z elements: it detects carbon, nitrogen, and oxygen edges and resolves near–edge fine structure associated with bonding, hence distinguishing, in principle, between chemical states [33, 34]. EDS, by contrast, excels for medium to heavy elements and provides rapid survey maps over wide fields. Representative examples are shown in Fig. 1.1(a–c) for cryo–EM structure, and Fig. 1.1(d–f) for EM microanalysis.

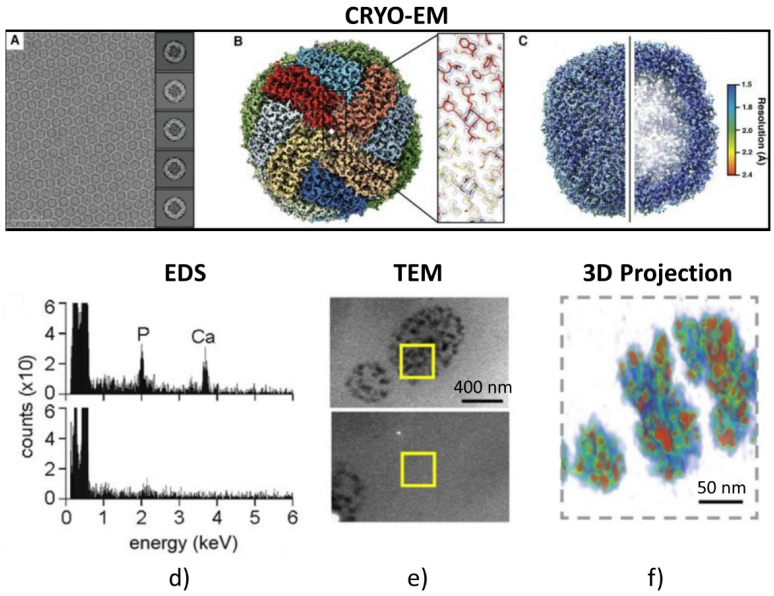

Figure 1.1: Cryo–EM structure and EM chemistry. (a–c) ∼1.75 Å mouse apoferritin reconstruction [35]: aligned/dose-weighted micrograph with class averages; final density coloured by subunit with a zoom; local-resolution map. (d–f) Mitochondrial granules [4]: EDS spectra from boxed ROIs reveal Ca and P enrichment; granules shown against projected BF volume densities (inverted contrast). Together, these panels highlight cryo–EM's structural power and the complementary, dose/thickness-limited chemical insight from EM microanalysis.

The electron beam, central to TEM's effectiveness, also presents a drawback for soft matter, due to radiation damage. Even in cryogenic conditions, the allowable dose is finite and sets a trade–off between signal-to-noise, resolution, and tilt-series coverage; improving one dimension competes with sample survivability [36]. Single–particle workflows face additional practical issues such as preferred orientation and missing views, which can bias reconstructions and demand

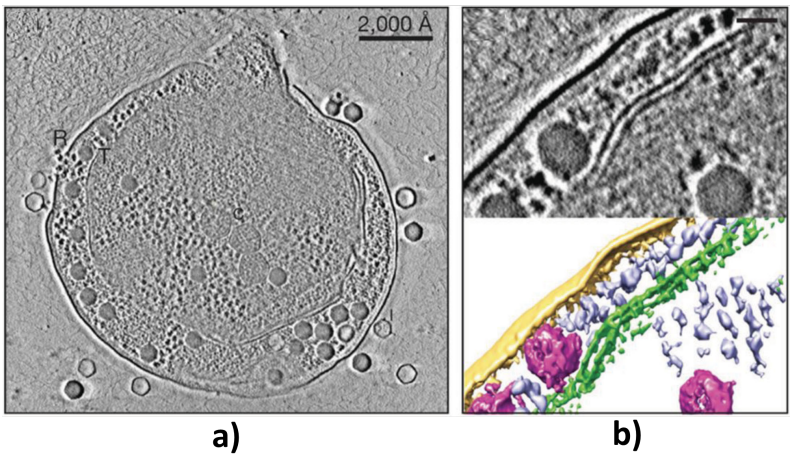

Figure 1.2: Phase-plate TEM imaging of a cyanophage assembling inside marine cyanobacteria.[3] (a) Sectional overview of a late-stage infected *Syn5*, including labelled cellular components and phages: carboxysomes, infecting phages, ribosomes, and thylakoid membranes. (b) Higher-magnification views and corresponding 3D reconstructions of cellular components: thylakoid membrane (green), carboxysome (blue), cell envelope (yellow), and ribosome (purple). The figure highlights cryo-(T)EM's strength in cellular ultrastructure and motivates complementing it with quantitative 3D chemistry.

strategies like stage tilting or engineered supports to diversify angular sampling [37]. For chemistry, EDS in thin, light–element–rich matrices suffers from low fluorescence yield, absorption, and overlapping lines, making absolute quantification of C/N/O challenging. EELS alleviates some of those issues, but at the cost of dose, strict thickness control, and careful deconvolution of plural scattering; these constraints narrow the time window during which biological samples can be preserved [33, 34]. In summary, TEM offers exceptional structural resolution, and when combined with EELS and EDS, enables chemically sensitive visualizations; however, achieving quantitative three-dimensional light-element stoichiometry at the nanometre scale under practical dose limits is still challenging. A cellular, phase-plate TEM example is shown in Fig. 1.2, highlighting ultrastructure in situ.

Atomic Force Microscopy (AFM) provides high-resolution topographical data crucial for studying living cells and biomaterials in various conditions [38, 39]. Recent advances have expanded its applications from imaging to measuring mechanical properties at biologically relevant speeds [40]. Despite its excellence for surface morphology and mechanics, AFM remains inherently two-dimensional and requires additional methods for 3D modeling; chemical specificity is limited unless augmented with functionalised tips or techniques like AFM–IR or TERS, as AFM alone is insufficient for bulk 3D chemical composition analysis.

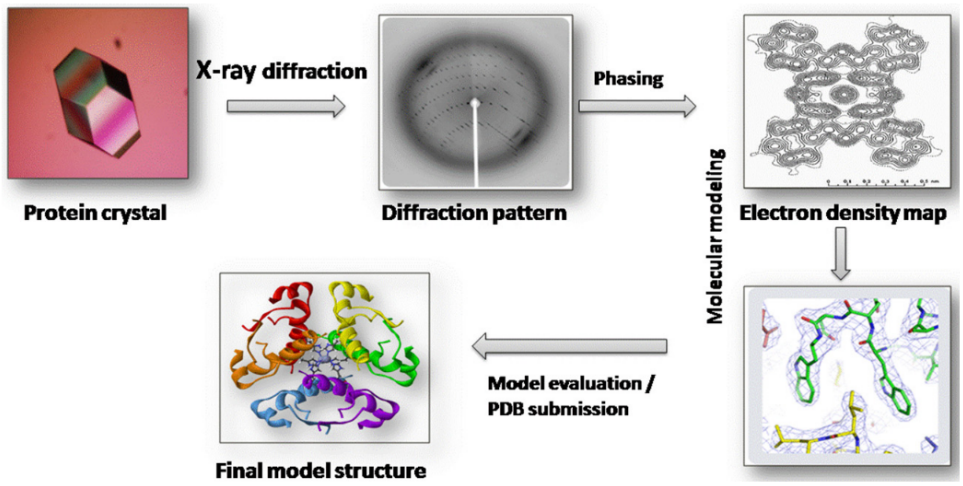

Figure 1.3: Schematic diagram showing the workflow for the structural determination of proteins by X-ray crystallography. Reproduced from [41]

X-ray crystallography, whose typical workflow is displayed in Fig. 1.3, has been one of the main methods for determining biomolecular 3D structures at (near-)atomic resolution by interpreting diffraction from well-ordered crystals [42]. Its central constraint is the requirement to grow high-quality crystals, often under non-physiological conditions, which can denature sensitive specimens, trap non-native conformations, or exclude flexible regions; crystallization thus remains a major bottleneck, especially for membrane proteins and large, dynamic assemblies [43, 44]. Even when crystals are obtained, lattice contacts may bias backbone and side-chain conformations and suppress native dynamics, complicating functional interpretation [45]. Despite these caveats, X-ray crystallography continues to deliver precise coordinates foundational for mechanism and ligand design, while advances in automation, micro crystallography, and time-resolved/serial methods at synchrotrons and XFELs mitigate some limitations without removing the fundamental need for crystallization [46].

Nuclear magnetic resonance (NMR) is *chemically rich*: in solution, it reveals structural and dynamic details with high specificity *via* isotopic labelling and multi-dimensional experiments; in the solid state, high fields and fast magic–angle spinning extend these capabilities to non-crystalline systems such as membranes or cell walls [47, 48]. Yet, NMR is fundamentally a bulk technique, providing ensemble-averaged information rather than nanoscale spatial maps.

What remains scarce is nanoscale, 3D, quantitative *light-element* chemistry: this is the gap Atom Probe Tomography (APT) can fill. By field–evaporating atoms from a needle–shaped specimen

and time–of–flight measuring their mass–to–charge ratios, APT is a technique which enables the reconstruction of three–dimensional compositional maps with sub–nanometre resolution and absolute counting statistics [6, 7, 49, 50]. In favorable regimes, it reaches p.p.m. sensitivity and resolves isotopes, making it particularly powerful for light elements as well, such as carbon, nitrogen, and oxygen. Hydrogen is also detectable, though its reliable quantification requires careful control of backgrounds, adsorbates, and experimental artefacts [51].

Historically, APT emerged from field ion microscopy (FIM) introduced by Müller in 1951 [6]. The atom probe field ion microscope (APFIM, 1967) coupled FIM geometry to time-of-flight mass spectrometry, enabling chemical identification of field-evaporated ions [6, 52]. A major advance was the local electrode atom probe (LEAP, 1996), which established the modern instrument architecture [53]. The adoption of laser pulsing broadened APT beyond good conductors, enabling routine analysis of semiconductors, oxides, and minerals [53, 54]. Ultrafast terahertz (THz) pulses to assist APT analyses have recently been successfully studied in the case of conductive materials, but the capabilities and the limits of this new approach remain to be explored, in particular in the case of low electrical conductive materials.

APT and EM can be used together effectively in scientific workflows for advanced material analysis. Cryo-EM or TEM can first be used to map the structure in detail and flag regions of interest. Those regions are then extracted by focused ion beam lift-out to make site-specific specimens for APT. In this workflow, EM provides detailed structural imaging under dose-optimised conditions but struggles with quantifying lighter elements; APT excels at providing quantitative chemistry, including atomic-level stoichiometry, in 3D at the nanoscale.

Nuclear Magnetic Resonance (NMR) and related spectroscopies provide orthogonal information on chemical states and dynamics, but they probe strictly *ensemble-averaged* signals over macroscopic sample volumes. In standard liquid-state NMR, a 5 mm tube typically contains ∼0.5–0.6 mL of solution, corresponding to ∼500–600 mm^3 of analysed material [55, 56], while solid-state NMR experiments commonly rely on magic-angle-spinning rotors with sample volumes ranging from a few to several tens of microliters (i.e. ∼1–100 mm^3), depending on rotor diameter and probe configuration [57]. As a consequence, the volume probed by NMR is many orders of magnitude larger than the nanoscale sub-volumes accessed by atom probe tomography, which may not be statistically representative of the bulk on their own; a multimodal approach

is therefore required to bridge ensemble-averaged and local chemical information in complex biomaterials.

Key challenges for biological and soft materials include detecting light elements and isotopes with high precision in very small volumes without harming the specimen; balancing dose/perturbation against information content in tomography, EELS, or multi-dimensional spectroscopy; and correlating structural maps from EM with absolute composition at the same nanoscale locations, especially across interfaces in hybrid systems. Existing methods address parts of these challenges, but none alone achieves complete 3D, quantitative, light-element-sensitive analysis at the nanoscale.

APT is not without caveats when applied to bio–materials. Organic molecules fragment during field evaporation, and laser assistance can introduce thermal broadening that degrades peak shapes and elevates baselines. Insulating matrices charge, distort local fields, and complicate the coupling of the excitation pulse to the apex. These are active areas of development and are central to this work: we explore terahertz (THz)–assisted evaporation to minimise thermal input while preserving strong, transient field enhancement; we compare surface metallisation strategies (chromium coating and graphene encapsulation) to stabilise the electrostatic boundary conditions and improve field coupling on insulating silica; and we benchmark performance against conventional ultraviolet and deep–UV laser assistance. Although composition fidelity is known to depend on the local electric field, a field–dominated regime driven by ultrafast THz transients differs fundamentally from a high static-field regime: the field enhancement is strong but short-lived, reducing the need for elevated DC fields and limiting thermally activated, non-correlated evaporation. In this way, evaporation remains field-controlled while mitigating sequence distortions and multiplicity-driven artefacts, thereby improving compositional fidelity. In parallel, specimen preparation and environmental control, whether through cryogenic handling, encapsulation, or dehydration routes, remain essential to credible light–element analysis. [58–60].

In this chapter, we first outline core APT principles, then examine laser-assisted evaporation: the enabling mechanisms for non-metals and the constraints imposed by thermal excitation. We next introduce biomaterials, focusing on sol–gel silica (its synthesis, relevance, and utility as a matrix for biomolecule encapsulation) and discuss specimen surface engineering strategies such

as thin chromium coatings and graphene encapsulation. Lastly, we present the fundamentals of THz-assisted APT.

1.2 Overview of APT

Atom probe tomography (APT) operates by *field evaporation*: atoms at the apex of a needle-shaped specimen are ionised and ejected under an intense electric field generated by a standing DC bias and short triggering pulses (high-voltage or laser). The DC voltage establishes a high field at the nanometric tip, while the superposed pulse transiently raises the local field to the threshold for ion emission (Fig. 1.4).

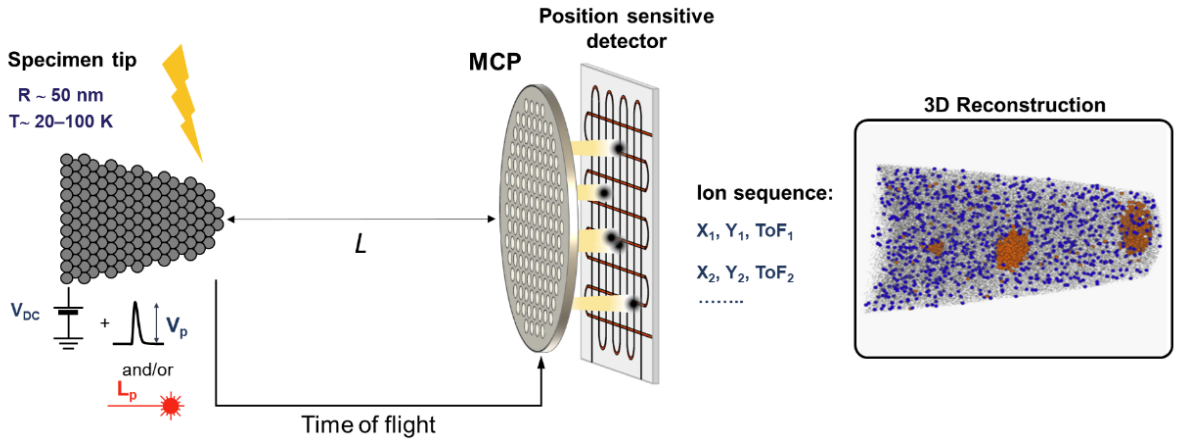

Figure 1.4: Atom probe tomography (APT) schematic. A DC-biased, cryogenic nanotip is pulse-triggered (voltage or laser/THz) to field-evaporate ions, whose (X, Y) impacts and ToF are recorded at a position-sensitive detector. Mass-to-charge values are then used to reconstruct a 3D atom map.

In APT, the specimen must be sharp enough to focus the electrostatic field at its apex. In a spherical approximation, the surface potential and field are $V = (4\pi\varepsilon_0)^{-1}Q/R$ and $F = (4\pi\varepsilon_0)^{-1}Q/R^2$, which immediately gives $F = V/R$. Real emitters are better described as a hemispherical cap on a conical shank within an electrode structure; these geometric and boundary–condition effects are gathered into a specimen–instrument *field factor* k_F (often written K_f), yielding the working relation

$$F = \frac{V}{k_F\, R},$$

with k_F typically $2-8$ and dependent on shank angle, apex shape, and extractor coupling [61–65]. Fields required for field ionization/evaporation are $\sim 10^{10}\,\mathrm{V\,m^{-1}}$ (tens of $\mathrm{V\,nm^{-1}}$), readily

reached for radii of a few–tens of nanometres at kilovolt biases. Because the field decays rapidly away from the apex, small changes in tip shape or local electrostatics can affect ion trajectories and reconstruction fidelity.

To initiate evaporation, a short pulse (high voltage pulses for good conductors) briefly increases the apex field above the binding energy of surface atoms, which are then accelerated toward the detector. The mass-to-charge ratio (MCR) follows from time of flight (ToF) using energy conservation [66]:

$$\mathrm{MCR} = \frac{m}{n} = 2eV\left(\frac{\mathrm{ToF}}{L}\right)^2, \tag{1.1}$$

with m the ion mass, n its charge state, $V = V_{\mathrm{DC}} + V_{\mathrm{Pulse}}$ the total accelerating potential (in general, the potential difference acting between the tip apex and the detector), e the elementary charge, and L the flight path length.

Reliable APT analyses require precise specimen preparation: the sample is shaped into a tip with $R \lesssim 100$ nm to achieve the required fields [67]. Electro-polishing and focused ion beam (FIB) milling are the standard routes [68]. Modern position-sensitive, time-resolving detectors record both impact coordinates and ToF [69], enabling faithful three-dimensional reconstructions of chemistry and structure.

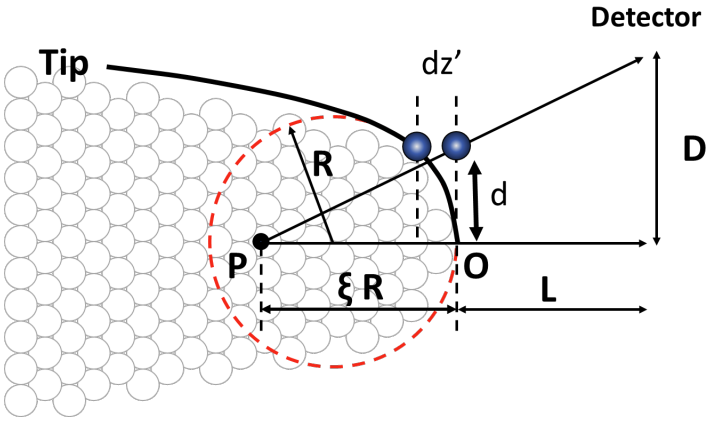

Figure 1.5: Point–projection geometry (adapted from [6]). The projection point P lies on the tip axis at $OP = \xi R$ from the apex (local radius R). The detector is at distance L from the apex with $L \gg \xi R$.

In reconstruction, ion trajectories are approximated as rays emanating from a *projection point* P located on the tip axis a distance $OP = \xi R$ from the apex, where R is the local radius of curvature and ξ the image–compression factor (Fig. 1.5) [70]. With the detector at distance L

($L \gg \xi R$), the point–projection magnification is:

$$M_{\text{proj}} = \frac{D}{d} = \frac{L + \xi R}{\xi R} \approx \frac{L}{\xi R} \tag{1.2}$$

thus lateral specimen coordinates follow by demagnifying detector coordinates:

$$x = \frac{X_D}{M_{\text{proj}}}, \qquad y = \frac{Y_D}{M_{\text{proj}}} \tag{1.3}$$

Because atoms are first placed on the *tangent plane* at the apex, a spherical curvature correction returns them to the cap of radius R:

$$dz' = R\left(1 - \sqrt{1 - \frac{x^2 + y^2}{R^2}}\right) \approx \frac{x^2 + y^2}{2R} \tag{1.4}$$

valid at small emission polar angle ($r = \sqrt{x^2 + y^2} \ll R$). In practice, the depth of the i-th ion is then accumulated as $z_i = \left(\sum_1^i dz\right) + dz'_i$, where dz is the mean depth increment from the evaporation sequence.

1.2.1 Principles of APT

Field evaporation is the field-induced removal of an atom from its host lattice, comprising ionisation and desorption under an intense electric field. The sequence is sketched in Fig. 1.6a, and its potential-energy landscape is illustrated in Fig. 1.6b. The external field polarises surface atoms and, once sufficiently strong, lowers the bonding barrier so that an atom can detach while losing electron(s) to the solid and accelerate away as an ion. Early models framed this process as thermally assisted escape over a field-lowered barrier [71–73]. In Müller's *image-hump* picture, the atom becomes fully ionised at a critical distance, whereas Gomer's *charge-draining* model emphasises progressive charge removal during departure [72]; both admit evaporation by thermal activation, with tunnelling possible when the barrier thins.

Within the image-hump framework, the external field lowers the ionic potential while image

forces attract the ion back to the surface, producing a field-dependent *Schottky hump* $Q(F)$ that must be crossed [73]. If this saddle lies below the atomic-state minimum, the activation energy is the difference between the two curves at their intersection; this construction also underlies the widely used charge-draining interpretation [74–76]. Early assumptions of direct emission as an n-fold charged ion [71, 72] were revised by later work showing predominantly single (or at most double) charge states at emission with subsequent *post-ionisation* in the near field [77–79]. Quantum-mechanical (*ab initio*, DFT) treatments have been attempted [80–87], though their quantitative range of validity remains debated [88].

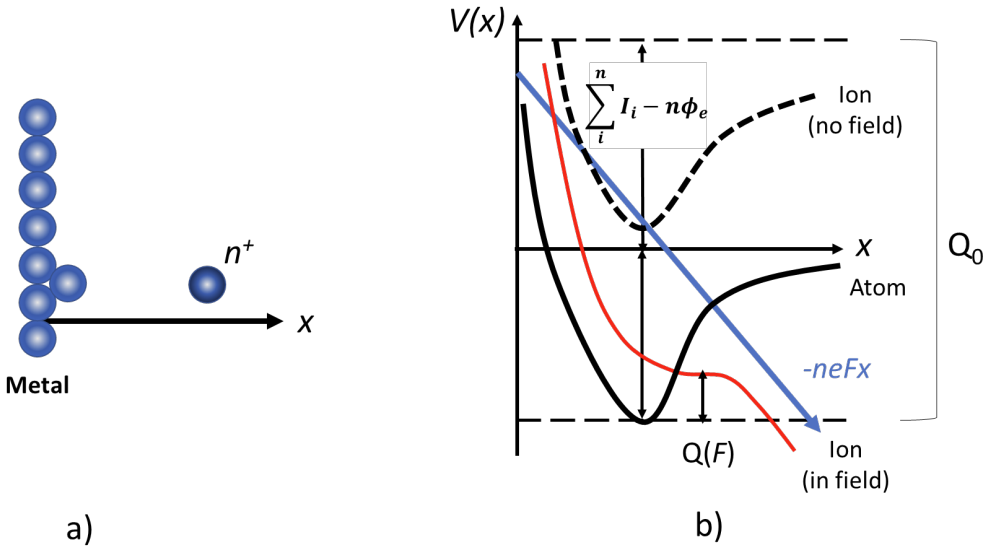

Figure 1.6: (a) Field evaporation process; the adatom is shown in grey and the emitted ion in black. (b) Atomic and ionic potential-energy diagrams with and without an applied electric field. V is the potential, Λ the sublimation energy, n the degree of ionisation, I_i the ith ionisation energy, and ϕ_e the work function. Q_0 and $Q(F)$ are the energy barriers without and with field, respectively. Reproduced from [6].

For practical use, an important parameter to consider is the activation barrier versus field. A commonly adopted linearised form that captures experimental trends at $T > 0$ is

$$Q_n(F) \;=\; Q_0\left(1 - \frac{F}{F_{\mathrm{EV}}}\right), \tag{1.5}$$

where Q_0 is the zero-field activation energy (typically 0.2–1 eV [89]) and F_{EV} is the (zero-Kelvin) evaporation field. For completeness, the image–hump picture (Fig. 1.6(a,b) yields the

Born–Haber–type zero-field energy,

$$Q_0 = \Lambda + \sum_{i=1}^{n} I_i - n\phi_e, \tag{1.6}$$

with Λ the sublimation energy, I_i the ith ionisation energy, and ϕ_e the work function. An applied field F then lowers the barrier *via* the Schottky term

$$Q(F) = Q_0 - \sqrt{\frac{n^3 e^3}{4\pi\varepsilon_0}\, F}, \tag{1.7}$$

(optionally with a small polarisability correction $-\frac{1}{2}\alpha_p F^2$). Gomer's charge–draining view [72, 73] is consistent with thermally activated crossing and tunnelling in the thin-barrier limit. While no single microscopic model captures all materials and conditions [88, 90], Eqs. (1.5)–(1.7) bracket the field trend observed experimentally.

The evaporation rate reflects the interplay of field and temperature at the apex. In an Arrhenius description,

$$\Phi_{\text{evap}} \;=\; \nu_0\, N_{\text{king}}\, \exp\!\left(-\frac{Q(F)}{k_B T}\right), \tag{1.8}$$

with attempt frequency ν_0, number of highest-field sites N_{king}, barrier $Q(F)$, and emitter temperature T. Higher F (smaller Q) or higher T exponentially increases the rate. Arrhenius behaviour has been widely reported [78, 89–91], with $\nu_0 \sim 10^{11}$–10^{13} Hz (some field dependence) and measured activation energies <1 eV [89]. At sufficiently low T and for light ions, tunnelling yields a weak T-dependence [73, 90, 92, 93].

Field–Temperature Calibration

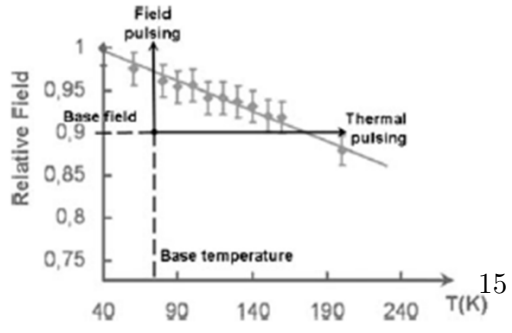

Figure 1.7: Calibration of field versus temperature at constant detection rate (tungsten). Data from [94], reproduced by [6].

By combining Eqs. (1.5) and (1.8), a compact relation between the field required to sustain a given rate and the specimen temperature is ob-

tained:

$$\frac{F}{F_{\text{evap}}} \approx 1+\ln\left(\frac{\Phi_{\text{evap}}}{\nu_0}\right)\frac{k_B T}{Q_0}. \quad (1.9)$$

This linear-in-T trend is consistent across materials [78, 89, 90, 94, 95]. An example at fixed detection rate is shown in Fig. 1.7 (tungsten data from [94], reproduced by [6]). The field needed to maintain a chosen detection rate is highly sensitive to the surface temperature: to ensure ions are time-correlated with excitation pulses, inter-pulse evaporation must remain negligible (low enough DC field at the base temperature), while the pulsed excursion (HV or laser-induced thermal) must be sufficient that relevant species evaporate predominantly during the pulse. In HV pulsing, this is tuned *via* the pulse fraction; in laser pulsing it is tuned *via* the temperature excursion at nearly fixed DC field. If the DC field (or base T) is too high, low-field species evaporate between pulses (composition bias, degraded depth fidelity); if the pulsed excursion is too small, high-field species are retained (sequence distortions) [6, 78, 96, 97]. These conditions also promote field-driven surface migration for species that linger, degrading lateral resolution [70, 98–100]. A careful field–temperature calibration, validated against element-specific curves, is therefore essential.

Post-ionization

Early evaporation models could not reproduce the observed charge-state distributions. Haydock and Kingham therefore proposed *post-ionisation*: atoms depart the surface predominantly as singly (sometimes doubly) charged ions and are further ionised in the intense near field, potentially through successive steps [77, 79]. The mechanism is summarised in Fig. 1.8.

By analogy with field ionisation, the $(n{+}1)$ step occurs at a critical distance

$$x_c = \frac{I_{n+1} - \phi_e}{F}, \quad (1.10)$$

with I_{n+1} the $(n{+}1)$th ionisation energy, ϕ_e the work function, and F the local field. The post-ionisation probability is thus field dependent and also sensitive to the residence time in the ionisation zone (ion velocity, hence mass). Isotope-dependent charge-state frequencies have been observed accordingly [92, 93]. Quantitative agreement with field-dependent charge states was

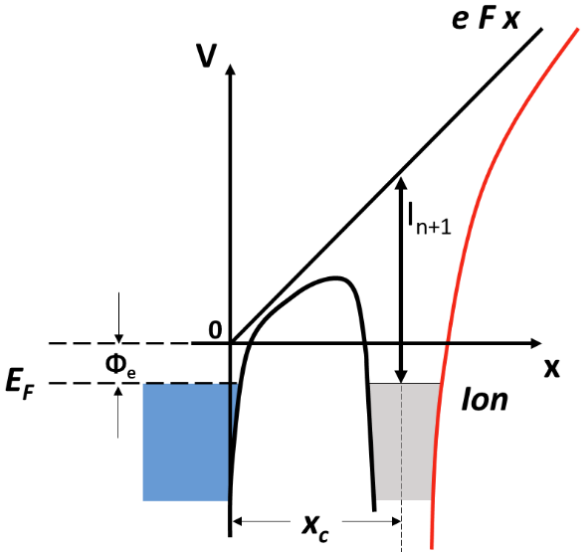

Figure 1.8: Potential-energy diagram of an ion near the tip in an electric field. I_{n+1}: $(n{+}1)^{\text{th}}$ ionisation energy; x_c: critical distance for the $(n{+}1)$ step; E_F: Fermi energy; ϕ_e: surface work function. Adapted from [6].

shown for Rh [77, 79]; Kellogg further demonstrated that the *average* charge state of W requires a multi-stage sequence, inconsistent with single-step or charge-hopping pictures [78]. Kingham subsequently tabulated charge-state probabilities $P_n(F)$ for many elements, the *Kingham curves* [79], which underpin standard practice [6, 7, 10].

1.3 Laser–Assisted APT

Since the late 1970s, short laser pulses have been used to trigger field evaporation in atom probes. Tsong and co-workers first demonstrated photon-assisted processes [101–103] and, together with Kellogg, implemented the first pulsed-laser source on an AP microscope [95, 104]. Many variants followed [105, 106], and modern instruments employ sub-nanosecond [107], picosecond [108], and femtosecond sources [11, 109]. Compared with HV pulsing, laser pulsing extends APT to poorly conducting materials (semiconductors, oxides, polymers) and can yield narrower energy spreads and improved mass resolution in metals, while reducing electrostatic/mechanical stress and the risk of specimen failure [15, 110–112]. Although several routes can contribute (photoionisation, transient field enhancement, and thermally assisted evaporation [15])it is now widely accepted that, for pulse durations $\gtrsim$ 100 fs, laser-assisted APT is predominantly *thermal*. Immediately after absorption the electron system heats while the lattice remains "cold"; over the electron–phonon coupling time (hundreds of femtoseconds to a few picoseconds) energy flows to

the lattice [113–115], with times depending on material and tip geometry [116–119]. For pulses longer than this coupling time (typically ∼1 ps), electrons and lattice are effectively coupled during the pulse, the surface temperature rises rapidly, and the elevated temperature in the high DC field triggers evaporation [101, 102].

1.3.1 Physical mechanisms of laser-pulse–assisted field evaporation

Field evaporation in APT reflects the interplay of optical, thermal, and electronic effects. Under laser excitation, several pathways are possible; here we focus on the two most relevant: *(i)* resonant photo-ionization of surface atoms and *(ii)* thermally assisted evaporation *via* a transient temperature rise.

Photo–Ionization

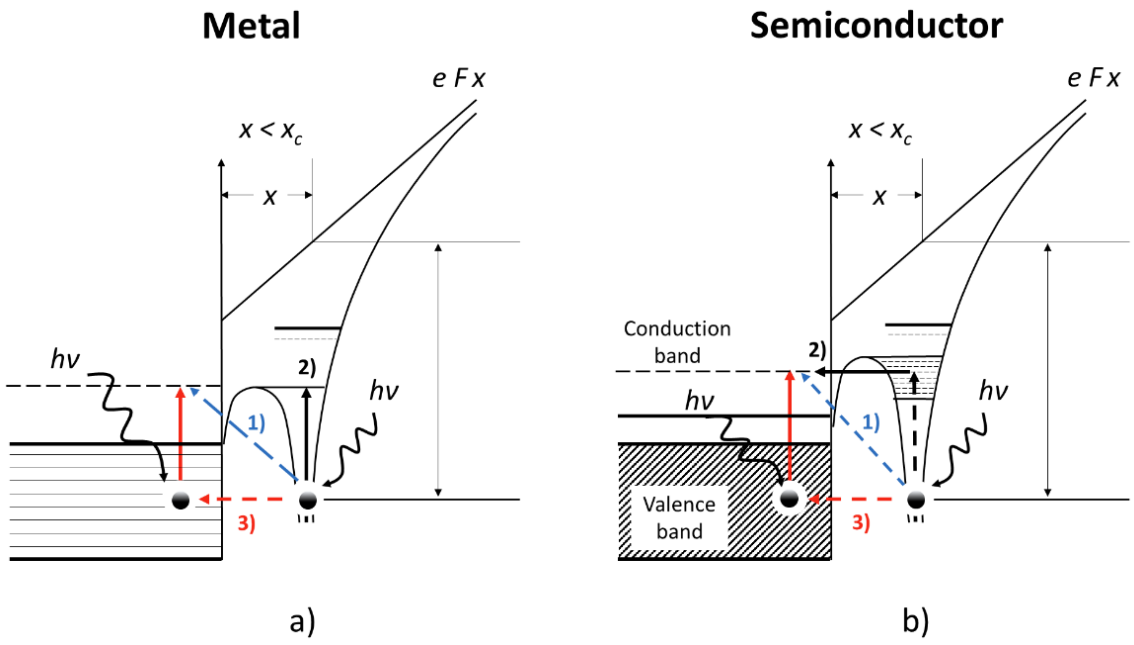

Figure 1.9: Illustration of the photo-ionization mechanism for (a) metallic and (b) band-gap (semiconductor) materials under an electric field. Arrows indicate electron excitation (red), relaxation (blue), and tunnelling (black) pathways. Adapted from [110].

Photo-ionization is a resonant pathway in which one or more photons promote a surface-adatom electron to a vacant state, thereby ionizing the adatom [120, 121]. Tsong and co-workers identified three routes [101]: (1) direct tunnelling of an adatom electron into an empty bulk state; (2) photon-assisted excitation followed by tunnelling into the conduction band; and (3) photon creation of valence-band holes enabling tunnelling into the valence band. In metals (Fig. 1.9(a)),

the high electron density and mobility favour fast re-neutralisation, so photo-ionization is not observed [13]. In band-gap materials (Fig. 1.9(b)), the surface field bends the bands and suppresses rapid electron–hole recombination, stabilising the ion long enough for field evaporation [110, 122]. Kinetically, photo-ionization is quasi-instantaneous, whereas field evaporation proceeds on a $\sim$0.5 ps timescale [123, 124]. Within this picture, atoms are first ionised to 1+ and then post-ionised near the tip (Kingham theory) [125]; an activation barrier Q_n^{ionic} reduces the effective photo-ionization probability by about an order of magnitude [124]. Photon-induced evaporation also modifies ion-energy distributions, giving peaks with more slowly rising or quasi-symmetric leading edges compared to conventional field evaporation [13]. Experimentally, photon-assisted evaporation of Si has been demonstrated at relatively low fields with nanosecond pulses [121] and at low laser energy with sub-picosecond pulses [126].

Thermally Assisted Evaporation

A short laser pulse can trigger field evaporation by depositing optical energy that is rapidly transferred from excited electrons to the lattice (electron–phonon coupling in a few picoseconds), producing a transient temperature rise at the tip apex—the "thermal pulse." The evaporation sequence and its time–temperature window are sketched in Fig. 1.10(a). Early experiments showed that the emitter temperature can increase by a few hundred kelvin after a pulse, sufficient to thermally activate evaporation [78, 104, 127]. In this regime, the instantaneous evaporation rate follows an Arrhenius law with the time-dependent apex temperature, $\phi(t) = \nu \exp[-Q_n/(k_{\text{B}}T(t))]$. For a wire-like tip (1D diffusion), the apex temperature relaxes according to [94]

$$T(t, z{=}0) = T_0 + \frac{T_{\text{rise}}}{\sqrt{1 + 2\,t/\tau_{\text{cooling}}}}, \qquad \tau_{\text{cooling}} = \frac{w^2}{\alpha}, \tag{1.11}$$

where T_0 is the base temperature, α the thermal diffusivity, and w the effective (Gaussian) half-width of the heated zone. Immediately after electron–phonon thermalisation (defining $t = 0$ [128]), the axial temperature profile is often approximated as Gaussian,

$$T(t{=}0, z) = T_0 + T_{\text{rise}} \exp\!\left(-\frac{z^2}{2w^2}\right). \tag{1.12}$$

Pump–probe measurements on tungsten tips (femtosecond excitation at $\lambda = 800$ nm) directly confirm this behaviour: Fig. 1.10(b) shows an apex jump of ~ 160 K above $T_0 = 40$ K with cooling on the 10–100 ns scale, consistent with $w \sim 1.5$ μm [94]. Because ions can be emitted over the full cooling window, the spread in departure times broadens time-of-flight distributions and can therefore degrade mass resolution.

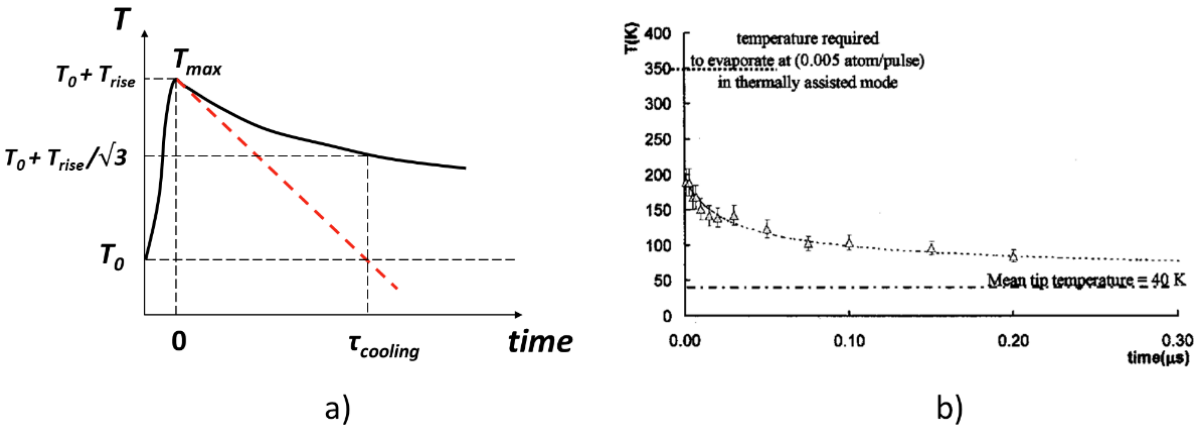

Figure 1.10: Thermally assisted evaporation. (a) A laser pulse produces a transient temperature rise at the apex followed by diffusive cooling that defines the evaporation time window (schematic). Adapted from [7]. (b) Measured apex temperature versus delay after the laser pulse on a metallic tip; the relaxation is well fit by $T(0,t) = T_0 + T_{\max}/\sqrt{1 + 2t/\tau_{\text{cooling}}}$ with $T_0 = 40$ K, $T_{\max} \approx 160$ K, and τ_{cooling} set by the heated width (~ 1.5 μm) [94].

In metals, minimising the thermal pulse, *i.e.* reducing the duration of significant overheating at the apex, improves mass resolution by compressing the evaporation time window. This can be achieved by adapting illumination parameters (shorter wavelength, tighter spot, shorter pulse), by modifying tip geometry (larger cone angle to improve heat sinking), and by lowering the base temperature. In particular, shorter wavelengths reduce the optical absorption depth and the effective heated width w, which sharpens peaks [129]. Additional discussions of radius and cone-angle effects are given in [7, 123, 129, 130].

For semiconductors and dielectrics, wavelength and fluence strongly influence both peak width and the long thermal tail (slow evaporation during cooling). Figure 1.11 displays representative spectra under varied optical conditions: panel 1.11(a) shows metallic (steel) data versus wavelength; panel 1.11(b) shows a non-metallic (silicon) specimen at fixed $\lambda = 1030$ nm with increasing pulse energy; and panel 1.11(c) shows the same non-metallic specimen versus wavelength at fixed fluence. In these examples, higher energy at 1030 nm reshapes peaks through thermal broadening, while longer wavelengths can extend the tail by increasing the heated vol-

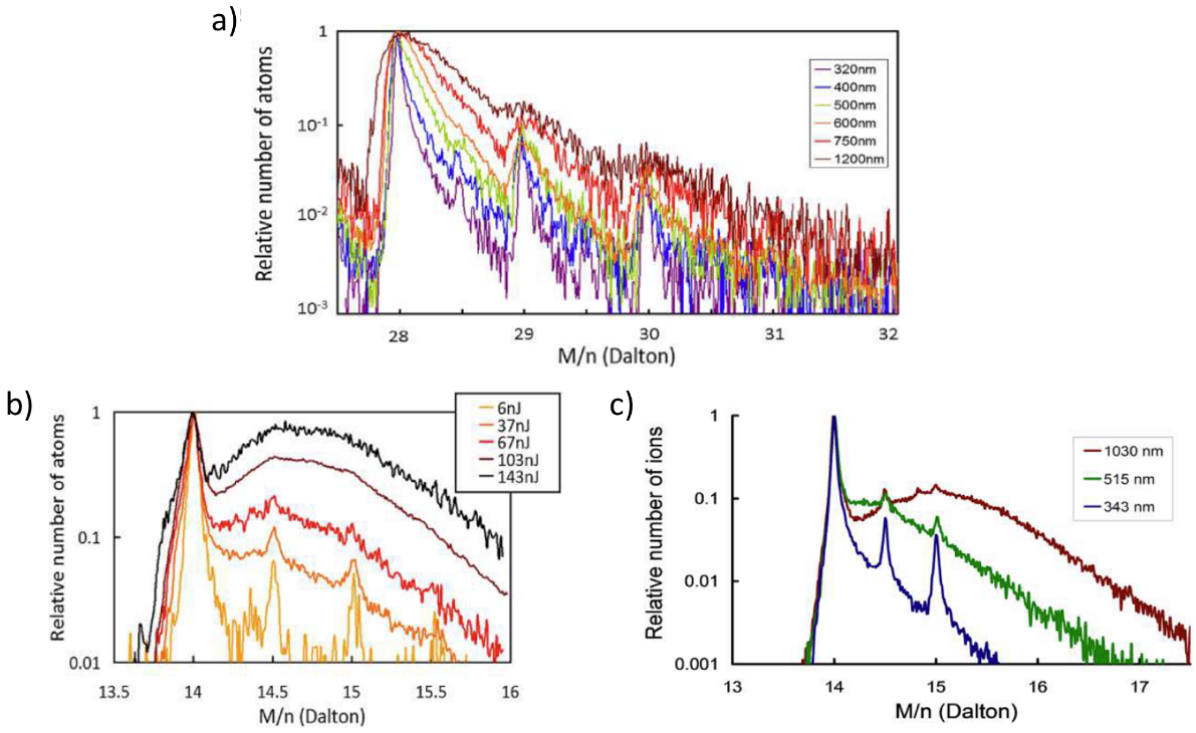

Figure 1.11: Representative laser-assisted APT spectra adapted from [7]. (a) Metallic specimen (steel tip) versus laser wavelength. (b) Non-metallic specimen (silicon tip) versus laser energy at fixed $\lambda = 1030$ nm. (c) Same non-metallic specimen versus wavelength at fixed energy.

ume and slowing cooling [7]. In addition, the appearance of a local minimum following the main peak, succeeded by a delayed secondary maximum, is consistent with a two-step thermal response: an initial rapid temperature rise at the apex driven by direct laser absorption, followed by a delayed heat flux diffusing from the tungsten shank (pre-tip) toward the apex. This secondary thermal contribution, occurring on longer time scales, reactivates evaporation after a transient cooling period and gives rise to the observed secondary maximum in the time-of-flight distribution [131, 132]. Finally, defects introduced during FIB preparation, together with the applied DC field, can further alter absorption pathways and transient heating, as evidenced by the laser–assisted responses reported in [133, 134].

1.4 Atom probe tomography of bio-materials: state of the art

Atom probe tomography (APT) has gradually moved from metals into biology because it couples near-atomic spatial detail with chemical specificity. Early results that this might be possible go back to Anway's 1969 observations of water under high fields on tungsten [135] and to Panitz's field-ion microscopy and early atom-probe experiments on macromolecular assemblies,

in the 1980s [136–138]. Those studies did not yet deliver the quantitative, three-dimensional reconstructions of modern LEAP instruments, but they set a clear direction that has since matured into bio-APT [20, 139].

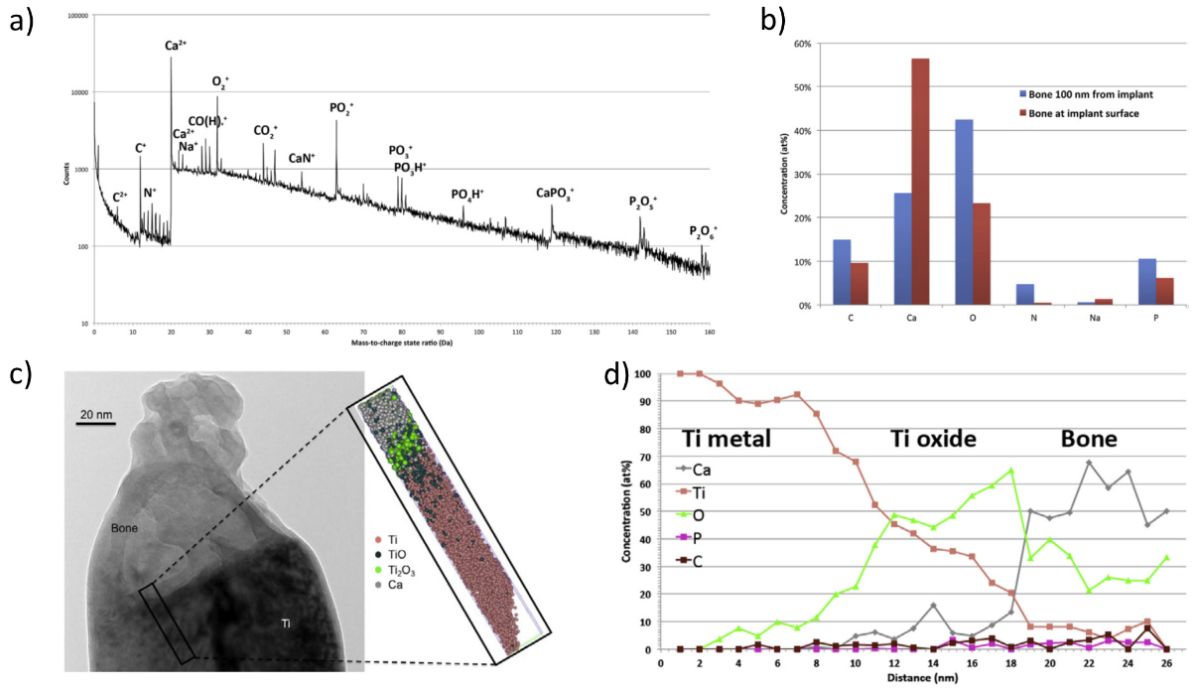

Figure 1.12: Bio-APT at a bone–implant junction: (a) APT mass spectrum acquired from bone ∼100 nm from the implant surface; (b) composition comparison across the bone–implant interface; (c) BF-TEM of an APT tip with inset atom map; (d) concentration profile across the interface (at.%). Note that the inorganic signal in (a,b,d) arises from the *native biomineral* (bone apatite) and is distinct from the exogenous metallic implant. Adapted from [140].

A natural first step for bio-APT was to investigate *biominerals*, *i.e.*, tissues in which an *endogenous, native inorganic* phase (such as carbonated apatite in bone or magnetite in chiton teeth) coexists with an organic matrix and thus provides strong chemical contrast. Building on geoscience applications of APT [141–146], Gordon and Joester resolved organic/inorganic interphases at magnetite boundaries in chiton teeth [147], and similar strategies soon extended to bone and dental tissues, where APT can map gradients across *biological* mineral–organic interfaces (Fig. 1.12) [140], revealing hierarchical chemical organisation at tens-of-nanometres length scales [17, 140, 148–152]. Importantly, in this context "inorganic" refers to the tissue's *own* mineral and not to artificial metallic implants. When an implant is present, it serves to illustrate that APT can probe composition right up to the bone–implant interface while still distinguishing the endogenous mineral from the exogenous metal. In parallel, APT was adapted to softer organic targets, from self-assembled monolayers and molecular films [153–156] to playful

demonstrations of crystallinity in everyday materials [157, 158].

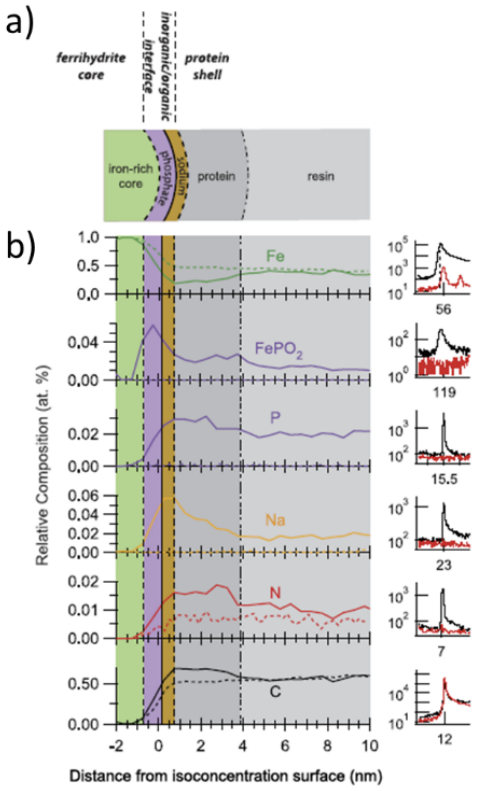

Figure 1.13: Composition profiling of ferritin embedded in Lowicryl resin (adapted from [19]). (a) Schematic indicating the Fe,O-rich ferrihydrite core, a narrow P-enriched interphase, and the protein shell within the resin. (b) Proxigram composition profiles for Fe, $FePO_2$, P, Na, N, and C across the interface; small panels at right show the corresponding mass-spectral regions used for ranging.

For soft, insulating biomolecules, placing the protein inside a *solid* host is considered one of the most reliable routes. Perea *et al.* embedded ferritin in a UV-cured acrylic resin and stabilised voltage pulsing with a thin Cr overcoat [19]. The matrix choice was deliberate: the resin is mechanically forgiving and, crucially, chemically distinct from the protein, a C-rich, N-poor background that makes the N-rich shell and Fe/P-bearing core stand out. With the surrounding matrix composition characterised in advance (APT of the bare resin) and aided by ferritin's roughly spherical geometry, they could map the matrix–protein interface. In proxigrams this appears as a clean sequence: Fe,O-rich core, a narrow P-enriched interphase, then the N/Na-rich shell, set against the polymer background (Fig. 1.13). This chemical contrast enabled the identification of key interfacial features in individual proteins.

Sundell *et al.* immobilised single Immunoglobulin G (IgG) molecules in amorphous SiO_2 *via* sol–gel chemistry and analysed them by laser APT [18]. The glass host withstands Maxwell

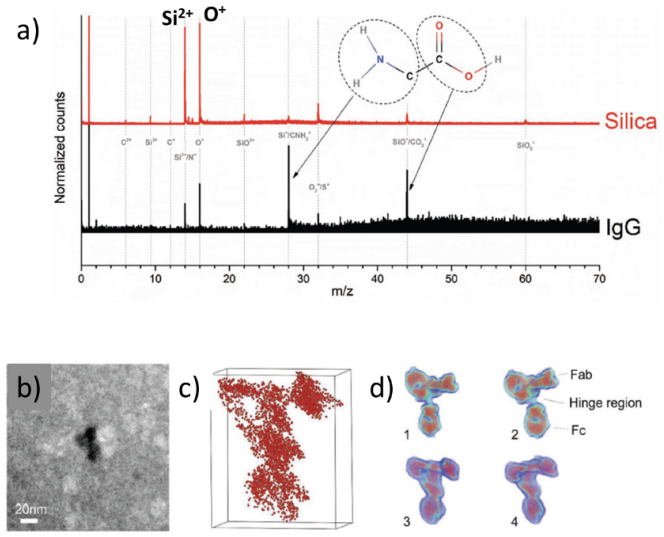

Figure 1.14: IgG embedded in a water-glass–derived silica matrix (adapted from [18]). (a) Annotated mass spectra on a linear scale from the silica matrix (red, top) and from an IgG-enriched subvolume (black, bottom); arrows mark peaks from amino-acid fragments. (b) Bright-field TEM micrograph of a single IgG inclusion in the silica matrix (20 nm scale bar). (c) APT 3D point-cloud of C-bearing ions from the IgG subvolume. (d) Isodensity reconstructions of the same subvolume from four viewing directions, resolving the Fab arms, hinge region, and Fc domain.

stresses that would fracture soft matter, and the Si/O background leaves room for robust organic fragments, e.g. $CNH_x^+ \sim 30$ Da and $CO_2{}^+ \sim 44$–45 Da, to mark the protein. With simple thresholding on C-bearing ions, the reconstructions recover the familiar Y-shape, with arms, hinge, and Fc domain visible at the ∼1–2 nm level, despite residual overlaps such as N^+ vs. Si^{2+} (Fig. 1.14).

Translating this sensitivity to fully *hydrated* systems is harder. Ultra-high vacuum strips water from surfaces, and cryogenic handling can turn native liquid into hexagonal ice or introduce transfer artefacts. Here, historical ramped field-desorption studies on adsorbed water [135, 159–164] remain surprisingly relevant: they established that evaporation proceeds mainly as $(H_2O)_nH_3O^+$ clusters, with cluster size shrinking as the field rises [160], and that colder or thicker films demand higher fields due to dielectric screening [159]. Modern workflows fold these lessons into cryo-APT and encapsulation protocols that allow analysis of aqueous solutions, liquid/solid interfaces, and even pure water [165–174]: liquids are stabilised either physically (encapsulation) or thermally (cryo), while the analysis remains genuinely chemical and three-dimensional.

Normally, bio-samples are fragile and may suffer from thermal accumulation, drifting baselines,

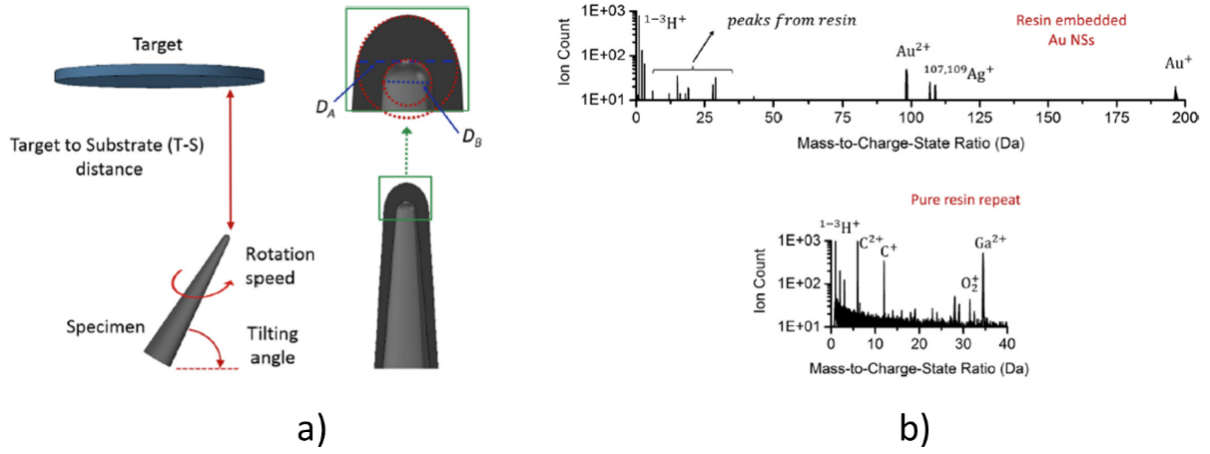

Figure 1.15: (a) Sputter-deposition geometry and inputs: target–substrate (T–S) distance, specimen rotation, and tilt. The inset illustrates the coated apex and the response variables D_A and D_B (end-tip diameter before/after coating). (b) Mass spectra comparison: resin embedded with Au nanospheres (top) showing pronounced Au^+/Au^{2+} and $^{107,109}Ag^+$ peaks, versus a pure-resin control (bottom) dominated by low-m/z polymer fragments.

or low yield. In order to use HV pulsing, the tip is covered by a nanometric-scale conductive layer, so the apex behaves electronically like a metal during evaporation. Two routes appear repeatedly in the literature and are complementary rather than competing. Adineh *et al.* used an *ex situ* sputter coater to lay down ultrathin noble-metal shells (optimised here with Ag) while tuning distance, rotation, and tilt to limit apex shadowing [175]. The resulting $\lesssim$10 nm films preserve sharpness yet equalise the surface potential; in practice, they lift the signal-to-noise, suppress polymer fragments, and stabilise the detection rate, as the comparison with uncoated resin controls makes clear (Fig. 1.15).

Schwarz *et al.* instead deposited chromium *in situ* in the dual-beam FIB, sputtering from a Cr lamella while rotating the specimen to achieve uniform 360° coverage [176]. This preserves vacuum continuity and gives very homogeneous ∼10 nm shells over several hundred nanometres of the shank without blunting the apex. The spectral outcome is similar: sharper major peaks, shorter tails, and improved visibility of minor isotopes, with Ca-bearing dentin offering a clear demonstration (Fig. 1.16).

Ex situ sputtering is tool-simple and material-flexible but is more sensitive to line-of-sight shadowing at the very tip; *in situ* coating offers better geometric control and vacuum continuity, at the cost of a more involved workflow.

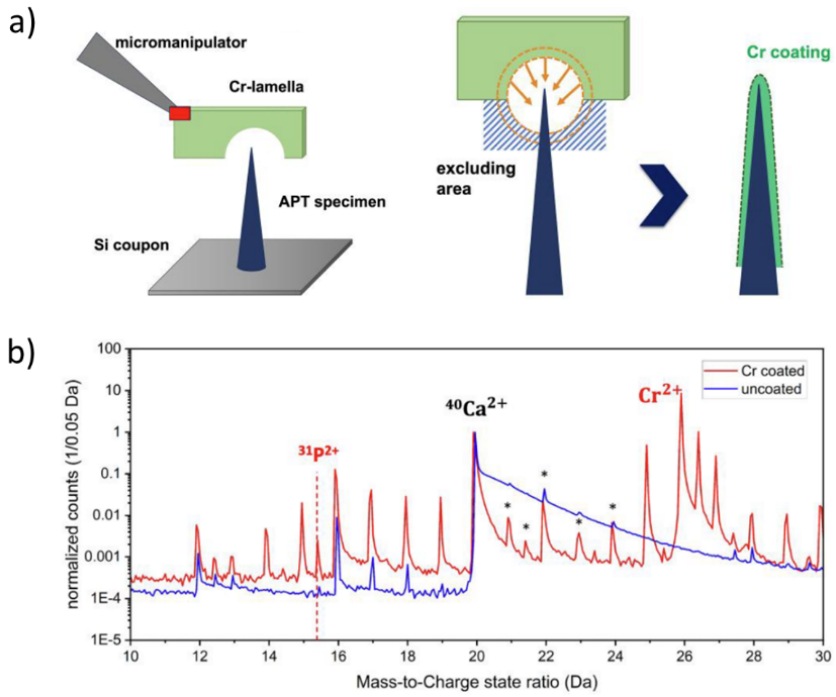

Figure 1.16: (a) In-situ Cr coating in the FIB: a Cr lamella is positioned to sputter-coat the exposed apex while shaded regions are screened. (b) Dentin spectra normalized to $^{40}Ca^{2+}$: coated (red) shows lower background and sharper Ca isotopes than uncoated (blue); Cr^{2+} lines appear near 24–28 Da.

Single-layer graphene sheets can also be employed as an ultrathin conductive film that both carries current and seals liquids. Originally developed to enable voltage-pulsed APT of hydrated cells [177], graphene encapsulation was soon extended to solutions containing nanoparticles or proteins [165–167, 177]. Despite its exceptional mechanical strength, graphene does not impose prohibitively high evaporation fields in practice: owing to its single-atom thickness and intimate contact with the underlying specimen, it progressively ruptures or is locally removed during the early stages of evaporation, allowing the analysis to proceed through the encapsulated material rather than through a thick and rigid overlayer.

From an optical standpoint, graphene exhibits a well-known and modest absorption of approximately 2.3% per layer over a broad spectral range, including the near-UV and near-infrared regimes typically used in laser-assisted APT. As a consequence, graphene contributes only weakly to laser-induced heating, while its high in-plane thermal conductivity facilitates rapid lateral heat dissipation, mitigating local thermal accumulation at the apex [166, 178, 179]. In addition, graphene mitigates two familiar cryo–UHV challenges, which is the formation of crystalline ice and rapid water loss, by acting as an efficient diffusion barrier, particularly effective for small

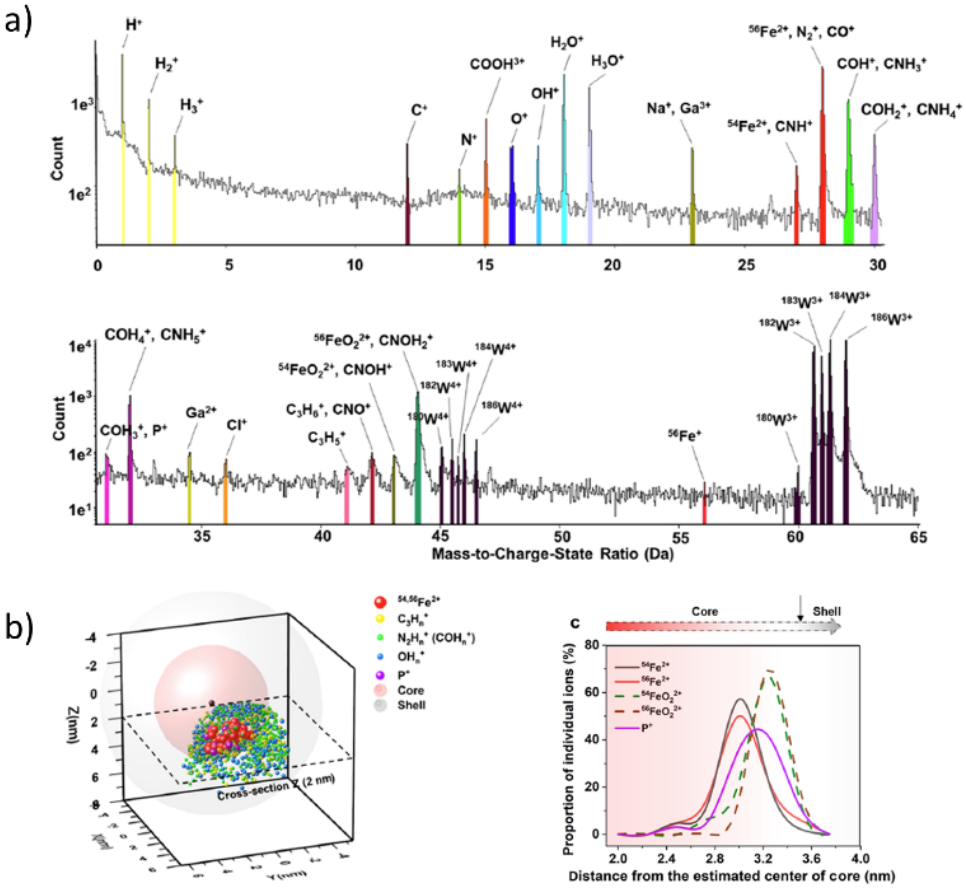

Figure 1.17: Graphene-encapsulated ferritin (reproduced from [165]). (a) Mass spectrum with water-related ions, organic fragments, and Fe species. (b) Cluster analysis reveals a Fe-rich core and proteinaceous shell.

tip radii [180, 181].

In the specific case of hydrated proteins, Qiu *et al.* [165] floated graphene over micrometric droplets placed on pre-sharpened W tips, adjusting the transfer to stabilise the liquid layer while keeping the surface conductive for voltage pulsing. The resulting spectra (Fig. 1.17(a)) carry water-related ions, organic fragments, and Fe species, and clustering recovers the ferritin core–shell architecture (Fig. 1.17(b)).

1.5 Silica as a candidate for bio-molecules encapsulation for APT study

Silica (SiO_2) is one of the most abundant materials in the Earth's crust and appears in a wide range of natural and synthetic forms. In nature, it occurs both as crystalline polymorphs such as quartz [182–184] and as amorphous silica without long-range order [185]. It is also the main constituent of glass and sand, and it underpins a large number of technical and industrial applications where it is often used in colloidal form. Structurally, silica consists of a network of silicon atoms tetrahedrally coordinated by oxygen, with oxygen atoms bridging between two silicon centers to form a three-dimensional network.

Amorphous silica is of particular interest for APT. Beyond its ubiquity and technological relevance, it provides a versatile host matrix for biomolecules, enabling immobilization and encapsulation strategies [186–188]. Inspired by naturally occurring silicification in organisms such as diatoms, sol–gel derived silica matrices have been used to encapsulate proteins, improving their activity and stability [189–192]. This makes silica a model system for probing the challenges of biomaterial analysis with APT.

At the same time, silica exhibits properties that complicate APT analysis. Amorphous silica generally displays a high degree of porosity and a correspondingly large surface area. These features can be quantified by nitrogen physisorption, where the surface area is extracted using the BET method [193] and the pore size distribution inferred by models such as BJH (mesopores, 2–50 nm) [194] and Horvath–Kawazoe (micropores, < 2 nm) [195]. Such porosity affects the evaporation behavior of tips during APT analysis, it reduces reconstruction fidelity, and enhances surface chemistry effects.

Synthetic routes further influence silica's structure and properties. The widely used Stöber process, based on hydrolysis and condensation of tetraethyl orthosilicate (TEOS), is strongly pH-dependent: hydrolysis dominates under acidic conditions, while condensation is faster under basic conditions, leading to gels with distinct porosity [196–199]. Alternative sol–gel routes rely on aqueous alkaline silicates ("water glass"), which gel upon neutralization and can be shaped into bulk or thin films [200]. The details of these pathways affect pore size, network connectivity, and the distribution of silanol groups, all of which play a role in tip stability and evaporation under high fields.

For APT, these characteristics imply both opportunity and challenge. On the one hand, silica is an attractive matrix for bio-encapsulation and a technologically relevant oxide. On the other hand, its porosity, charging behaviour, and sensitivity to preparation conditions complicate field evaporation and accurate reconstruction. These problems motivate the dedicated experimental and modelling studies [18, 30, 201] on the subject.

Sol–gel silica provides a robust, chemically clean host for proteins, but it is amorphous and insulating, therefore reproducible, high-quality spectra demand tight control of the field–temperature balance, often with the aid of thin conductive layers (Cr sputter films or graphene encapsulation). Against this backdrop, the next chapter introduces *THz-assisted* APT as a complementary trigger to conventional UV/visible pulsing. THz transients deposit less energy on the apex than UV, and prior work on metals has shown that THz can drive predominantly *athermal* (field-dominated) evaporation [24]. In principle, this mitigates the thermal excursions that, under UV, broaden peaks, raise backgrounds, and risk denaturing biomolecules embedded in silica.

1.6 Introduction to THz-Assisted Atom Probe Tomography

1.6.1 THz Radiation Properties

Terahertz (THz) radiation spans the spectral region between microwaves and the infrared, approximately 0.1 THz $\lesssim \nu \lesssim$ 30 THz, corresponding to wavelengths $\lambda \approx 3$ mm to 30 μm; this portion of the electromagnetic spectrum is highlighted in Fig. 1.18. A useful reference point is $\nu = 1$ THz $\Rightarrow \tau = 1/\nu = 1$ ps, $\lambda = c/\nu = 300$ μm, $E_\gamma = h\nu \approx 4.1$ meV. Because meV photon energies lie well below typical electronic band gaps, THz fields are generally non-

ionizing and deposit comparatively little heat versus UV/visible light. Many dry dielectrics are relatively transparent in this band, whereas water is strongly absorbing [202, 203]. In the time domain, single-cycle THz transients are sub- to few-picosecond in duration, consistent with ion-evaporation times, making them promising for field-driven (rather than thermally driven) triggering in APT. Free-space THz sources commonly deliver peak fields in the order of tens to hundreds of $\mathrm{kV\,cm^{-1}}$ range; at nanosharp emitters, these fields can be substantially amplified by near-field enhancement effects arising from geometric field concentration and antenna-like coupling at the tip apex [204–206]. In practice, the effective apex field is not set by the incident THz amplitude alone, but is carefully controlled through the emitter geometry (apex radius and shank angle), the electrostatic boundary conditions, and the applied DC bias, which together define the local field enhancement factor. A detailed discussion of the near-field enhancement mechanism and of the criteria used to select the appropriate THz field strength for controlled evaporation is provided in Sec.1.6.2.

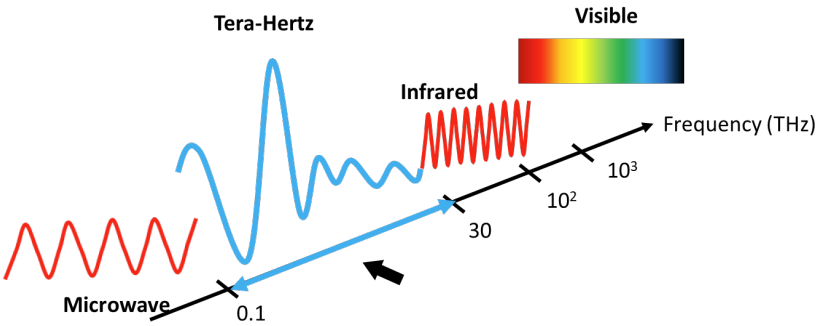

Figure 1.18: Electromagnetic spectrum highlighting the THz band (shaded): $\nu \sim 0.1$–10 THz, $\lambda \sim 3$ mm–30 μm. At 1 THz, the period is 1 ps and the photon energy is ~ 4.1 meV. Adapted from [207].

1.6.2 THz evaporation mechanism

THz assistance alters the emission physics in APT. In a pump–probe study on Al tips [24], a single-cycle THz transient and a NIR pulse were applied with a variable delay, and the evaporation rate was recorded. Three behaviors emerged: (i) THz arrives *before* NIR — the rate is unchanged; (ii) THz and NIR *overlap* — the rate remains nearly constant; (iii) NIR arrives *before* THz — the rate rises markedly. This asymmetry indicates that NIR mainly heats the apex (thermal assistance), whereas THz triggers emission without appreciable heating (athermal, field-driven).

We have seen that the evaporation rate depends on the lattice temperature T and on the activation barrier $Q(F)$, which decreases with increasing surface field F. Near-infrared (NIR) excitation primarily increases T through electronic and lattice heating [132], whereas a THz pulse predominantly boosts F with a negligible thermal contribution [208]. A simple model treating NIR as a ΔT excitation and THz as a ΔF excitation reproduces the delay dependence of the measurements, corroborating an athermal, field-driven evaporation mechanism under THz drive [24].

In this configuration, the advantage of a THz pulse over a combination of electrical pulsing and IR illumination lies in the ultrafast and highly localized nature of the THz field enhancement: the THz transient directly modulates the surface field on sub-picosecond timescales and at the apex itself, without introducing significant Joule heating or long-lived thermal diffusion from the shank. By contrast, electrical pulsing is limited by circuit bandwidth and rise time, while IR excitation inevitably couples energy into the lattice, broadening the evaporation time window and increasing thermal artefacts. As a result, THz excitation enables a temporally gated, field-dominated evaporation regime that is not accessible through conventional HV + IR schemes.

On the field–temperature diagram introduced in Fig. 1.7, near-UV pulses primarily shift the operating point horizontally (increasing T at nearly fixed F as shown in Fig. 1.19(a)), so evaporation continues over the cooling window and mass peaks acquire long, thermal tails. In contrast, a single-cycle THz transient is commensurate with ion departure times, deposits little heat, and vertically increases F with $\Delta F \gg \Delta T$; this opens a short, field-limited emission gate and suppresses thermal tailing (Fig. 1.19(b)).

Field evaporation requires apex fields of several $\mathrm{V\,nm^{-1}}$. Free-space UV and THz amplitudes are far smaller ($10^{-4} - 10^{-2}\,\mathrm{V\,nm^{-1}}$). While in the case of UV pulses the antenna effect is inhibited by the small ratio λ_{UV}/R_{tip} (Fig. 1.20(a)), on the contrary THz-APT relies on near-field *antenna* enhancement (Fig. 1.20(b)) at the apex: when $\lambda_{THz} \gg R_{tip}$, the local field is amplified by $\eta = F_{\mathrm{apex}}/F_{\mathrm{incident}}$ up to $\sim 10^3$ as in the case of aluminium tips (Fig. 1.20(c)). With a subthreshold DC bias, the instantaneous field becomes

$$F_{\mathrm{Tot}}(t) = F_{\mathrm{DC}} + \eta\, F_{\mathrm{incident}}(t),$$

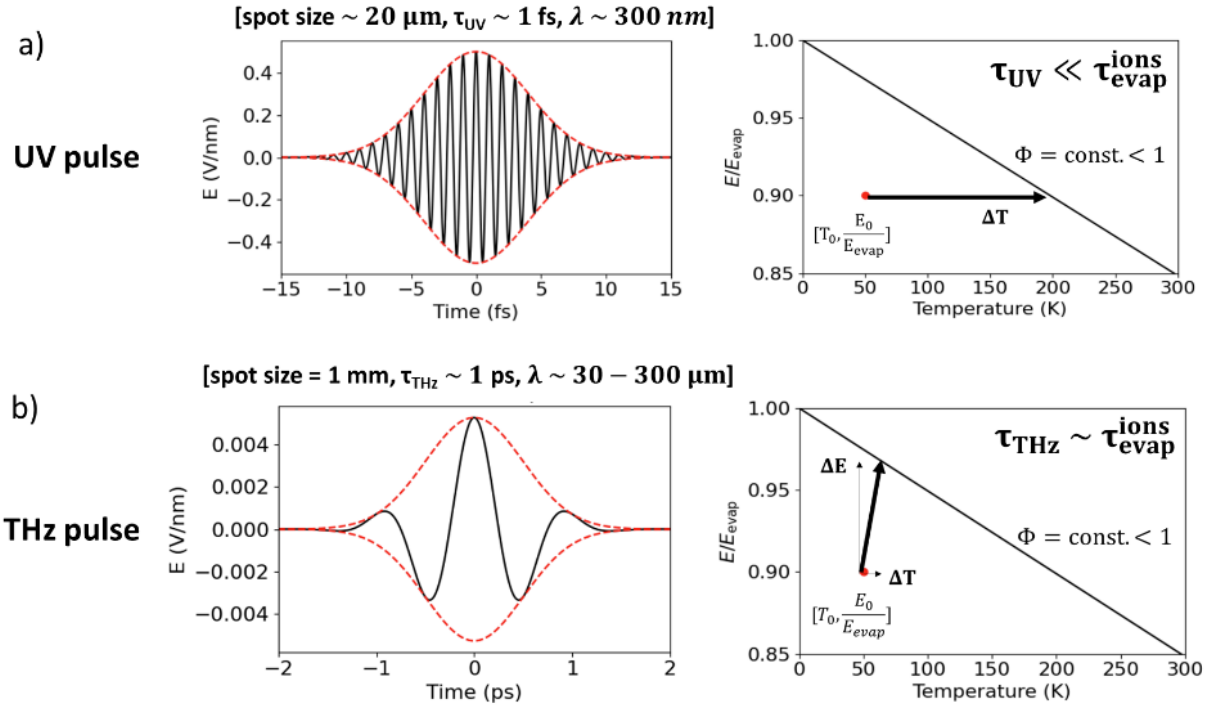

Figure 1.19: Comparison of optical (UV) and THz driving in APT. (a) Top–left: representative UV pulse (few-fs carrier under a sub-10 fs envelope). Top–right: field–temperature operating map for UV; with $\tau_{\mathrm{UV}} \ll \tau_{\mathrm{evap}}$ ions cannot follow the optical field, so evaporation proceeds mainly by a *horizontal* thermal shift ΔT at nearly fixed field. (b) Bottom–left: single-cycle THz transient with period 0.3–3 ps, comparable to ion departure times. Bottom–right: corresponding map for THz; weak absorption implies small heating, while the drive produces a *vertical* field increase ($\Delta F \gg \Delta T$), enabling primarily field-driven evaporation. Axes and values are realistic; red dashed curves indicate pulse envelopes.

so incident THz transients can momentarily exceed F_{evap}.

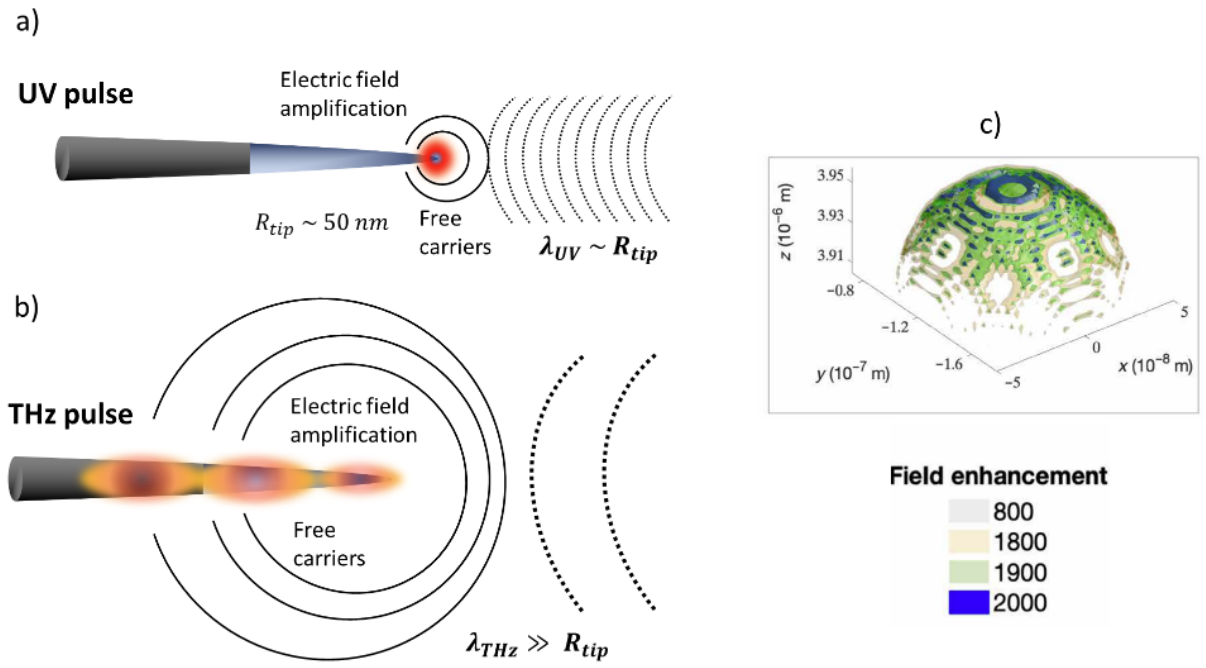

Figure 1.20: Near-field amplification at a nanotip. (a,b) Comparison between UV ($\lambda_{\text{UV}} \sim R_{\text{tip}}$) and THz ($\lambda_{\text{THz}} \gg R_{\text{tip}}$) illumination. In the UV, the wave "resolves" apex details, and the near-field enhancement is modest; in the THz, the tip behaves as an electrically small antenna, driving strong charge accumulation and a highly confined apex field. (c) Isosurface plots of the 3D field distributions calculated numerically for an Al tip at 2 THz for different enhancement factors [24].

Figure 1.21 reports near-field maps of the THz electric field around nanotips under plane-wave illumination. The *left* panel reproduces the FDTD (Lumerical) simulation of a purely metallic tip from Houard *et al.* [27], showing a strong capacitive concentration at the apex with a frequency-dependent enhancement that reaches $\eta \sim 10^3$ for few-THz spectra. In contrast, the *right* panel shows an analogous FDTD calculation for a silicon tip (same nominal geometry), yielding only a modest enhancement $\eta \approx 3.5$ (unpublished Lumerical result, this work). This side-by-side comparison confirms that the THz "antenna" effect is intrinsically *metallic*: conduction electrons in metals support surface currents that funnel the incident field into a nanometre-scale hot spot, whereas the finite conductivity and dielectric response of semiconductors/insulators at THz frequencies prevent substantial field build-up. Practically, THz-assisted field evaporation *via* direct field boosting is therefore far more efficient for metallic emitters than for wide-bandgap or weakly doped semiconductor tips.

In [24], the near THz field at the apex of the APT sample was measured using an NIR + THz pump–probe that maps a delay-dependent photocurrent to a rectified THz voltage at the apex

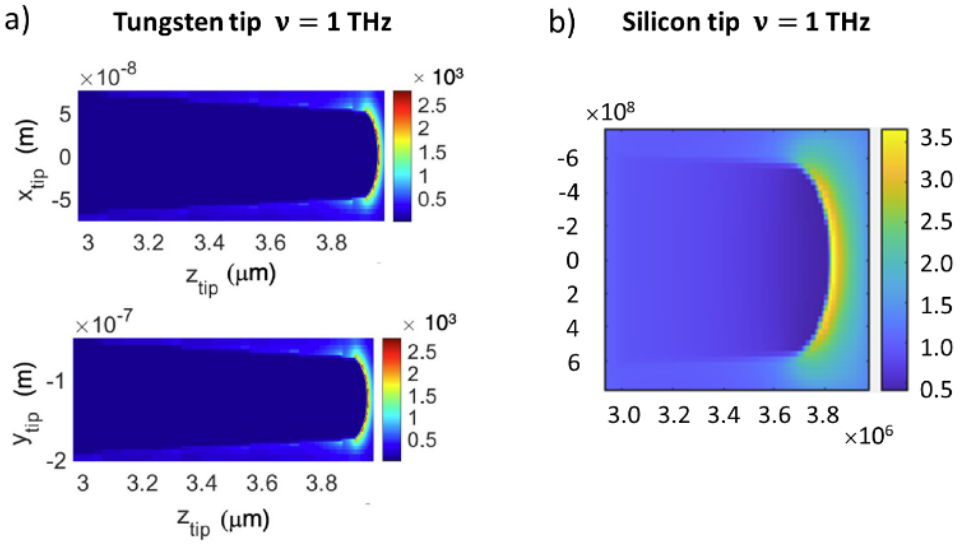

Figure 1.21: Near-field THz maps around nanotips (single composite image). (a) metallic nanotip under THz illumination—FDTD (Lumerical) field map showing strong apex concentration with a frequency-dependent enhancement up to $g \sim 10^3$; reproduced from Houard *et al.* [27]. (b) silicon nanotip with the same nominal geometry—analogous FDTD (Lumerical) simulation yields only a modest enhancement $g \approx 3.5$ (unpublished). Metals thus exhibit a pronounced THz "antenna" effect, whereas semiconductors/insulators show little amplification.

(Fig. 1.22).

The rectified potential is converted to a local near-field amplitude *via*

$$F_{\mathrm{THz}}(t) \;=\; \frac{V_{\mathrm{THz}}(t)}{k_f\, R_{\mathrm{tip}}}, \tag{1.13}$$

where R_{tip} is the apex radius and $k_f \in [2, 8]$ is a geometry factor (experimentally determined or obtained from electrostatic modelling). Applying this analysis, we find an apex-field enhancement of $\eta \equiv F_{\mathrm{apex}}/F_{\mathrm{incident}} \approx 2 \times 10^3$ was obtained.

1.6.3 Experimental studies on Al and LaB_6 tips

The first benchmark of THz versus NIR was performed on a simple metal (Al) under *identical* DC bias and detection rate so that the only controlled variable is the driving field [24].

Under THz drive, the Al^+ peak narrows substantially (up to $\sim 4\times$ improvement in $\Delta M/M$ at 10^{-1} % height) and lattice planes are well resolved in the reconstruction along $\langle 002 \rangle$, $\langle 113 \rangle$, and $\langle 224 \rangle$ (see Fig. 1.23).

The second published study, comparing THz and NIR *on the same tip* at matched bias/detection

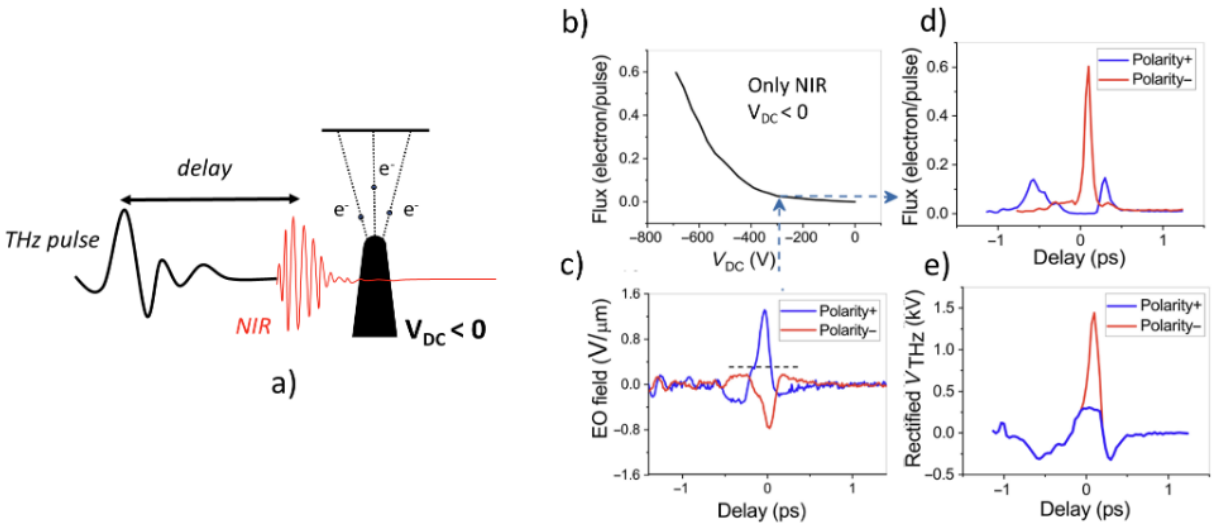

Figure 1.22: Rectified terahertz voltage at the tip apex. Adapted from [24]. (a) Schematic of the NIR + THz pump–probe arrangement at a biased metal tip. (b) Current–voltage characteristic of NIR–driven electron emission from an Al tip (apex radius $\sim$ 70 nm) at $I_{\mathrm{NIR}} = 2.3\,\mathrm{GW\,cm^{-2}}$. (c) Two THz transients with inverted polarity measured by Electro-Optic (EO) sampling outside the APT chamber. (d) Photocurrent modulation at the tip for the THz waveforms of (c) at $V_{\mathrm{DC}} = -300$ V and $I_{\mathrm{NIR}} = 2.3\,\mathrm{GW\,cm^{-2}}$. (e) Rectified THz waveform at the apex reconstructed from (b) and (d).

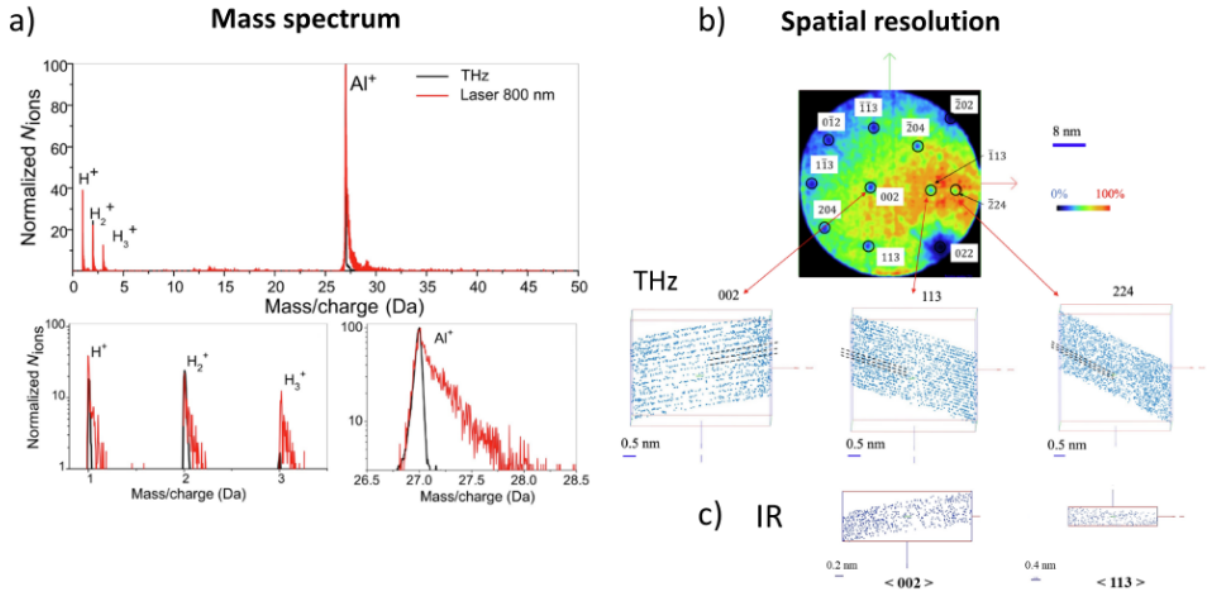

Figure 1.23: THz- vs. NIR-assisted APT on Al [24]. (a) Overlaid spectra for pure Al ($\sim 10^5$ ions) at $V_{\mathrm{bias}} = 9$ kV, $T = 50$ K, 0.01 ions/pulse; NIR reference at $I_{\mathrm{NIR}} = 2.3\ \mathrm{GW\,cm^{-2}}$. Inset: H and Al^+ on a semi-log scale. (b) THz: detector map and 3D reconstruction resolve planes along $\langle 002 \rangle$, $\langle 113 \rangle$, $\langle 224 \rangle$. (c) NIR at the same bias and rate: broader peaks and blurred planes.

rate, was reported on a LaB_6. Figure 1.24 compiles four diagnostics that separate spectral purity, spatial fidelity, event statistics, and stoichiometry [209].

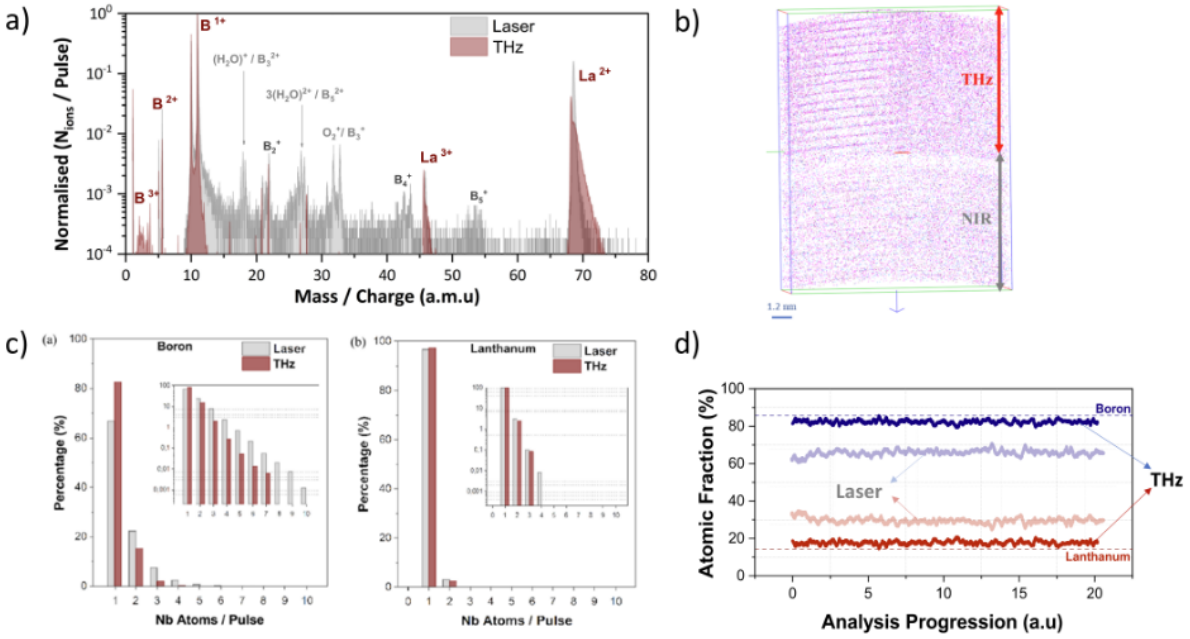

Figure 1.24: THz vs. NIR on LaB_6 [209]. (a) Overlaid spectra (THz red; NIR grey): THz sharpens B^+, B^{2+}, B^{3+} and La^{2+}/La^{3+} on a lower background; NIR shows elevated continuum and broader features. (b) Thin-slab view along the analysis direction: atomic planes visible in the THz segment (top, red bracket) but indistinct in the NIR segment (bottom, grey bracket). (c) Event multiplicity for B (left) and La (right): THz favours singles; NIR exhibits a pronounced multi-hit tail. (d) Running composition: THz maintains near-stoichiometric La:B (B ∼86 %, La ∼14 %) with small scatter; NIR shows larger fluctuations and drift.

On LaB_6, THz assistance again yields *cleaner* spectra (narrower elemental peaks, fewer molecular sidebands, lower baseline), *sharper* lattice planes in thin-slab views, a strong shift toward *single-ion* events in the multiplicity histograms for both B and La, and a *steadier* near-stoichiometric running composition (B ∼86 %, La ∼14 %) with reduced scatter and drift. Together with the Al benchmark, these data indicate that THz operates in a regime with $\Delta F \gg \Delta T$: the surface field is momentarily above threshold, shortening the emission window and improving both mass and spatial metrics [24, 209]. Similarly, the enhanced instantaneous field aligns with Kingham's framework by boosting post-ionization probabilities, thereby aiding in the stabilization of charge-state distributions for quantitative analysis.

1.7 Conclusion

Performing microscopy on insulators and biological samples *at the atomic scale* is constrained because no single established technique simultaneously delivers atomic (or near-atomic) *spatial* resolution and quantitative *chemical* resolution without perturbing the specimen. Cryo-EM/TEM achieves outstanding structural detail but faces strict dose limits that hinder fully quantitative, three-dimensional light-element chemistry; AFM excels at surface morphology yet lacks true volumetric composition; X-ray crystallography yields precise coordinates at the cost of crystallization that can trap non-native states; and NMR provides chemically rich, ensemble information without nanoscale spatial mapping. In contrast, *atom probe tomography* (APT) can be integrated as a complementary technique that provides *both* three-dimensional spatial resolution at the atomic scale *and* quantitative, isotopically sensitive chemistry, filling the gap left by other techniques.

We presented the working principles of APT and the physics of field evaporation, including field–temperature interplay, post-ionization, and the roles of electrical (HV) and laser assistance. We reviewed studies applying APT to different classes of biosamples and soft/insulating systems, highlighting the solutions adopted to optimise results, such as thin metallic coatings (e.g., Cr sputtering and graphene encapsulation) as engineering measures to improve field enhancement during APT analyses. Within this context, we justified *sol–gel silica* as a promising encapsulation matrix for proteins, but with challenges associated to its porosity and insulating character.

Finally, we introduced *THz-assisted* APT as an alternative triggering mechanism that is intrinsically closer to an athermal, field-dominated regime. Intense single-cycle THz transients, enhanced at nanosharp tips, can raise the instantaneous field (ΔF) with negligible heating (ΔT), thereby shortening the emission window, sharpening mass peaks, and reducing multiplicity—features already demonstrated on conductive benchmarks and directly relevant to insulating hosts. By curbing the thermal load typical of UV/deep-UV laser assistance, THz drive is expected to reduce heat-induced damage and denaturation, a decisive advantage for biosamples.

CHAPTER 2

Materials and Methods

2.1 Introduction

This chapter establishes the practical framework used throughout this thesis for atom probe tomography (APT), focusing on *how* experiments were executed and *how* data were transformed into quantitative results. Building on the physical background and literature context presented in Chapter 1, we restrict ourselves here to implementation details: APT analysis chamber specifications, evaporation control, complete data workflow (acquisition metadata, mass-spectrum treatment, 3D reconstruction and clustering protocols) using the home-built GPM3D software. Two THz-assisted platforms (Tera-SAT: *TERAhertz-assisted Sonde Atomique Tomographique*) were operated during this thesis at the Groupe de Physique des Matériaux (GPM) and CORIA laboratories, Université de Rouen. The first system, operating at a 1 kHz repetition rate, generates broadband THz bursts via two-color plasma in dry air with controllable pulse shape and polarity [24, 27, 30, 209]. This setup was already fully operational at the start of the present PhD work and was used as a mature platform for systematic THz-assisted APT investigations.

In December 2024, the analysis chamber from this system was transferred to CORIA laboratory and integrated with a new high-repetition-rate THz source based on optical rectifica-

tion in $LiNbO_3$ using a tilted-pulse-front configuration. This second platform, operational by March 2025, delivers stable single-cycle THz pulses at 100 kHz, pumped by a Yb-based femtosecond laser [210–212]. While the core THz source development and optimisation were carried out by the CORIA team, the present work primarily involved the use of this emerging platform for atom probe measurements, with ongoing optimisation efforts focused mainly on THz beam delivery and focusing at the specimen.

For assessment against established instruments, we also employed laser-assisted systems with distinct wavelengths and flight-path geometries: the LAWATAP operated in the UV at $\lambda = 343$ nm (straight flight path) and the LEAP 5000XS at $\lambda = 355$ nm (straight). In addition, deep-UV measurements at $\lambda = 257.5$ nm using a reflectron-equipped LEAP 6000XR were performed by our collaborators at Chalmers University on sol–gel silica (not by the author of this thesis). The differing photon energies, repetition rates, and optics across these platforms allow controlled comparisons of energy input and field/thermal effects under otherwise similar conditions.

Sol–gel silica was selected as a core material for both its methodological challenge and its relevance to APT analysis of bio-materials at room temperature. When synthesized near neutral pH from ion-exchanged sodium silicate, it provides a chemically gentle host matrix for embedding biomolecules without substantial structural alteration [18, 213–215]. Within this chapter we therefore detail the exact recipes, batch identifiers, and preparation workflows actually used in our experiments (electropolishing, FIB micromachining, and surface engineering). In particular, we document chromium coatings deposited by PECS sputtering and graphene encapsulation protocols, both designed to enhance the local electric field at the apex and stabilize evaporation.

2.2 Practical Principles of Atom Probe Operation

While the theoretical foundations of atom probe tomography (APT) are presented in Chapter 1, this section gives a practical overview of APT data treatment and the operating principles relevant to the instruments used in this work, namely commercial laser-assisted systems (LAWATAP, LEAP 5000XS, LEAP 6000XR) and the THz-assisted setups developed at GPM. The focus will be on time-of-flight (ToF) mass spectrometry and on volume reconstruction, emphasising the aspects that control data optimisation and interpretation. ToF mass spectrometry (ToF-MS) is central to APT: each ion's ToF yields its mass-to-charge ratio (MCR) for chemical identification.

The process involves: (i) pulse-synchronised detection and event classification; (ii) conversion ToF $\rightarrow$ MCR and spectrum construction; and (iii) assessment of spectral quality (mass resolution, signal to noise ratio, peak overlaps).

2.2.1 Ion Detection and Signal Processing

Once ions are field-evaporated from the specimen surface, they are accelerated by the extraction voltage V and traverse the flight path L to the detector. Because the electric field decreases in a few nanometers from the tip apex, the potential energy of the ions is converted in kinetic energy in a short timescale (few picoseconds). Therefore the kinetic energy:

$$E_k = \tfrac{1}{2} M v^2 = neV \tag{2.1}$$

relates the ion mass M, charge state n, and velocity v to V (with e the elementary charge). The corresponding time of flight is

$$ToF = \frac{L}{v} = L\sqrt{\frac{M}{2neV}}, \tag{2.2}$$

linking the measured arrival time directly to the mass-to-charge ratio M/n.

The primary detection stage uses microchannel plates (MCPs) as electron multipliers: an incoming ion strikes a tilted microscopic channel (diameter $\sim$10 µm, bias angle $\sim$8°), liberating secondary electrons that undergo avalanche multiplication under the applied bias, generating a fast electron cloud at the MCP exit (gain 10^6–10^7). This cloud impinges on a delay-line detector (DLD) with two orthogonal lines. The signals induced on each line propagate toward both ends; the differences in arrival times yield the impact coordinates (X, Y) with sub-100 µm precision. In parallel, the arrival time referenced to the evaporation pulse provides t. The detector coordinates are projected back to the specimen surface *via* the point-projection model, as in Eq. (1.3), at page 13.

Analog pulses from the MCP/DLD are amplified, shaped by constant-fraction discriminators (CFDs) to suppress time-walk, and converted to logic pulses. A time-to-digital converter (TDC)

records the relevant time differences with ∼50 ps resolution, supplying both the position and the ToF timestamps. This process enables high mass-resolving power and allows registration of multi-hit events (several ions per pulse). Modern DLD systems reach overall detection efficiencies of 50–80%, mainly limited by the MCP open-area ratio and transport losses of the electron cloud. Multi-hit capability enables separation of ions arriving within nanoseconds, which is essential when analysing correlated evaporation and field-dissociation products.

The acquisition of ion impacts events is synchronised to the excitation pulses. After each pulse, the timing electronics open a fixed *detection window*; any detector signal above threshold within this window is assigned to that pulse and its ToF computed. A small timing offset t_0 between the electronic trigger and the effective pulse at the tip is accounted for on the ToF axis (Fig. 2.1). Because evaporation is stochastic, the stream contains *blank*, *single*, and *multiple* events. The *detection rate* (average ions per pulse) provides feedback during acquisition; a control loop adjusts V_{DC} to maintain this rate as the tip shape evolves. The repetition rate and window length set the usable ToF range; very heavy ions or complex molecules may lie outside this window and contribute to low-m/n background (10–30 Da).

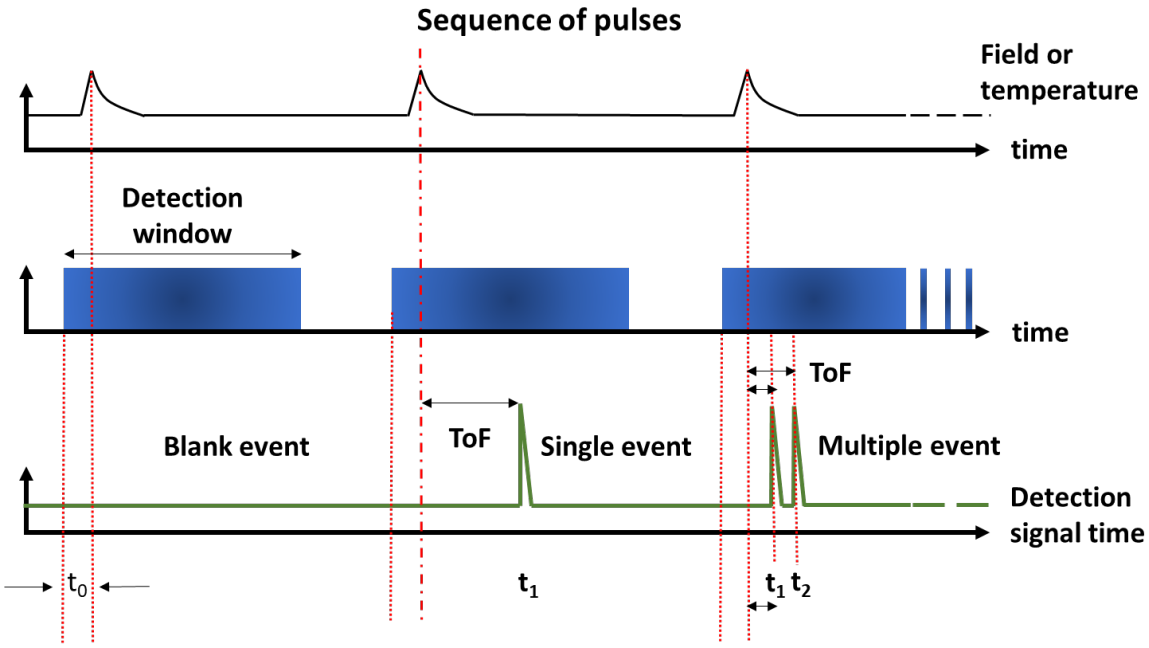

Figure 2.1: Schematic detection sequence. After each excitation pulse a detection window opens; events are recorded as blank, single, or multiple. t_0 denotes the trigger offset; t_1, t_2 are example ion ToFs. Reproduced from [6].

A *multiple event* occurs when a single pulse yields more than one detected ion; the number

per pulse is the event *multiplicity*. Certain chemistries favour high multiplicity, notably when molecular ions form and field-dissociate, producing near-simultaneous arrivals [216, 217]. Because arrivals are close in space and time, they probe detector limits: MCP cascades can overlap and the effective transfer function becomes complex [218]. Under stochastic detection with ∼57% efficiency, the probability that a detected double originated from ≥10 evaporated atoms is small but non-negligible [219]; statistical corrections for information lost to limited efficiency have been proposed [219]. As multiplicity is chemistry-dependent, composition biases beyond counting statistics can arise [216–219].

Because the electric field decays within a few nanometres of the apex, most potential energy is converted into kinetic energy within a few picoseconds; thus the measurable ToF primarily reflects the drift over L. In laser pulsing, $V = V_{\mathrm{DC}}$; in HV pulsing, $V = V_{\mathrm{DC}} + V_p$ with $V_p \approx 10$–30% of V_{DC}. Typical $L \sim 10$–50 cm and $V \sim 1$–10 kV yield ToFs of ~ 1–5 μs.

Note. A legacy expression replaces $\mathrm{ToF} - t_0$ by the measured t_f and introduces a units constant k so that $M = k\,V\,(t_f/L)^2$; for L in m, t_f in μs, and V in kV, $k = 0.192973$. This is equivalent to Eq. (1.1) when t_0 is negligible or included in the calibration.

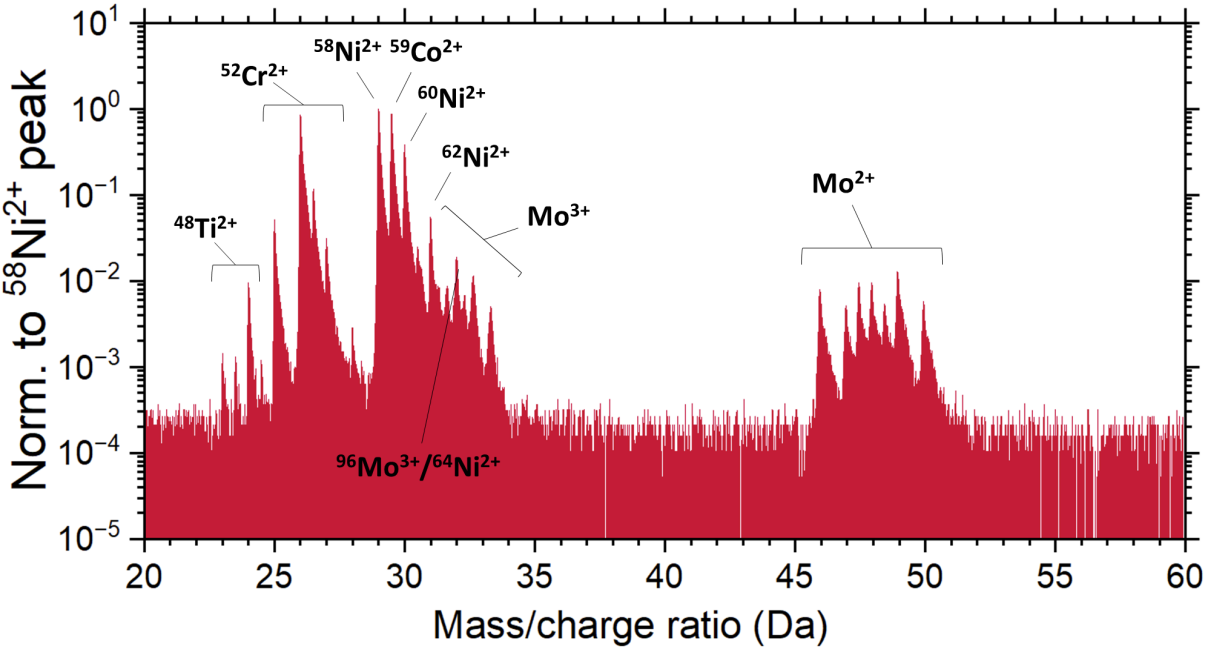

Figure 2.2: Mass spectrum of a Ni–based superalloy (NS8) acquired in *electric mode* on a LEAP 5000XS, intensities normalised to the $^{58}Ni^{2+}$ peak (log scale). Labeled features include Ti^{2+}, Cr^{2+}, the Ni^{2+} multiplet with $^{59}Co^{2+}$, a Mo^{3+} group (31–33 Da), and the Mo^{2+} isotopes (46–52 Da). The overlap $^{96}Mo^{3+}/^{64}Ni^{2+}$ is indicated at $\sim$ 32 Da. The background level is measured on a peak–free window: 55–60 Da.

2.2.2 Mass spectrum construction

Starting from the offset-corrected flight times (ToF $- t_0$), each ion is mapped to its mass-to-charge ratio *via* Eq. (1.1), and the resulting values are histogrammed to form the mass spectrum. Mass spectra are therefore histograms of mass-to-charge values; finite instrument response and binning impart a finite peak width, so the display binning must balance peak fidelity and noise. Figure 2.2 (HV mode, LEAP 5000XS) illustrates typical isotopic families used for assignment: Ti^{2+} ($\sim$ 24 Da), Cr^{2+} ($\sim$ 26 Da), the Ni^{2+} multiplet (29–31 Da) with $^{59}Co^{2+}$, Mo^{3+} (31–33 Da), and Mo^{2+} (46–52 Da). A common overlap appears near 32 Da between $^{64}Ni^{2+}$ and $^{96}Mo^{3+}$; quantification proceeds from integrated peak areas after choosing mass windows and deconvolving overlaps. The baseline (background) mainly reflects random ions recorded within the detection window (residual gas, adsorbates) plus a small detector contribution, and it increases with detection rate [141, 220]. We estimate it from a peak-free high-m/n window; in Fig. 2.2 the baseline is $\sim 10^{-4}$ of the $^{58}Ni^{2+}$ peak, setting the practical detection limit and corresponding signal-to-noise ratio (SNR) for weak species in this dataset.

In HV pulsing, the *pulse fraction*, which is HV pulse amplitude divided by DC voltage, must generally increase as the tip radius (and thus required voltage) grows, so that evaporation remains confined to the pulses and low-field species are not lost between pulses. In laser pulsing there is no universally accepted analogue. Terms such as *field reduction*, *effective pulse fraction*, or *equivalent pulse fraction* have been proposed by comparing the voltages needed to trigger evaporation in situ [109, 221], under HV pulsing [11], or in DC evaporation [108, 222]. Because evaporation durations differ by mode and depend on the specimen, direct numerical equivalence is ambiguous; further ambiguity stems from heterogeneous reporting of laser parameters (energy, power, intensity/fluence, wavelength, illumination geometry).

The mass resolution $M/\Delta M$ reflects both instrumental statistics and evaporation dynamics:

$$\frac{M}{\Delta M} = \frac{1}{\sqrt{\left(\frac{\sigma_V}{V}\right)^2 + \left(\frac{2\,\sigma_{\text{timing}}}{t_{\text{flight}}}\right)^2 + \left(\frac{2\,\sigma_{t_0}}{t_{\text{flight}}}\right)^2}} + f_{\text{pulse}}(t_d), \tag{2.3}$$

where the first term gathers voltage stability σ_V, timing jitter σ_{timing}, and start–time uncertainty σ_{t_0}; $f_{\text{pulse}}(t_d)$ accounts for departure-time broadening. Modern systems reach timing accuracy < 100 ps and voltage stability of a few volts per 10 kV; flight-length accuracy is typically better

than 1 mm [223]. On wide-FOV instruments in HV pulsing, typical resolutions at 27 u.m.a. are ~ 500 (FWHM) and ~ 100 (FWTM); energy-compensation optics (reflectron [224–226] or dual counter-electrode [227]) can raise FWTM to ~ 400 [228]. In laser pulsing, straight-flight–path instruments have reported a $M/\Delta M > 1000$ at FWHM [108, 229]. Increasing t_{flight} (longer paths, retardation, reflectrons) further improves resolution [106, 230].

Peak shapes differ systematically between triggering modes: in HV pulsing, evaporation is effectively instantaneous and peaks show reproducible, asymmetric energy-deficit tails toward higher m/n; in laser pulsing, thermally assisted evaporation during the cooling interval broadens peaks and typically elevates the baseline.

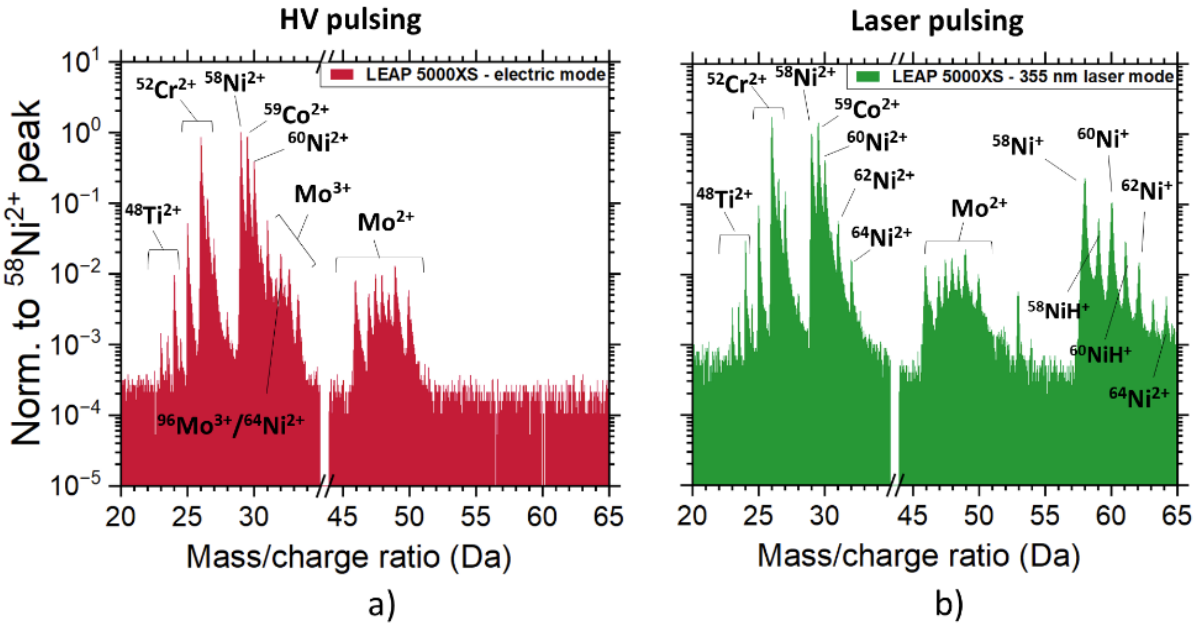

Figure 2.3: Mass spectra of a Ni-based superalloy (NS8) acquired on the same LEAP 5000XS in (a) HV mode and (b) 355 nm laser mode, normalised to $^{58}Ni^{2+}$ (log scale). The laser spectrum shows a shift toward Ni^{+} and NiH^{+}; HV emphasises Ni^{2+}. Isotope envelopes for Ti^{2+}, Cr^{2+}, Co^{2+} are resolved in both; the $^{96}Mo^{3+}/^{64}Ni^{2+}$ overlap near 32 Da is visible in HV.

Figure 2.3 compares spectra from the *same* NS8 tip acquired in HV and 355 nm laser modes. The laser dataset exhibits (i) a charge-state shift toward lower charge with strong Ni^{+} and noticeable NiH^{+}, (ii) broader peaks and a higher baseline due to higher sample temperature and (iii) similar isotope envelopes for Ti^{2+}, Cr^{2+}, Co^{2+}. In HV mode, Ni^{2+} dominates and peaks present narrower profiles with energy-deficit tails; overlaps such as $^{96}Mo^{3+}/^{64}Ni^{2+}$ at ~ 32 Da are clearly visible. Overall, either mode can deliver superior mass resolution depending on operating conditions (pulse fraction or laser energy/duration/spot, base temperature, standing

voltage, tip geometry); the NS8 comparison highlights the practical trade-off between peak width, baseline level, and charge-state distribution for quantitative analysis.

Estimating surface field from charge–state ratios.

Rather than reading F from published Kingham curves, we use the direct inversion of Tegg *et al.* from the measured *charge–state ratio* (CSR) to F [231]:

$$\mathrm{CSR} = \frac{C_{i,n+1}}{C_{i,n}},$$

where $C_{i,n}$ and $C_{i,n+1}$ are background–subtracted counts (integrated peak areas) for species i at charge states n and n+1. For the CSR pairs relevant to this thesis (Silicon and Nickel), the surface field is approximated by

$$F \;=\; a\left(1 - \frac{b}{\mathrm{CSR}^{\,0.3} + b + 0.256}\right) \quad (\mathrm{V/nm}), \tag{2.4}$$

with the element/CSR–specific parameters (a, b) listed in Table 2.1.

It should be noted that Eq. (2.4) is an empirical parametrization derived by Tegg *et al.* from systematic experimental charge–state data, rather than a first-principles quantum-mechanical calculation. The functional form is nonetheless physically motivated by the Kingham post-ionization framework, in which field-dependent tunnelling and ionization probabilities govern charge–state formation in the near-field region above the surface. The fitted parameters (a, b) therefore encapsulate the underlying quantum-mechanical field-ionization behavior, while providing an inversion from measured CSR values to surface electric field.

Figure 2.4 illustrates the F(CSR) relations for silicon and nickel using these coefficients. For additional elements and CSR pairs, see [231].

Table 2.1: Model parameters a and b from Eq. (2.4) for Ni and Si and the CSR pairs explored.

Element	CSR pair	a	b
Ni	2 + /1+	28.52	0.2209
	3 + /2+	73.31	0.2123
Si	2 + /1+	23.00	0.2094
	3 + /2+	65.71	0.2049
	4 + /3+	92.78	0.1893

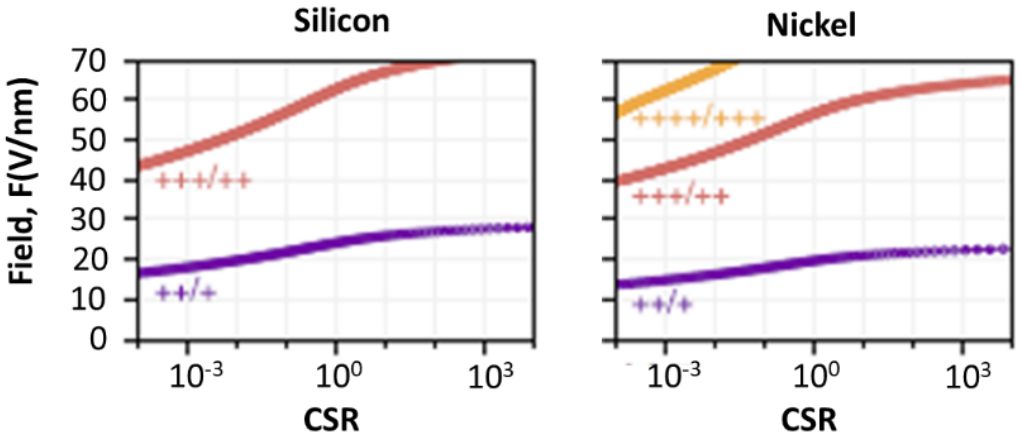

Figure 2.4: Surface field $F(\mathrm{CSR})$ for silicon and nickel, computed from Eq. (2.4) using the parameters in Table 2.1. For more elements and CSR pairs, see [231].

Workflow. (i) Range the spectrum to obtain $C_{i,n}$ and $C_{i,n+1}$; (ii) form $\mathrm{CSR} = C_{i,n+1}/C_{i,n}$ (globally, *via* detector maps, or along proximity profiles); (iii) evaluate Eq. (2.4) with (a, b) from Table 2.1 to obtain F.

Uncertainty and data volume. Because $F(\mathrm{CSR})$ can be shallow, CSR noise must be minimised. Assuming Poisson counting statistics,

$$\frac{\Delta\mathrm{CSR}}{\mathrm{CSR}} \approx \sqrt{\frac{1}{C_{i,n+1}} + \frac{1}{C_{i,n}}}, \tag{2.5}$$

so reaching $\lesssim 1\%$ relative uncertainty typically requires $\gtrsim 10^4$ counts in the *smaller* of the two peaks. This estimate applies to *local* CSR evaluations, where the ratio is computed within a restricted spatial or temporal subset of the data. When CSR values are averaged globally over the full dataset, statistical uncertainty is reduced by increased counting statistics, but at the expense of spatial or temporal resolution and with the implicit assumption of a uniform surface field across the analysed volume.

CSR-based field estimates inherit the assumptions of post-ionization theory [79, 232–234]; if only one charge state is populated (e.g. Zn mainly as Zn^{2+}), another element must be chosen. While this approach has been extensively validated for metallic systems, applications to oxides and semiconductors require caution [235], as non-metallic specimens may exhibit local charging, band bending, defect-assisted evaporation, or molecular ion formation, which can perturb charge–state populations and violate the assumptions underlying metal-based post-ionization models.

Standard Deviation on Compositions

Let N be the total number of detected ions and n those ranged to element A, so the measured concentration is $C = n/N$. Because detection is binary with efficiency Q, the number of ions actually evaporated before N are detected follows a negative–binomial process with mean N/Q and variance $N(1-Q)/Q^2$ [236]. Building on this, two practical uncertainty cases are commonly used [236, 237]. For whole-specimen (global) composition—when the analysed volume is representative and atoms are randomly distributed—the standard deviation is

$$\sigma = \sqrt{\frac{C(1-C)}{N}}. \tag{2.6}$$

For local/ROI composition (e.g., clusters, proxigrams, small sampling boxes), where selection procedures and finite detection efficiency inflate the variance, a conservative estimate is

$$\sigma = \sqrt{\frac{C(1-C)(1-Q)}{N}}, \tag{2.7}$$

with N the ion count inside the ROI. In practice, use Eq. (2.6) for global compositions and Eq. (2.7) for ROIs where counting losses and selection biases are non-negligible [236].

2.3 3D volume Reconstruction

APT reconstruction converts the time–stamped detector hits into two coupled products: a calibrated, ranged mass spectrum and a three-dimensional (3D) point cloud of ions. In practice, Eq. (1.1) maps each offset-corrected flight time (ToF $- t_0$) to m/n; peaks are then identified, calibrated to a small set of well-known isotope/ion references, and ranged. In parallel, detector coordinates are back-projected to 3D using a tip-projection model. The resulting files (.pos, .epos, and newer .apt/.ato) can be read by common analysis environments such as MATLAB or Python [6]. Although software-assisted, the procedure remains user-guided (e.g. the CAMECA IVAS workflow widely used on LEAP systems [54]); in this thesis, mass-spectral analysis, 3D reconstruction, clustering, and compositional analysis were performed primarily with the in-house *3DGPM* software.

Reconstruction typically starts by restricting the dataset to the region of interest: a circular

aperture on the detector hit map limits the field of view in (X, Y), and an appropriate voltage or depth interval selects the segment along z. Geometry is then corrected to account for projection from an approximately spherical tip onto a flat detector, while kinematics are adjusted for small energy variations as V_{DC} evolves during the run [6]. After converting ToF to m/n with Eq. (1.1), calibration aligns the chosen reference peaks to their exact positions and *ranging* assigns mass windows to all species—an operation that directly conditions quantitative composition. Finally, the 3D scale and aspect ratio are set by combining stoichiometric information (atomic volumes) with external constraints such as SEM/TEM images and, when available, crystallographic markers (pole spacing, plane spacings) [220, 238]. For very large datasets ($>10^8$ ions), interactive steps are often performed on a sampled subset; if minor peaks are added later, the reconstruction is re-run so those ions contribute volume to the final 3D map.

The 3D reconstruction rests on a model that relates the ion impact position on the detector (X, Y) to its emission coordinates on the specimen surface (x, y) and to its depth z at evaporation [70]. The principal parameters are:

- **Image compression factor $\boldsymbol{\xi}$.** This parameter describes the angular compression of ion trajectories as they leave the tip. It primarily controls lateral calibration. Near the tip axis (small polar angle θ), ξ can be taken as constant or, to first order, vary approximately linearly with θ^2. More details can be found in Chapter 1.

- **Initial tip radius $\boldsymbol{R}$.** Estimated from SEM/TEM imaging or voltage reconstructions, R sets the lateral scaling *via* point–projection magnification. For flight-path length L and compression ξ,

$$M \;\approx\; \frac{L}{\xi\, R}, \tag{2.8}$$

  giving the detector–to–specimen transverse scaling

$$\Delta x_{\mathrm{spec}} \;\approx\; \frac{\Delta X_{\mathrm{det}}}{M} \;=\; \Delta X_{\mathrm{det}}\, \frac{\xi\, R}{L}. \tag{2.9}$$

- **Field factor $\boldsymbol{k_F}$.** Links the applied voltage V and radius R to the surface field, $F = V/(k_F R)$. Together with ξ, k_F is critical for depth calibration because it governs how R

evolves with V during the run.

- **Cone (shank) angle α.** The conical shank influences both k_F and ξ. Larger α reduces apex field and modifies trajectories, potentially introducing lateral distortions and spatial resolution variations within the reconstructed volume.
- **Detection efficiency Q.** Enters the density and volume calibration through the counted/evaporated atom ratio.

2.3.1 Reconstruction protocols used in this thesis

Three complementary protocols (implemented in 3DGPM software) were employed for 3D reconstruction, alongside the IVAS baseline for LEAP datasets:

- **E–β method.** Uses the evolution of the applied voltage during the run to update (x, y, z) with fixed inputs (ξ, projection point). The variation of R is implicitly linked to the voltage history.
- **Cone–angle method.** Geometrically prescribes the specimen radius evolution from an initial R and a fixed shank angle α. The projection point remains fixed; scaling follows the imposed geometry.
- **SEM/TEM–image method.** Incorporates an external micrograph of the tip to define the radius evolution explicitly. The user provides a set of radii along the shank extracted from the image; the projection point is fixed and ξ is tuned to match the observed shape.

2.4 Atom Probe Instrumentation: Laser-Assisted and Terahertz-Assisted Systems

To ensure the integrity of the field evaporation process and the detection of ions coming only from the sample, the APT analysis chamber must operate under ultra-high vacuum (UHV) and the specimen must be kept at cryogenic temperatures. A typical base pressure in the order of 10^{-11} mbar is maintained during acquisition.

In parallel, cryogenic temperatures, typically in the range of 20–80 K, are employed to stabilize the specimen and control thermal effects during pulsed field evaporation. Low temperatures

suppress spontaneous evaporation between pulses, reduce surface diffusion (particularly of mobile species such as hydrogen), and preserve the morphology of thermally sensitive materials. Temperature control is achieved through liquid helium or nitrogen cooling, or by closed-cycle cryostats (e.g., Joule–Thomson or Gifford–McMahon systems), often combined with active thermal regulation and radiation shielding. [6, 7, 13, 15]

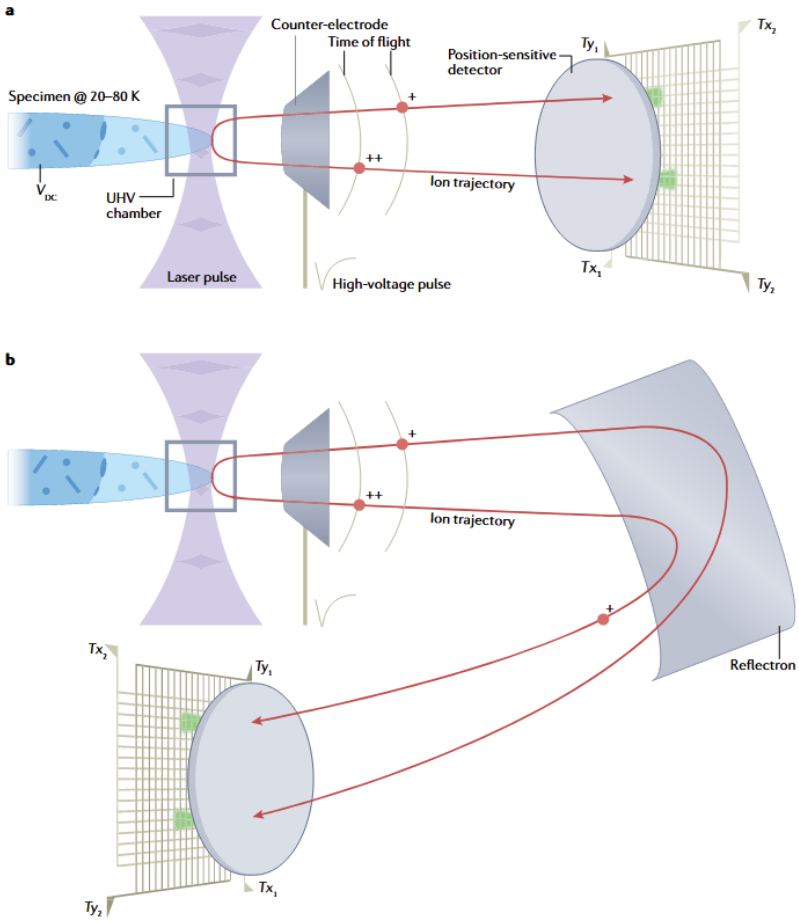

Figure 2.5: Schematics of atom-probe instrumentation and field evaporation (adapted from [239]). Inside view (not to scale) of an ultra-high-vacuum analysis chamber for (a) a straight flight-path instrument and (b) a reflectron-fitted instrument.

For THz-assisted APT experiments, the UHV chamber was customized to accommodate optical access for the THz beam and to allow the use of external cryogenic cooling.

Atom probes are built either with a *straight* flight path or with an ion *reflectron* that folds the trajectory to increase the time-of-flight (ToF) before detection (Fig. 2.5) [15, 239]. In a straight geometry (Fig. 2.5(a)), ions travel directly from the apex to the position-sensitive detector; this maximizes field-of-view and count rate, and minimizes ion–wall interactions. In a reflectron-

fitted instrument (Fig. 2.5(b)), ions are energy-focused after a longer effective path, which can substantially improve mass resolution by virtue of the increased ToF, at the cost of a reduced field-of-view and a greater sensitivity to trajectory aberrations [239]. Extending the overall flight path reduces the imaged surface area at the specimen for a given detector size and geometry. After rapid acceleration in the near-field at the apex, ions travel essentially in free space at constant velocity; thus no additional forces act to modify their trajectories beyond the initial projection [6]. With these trade-offs in mind, the following sections describe the straight-path LAWATAP and the LEAP systems (straight 5000XS and reflectron 6000XR), highlighting their operating envelopes and use cases.

2.4.1 Laser-Assisted Wide-Angle Tomographic Atom Probe

The Laser-Assisted Wide-Angle Tomographic Atom Probe (LaWaTAP) uses a ytterbium-doped laser operating at 1030 nm. This laser generates ultrashort pulses with a duration of 350 fs at a repetition rate of 100 kHz. The laser wavelength of 1030 nm is converted into its second and third harmonics at 515 nm ($\approx$ 2.4 eV, green) and 343 nm ($\approx$ 3.6 eV, UV) using two β-barium borate (BBO) crystals (Fig. 2.6 (a)). The laser energy of the 343 nm beam can vary between 10 and 50 nJ per pulse and is focused on the sample in a spot with a diameter of 30 μm, which corresponds to an energy density between 17 and 70 J/ m^2 [29]. A photograph of the instrument layout is provided in Fig. 2.6 (b).

During analysis, layer-by-layer evaporation progressively increases the apex radius R, and the applied voltage V is therefore raised to sustain a constant detection rate rather than a strictly constant surface field. As a result, the surface field $F \sim V/R$ generally decreases slowly over the course of the analysis, while remaining within the evaporation window; in practice, electrostatic stress typically limits the maximum voltage to $V \lesssim 15\,\mathrm{kV}$. The LAWATAP attains high mass-resolving power (MRP $\gtrsim 10^3$ at light-mass peaks) without reflectron/time-focusing optics, as demonstrated on *Al* alloys and low-doped *Si* with narrow Al peaks and fully resolved Si isotopes in the original instrument report [240]. This performance is supported by a custom MCP/advanced delay-line detector (MCP/aDLD) with sub-100 ps timing (timing accuracy $\sim$70 ps; dead-time $<$ 1.5 ns) [223]. The overall ion-detection efficiency is mainly limited by the MCP open-area ratio, yielding practical efficiencies near $\sim$60%, consistent with independent

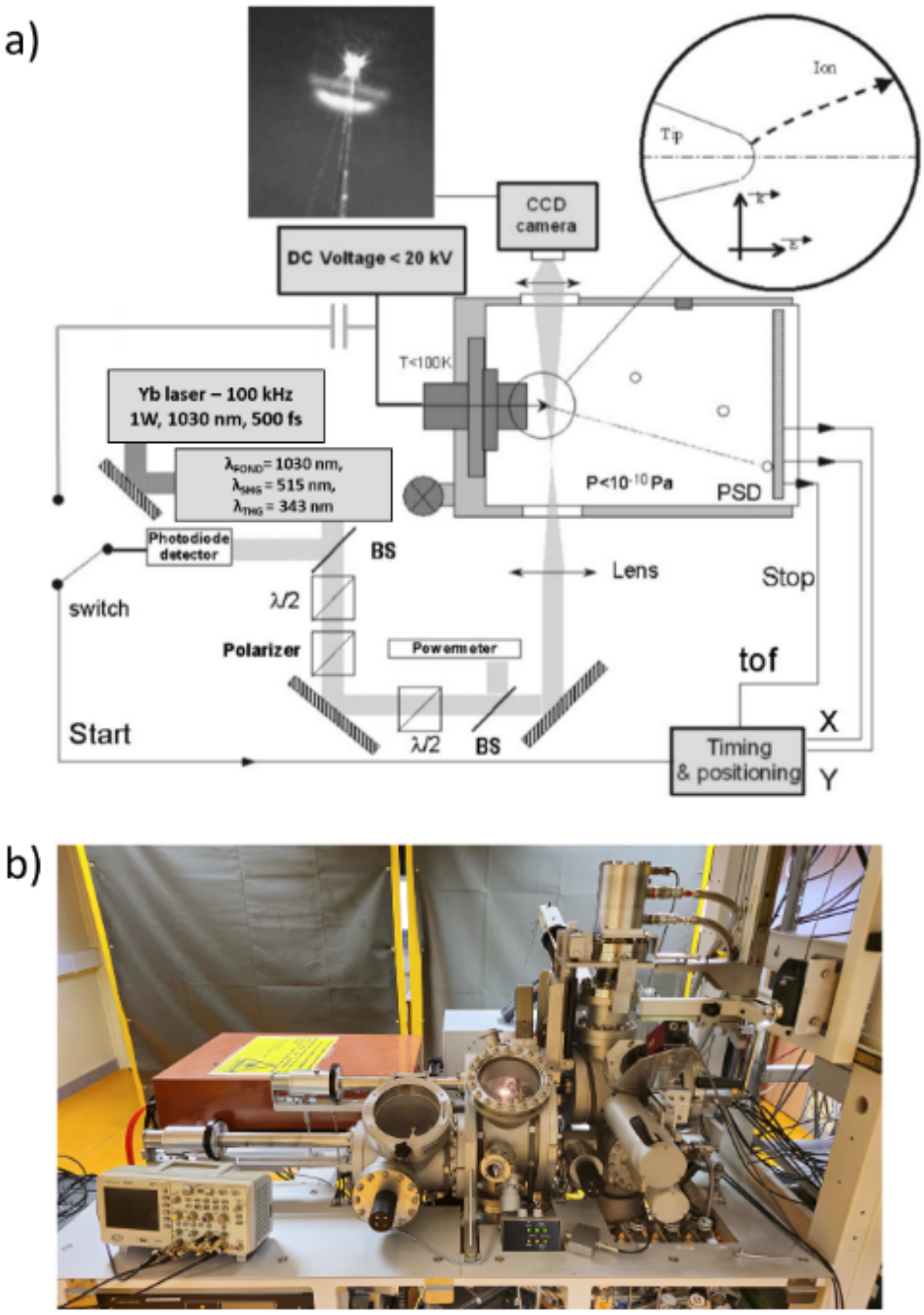

Figure 2.6: (a) Schematic diagram (adapted from [11]) of the LAWATAP setup. The system uses a Yb-doped fiber laser at 1030 nm, 100 kHz, and 500 fs pulses. (b) Photograph of the LAWATAP at GPM (Rouen) showing the airlock, intermediate storage chamber, and main analysis chamber under cryogenic UHV conditions.

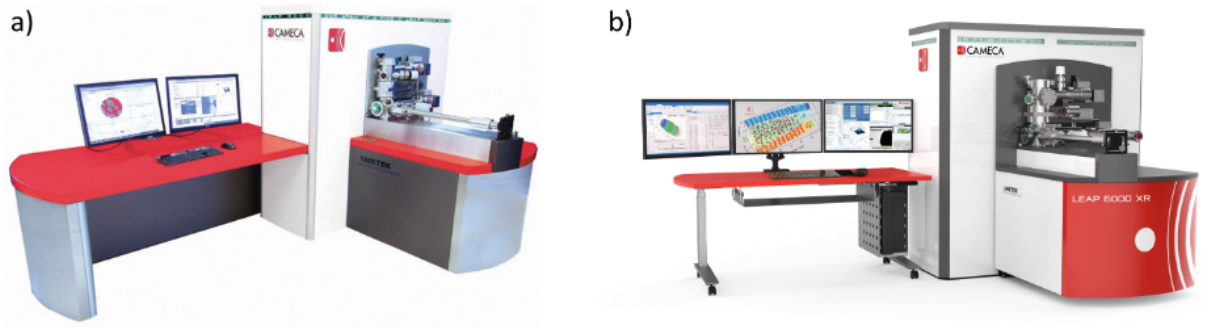

Figure 2.7: (a) CAMECA - LEAP 5000XS. (b) CAMECA - LEAP 6000XR

MCP studies on tungsten [241, 242] and Fe-based alloys [243].

2.4.2 Local Electrode Atom Probe (LEAP) systems

The CAMECA Local Electrode Atom Probe (LEAP) series comprises two high-performance instruments, namely, LEAP 5000XS and LEAP 6000XR which are present in this study as commercial standards for comparison with THz-assisted atom probe tomography (Fig. 2.7(a,b)). Both systems are engineered for atomic-scale three-dimensional compositional analysis and function under ultra-high vacuum (UHV) conditions, maintaining a base pressure below $< 10^{-10}$ mbar. Furthermore, they are equipped with cryogenically cooled stages that preserve specimen temperatures within the range of 20 to 60 K.

- The LEAP 5000XS instrument is characterized by a linear flight path geometry of approximately 10 cm and supports both ultraviolet (UV) laser pulsing at 355 nm and high-voltage (HV) pulsing (Fig. 2.7(a)). The UV laser source generates sub-15 ps pulses with adjustable energies ranging from 10 to 1000 pJ, operating at repetition rates up to 1 MHz, focused by a lens; HV pulses are used for metallic samples. The LEAP 5000XS system utilizes a dual microchannel plate (MCP) and delay-line detector (DLD), achieving detection efficiencies as up to 50%.

- In contrast, the LEAP 6000XR is equipped with a deep-ultraviolet (DUV) femtosecond laser at 257.5 nm (4.81 eV) and integrates a reflectron electrostatic lens within the time-of-flight (ToF) mass spectrometer (Fig. 2.7(b)). It can be operated with laser pulse energies between 100 and 250 pJ, corresponding to an energy density between 30 and 80 J/m^2, with repetition rates reaching 500 kHz. The high-energy DUV laser facilitates efficient surface

absorption in wide-bandgap materials, such as sol-gel silica, while the reflectron compensates for initial kinetic energy dispersion, thereby enhancing peak definition and mass resolution. Its high-numerical-aperture optical system precisely focuses sub-picosecond pulses onto the specimen apex, permitting high-resolution analysis of insulating or low-conductivity materials.

The LEAP 6000XR was not directly operated by the author, but rather utilized by collaborators at Chalmers University of Technology to examine sol-gel silica specimens (Fig. 2.7b). This approach facilitated a systematic comparison of UV-driven field evaporation using a deep-UV source at 257.5 nm, where silica's absorption is notably more intense against the LaWaTAP (343 nm) and LEAP 5000XS (355 nm) (see Chapter 3). The inclusion of a reflectron in the LEAP 6000XR extends the flight path from 10 cm to 38.2 cm compared to the XS series [29, 244]. All LEAP datasets were processed using the commercial CAMECA IVAS software.

2.4.3 Terahertz-Assisted APT Systems (Tera-SAT)

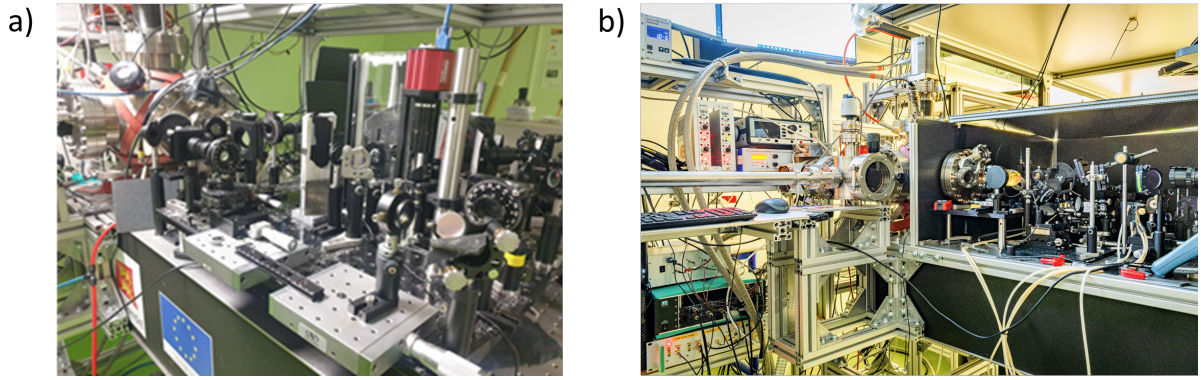

Figure 2.8: (a) Picture of the low repetition rate (1 kHz) TERA-SAT setup at GPM laboratory, Rouen. (b) Picture of the new high repetition rate (100 kHz) TERA-SAT setup, at Coria laboratory, Rouen.

The two Tera-SAT platforms used in this work are shown in Fig. 2.8(a,b).

Low-Repetition-Rate THz-Assisted APT (1 kHz)

THz-assisted APT uses strong, ultrafast electric fields generated by single-cycle THz pulses (Fig. 2.9). The THz generation system is centered around a commercial Ti:Sapphire laser chain (Spitfire, Spectra-Physics), which produces near-infrared (NIR) pulses at a central wavelength of 800 nm with a pulse duration of approximately 35 fs and a repetition rate of 1 kHz. These pulses are generated *via* chirped-pulse amplification (CPA) of sub-35 fs seed pulses emitted at 80 MHz

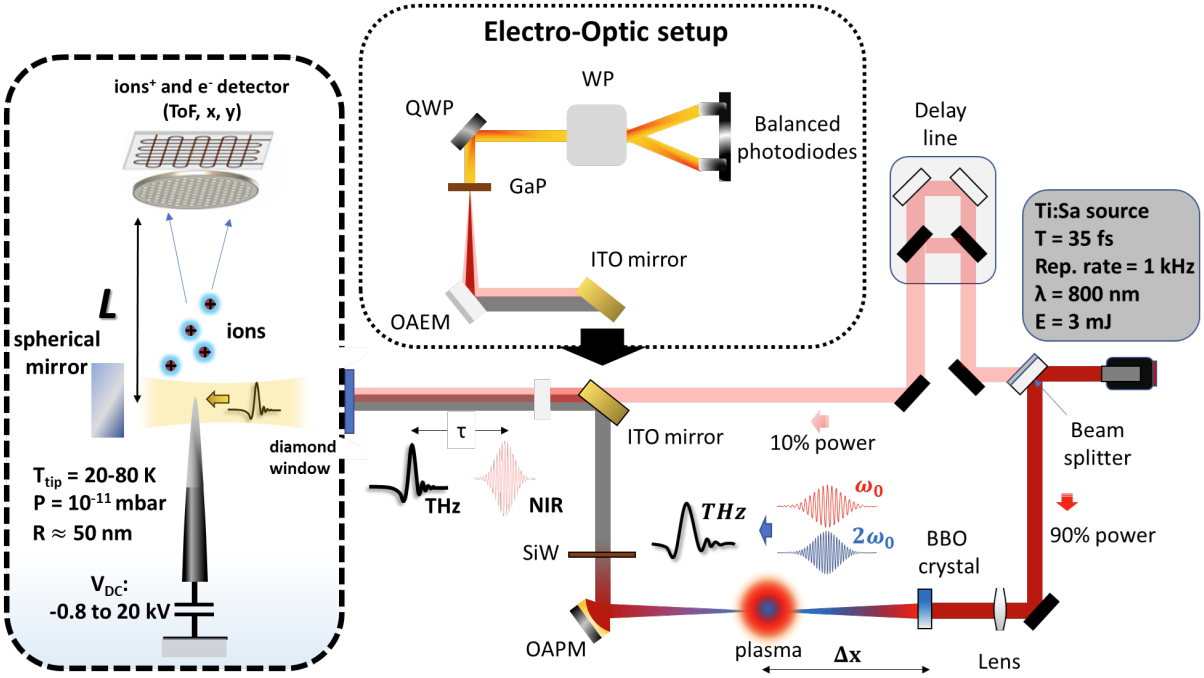

Figure 2.9: Low repetition rate TERA-SAT setup (1 kHz). THz radiation generation involves a two-color plasma process where a high-energy NIR beam is focused through a lens and a BBO crystal, converting part of the fundamental wave into its second harmonic to produce a bi-chromatic femtosecond beam. This beam forms a plasma filament that emits a broadband THz pulse.

from a passively mode-locked Ti:Sapphire oscillator. The final output delivers up to 2.5 mJ per pulse in a Gaussian TEM_{00} spatial mode, i.e. the fundamental transverse electromagnetic mode characterized by a single-lobe, near-Gaussian intensity profile and minimal wavefront distortions, with a beam diameter of 8 mm. The optical layout is designed to split the laser output into two beams with a 90/10 energy ratio. The higher-energy portion (∼90%) is directed toward THz generation and is mechanically chopped at 500 Hz to enable lock-in detection. The remaining fraction serves either as a probe for electro-optic (EO) sampling diagnostics or as an auxiliary source for triggering controlled electron or ion emission. Both pulse trains can be temporally stretched and compressed independently, allowing fine adjustment of their respective durations. The pulse duration of the high-energy beam used for THz generation is measured with an autocorrelator and maintained at 35 fs [24, 27, 28, 30].

The generation of THz radiation is achieved through a two-color plasma generation process (see Fig. 2.9). The high-energy NIR beam is first polarized using a half-wave plate and then focused into a gaseous medium, typically ambient air or nitrogen (N_2), using a plano-convex lens with a 30 cm focal length. Air and N_2 are commonly employed because they readily sustain

stable femtosecond laser-induced plasmas at atmospheric pressure, provide efficient two-color ionization dynamics for THz generation, and exhibit negligible absorption in the generated THz spectral range. In addition, nitrogen allows operation under controlled conditions by suppressing humidity-related effects while preserving comparable THz conversion efficiency. Before reaching the focus, the beam passes through a beta barium borate (BBO) crystal, which converts a portion of the 800 nm fundamental wave (FW) into its second harmonic (SH) at 400 nm. The collinear FW and SH pulses form an intense, bi-chromatic femtosecond beam that initiates a plasma filament upon interacting with the gas. This plasma drives an asymmetric electron current *via* strong-field ionization and electron acceleration, resulting in the emission of a single-cycle broadband THz pulse spanning frequencies from 0.1 THz to over 40 THz [22, 245]. The relative optical phase between the FW and SH components is adjustable by varying the spatial delay of the BBO crystal, enabling precise control over polarity of the resulting THz waveform [22, 24, 30, 129]. The THz field amplitude is varied by reducing the energy pump beam and the pump beam chirp allows the control on THz polarization [246]. Such tunability is critical for selectively enhancing or suppressing the effective electric field at the tip apex, providing fine control over the conditions under which field evaporation occurs.

From a physical point of view, THz emission in the two-color plasma scheme originates from the breaking of temporal symmetry in the laser-driven electron dynamics. In the presence of both the fundamental and second-harmonic fields, the combined optical waveform becomes asymmetric over an optical cycle, leading to a net directional drift of ionized electrons immediately after tunnel ionization. This sub-cycle electron acceleration produces a transient macroscopic current density in the plasma, whose time derivative acts as the source of broadband THz radiation. The efficiency, polarity, and waveform of the emitted THz pulse are therefore governed by the relative phase, amplitude ratio, and temporal overlap of the two optical fields, as well as by plasma density and ionization dynamics [22, 129, 245, 247]. In this framework, THz generation is intrinsically a non-thermal, ultrafast process occurring on femtosecond timescales, yielding single-cycle pulses with a stable carrier–envelope phase that can be directly tuned through optical phase control.

Following generation, the THz beam is collimated using a gold-coated off-axis parabolic mirror with a 50 mm focal length, a 25 mm aperture, and a 2 mm central hole that removes most of the

residual NIR light. Additional filtering is achieved using a high-resistivity silicon wafer, which transmits the THz radiation while blocking any remaining optical components. The beam can then be steered toward either the electro-optic (EO) diagnostic setup or the atom probe analysis chamber.

In the case of diagnostics, the THz pulse and the NIR probe beam are focused onto a 100 µm-thick GaP crystal using a second parabolic mirror with a 100 mm focal length. GaP is used as the EO sensor because it exhibits a strong and fast Pockels effect in the THz range, enabling a linear and sub-picosecond modulation of its refractive indices in response to the instantaneous THz electric field, while remaining transparent at the probe wavelength. The temporal overlap between THz and probe pulses is adjusted *via* a motorized delay line.

Inside the EO crystal, the THz field induces a transient birefringence that converts the initially linearly polarized probe into elliptically polarized light. This ellipticity can be decomposed into right- and left-handed circular components; a quarter-wave plate converts these components into orthogonal linear polarizations, which are then separated by a Wollaston prism and detected on two balanced photodiodes. The differential detection suppresses common-mode intensity noise and directly yields a signal proportional to the probe ellipticity, and thus to the instantaneous THz electric field [248].

For atom probe experiments, the THz beam is directed into a custom-built ultra-high vacuum (UHV) chamber through a THz-transparent window, typically made of crystalline quartz or silicon, with transmission efficiency exceeding 50% in the 0.1–10 THz frequency range. Inside the chamber, the beam is focused onto the apex of a needle-shaped specimen using a spherical gold mirror, with a focal length of 25 mm, mounted on a precision stage. The chamber itself is equipped with a cryogenically-cooled specimen stage maintained at 50 K using a closed-cycle cryostat, and a base pressure consistently below 10^{-10} mbar to ensure surface cleanliness and prevent contamination during analysis.

In this THz-assisted APT setup, ions travel a field-free path of $\sim$100 mm to a position-sensitive detector (PSD) comprising a chevron micro-channel plate (MCP) stack coupled to a Roentdek delay-line anode (two orthogonal wire pairs, multi-hit capable).

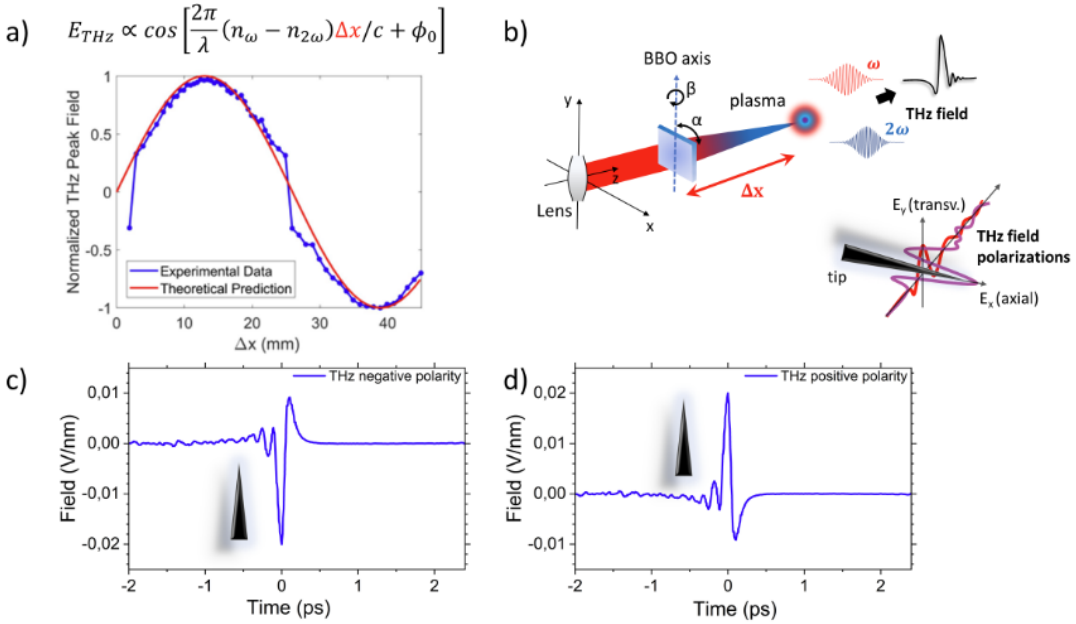

Figure 2.10: THz pulse polarity control. a) THz peak field versus BBO-to-focus distance at different laser chirps. Blue data points represent values obtained from experimental observations, while the red curve corresponds to the result derived from the theoretical model described by the equation above [246]. b) Changing the physical distance between the BBO crystal and the plasma region allows polarity control. c) Typical negative THz pulse (opposite sense along the tip axis). d) Typical positive THz pulse (same sense along tip axis.)

THz pulse control and characterization An essential feature of THz-assisted atom probe setups is the ability to control the polarity of the THz electric field at the specimen tip, as the dominant half-cycle of the THz waveform can either enhance or counteract the applied DC bias. The specific implementation of polarity control depends on the THz generation mechanism used. In the case of the low-repetition-rate (1 kHz) setup, based on two-color plasma generation in air or nitrogen, the polarity of the emitted THz pulse is governed by the relative phase between the fundamental (ω, 800 nm) and second harmonic (2ω, 400 nm) laser pulses. Varying the chirp of the fundamental pulse or adjusting the distance between the BBO crystal and the plasma filament provides means to tune the waveform's symmetry (Fig. 2.10(a)) [246, 248].

Because the ω and 2ω pulses propagate in air with different refractive indices, their relative phase drifts with the BBO–plasma spacing Δx (Fig. 2.10(b)). This phase drift maps directly onto the sign of the dominant half-cycle of the emitted THz field. In the small-signal model used for calibration (see [246]), the normalized THz peak scales approximately as

$$\frac{E_{\mathrm{THz}}}{E_{\mathrm{THz}}^{\max}} = \sin\Big(\tfrac{2\omega}{c}\,(n_{2\omega} - n_\omega)\,\Delta x + \phi_0\Big),$$

which yields the sinusoidal trend observed experimentally in Fig. 2.10(a) (blue) and predicted theoretically (red). By translating the BBO crystal (tuning Δx) it is possible to invert the waveform's dominant lobe at the tip: Fig. 2.10(c) shows a *negative-THz* pulse (main negative lobe along the tip axis in the opposite verse), whereas Fig. 2.10(d) shows a *positive-THz* pulse (main positive lobe aligned with the tip axis). In practice, we call "positive THz" the case where the dominant half-cycle *adds* to the applied DC bias at the tip (favouring cation evaporation), and "negative THz" the case where it *subtracts* from it.

100 kHz THz System – Lithium Niobate Optical Rectification

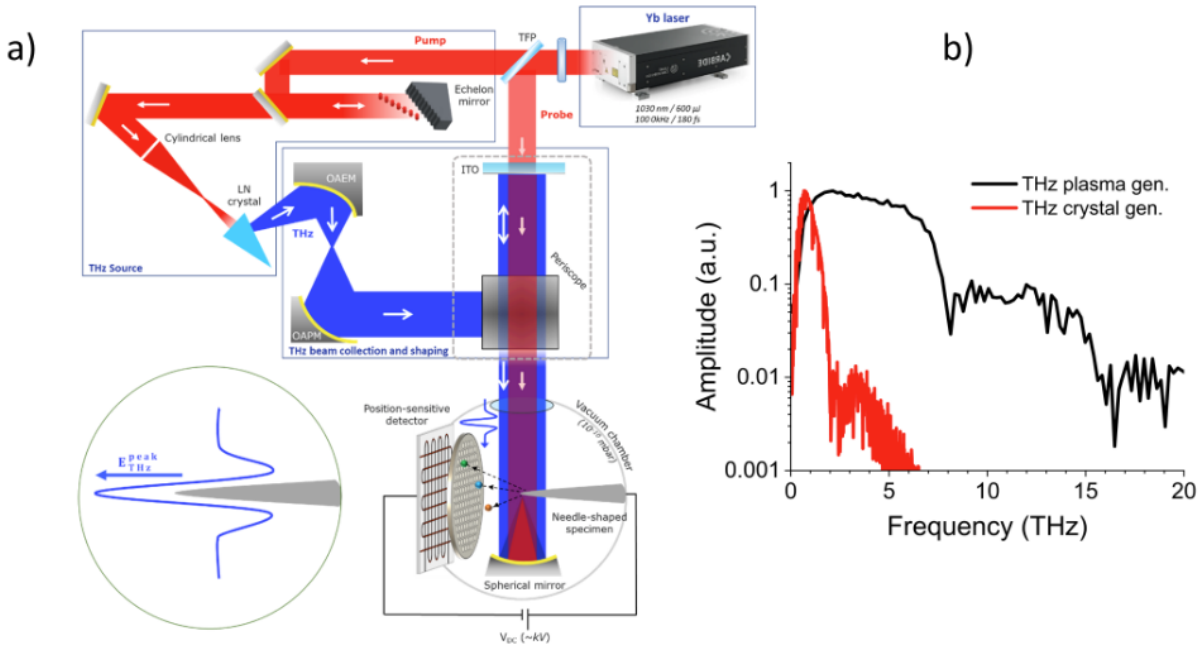

Figure 2.11: (a) High repetition rate TERA-SAT setup. THz generation involves optical rectification in lithium niobate crystal. *Courtesy of Léo Guiramand* (b) Spectral amplitude (normalized) for low (black curve) and high (red curve) repetition rate TERA-SAT systems obtained by applying FFT on the respective electro-optic signals.

The high-repetition-rate THz setup employs a CARBIDE Yb:solid-state laser (sub-200 fs, 1030 nm, 600 μJ/pulse) and a tilted-pulse-front pumping (TPFP) geometry to generate THz radiation *via* optical rectification in lithium niobate (LN) (Fig. 2.11(a)). A wavefront-tilted beam meets the phase-matching condition for THz generation in the LN crystal. The THz pulse is collected, collimated, and directed into the APT chamber *via* an ITO-coated beam combiner and sapphire window.

This system delivers 1.1 ps-wide THz pulses with peak fields estimated up to 170 kV/cm, a value

that is almost five times lower than the maximum field achieved in the low-repetition-rate TERA-SAT system, namely 800 kV/cm, based instead on two-color plasma generation. This difference in field strength directly impacts the evaporation regime and material compatibility. When analyzing the THz waveform *via* electro-optic sampling, followed by Fast Fourier Transform (FFT) analysis of the temporal trace, it becomes evident that the spectral amplitude of the high-repetition-rate system is mostly concentrated in the 0–2 THz frequency range. In contrast, the low-repetition-rate TERA-SAT system generates a significantly broader spectrum (above 40 THz), with detectable amplitude stopping at around 10 THz, as visualized on a logarithmic scale in the frequency domain, because its spectral response is cut by the GaP electro-optic crystal around that frequency (Fig. 2.11(b)).

While the 100 kHz system lacks waveform tunability, its high throughput and long-term stability (power fluctuation $< 0.2\%$ over 2 hours) make it ideal for systematic studies and large-volume data acquisition. In this configuration, the THz waveform is inherently single-polarity due to the rectification process and the fixed crystal orientation. However, polarity inversion can still be achieved by introducing a reflective optical element into the THz beam path. The reflection introduces a π phase shift, which effectively inverts the electric field of the pulse in time, thereby switching the polarity of the dominant half-cycle, without modifying the crystal orientation or laser beam parameters, providing rapid and reliable control over the THz field direction at the specimen apex. When using this setup, before starting any experiment, we enclose the THz beam path in a sealed box and purged it with dry air to keep the relative humidity below 10%, thereby minimizing atmospheric water-vapor absorption and delivering more THz energy to the tip. Water vapor has strong absorption in the THz range, so THz setups are routinely operated in dry air or nitrogen to reduce loss and spectral distortion; doing so measurably improves transmitted field and signal quality [249].

2.5 Samples

This work primarily involves the *sol–gel silica* matrices introduced in the previous chapter 1, studied both as thin films and as bulk specimens. In addition to silica, several metallic materials were analysed for specific experimental roles: tungsten was used as a pretip substrate for mounting and supporting silica lift-outs. Pure aluminium and pure nickel served as conductive

reference samples to commission and benchmark the THz-assisted atom probe systems. The NS8 nickel-based superalloy was investigated as a technologically relevant case study to test the performances of our THz-assisted APT high repetition rate setup. The following subsections describe the synthesis protocols and physical characteristics of the different sample types prior to their preparation into APT specimens.

2.5.1 Synthesis of sol–gel silica: water glass method

To study biomolecules, particularly proteins, using APT, we use an embedding approach in which proteins are incorporated into a solid silica matrix. This preserves proteins in their native aqueous state while the surrounding water is replaced by a silicon–oxide network formed through a gentle sol–gel process. Because conventional acid/base catalysis risks denaturation, we neutralize an alkaline sodium–silicate ("water glass") solution by cation exchange to reduce the pH and initiate gelation under bio-compatible conditions. This method has been successfully used in prior instances for preparing materials for APT analysis [18, 190]. The complete workflow is shown in Fig. 2.12.

Silica is synthesized from a commercial sodium–silicate stock (sigma-Aldrich) diluted 1:3 with Milli-Q water (Millipore, $> 18.2\ \mathrm{M\Omega \cdot cm}$) and passed through an ion-exchange column assembled in a plastic syringe. Briefly, a 20 mL syringe is packed with 0.5–1 cm of glass wool at the outlet, a perforated plunger seal, and ~ 2.5 g of a strong-acid cation-exchange resin (e.g., Dowex/AmberChrom 50WX8). The resin is regenerated and stored in NaOH (4 M), then flushed with water, activated by 10 mL of HCl (1 M), and equilibrated by passing small water aliquots until the effluent pH reaches 4–6 [18, 190]. Subsequently, 2.5 mL of the diluted silicate is passed through the column to yield a neutralized sol (typically pH $\approx$ 5–8). Because gelation begins rapidly after neutralization, the sol can be optionally held on ice to slow condensation; the final pH is tuned by adjusting the post-activation water volume and its pH.

In general, during and after the ion exchange process, the pH of the sol substantially influences the structure and characteristics of the resultant gel. At lower pH levels (4–5), hydrolysis predominantly occurs, which results in a slower gelation process and the formation of more open network structures characterized by an abundance of terminal silanol (–SiOH) groups. This structure enhances porosity and increases the density of defect states, such as non-bridging

oxygen hole centers (NBOHCs), which absorb in the near-UV range and affect laser absorption properties. As the pH approaches neutral (6–7), condensation reactions become more dominant, forming a denser silica network with fewer reactive groups.

These gels tend to be mechanically stronger but show reduced optical absorption in the UV spectrum and might have lower surface reactivity. Post ion exchange, the sol is cast into polypropylene or polystyrene molds and allowed to gel at ambient temperature, typically within 1–2 hours. The gel is aged in its original solvent for up to 7 days to promote additional condensation and enhance structural integrity. This aging process increases cross-linking density and boosts the gel's resistance to mechanical deformation during later processing. After aging, the gel is carefully rinsed with deionized water to eliminate excess ions and then dried at 37 °C. Slow drying is crucial as it prevents pore collapse and maintains mesoporosity. The final dried gels are usually translucent, easy to cleave, and mechanically robust enough for handling and focused ion beam (FIB) applications.

Biomolecules embedding For biomolecule encapsulation, in the case of production of bulk samples, the desired biomolecule is added immediately after ion exchange to reach the target concentration in the sol. The loaded sol is cured at 37°C in oven for 48 hours to complete gelation.

The sample can be reshaped also in a 2D geometry, in which the protein solution is embedded in a silica thin film (200 nm thickness) by spin-coating a sodium silicate solution on silicon wafers, immediately after pH adjustment according to the previously described procedure. The silicon wafers coated with a 10 nm thin chromium film were acquired from Substrata, Ångström Engineering, and heat treated at 600 °C to improve the adhesion between the layers and the silica film. The wafers were cleaned by ultrasonication in isopropanol followed by ethanol and after that, treated in a UV/O_3 oven. Representative photographs and schematics of the bulk and film samples are shown in Fig. 2.13(a–e). Panel 2.13(f) displays a *TEM* micrograph of a silica film embedding ferritin molecules, on the same fashion of the preparation shown in [250].

The specific surface area and pore-size distribution of representative gels were determined by nitrogen sorption measurements (e.g., ASAP 2020, Micromeritics), a standard technique to characterize porosity in amorphous solids. In this approach, the amount of adsorbed N_2 as a function

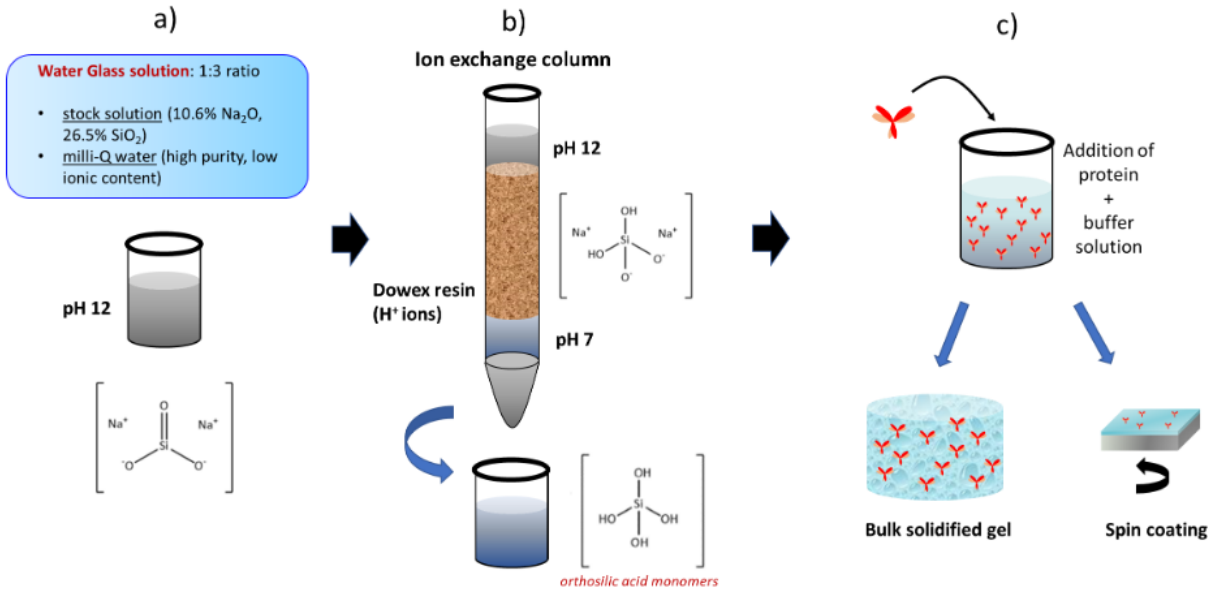

Figure 2.12: Sol–gel silica preparation by the water-glass route. (a) Sodium silicate solution; (b) ion-exchange process in a plastic syringe; (c) addition of the biomolecule and gel solidification into bulk or spin-coated samples.

of pressure provides information on both the accessible surface area and the characteristic pore dimensions. The Brunauer–Emmett–Teller (BET) method was used to extract the total specific surface area from the adsorption isotherm [251]. Micropores (typically < 2 nm) were analysed using the Horváth–Kawazoe (HK) model, which is sensitive to narrow pore widths [252], while mesopores (2–50 nm) were evaluated using the Barrett–Joyner–Halenda (BJH) method applied to the desorption branch of the isotherm [253].

Typical values for the sol–gel formulations used in this work are a BET surface area of $\sim 5.9 \times 10^2$ m^2 g^{-1}, an average micropore width of ~ 6.8 Å, and a mesopore diameter of ~ 40 Å. Together, these parameters indicate a hierarchical micro–mesoporous network, combining a high internal surface area with pore sizes compatible with molecular diffusion and solvent exchange, while remaining sufficiently small to enable gentle confinement and stabilization of embedded biomolecules.

Silica films were prepared by spin coating neutralized water-glass sols (pH adjusted to 5) at 1750 rpm for 90 s and drying at 37 °C. Before FIB work, both bulk surfaces and films were sputter-coated with a thin conductive metal layer (usually less than 10 nm layer of Pt, C or Au).

Choice of proteins We selected three proteins: ferritin, GFP, and ^{13}C-labelled GFP. Ferritin was chosen because it has been successfully embedded for APT in other matrices (e.g., polymer resins and *via* graphene encapsulation) [166, 254], and we aimed to test whether sol–gel silica affords similarly clean outcomes, as previously observed for IgG [18]. In principle, ferritin is also straightforward to localize thanks to its iron-rich core: detection of Fe isotopes (notably Fe^{2+} at 28 Da) can serve as a molecular proxy—though this is complicated by the Fe^{2+}/Si^{+} overlap at ∼28 Da, which challenges peak assignment in silica matrices [255]. Beyond serving as a metrological probe, ferritin is biologically relevant, as its apoferritin shell can encapsulate therapeutics such as cisplatin, enabling "Trojan horse" delivery.

From a structural point of view, ferritin is a nearly spherical protein complex with an outer diameter of ∼12 nm, composed of 24 subunits forming a hollow shell that encloses a ∼8 nm iron-oxide mineral core. This well-defined core–shell architecture makes ferritin a convenient reference system for testing spatial localization and chemical sensitivity in APT.

GFP was selected as a compact (∼5 nm) and widely characterized protein that is easier to model than larger antibodies; its inherent fluorescence additionally permits complementary photoluminescence characterization if desired [256, 257]. Structurally, GFP adopts a rigid β-barrel fold composed of 11 β-strands surrounding a central α-helix that hosts the chromophore. This relatively robust and symmetric architecture, with a molecular mass of ∼27 kDa, makes GFP a useful benchmark for assessing the preservation of small, globular proteins within the silica matrix.

Finally, ^{13}C-labelled GFP provides an isotopic handle that enables unambiguous identification of protein-derived carbon in the mass spectrum. By shifting the dominant carbon-containing fragments relative to the natural-abundance background, ^{13}C labelling facilitates discrimination between protein signal and matrix- or contamination-related carbon, and can be cross-validated with ToF–SIMS ion maps to localize ^{13}C-enriched regions [258].

Protein embedding recipes

The list of the main samples used throughout this thesis is provided in Fig. 2.13:

Silica thin-film samples (ferritin & reference).

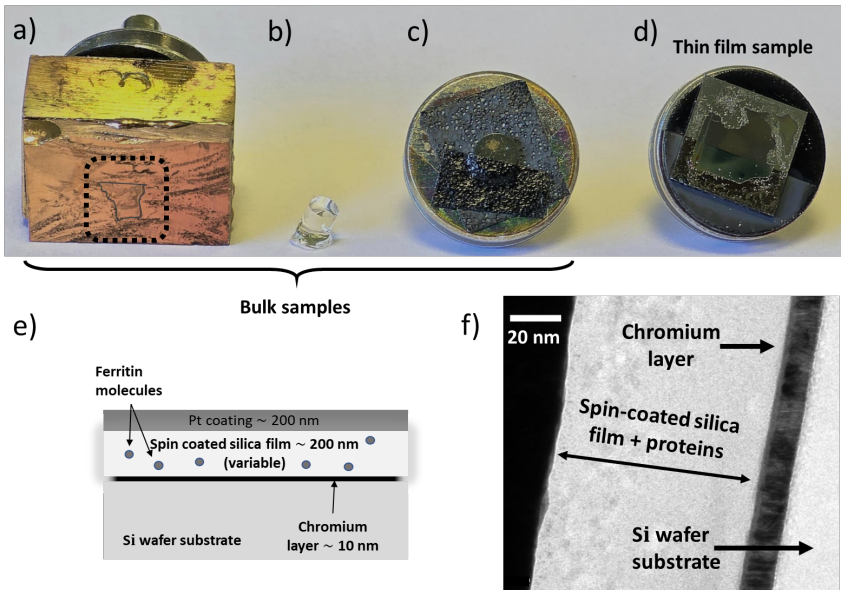

Figure 2.13: Silica samples: a) Sample 5: conductive resin-embedded and Au coated sol-gel with 13C-labelled GFP protein (region of interest highlighted by black guiding line). b) Sample 1: Empty sol-gel silica bulk sample. c) Empty sol-gel fixed on sample holder by carbon tape and carbon coated (pre-FIB operation). d) Sample 4: Spin-coated thin film sol-gel silica embedding ferritin molecules fixed in the same way on the same support. e) Schematics of a spin-coated sample. f) TEM micrograph showing an overview of ferritin molecules embedded in a silica film as example of spin-coating outcome (*courtesy of Gustav Eriksson).*

1. **Sample 1 - Empty silica sol-gel:** spin coat 250 µL neutralized water-glass (pH 5) at 1750 rpm for 90 s.

2. **Sample 2 - ferritin embedded in sol-gel:** 225 µL of the same water-glass + 25 µL ferritin (10 mg/mL in PBS); spin coat as above. For this sample the ferritin concentration is 1.00 mg/mL.

Bulk silica samples (ferritin & reference).

1. **Sample 3 - Empty silica sol-gel:** 250 µL water-glass solution diluted 1:3 with Milli-Q water (stock ∼10.6% Na_2O, ∼26.5% SiO_2); adjust to pH 6.5 before drying.

2. **Sample 4 - ferritin embedded in sol-gel:** same water-glass solution with 25 µL ferritin (10 mg/mL in PBS) added. For this sample the ferritin concentration is 0.91 mg/mL.

GFP related samples

1. **Sample 5 - GFP–silica bulk:** GFP in 0.05 M phosphate buffer (pH 7); water glass = 1:3 sodium silicate in Milli-Q (stock ∼8% Na_2O, ∼27% SiO_2); per sample: 0.300 mL water

glass + 0.075 mL protein (total 0.375 mL); protein diluted 5× (final $C = 0.20\,C_0$). For this sample, the GFP concentration is 0.10mg/mL

2. **Sample 6 - ^{13}C–GFP bulk silica:** The ion-exchange column was equilibrated by passing water until the effluent ("extrudate") reached pH ≈ 5. The diluted sodium–silicate solution, after passing through the column, had a final pH of 8. To 250 µL of this silicate, 50 µL of ^{13}C-labelled GFP solution (1 mg/mL) was added. For this sample the ^{13}C-labelled GFP concentration is 0.167 mg/mL.

All samples were dried at 37 °C.

2.5.2 Other materials

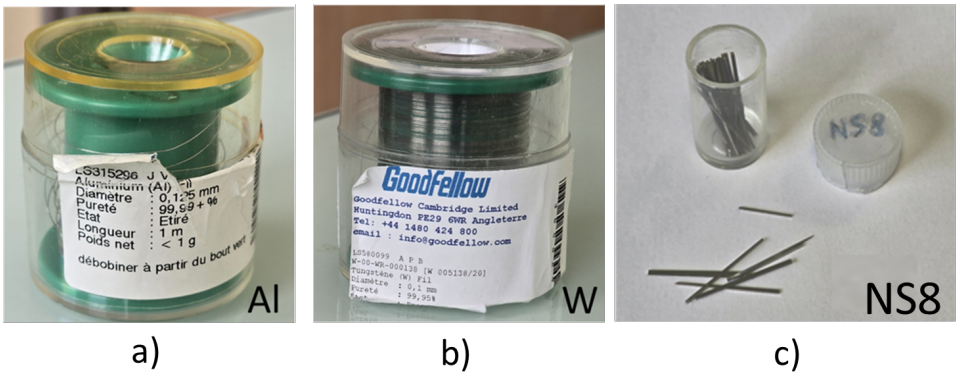

Figure 2.14: Materials treated by electropolishing: (a) Aluminum rod. (b) Tungsten rod. (c) NS8 Nickel superalloy sticks.

In addition to sol-gel silica, a range of metallic and ceramic materials were analyzed in this thesis, including pure aluminum, pure nickel and the nickel-based superalloy NS8 (Fig. 2.14), with the first two used as test-samples or tip supports for sol-gel silica chunks, and the latter being the only one presented in Chapter 5. These materials were chosen to benchmark the behavior of different classes of conductors and insulators under laser-assisted and terahertz-assisted atom probe conditions. Below is a summary of the physical characteristics, source forms, and sample preparation strategies applied for each.

Tungsten (W) Tungsten wires (99.958%, diameter = 0.1 mm, Goodfellow) were used as support posts for lift-out and mounting of sol-gel silica and crystalline specimens. The pretips were prepared by standard electropolishing in 3% NaOH, producing sharp tips suitable for FIB

attachment and minimal thermal drift during APT acquisition. Tungsten's high conductivity and mechanical stiffness make it a reliable base for non-conductive specimen mounting.

Aluminum (Al): High-purity aluminum wire (99.99%, Goodfellow, $\varnothing = 0.125$ mm) was used to produce tips for APT. Two fabrication approaches were applied: (i) direct electropolishing, and (ii) electropolishing followed by focused ion beam (FIB) refinement. The former allowed for rapid sample throughput, while the latter enabled reproducible tip radii below 100 nm for optimal evaporation control. Aluminum served both as a calibration standard and a testbed for THz-APT under high repetition rates, due to its high electrical conductivity and well-characterized evaporation behavior.

NS8 Superalloy: The **NS8** superalloy is a nickel-based alloy designed as a variant of the N18/Astroloy systems, but elaborated *without* additions of boron or zirconium. Its nominal composition is centered on Ni (53.3 at.%), with significant amounts of Cr (15.7 at.%), Co (15.5 at.%), Al (8.2 at.%), Ti (4.4 at.%) and Mo (2.8 at.%), as well as controlled traces of C (920 ppm), S (20 ppm) and O (78 ppm). The microstructure, shown in Fig. 2.15, consists of a γ *matrix*, a Ni-rich, substitutional solid solution with an FCC lattice in which the different alloying species are randomly distributed and that is comparatively soft, and ductile and coherent γ' *precipitates* with an ordered primitive-cubic ($L1_2$) structure of nominal composition $Ni_3(Al, Ti)$. The ordered nature and coherency of γ' impede dislocation motion and thus provide the primary strengthening mechanism. The metallurgical elaboration is followed by a specific heat treatment aimed at stabilizing this two-phase architecture and the strengthening γ' phase: a solutionizing step at 1100 ℃ for 4 h with cooling at 50 ℃/min, followed by two aging treatments at 700 ℃ for 24 h and at 800 ℃ for 4 h, both air cooled. This combination of chemistry and thermal processing promotes controlled γ' precipitation, providing NS8 with high mechanical strength while avoiding the intergranular segregation effects typically influenced by B and Zr in other superalloys.

Samples were prepared from wire stock using two methods: (i) electropolishing alone and (ii) electropolishing followed by focused ion beam (FIB) milling to refine the tip geometry.

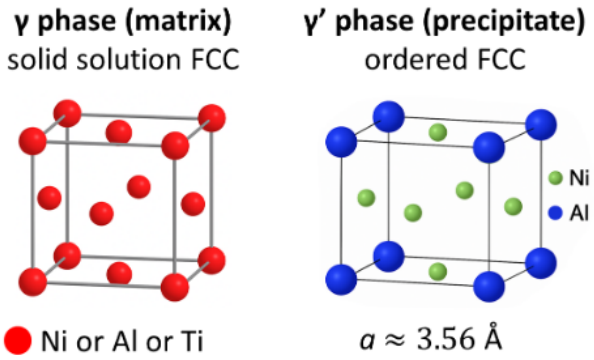

Figure 2.15: Schematic of the two principal phases in a Ni-base superalloy: γ (matrix), an FCC solid solution with random atomic distribution and ductile character; and γ' (precipitate), an ordered primitive-cubic ($L1_2$) phase of nominal composition $Ni_3(Al, Ti)$ whose ordered lattice blocks dislocation glide and provides strengthening.

2.6 Electrochemical and Ion Beam-Based Specimen Preparation

2.6.1 Specimen preparation by electropolishing

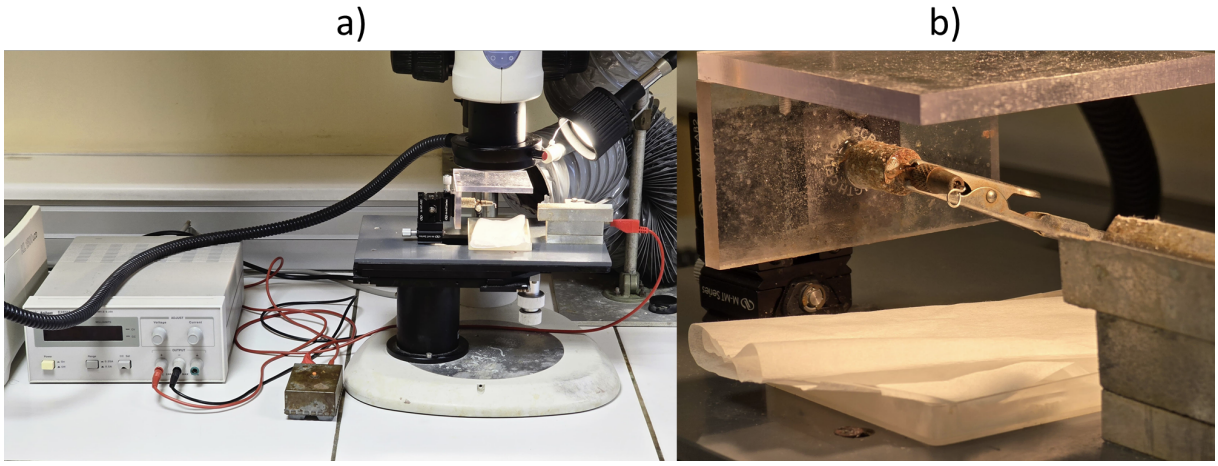

Figure 2.16: (a) Overview of the assembly composed of a direct current voltage power supply, an optical microscope operating in reflection, a specimen stage, and a platinum microloop of 5 mm diameter. (b) Closer view of the specimen facing the microloop under the objective lens.

Electropolishing is a reliable route to fabricate sharp, needle-shaped APT specimens from conductive materials [259]. The setup used here (Fig. 2.16) comprises a DC power supply, a reflection optical microscope, a specimen stage, and a Pt microloop. We applied the microloop technique to W, pure Al, and the Ni-based superalloy NS8, using material-specific electrolytes and procedures to obtain apex radii < 100 nm and stable evaporation.

In practice, a short segment of wire (anode) is positioned against a counter-electrode (cathode)

and brought into contact with electrolyte confined in a fine loop (inner diameter ∼200–500 µm). A controlled DC bias drives anodic dissolution at the liquid–metal meniscus while the polishing current is monitored in real time. To form the final taper, the apex is kept just *outside* the electrolyte and the wire is swept *horizontally* across the loop to build a localized *neck* a short distance from the end (Fig. 2.17(a,b)); [6, 7]). Once a well-defined neck is visible, brief voltage pulses are applied while moving the sample horizontally back and forth using the optical microscope stage control knobs in order to break the neck cleanly, yielding a final sharp tip with a radius below 100 nm, compatible with APT analysis (Fig. 2.17(c)); [7]).

Optimal polishing occurs on the *plateau* of the characteristic I–V curve (Fig. 2.17(d)), between lower and upper thresholds ($V_1 < V < V_2$): below V_1 material is merely etched without sharpening, and above V_2 pitting roughens the surface, degrading APT performance [6]. Achieving repeatability depends on (i) electrolyte choice and concentration, (ii) applied voltage (typically 5–15 V), (iii) meniscus stability at the loop, and (iv) timing the stop on the current decay. The method is limited to electrically conductive materials and is not site-specific, in contrast to the FIB-based approach, which will be described next.

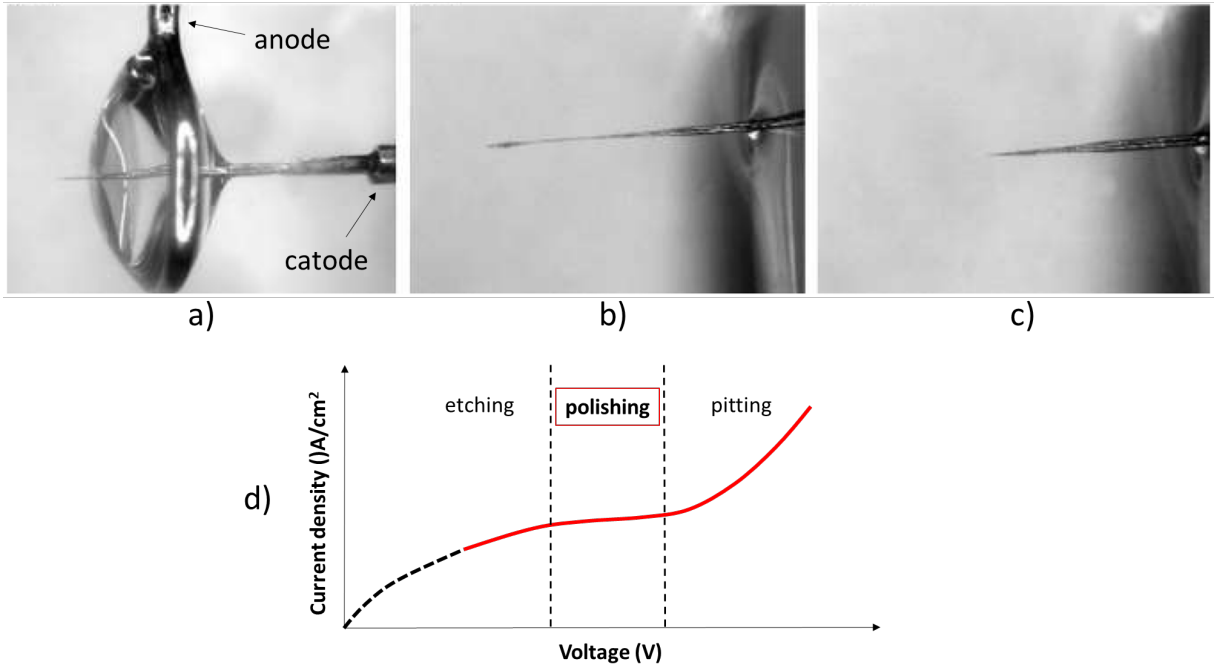

Figure 2.17: Electropolishing method. [7] (a) Low-concentration electrolyte is loaded into the microloop; a neck is formed a short distance from the apex by keeping the specimen apex just outside the electrolyte. (b) Optical image of the neck produced by the method in (a). (c) Final sharp needle obtained by breaking the neck with brief voltage pulses. d) Characteristic electropolishing curve. The central plateau represents the ideal voltage range for achieving a stable electropolished APT sample. Adapted from [6].

Tungsten (W) Tungsten pretips, used as substrates for sol-gel silica lift-outs, were prepared using a 3% sodium hydroxide (NaOH) aqueous solution, due to its efficient oxide formation and dissolution balance, yielding uniform surface finish and sharp tips with minimal redeposition.

Aluminum (Al), and NS8 Superalloy These materials were electropolished using a two-step approach with perchloric acid ($HClO_4$) in butoxyethanol or acetic acid, following protocols inspired by the literature and practical procedures outlined in [7]. The first step employed a higher acid concentration (60% $HClO_4$ in butoxyethanol or glacial acetic acid) to remove bulk material and pre-shape the taper. The second step used a diluted solution (10% $HClO_4$) to refine the apex and minimize surface roughness. Voltages ranged between 10–15 V, with polishing durations of 10–30 seconds per step. This dual-stage strategy enabled improved reproducibility and smoother profiles, essential for materials such as NS8 which contain multiple phases (e.g., γ/γ' structure). After electropolishing, all samples were rinsed in ethanol and stored under controlled vacuum conditions.

2.6.2 Focused Ion Beam-based specimen preparation

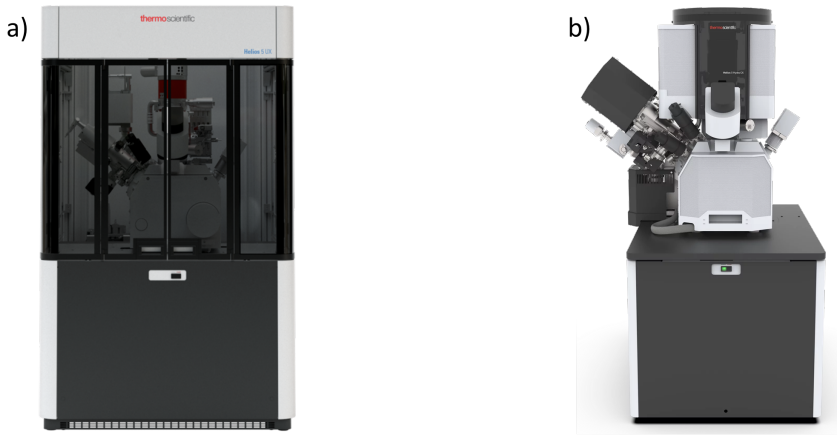

Figure 2.18: (a) Thermo Fisher Helios 5 UX Ga FIB; (b) Thermo Fisher Helios 5 PFIB (Xe).

To fabricate sharp atom probe needles, a focused ion beam (FIB) is often employed, typically paired with a scanning electron microscope (SEM). The FIB-SEM serves as a precise milling device for shaping or removing specific sections of materials in a regulated manner, achieving a resolution comparable to SEM. Focused ion beam (FIB) systems facilitate the site-specific extraction and formation of APT tips with radii less than 100 nm. Most FIB-SEM setups

utilize a liquid gallium source primarily due to gallium's relatively low melting point. However, there is an increasing trend in using plasma FIB (P-FIB) instruments equipped with a plasma xenon source, replacing the liquid gallium. The primary advantage of this technology is the decreased beam-induced damage attributed to xenon's reduced penetration depth. Additional advantages include the ability to mill at higher current levels and increased milling speed [260–262].

In this work we used two dual-beam platforms (Fig. 2.18(a,b)): a Thermo Fisher Helios 5 UX Gallium FIB for for site-specific extractions and final apex shaping of fragile, low-density matrices due to its higher precision and a Thermo Fisher Helios 5 Plasma-FIB (Xenon source) for rapid bulk removal.

Both instruments include high-resolution SEM columns, a Gas Injection System (GIS) for *in situ* Pt/W deposition, and micromanipulators for lift-out and transfer. Insulating specimens (e.g. bulk sol–gel silica) were sputter-coated with a 10–20 nm conductive overlayer (C, Pt, or Ag) to mitigate charging during lift-out; welding was done by Ion Beam-Induced Deposition (IBID, using Pt or W gas), typically at 30 kV with 0.1 nA for W gas or 30–41 pA for Pt gas. Pre-shaped W supports with a ∼2 µm flat platform ensured stable mounting and centered annular milling.

General workflow. The parameters adopted during the tip preparation are usually dependent on the material, but in full generality a protective Pt cap is first deposited over the region of interest (ROI) by a Gas Injection System (GIS), after which trenches are milled to isolate a chunk (2.19(a-c)). The micromanipulator is then attached by GIS, the base is cut to free the piece, and the chunk is extracted and mounted onto a flat-top W pretip as shown in 2.19(d-g). Shaping proceeds *via* successive annular milling steps, with the ion current progressively reduced from ∼1 nA to 30–50 pA until an apex < 100 nm is obtained. Finally, a low-kV Ga^+ clean (2–5 kV, 1–3 min) removes the amorphous damage layer and implanted ions 2.19h-i) [6, 7].

The lift-out can be performed following two different undercut strategies:

- With the stage at 52°, two parallel trenches define a vertical wall; after returning to 0°, an undercut forms a cantilever that is extracted, chunked (3–5 tips), and mounted. A *single-side* IBID weld on the chunk–post interface is generally sufficient (Fig. 2.19; [6, 7]).

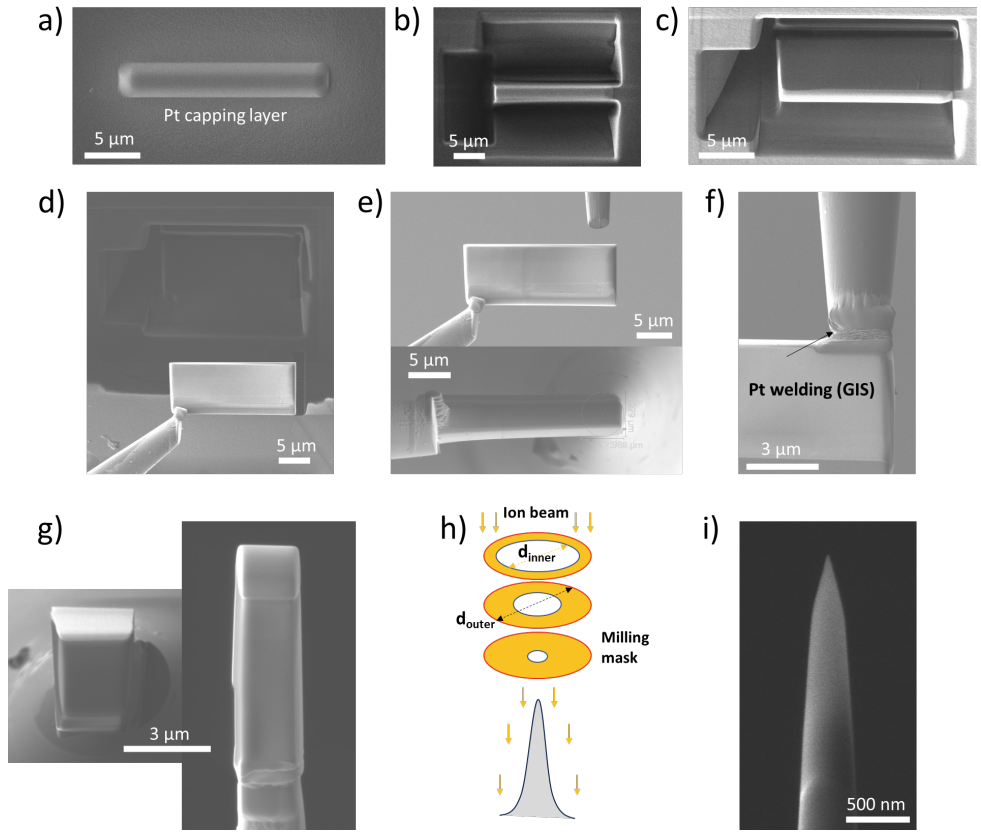

Figure 2.19: 52° "wall" method: (a-c) trenching, (d-g) lift-out and mounting on W post, (h-i) annular milling to form an APT needle.

- Two symmetric oblique cuts (stage tilted ∼22° so the ion beam is ∼30° to the surface normal) generate a self-isolating V-shaped chunk. The subsequent welding to micromanipulator, the transfer, annular milling, and low-kV clean procedures are the same as above; however, for silica films and other fragile lamellae we systematically used double-side IBID welds to reinforce the bond on the flat-top post. Figure 2.20(a,b) summarizes the distinct cut geometry illustrating representative mounting and sharpening outcomes.

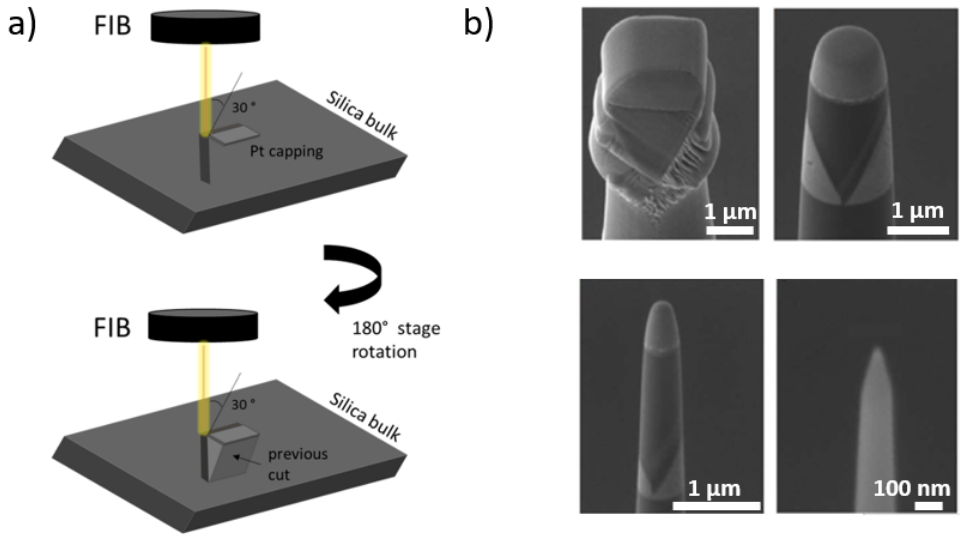

Figure 2.20: a) Cantilever ("V-shape") method: symmetric oblique cuts generate a V-shaped chunk. b) The lift-out, annular milling, low-kV clean steps are identical to the wall method, except that *double-side* GIS welding is used to mount the chunck on the pretip. *courtesy of G. Eriksson.*

Sol-Gel Silica Specimen FIB preparation recipe and useful parameters

The lift-out procedure begins with the deposition of a protective platinum capping layer over the region of interest (ROI) using the gas injection system (GIS). The platinum was deposited *via* ion beam-induced deposition (IBID) at 1 nA and 30 kV for 1 minute and 30 seconds. The resulting cap measured approximately 20 µm in length, 2 µm in width, and 1 µm in thickness. This layer protected the ROI from Ga^+ implantation, redeposition, and curtaining during subsequent milling.

Three trenches are milled to define the extraction wall: above, below, and to the left of the protected ROI. These were performed using a 52 nA beam at 30 kV for a total of 5 minutes. A horizontal undercut was then carried out at the base using a 4 nA beam at 30 kV, detaching the wall on three sides.

The micromanipulator needle is then brought into contact with the upper part of the chunk, and a localized weld was created using platinum GIS deposition at 41 pA and 30 kV for 1 minute, ensuring secure attachment between the chunk and the needle. After complete detachment, the chunk was transferred to an electropolished and FIB-shaped tungsten pre-tip featuring a previously cut flat platform approximately 2 µm in diameter.

Attachment to the pre-tip was achieved *via* a second GIS-assisted weld, using either tungsten or platinum as the deposition material, again at 41 pA and 30 kV for approximately 1:30 to 2 minutes. This ensured firm adhesion and optimal centering prior to annular milling.

The mounted sample undergoes then the following successive annular milling steps:

1. **Step 1:** 5 µm outer diameter / 2 µm inner diameter at 1 nA, 30 kV
2. **Step 2:** 4.5 µm outer / 1.5 µm inner at 0.4 nA, 30 kV
3. **Step 3:** 4 µm outer / 0.5 µm inner at 260 pA, 30 kV
4. **Step 4:** 3 µm outer / 0.1 µm inner at 41 pA, 30 kV

A final low-voltage cleaning step was applied using a 2 kV Ga^+ beam at 20–50 pA. This rastered over the tip region until approximately 150 nm of material was removed, effectively eliminating the amorphous or damaged surface layer caused by previous high-energy milling steps. This step improves the tip's field evaporation behavior by reducing Ga contamination and geometric irregularities.

Tips prepared using this protocol consistently exhibited apex radii below 20 nm, ensuring high-resolution performance during both laser- and THz-assisted APT experiments.

2.7 Coating methods

Metallic (and 2D) surface coatings are routinely used to make insulating APT specimens electrically manageable during FIB preparation and field evaporation [175, 176]. A thin, continuous conductor restores charge transport, suppresses charging/drift, and concentrates the local electric field at the apex (lightning-rod/antenna effect), which is especially beneficial for field-driven triggers like HV or THz pulsing. In this work we consider two complementary routes: a chromium film deposited by PECS sputtering, offering robust adhesion to silica, batch scalabil-

ity, and reliable junction bridging; and monolayer graphene encapsulation, providing ultrathin, minimally intrusive coverage with negligible added mass. In both cases, the aim is a continuous conductive path that bridges the silica–tungsten interface while keeping the apex appropriately exposed, typically with coatings on the order of tens of nanometres for chromium, and a single atomic layer for graphene, in order to stabilize evaporation, improve spectral quality, and increase mechanical stability and yield.

2.7.1 Deposition *via* PECS – Equipment and Parameters

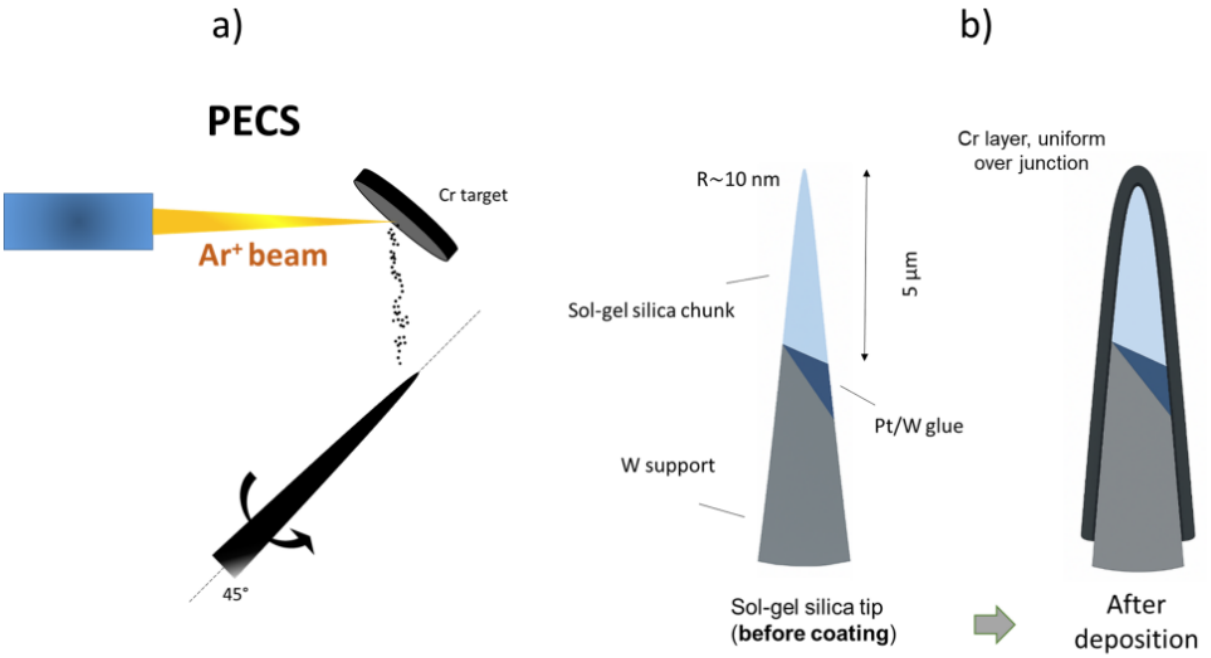

Figure 2.21: Chromium coating of sol-gel silica APT tips by PECS sputtering. a) Ar^+ beam at shallow incidence onto a continuously rotating holder to ensure uniform sidewall coverage while minimizing shadowing/rounding at the apex. b) After deposition, a conformal Cr cap ($\sim$ 10 nm) bridges the silica–W junction and covers the apex, providing a continuous conductive path and improved mechanical robustness for APT analysis.

Chromium was used to coat silica tips in order to eliminate charge accumulation and Schottky-like behavior at the silica-metal interface. As shown in Fig. 2.21, chromium was deposited in a Gatan PECS system using a broad-beam Ar^+ source and a Cr target. The chamber was pumped to $\sim 10^{-5}$ mbar and operated at an Ar partial pressure of $\sim 10^{-4}$ mbar during coating. Ar^+ ions at 5–6 keV sputtered the target at a rate of 0.2–0.3 Å/s. The stage was tilted by $\sim 45°$ and continuously rotated at $\sim$ 10 RPM to ensure conformal coverage of the shank and the silica–metal junction. Deposition for several minutes yielded a 7–10 nm Cr film; the concurrent mild ion etch promoted good adhesion to silica.

Post-deposition SEM, TEM and EDX analyses (Fig. 2.22(a,b)) confirmed uniform, well-adhered coatings without flaking or shadowing. Brief air exposure formed a thin native Cr_2O_3 passivation layer, improving environmental stability while preserving conductivity. Samples were stored under vacuum and when possible, transferred rapidly to the atom probe to limit contamination. The coating smooths surface asperities and reinforces the fragile silica geometry, reducing fracture risk under high fields and improving the THz field coupling.

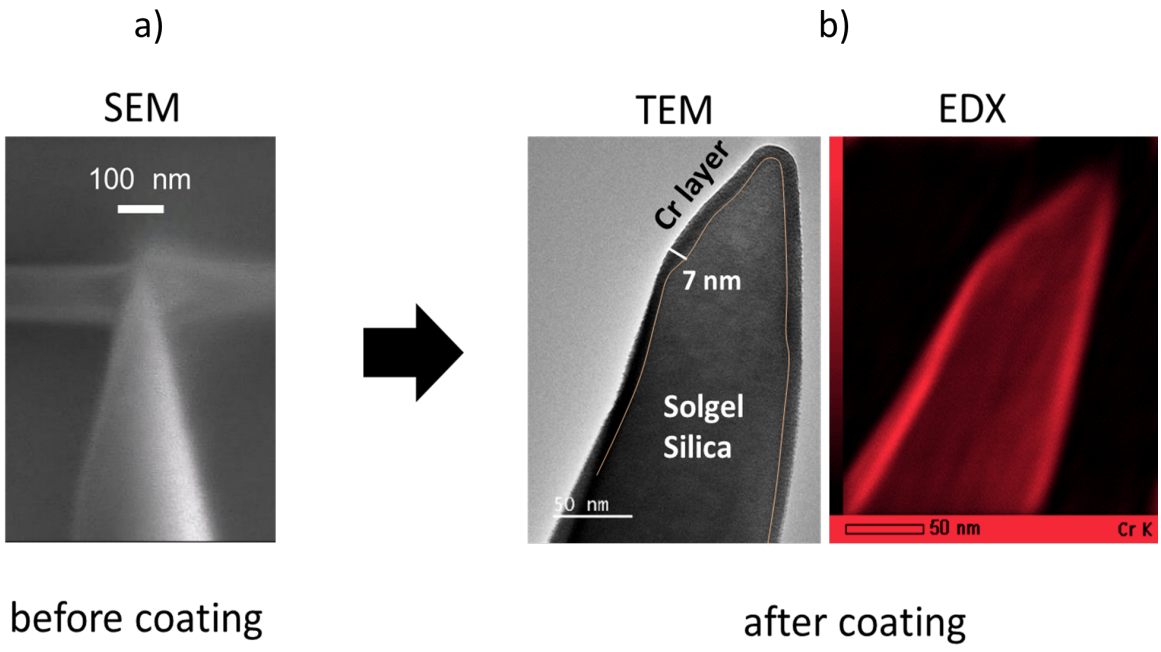

Figure 2.22: Chromium coating of sol-gel silica APT tips. (a) SEM of the apex after PECS sputtering. (b) TEM cross-section with EDX (Cr-K) confirming a 7 nm Cr shell uniformly covering the silica tip (the orange line guides its visualization). *Courtesy of Simona Moldovan*

.

While it is possible to metallize tips using in situ by redeposition techniques [176] or by gas injection systems (GIS) within the FIB *via* deposition of organometallic Pt or W layers, this approach has significant limitations:

- **Film Purity:** FIB-deposited metals typically contain less than 20% of the target metal, with the rest being carbonaceous residues and voids. This results in low electrical conductivity and increased risk of Ga implantation, which can alter specimen chemistry or lead to poor APT performance.
- **Coverage Uniformity:** FIB-GIS coatings are inherently anisotropic, leading to shadowing and incomplete coverage. PECS, on the other hand, delivers uniform coverage due to

continuous sample rotation and broad-beam deposition.

- **Contamination Control:** PECS introduces no external elements aside from the Cr and ambient oxygen. In contrast, GIS deposition introduces precursor-derived impurities, Ga ions (if Ga-FIB is used), or Xe-induced artifacts in PFIB, depending on vacuum quality [176].

- **Mechanical Properties:** PECS-deposited Cr films are dense and adherent, forming robust "shells" around the tip. GIS-deposited films are often porous or amorphous and less mechanically reinforcing.

- **Faster specimen production:** The ex-situ sputtering process was found to be more reproducible and time-efficient, allowing batch coating of tips without needing to interrupt the FIB workflow to rotate the tip in order to uniform the deposition. Specimen handling was carefully optimized to avoid contamination during vacuum transfer.

Based on these considerations, after evaluating both the FIB in-situ methodology and the PECS sputtering technique, we have chosen to proceed with the latter. Nonetheless, we remain open to the possibility of optimizing the in-situ approach for analyzing sol-gel silica in future investigations, as remarkable results have been obtained in the community so far using this method [176].

2.7.2 Graphene Coating for APT specimens

An alternative to PECS chromium sputtering for insulating APT tips is monolayer graphene encapsulation. When successful, graphene fully bridges the silica/metal pre-tip interface and circumvents the adhesion and flaking issues often seen with sputtered metals, providing a conductive skin that amplifies efficiently to external electric or THz fields while minimally perturbing tip geometry. While in previous studies [166, 177, 180, 263], this approach was introduced to encapsulate small liquid volumes containing biomolecules, in this work, we exploit graphene primarily for its electrical and thermal conductivities: a conformal mono- (or few-) layer coating over the apex, composed of a single-atom-thick sheet of sp^2 carbon (0.34 nm nominal thickness) provides an electrically continuous path, preserving the high field-enhancement factor required for evaporation, with the only drawback of altering the tip's apex geometry and curvature.

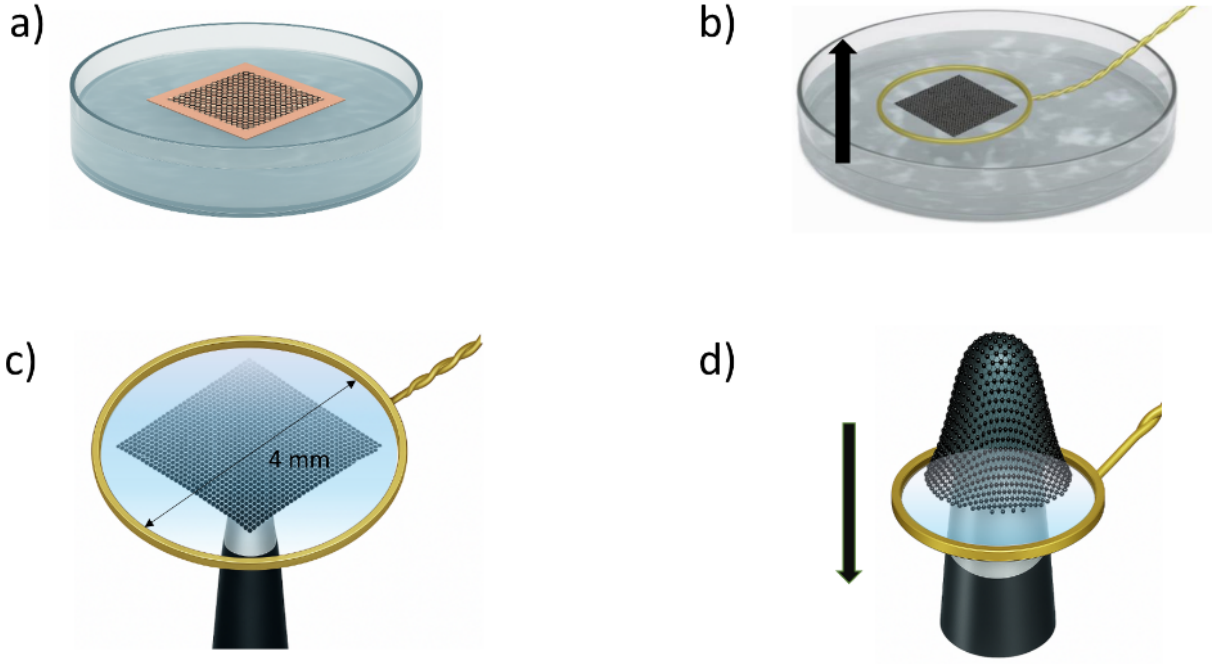

Figure 2.23: Schematic of the wet transfer process used to coat silica tips with graphene. (a) Dissolution of copper substrate with APS solution. (b) Retrieval of the graphene layer using a wire loop. (c) Wire loop holding graphene foil over the specimen's apex. (d) Final graphene encapsulated tip.

Wet Transfer Method Protocol

Here, we report the steps of the protocol used by pioneering works of Adineh et *al.* and Qiu et *al.* on the subject [59, 165, 166, 177]. In this work, the graphene encapsulation process, or "wet transfer method" (schematized in Fig. 2.23(a-d)) was performed using a polymer-free wet transfer technique adapted to the constraints of atomically sharp needle-shaped specimens. The entire process takes place in aqueous media, using Milli-Q grade ultrapure water and relies on capillary forces and surface tension for the transfer and alignment of the graphene film.

Graphene monolayers were first synthesized by chemical vapor deposition (CVD) on copper foil substrates. These foils were then cut into square pieces approximately 3 mm $\times$ 3 mm in size. The copper side of the graphene/Cu sheet typically appears uniformly metallic and bright, whereas the graphene-coated side exhibits a slightly brown tint with a delicate surface contrast. Special attention was paid to maintaining the correct orientation of the sheet during handling, as the graphene side is more fragile and should face upward during the etching process.

To release the graphene film, a 0.1 M ammonium persulfate (APS) solution was prepared by dissolving 600 mg of APS crystals in 20 mL of Milli-Q water. The graphene/Cu pieces were

gently introduced into a shallow glass Petri dish (6 cm in diameter and 2 cm tall) containing the APS solution, with the copper side facing downward. Over a period of several minutes, the copper substrate was gradually etched away, leaving the graphene sheet floating at the air-liquid interface (2.23(a))

Once the copper was fully dissolved, the APS solution was replaced with Milli-Q water to remove ionic contaminants and prevent chemical damage to the graphene. This was done using a peristaltic pump connected to a glass Pasteur pipette and fitted with a flexible Tygon tube. The solution was aspirated carefully to avoid disturbing or aspirating the graphene film. When the solution level reached the bottom of the Petri dish or when air bubbles began to form inside the pipette, the aspiration process was halted. Fresh Milli-Q water was then injected gently using a 20 mL syringe to refill the dish. This cycle of aspiration and refilling was repeated at least three times to ensure complete removal of APS residues.

To collect the graphene film, a thin loop made from 0.5 mm diameter stainless steel wire was prepared, with an inner diameter of approximately 4–5 mm. The size of the loop was chosen to match the dimensions of the floating graphene patch, as shown in Fig. 2.23(b,c). The loop was mounted on a custom manipulator derived from optical bench components, including a "holding arm" and a three-axis micrometer stage with a 20 mm vertical travel range and 5 mm motion capability in the x, y, and z directions. This setup allowed precise manual control of the loop position.

Importantly, the vertical descent (Fig. 2.23(d)) of the loop carrying the graphene film during the encapsulation phase was not done manually but was motorized. This motorized z-axis movement allows for precise control over the encapsulation speed during the approach of the graphene to the tip (Fig. 2.24(a,b)). This parameter is critical, as shown in previous studies, and is illustrated in Fig. 2.25(b) [264], where a linear relationship between encapsulation speed and tip radius was established. Encapsulation speeds that are too high can result in graphene fracture, whereas slower speeds tend to yield successful conformal coatings.

When the loop is lowered onto the floating graphene film, the graphene adheres to the water membrane and becomes suspended across the loop. The loop is then raised out of the water, carrying the graphene film stretched flat across its aperture.

The atom probe specimen, a silica tip mounted on a metallic post, is placed on a support block aligned beneath the graphene-carrying loop. The loop is then slowly lowered until the graphene film made contact with the apex of the tip. Upon contact, van der Waals forces and capillary action cause the graphene to conform to the shape of the tip, wrapping around its high-curvature surface without the need for external pressure or adhesives. The loop is then retracted, leaving the graphene film attached to the tip. In some cases, this process was repeated two or three times on the same tip using different regions of the same graphene piece to ensure full surface coverage and to seal potential holes, or grain boundaries in the initial layer. Figure 2.24(c) illustrates the different coating zones used on a single graphene sheet (multiple encapsulations visible as perforations). Because graphene layers strongly adhere to each other *via* van der Waals interactions, this multilayer approach did not result in delamination or shape distortion.

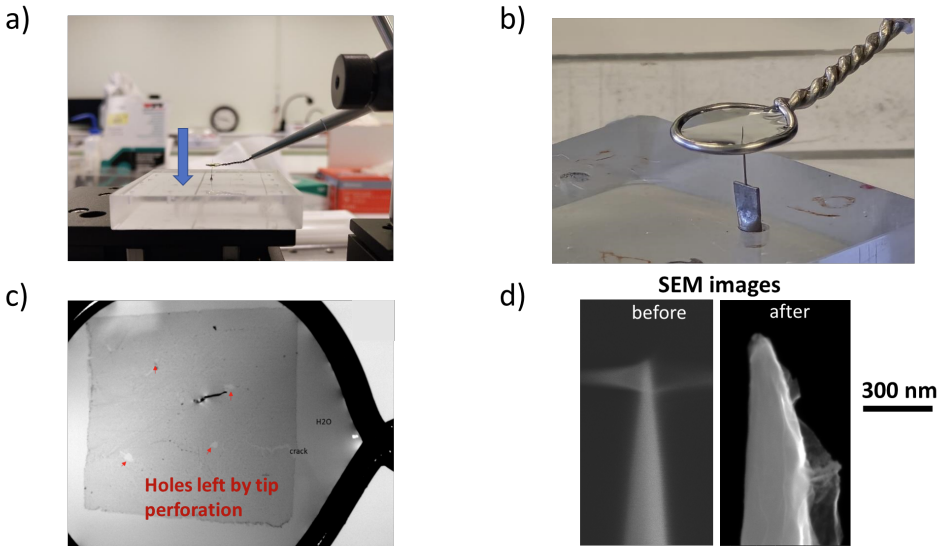

Figure 2.24: Implementation of the graphene wet-transfer used to encapsulate silica APT tips. (a) Wide view of the motorized setup highlighting the controlled z-axis descent of the wire loop carrying a water film with suspended graphene toward the tip. (b) Magnified view at the moment of contact. (c) Stereo-microscope view of the same graphene patch after multiple encapsulations, showing the holes left by multiple tip perforation. (d) SEM comparison of a silica tip before and after coating, evidencing the ultrathin graphene coating homogeneously covering the tip.

Quality Control High-resolution imaging on a Leica S9 stereo microscope. in order to localize cracks and holes in the graphene sheet after perforation by the tip (Fig. 2.24(a-c)), while continuity of the graphene coating was assessed by SEM imaging (Fig. 2.24(d)).

The vertical speed for the encapsulation process was set through the "NSC200 New Step Controller" software (Fig. 2.25(a)), which allows to control a motorized system which can move with

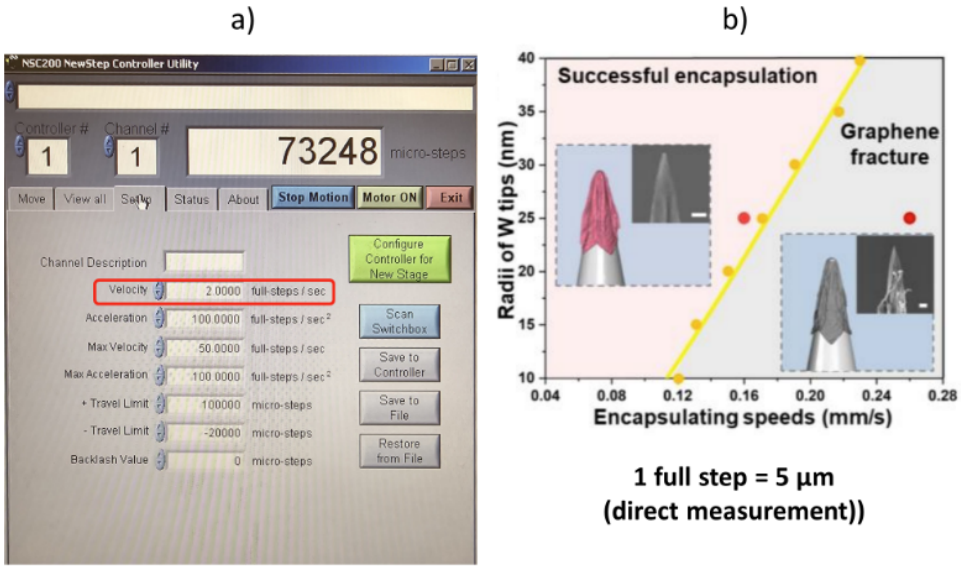

Figure 2.25: Motorized control and speed guideline. (a) NSC200 controller window used to set the motorized z-descent during graphene transfer. (b) Reference chart (pure W tips) of encapsulation speed vs. tip radius showing the success–fracture boundary used to select safe approach speeds.

micrometric precision steps along the z-axis. Although no parametric speed study was performed here for sol-gel silica, prior work on liquid-loaded W tips ([264]) shows that encapsulation speed governs membrane stress: as the sheet conforms to the tip, stresses localize first at the contact zone, then at wrinkle boundaries, reaching $\sim$ 74–84 GPa at moderate speeds (e.g., 0.16 mm s^{-1}), close to graphene's $\sim$ 100 GPa fracture strength. A near-linear relationship between allowable speed and tip radius was reported; for $R \approx 25$ nm, a critical speed of $\sim$ 0.17 mm s^{-1} was experimentally verified, with higher speeds causing catastrophic rupture (SEM-confirmed). These results set a practical upper bound for the z-axis descent rate in our encapsulation workflow (Fig. 2.25(b)).

We therefore maintained motorized z-axis motion within the safe regime inferred from tungsten-tip studies, improving reproducibility and tip-to-tip uniformity. Coating success was verified indirectly by uniform secondary-electron contrast in SEM, absence of charging, and improved mass-spectral peak shape/resolution in APT. Post-coating, specimens were stored in a vacuum-sealed desiccator to limit moisture and airborne contamination.

Previous tests on tungsten tips To set up the workflow, we first practiced on FIB-prepared tungsten tips and report representative outcomes of successful and failed encapsulations (Fig. 2.26(a-c), Fig. 2.27), as verified by SEM and TEM imaging. Initially, without

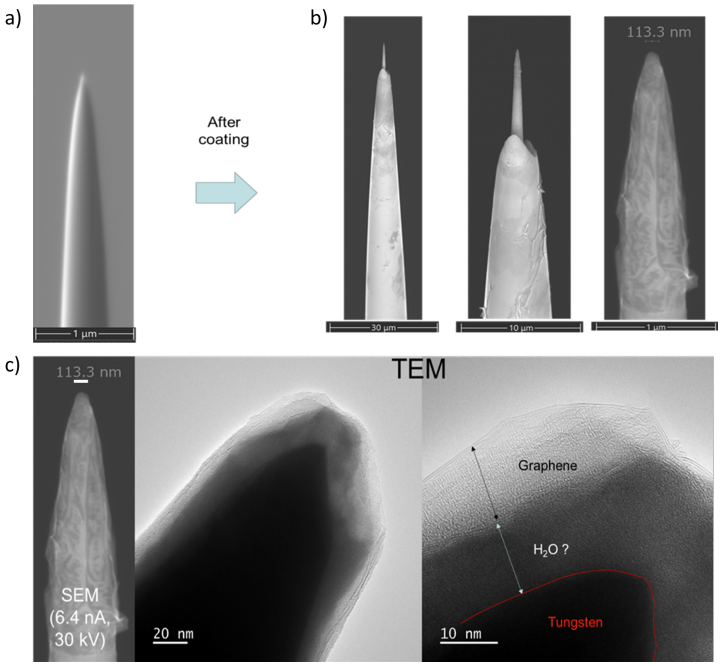

Figure 2.26: Successful graphene encapsulation for a pure tungsten tip. (a) SEM view before coating. (b) Progressive magnification evidences graphene presence at the apex. (c) Comparison SEM-TEM views: in TEM it is possible to distinguish more clearly several graphene layers capping on the tip.

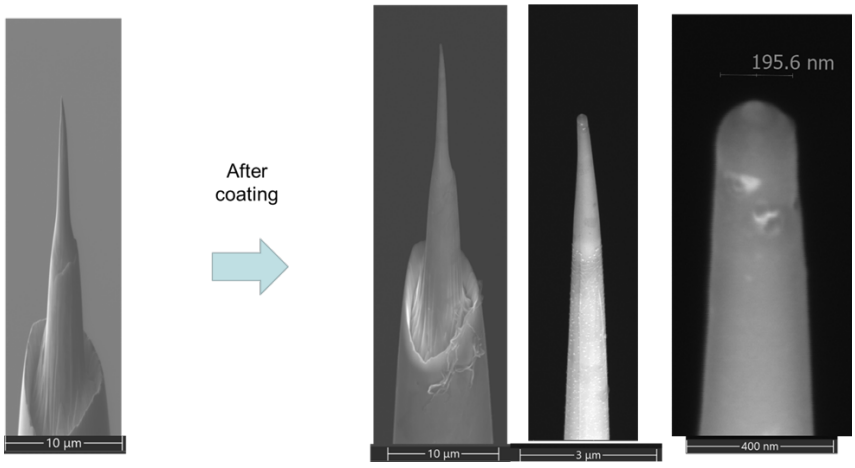

Figure 2.27: SEM image showing unsuccessful graphene coating on a pure tungsten tip. No graphene layer is visible at the apex.

motorized control, the z motion was adjusted manually by knob rotation at very low speed (a typical encapsulation takes $\sim$ 2 min for completing the vertical motion, but is subject to human error). We subsequently implemented the previously mentioned motorized system controlled *via* the legacy "NSC200 New Step Controller" software.

CHAPTER 3

Analysis of sol-gel silica samples by UV-laser assisted Atom Probe Tomography

This chapter introduces the experimental results obtained by UV–laser–assisted atom probe tomography (APT) on bare sol–gel silica samples, and on sol-gel samples embedding different kinds of biomolecules (ferritin, GFP protein, and ^{13}C–labeled GFP protein). These samples were analyzed to determine operating parameters that can guarantee a long duration for the APT analysis as well as maximize mass-spectral quality and 3D-reconstruction fidelity. Compositional analysis was also conducted for some of the following results.

All UV-assisted atom-probe experiments on sol-gel silica that were directly carried out by the author were performed at GPM laboratory on the LAWATAP instrument (CAMECA) at $\lambda = 343$ nm wavelength radiation. All deep-UV atom probe measurement were performed by collaborators from Chalmers University on a LEAP 6000XR at $\lambda = 343$ nm (see Chapter 2 for details about the instruments).

3.1 UV analyses (LAWATAP) of Thin film sol-gel silica samples embedding ferritin

At the beginning of this work, we investigated spin-coated sol–gel silica thin films with the specific aim of detecting embedded ferritin by UV–laser–assisted APT, focusing on **sample 2** with the feautures described in Sec. 2.5.1.

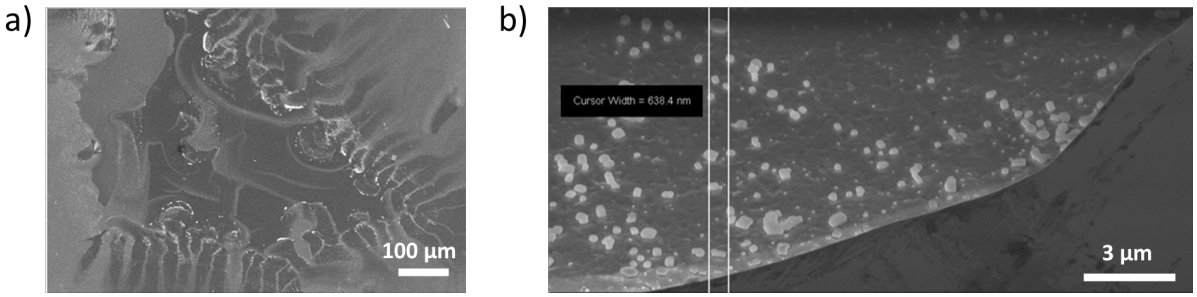

Figure 3.1: (a) SEM view of large are of the spin-coated sol–gel silica thin film sample contaning ferritin with partial edge wrinkling. (b) Magnified view on near-surface non-identified agglomerates (bright contrast).

Prior to needle preparation, a SEM inspection revealed preparation related issues, most notably partial edge delamination of the film and a dense population of sub-micrometric, near-surface agglomerates of uncertain origin (Fig. 3.1(a-b)).

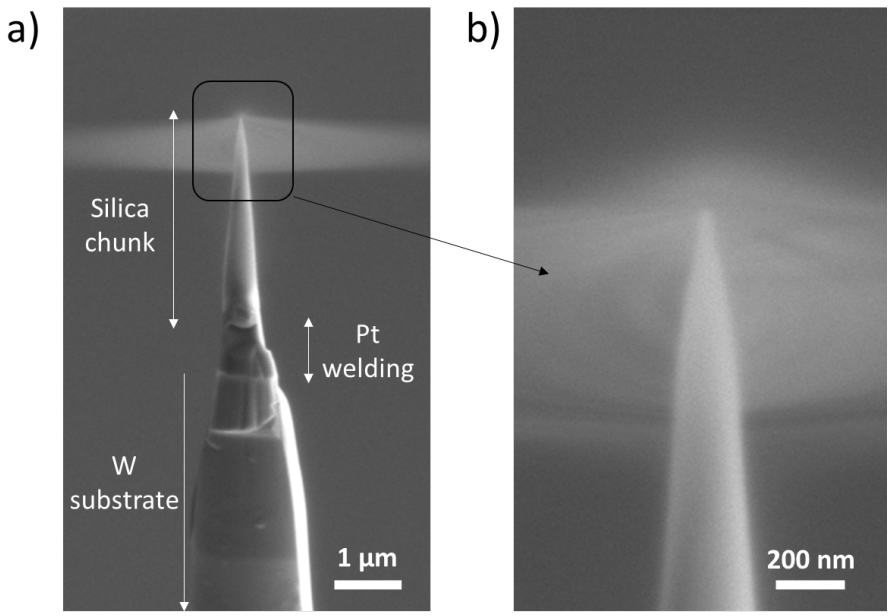

Figure 3.2: FIB-prepared APT sol-gel silica. (a) SEM imaging shows pronounced charging and degraded contrast; (b) magnification at the apex.

In the context of site-specific lift-out, we made sure to follow the provided guidelines concerning the sample, that is selecting regions from the middle of smaple where the silica film looked to be even. After FIB preparation, the SEM imaging of the tips revealed significant charging and degraded contrast quality. Additionally, no noticeable contrast variation attributable to the nominal 10 nm Cr marker layer was visible (Fig. 3.2).

Given the expected stack (∼200 nm sol–gel silica / 10 nm Cr / Si wafer), such strong charging would be unlikely if the silica cap were only ∼200 nm thick, as the underlying Si substrate should provide an efficient conduction path. In addition, during focused ion beam (FIB) preparation, no discernible contrast was observed between the sol–gel silica layer and the silicon substrate when milling cross-sections or defining the APT walls. Under typical imaging conditions, crystalline Si and amorphous silica exhibit sufficient contrast to allow their interface to be identified. The absence of such contrast in our specimens indicates that the Si/silica interface was not reached within the accessible milling depth.

Taken together, the persistent charging behaviour and the lack of a visible Cr/silica/Si interface during FIB preparation strongly suggest that, in the regions targeted for APT, the sol–gel silica layer thickness was on the order of several microns rather than a few hundred nanometres.

Accordingly, two APT analyses from Sample 2 are introduced in the next sections, with the scope of illustrating distinct evaporation conditions scenarios: a *low-field* regime and a *high-field* regime.

3.1.1 Low-field regime analysis

A 6.3×10^5–event acquisition was performed with manual tuning of the DC bias (automatic detection–rate control disabled). The laser energy was set to 32 nJ on LaWATAP (spot size ∼30 μm) [29], while the DC voltage was incrementally adjusted in an almost stepwise fashion.

Figure 3.3 partitions the voltage trace into three regions of comparable statistical weight (∼200–250 k events each), which were then used to extract the representative spectra in Fig. 3.4. The flux conditions vary across the three regions: stability improves markedly in Region 2 compared to Region 1, whereas a sudden burst marks the start of Region 3 immediately after a DC increment, and is accompanied by evident xenon diffusion. During the experiment, we realized that

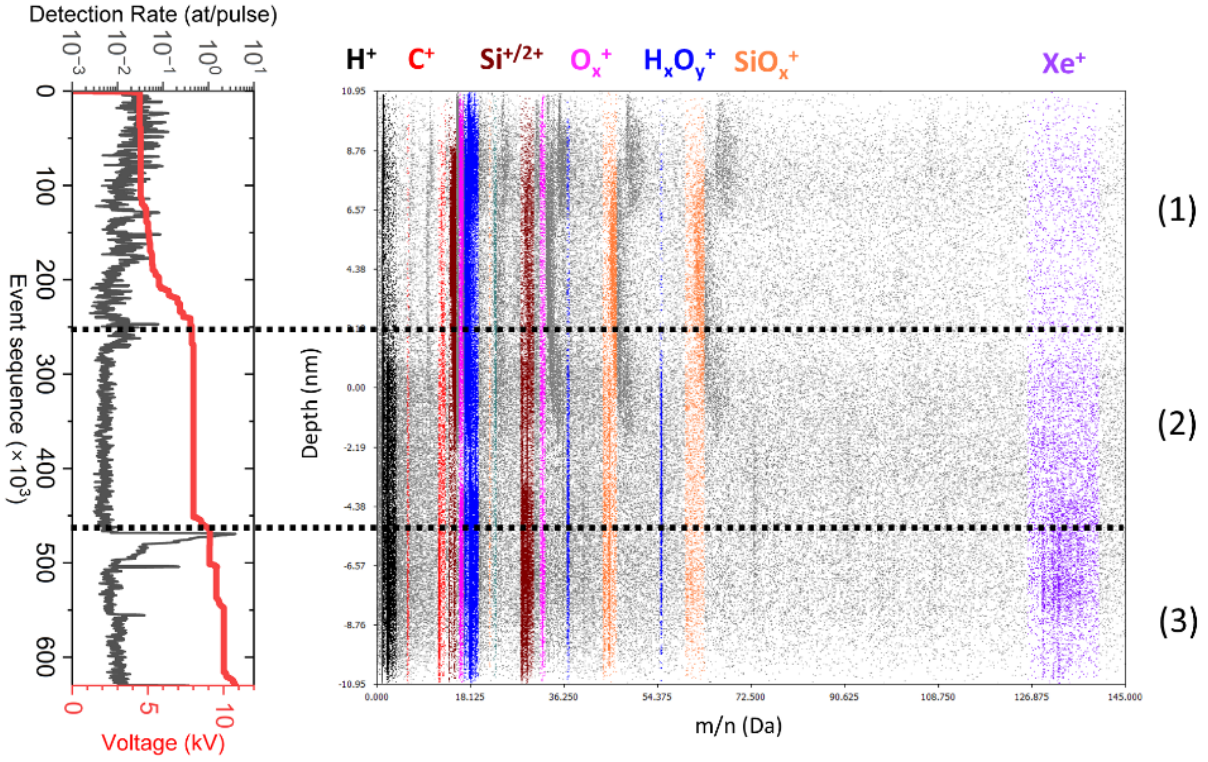

Figure 3.3: Acquisition evolution for the $6.3 \cdot 10^5$–event run on a thin-film sol–gel silica sample. Left: detection rate and DC voltage vs. event index. Right: mass–history diagram. Dashed black lines mark the interval boundaries used to define the three regions discussed in Fig. 3.4. The main detected species are indicated above in different colors.

the laser was *out of focus* until late in the run; consequently, the effective fluence at the apex was lower than the setpoint in the first half of the experiment. Proper focusing was reached only around Region 3 in Fig. 3.3. The tips were prepared in a Xe plasma FIB, so Xe^+ isotopes appear at $m/z \approx 124$–136 throughout.

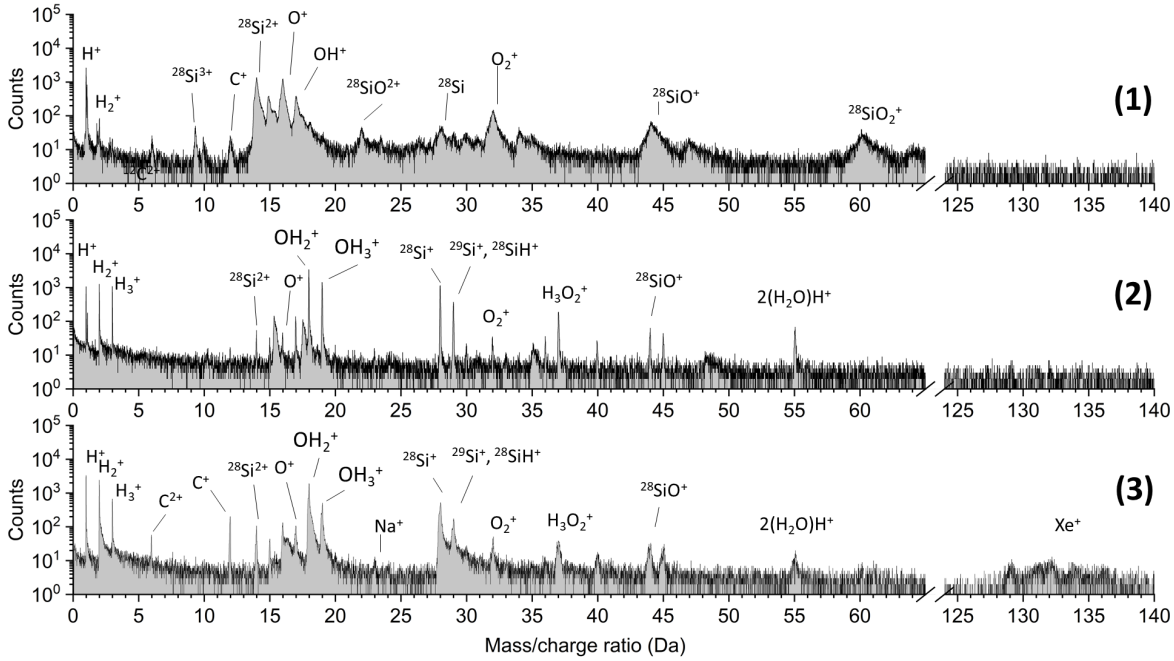

Figure 3.4: Mass spectra representative of the three regions indicated in Fig. 3.3. Region 1: 2.5×10^5 events, $V_{\mathrm{DC}} = 4.5$–$7.2\,\mathrm{kV}$, $E_{\mathrm{laser}} = 32\,\mathrm{nJ}$ (out of focus). Region 2: 2×10^5 events, $V_{\mathrm{DC}} = 7.5$–$8\,\mathrm{kV}$, $E_{\mathrm{laser}} = 32\,\mathrm{nJ}$ (out of focus). Region 3: 1.7×10^5 events, $V_{\mathrm{DC}} = 8$–$10.8\,\mathrm{kV}$, $E_{\mathrm{laser}} = 32\,\mathrm{nJ}$ (in focus). Detection–rate conditions are shown in Fig. 3.3.

The main features of the three regions (Fig. 3.4) are:

- **Region 1.** The tip radius was particularly small, producing a high field that explains the visibility of high charge states such as Si^{3+} at 9.33 Da and C^{2+} near 6 Da. This field effect was likely reinforced by the defocused laser, which minimized laser–induced thermal broadening. At the same time, substantial hydrogen and hydroxyl contamination complicates peak assignments; as this is the early stage of the analysis, surface cleaning of these species is ongoing. Continuous flux bursts are observed (see Region 1 in Fig. 3.3), suggesting ongoing minor ruptures throughout this phase.

- **Region 2.** In this case we hypothesize that a partial fracture increased the tip radius, reducing the field; consequently, higher charge states observed in Region 1 are no longer present. For instance, Si^+ now exceeds Si^{2+}, and Si^{3+} has vanished. Molecular hydrogen

is more prominent than in Region 1.

- **Region 3.** Thermal effects become evident: hydroxyl-related series (OH_x^+, $x = 1$–3) and Si^+ develop clear tails. Xe^+ emerges in the 124–136 Da range, consistent with enhanced diffusion as field and effective fluence increase.

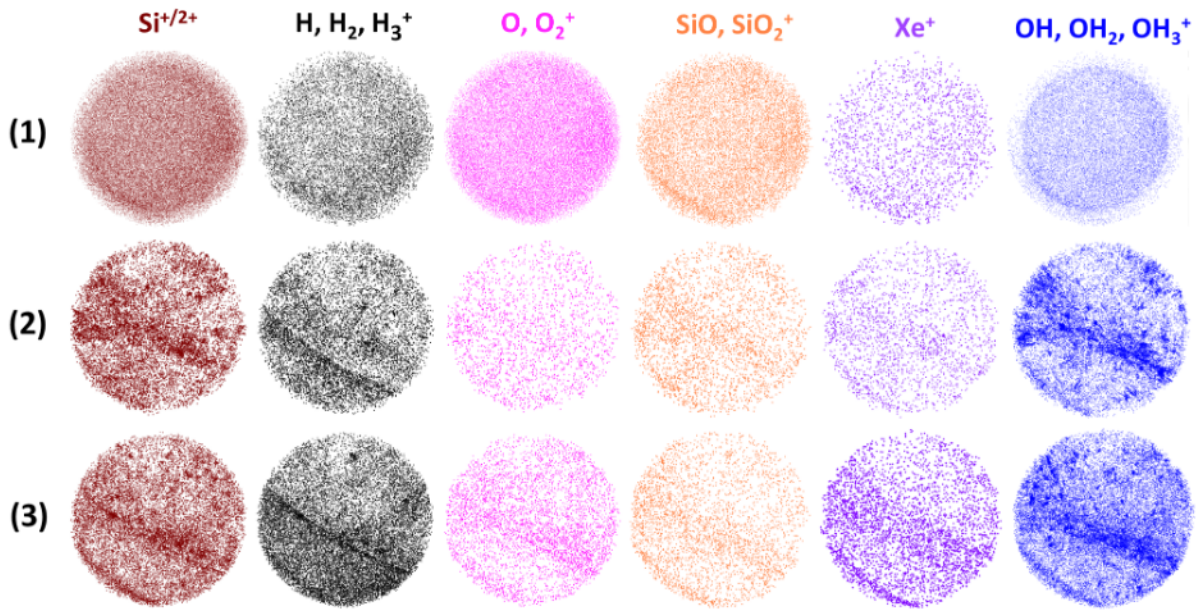

Figure 3.5: Detector hit-maps for the three analysis regions (1), (2), and (3).

Given the limited statistics of this dataset, Fig. 3.5 reports 2D hit-maps to visualize elemental distributions on the detector and their homogeneity. Region 1 shows a homogeneous distribution for the main species when the field at the tip was higher. In Regions 2 and 3, by contrast, the distribution is nonuniform and characterized by lines and/or circular dense spots, especially for hydrogen, hydroxyls, and silicon-related species. The likely tip rupture led to inhomogeneous evaporation and local field gradients across the tip surface. In Region 3, laser focusing dominates and, after the largest flux burst (around 460 k evaporated ions in Fig. 3.3), a noticeable xenon diffusion appears. This is consistent with field/temperature–assisted migration; the inhomogeneity indicates possible surface diffusion and/or transport through the sol–gel silica pores.

For a quantitative inspection uncontaminated by transient voltage changes (often concurrent with microfractures and flux spikes), we considered Region 2 as a whole, since it shows both a constant applied DC voltage and a constant average detection rate of $\sim 4 \times 10^{-3}$ atoms/pulse

over 2×10^5 events. The spectrum in Fig. 3.4 is dominated by elemental hydrogen (from the analysis chamber) and molecular ions (H_x^+, H_xO^+, O_2^+, SiO_x^+ with $x = 1$–2); Xe^+ was minimized by the interval choice.

In the presence of ferritin, iron-related peaks would be expected primarily as Fe^{2+} at ∼28 Da (and Fe^{3+} at ∼18.7 Da), although the Fe^{2+} signal overlaps with Si^+ in silica matrices. In the present spectrum, no discernible iron-related contribution is observed at these mass-to-charge ratios. The Si^{2+} signal at 14 Da is nearly absent, yielding $Si^{2+}/Si^+ \approx 3 \times 10^{-3}$ and an estimated apex field of $\sim 15.7\,\mathrm{V\,nm^{-1}}$ [231]. The early out-of-focus illumination increases the background level and, therefore, reduces the likelihood of identifying ferritin-related signatures in the spectrum; it also precludes reliable 3D reconstructions.

Given the difficulties in peak assignment and species recognition, a meaningful compositional analysis (e.g., stoichiometry and impurity quantification) was not achieved for this run. Nevertheless, the present experiment provides a reference for the subsequent high-field run, against which the influence of field and focusing on spectral clarity and spatial homogeneity can be directly compared.

3.1.2 High-field regime analysis

Figure 3.6 summarizes the second run on this thin-film sol–gel silica sample, performed at a constant UV laser energy of 25 nJ. In contrast to the low-field experiment, both the DC voltage and detection-rate traces show that the specimen remained sufficiently stable to enable effective automatic detection–rate control, set to $\sim 3 \times 10^{-2}$ atoms/pulse. The regulation persisted for $\sim 1.8 \times 10^6$ events, yielding the expected quasi-monotonic voltage ramp. Above the final voltage of 8.3 kV, the tip fractured and the analysis ended.

Figure 3.7 shows 3D reconstructions for the main species (Si, H, O, SiO, hydroxyls). To preserve a consistent depth scale across the transition, and in line with the successful automatic detection-rate trend that produced a smoothly increasing voltage, we applied an E_β rescaling (see Chapter 2). Si, O, and SiO are prevalent and homogeneously distributed, while hydrogen is uniformly present through the volume as well.

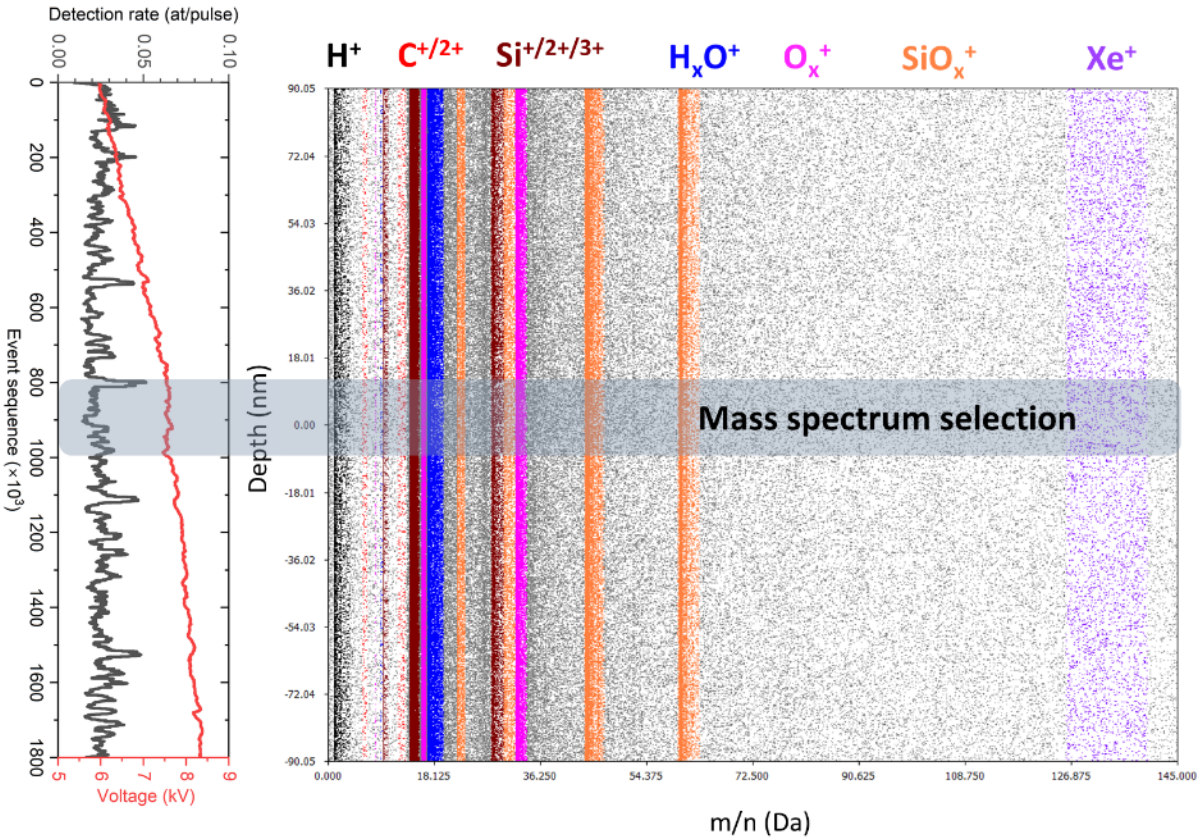

Figure 3.6: High-field run on thin-film Sample II. Left: detection rate and DC voltage vs. event index. Right: mass–history diagram with the 200k–event selection (gray band) used for mass spectrum. Conditions: $V_{\mathrm{DC}} = 5.8$–$8.3\,\mathrm{kV}$, det. rate $\sim 3 \times 10^{-2}$ atoms/pulse, $E_{\mathrm{laser}} = 25\,\mathrm{nJ}$.

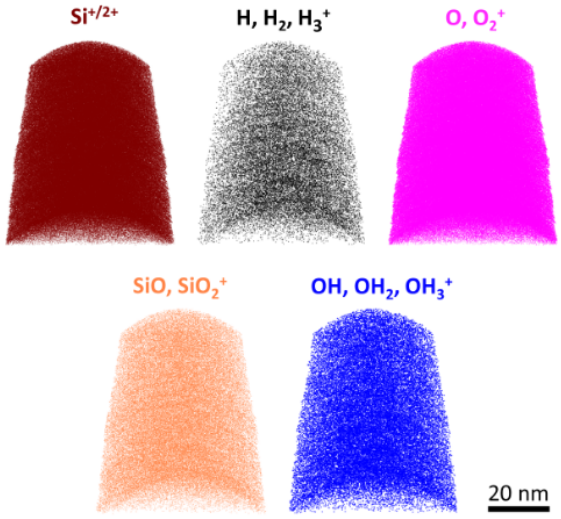

Figure 3.7: Species-resolved reconstructions for the high-field run. Before the fracture, Si^{2+}/Si^{3+}, O^+, and SiO^+ are prevalent and uniform; after the fracture, Xe^+, H_2O^+, and C^+ dominate and are inhomogeneous. The $E\beta$ method was used for 3D reconstruction.

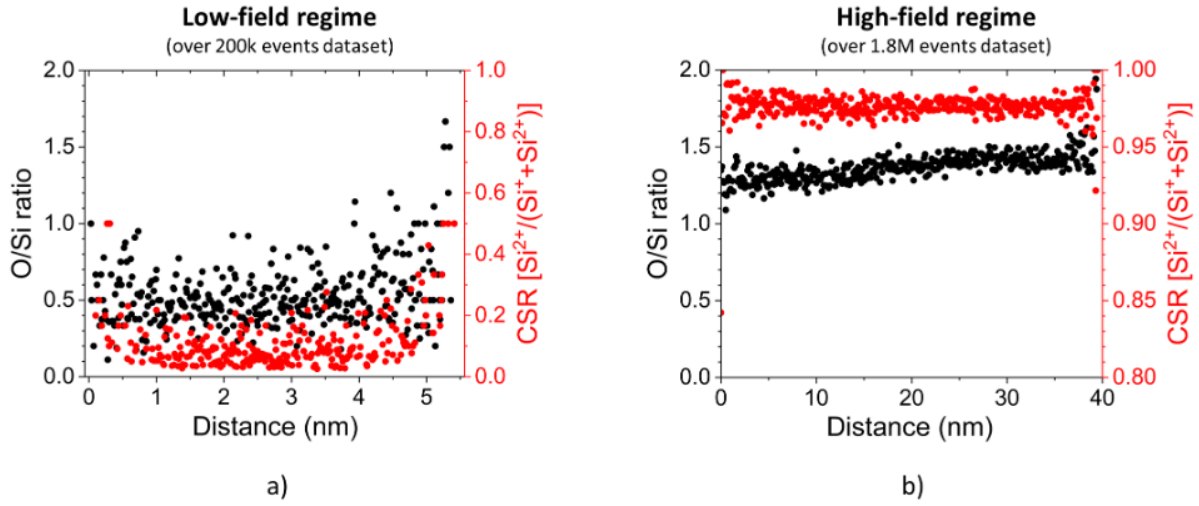

Figure 3.8: Depth profiles of O/Si ratio (black) and charge–state ratio (CSR, red) for the (a) low-field and (b) high-field datasets. Both show correlation between O/Si and CSR: higher field (higher CSR) increases O/Si, whereas lower field correlates with oxygen deficit.

Comparison between high- and low-field regimes in UV To place this run in context with the low-field dataset (Section 3.1.1), Fig. 3.8(a,b) plots the oxygen-to-silicon ratio (O/Si) and the charge–state ratio (CSR), expressed as $Si^{2+}/(Si^{+} + Si^{2+})$ for clarity, as a function of depth for the low- and high-field regime analyses. The dependence of measured composition on static field is well established and has been observed, for example, in GaAs and GaN by Di Russo *et al.* [265, 266], where variations in laser energy played a smaller role than the field in affecting stoichiometry. A similar field-driven behavior is found here for sol–gel silica: in both regimes, O/Si and CSR co-vary—higher CSR (higher field) approaches the stoichiometric O/Si $\approx$ 2, whereas lower CSR correlates with oxygen deficit. This is consistent with field-dependent neutral loss and reduced oxygen detection at low field [267]. For the high-field run, the pre-fracture portion exhibits the highest CSR, with O/Si $\approx$ 1.5.

For a controlled comparison, we selected a $\sim$200 k–event subset from the high-field run (gray band in Fig. 3.6), taken at an approximately constant voltage around $\sim$8 kV and an average detection rate around 1×10^{-2} atoms/pulse (for the high field analysis we reached 3×10^{-2} atoms/pulse at the same DC voltage value because this tip was thinner than the one related to the low regime analysis), and compared it to a $\sim$200 k–event subset from the low-field analysis at a similar DC voltage (7.5–8 kV; see Section 3.1.1). Both spectra are normalized to equal area (Fig. 3.9). The high-field spectrum shows markedly improved signal-to-noise and abundant high charge-state species (Si^{2+}, Si^{3+}, and SiO_x^{2+} with $x = 1, 2$), while molecular

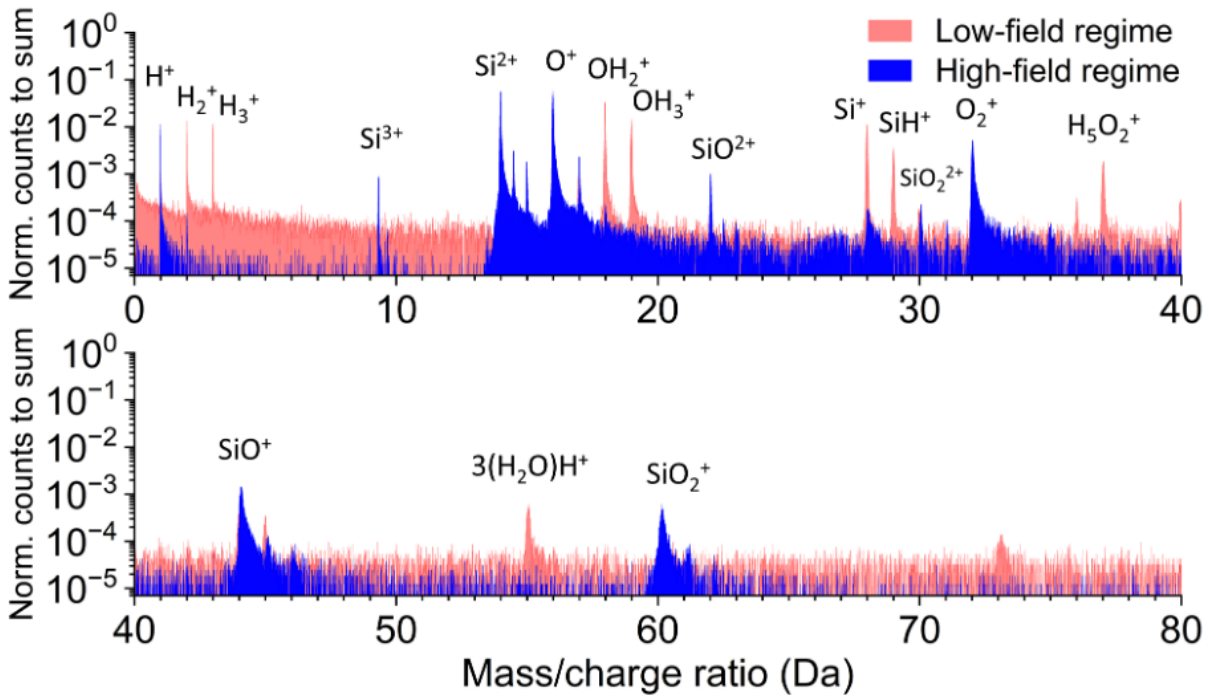

Figure 3.9: Mass spectra (normalized to equal area) comparison: low-field subset (red; ∼200k events, $V_{\mathrm{DC}} \sim 8\,\mathrm{kV}$, $E_{\mathrm{laser}} = 32\,\mathrm{nJ}$, detection rate of 1×10^{-2} atoms/pulse) and high-field subset (blue; ∼200k events, ∼8 kV, $E_{\mathrm{laser}} = 25\,\mathrm{nJ}$, detection rate of 3×10^{-2} atoms/pulse).

species prevalent at low field (H_2^+, H_3^+, and water-related peaks) are strongly suppressed. Using the CSR calibration (Section 2.2.2), the high-field subset yields $Si^{2+}/Si^+ \approx 310$, corresponding to an apex field of $\sim 22.2\,\mathrm{V\,nm^{-1}}$, compared with $\sim 15.7\,\mathrm{V\,nm^{-1}}$ for the low-field subset.

Despite the improved spectral quality and the homogeneous 3D reconstructions, no unambiguous Fe isotopic peaks or 3D clusters attributable to ferritin were observed. In addition to the expected low local concentration, the most intense Fe isotope (^{56}Fe, 56 Da) is doubly charged at high field and should appear as $^{56}Fe^{2+}$ at 28 Da, overlapping with Si^+ and possible CO^+/N_2^+ contributions, complicating attribution. Moreover, a corroborating signature at ^{54}Fe (5.9% natural abundance), expected either at 27 Da (2+) or 54 Da (1+), was not found. Given the homogeneous distributions of the dominant species and the lack of distinct Fe signatures, we cannot claim positive identification of ferritin in this dataset; nonetheless, high-field runs are well suited for composition benchmarking.

3.2 Near-UV vs deep UV-assisted APT on "bulk" sol–gel silica specimens

The initial motivation for selecting a thin-film sol–gel silica geometry was to increase the likelihood of detecting embedded proteins by atom probe tomography. By confining the biological material within a nominally thin silica layer, the three-dimensional search problem inherent to APT analyses was intentionally reduced to a quasi-two-dimensional one. In principle, such a geometry should concentrate the proteins within a limited evaporation depth, thereby maximizing the probability of intercepting them during the analysis and reducing the total analyzed volume required to observe protein-related signals.

In practice, however, this strategy proved less effective than anticipated. Post-fabrication observations suggested that the silica layer was likely thicker and more laterally extended than initially expected, leading to a dilution of the protein distribution along the analysis direction. As a consequence, the intended confinement effect was not achieved, and the probability of encountering protein-rich regions during APT acquisition remained low.

The yield of successful APT analyses on thin sol–gel silica films was therefore very low: over more than 20 attempts, only two samples produced the data previously reported. A hypothesis for these frequent failures is a tendency of the sample to break at the interface between the SiO film and the Si substrate. However, in our experiments we never collected a volume large enough to reach the silicon substrate at 200 nm depth; therefore, this remains an assumption that requires further investigation. To mitigate these limitations, we turned to bulk sol–gel silica specimens, i.e., small cylindrical blocks (dried at 37 °C for 48 h) cast with controlled protein loadings.

In this case, we prioritized volume acquisition (to test the sample's stability during analysis) on the bare sol–gel silica matrix. Accordingly, we analyzed Sample 3, introduced in Section 2.5.1.

Here, we focus specifically on comparing UV with deep-UV analyses on bare, bulk sol–gel silica specimens, as already reported and discussed in our recent publication [29].

In brief, sol–gel silica is amorphous and porous, hosting defects and adsorbates that modulate sub-bandgap absorption. Prior work shows that green (532 nm) illumination couples weakly to

silica [18] and often yields low ion counts and early fractures, whereas UV and deep-UV improve absorption and success rates; nevertheless, the density of laser-generated charge carriers remains insufficient to fully overcome silica's intrinsically low conductivity. Within this framework, the comparative analysis of bulk samples at 343 nm (LaWATAP) and 257.5 nm (LEAP 6000XR) is used to probe how defect-assisted absorption and field conditions influence mass-resolving power and thermal tails, composition indicators such as the O/Si stoichiometric ratio in correlation with field (*via* CSR), and the spatial homogeneity of reconstructions.

UV-assisted APT analyses were performed by the author at GPM laboratories while Deep-UV-assisted analyses were performed by collaborators at Chalmers University. Two bulk sol–gel silica samples, both prepared at Chalmers following Section 2.5.1, were independently analyzed at the two laboratories with LAWATAP and LEAP 6000XR instruments at base temperature of 50 K. In order to track the electrostatic field evolution on the tips during the analyses we use the silicon charge-state ratio (CSR), defined as Si^{2+} divided by the total number of Si ions, following Tegg et *al.* rivisited Kingham's approach as introduced in section 2.2.2. It is important to consider that, due to the significant differences between silica and elemental Si, field values ought to be regarded as approximations.

The mass spectra obtained with UV light (LaWATAP, 343 nm) and deep-UV light (LEAP, 257.5 nm) are shown in Fig. 3.10(a,b) for the m/n ranges 0–80 and 80–240 Da, respectively. The spectra are similar: the two main peaks can be unambiguously assigned to Si^{2+} at 14 Da and O^+ at 16 Da. The 16 Da peak is identified as O^+, not O_2^{2+}, in line with Ref. [268]. Additional peaks derived from silica correspond to Si^+ (28 Da), O_2^+ (32 Da), SiO^+ (44 Da), and SiO_2^+ (60 Da). Less prominent peaks consist of SiO^{2+} (22 Da), SiO_2^{2+} (30 Da), and Na^+ (23 Da), which are associated with the sodium-silicate preparation. Ions such as Pt, Ga, other derived from combinations of Pt and C, and elemental carbon C^+ at 12 Da, are present in all samples due to FIB-SEM processing. Molecular content varies with the energy/field conditions: notably, $Si_2O_2^+$ and Si_2O^+ disappear at low laser energy and higher static field, consistent with field-driven molecular ion dissociation [29, 267, 269]. The signal-to-noise ratio is better for deep-UV, with more distinct Pt, Ga, and C peaks (see Fig. 3.10(b)). To compare mass resolution, Fig. 3.10(c) shows a zoom of the Si^{2+} peak at 14 Da (from Fig. 3.10(a)). Here we clearly observe that while the mass resolution at 10% of peak height is 240 for deep-UV and 160 for UV, when calculated at 1% of the peak

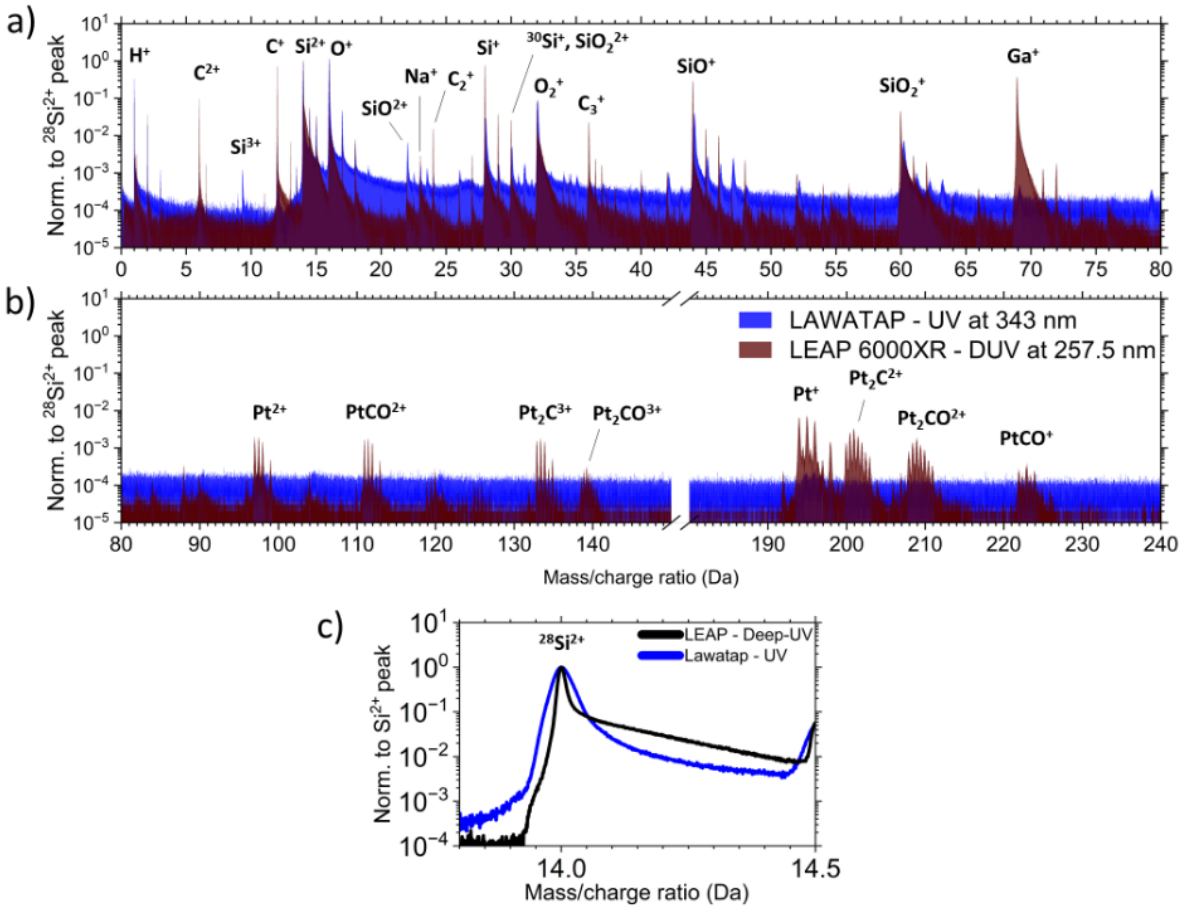

Figure 3.10: Mass spectra of silica samples for the ranges a) 0-80 and b) 80-240 of the m/n values: Deep-UV (LEAP, black) and UV (LaWATAP, blue), 17 million ions dataset for both analyses. E_{laser} = 250 pJ, (energy density of 80 J/m^2) for deep-UV, and E_{laser} =50 nJ, (energy density of 70 J/m^2) for UV. The detection rate set to 0.5% at/pulse at $T = 50$ K for deep-UV and to 0.25% at/pulse at $T = 50$ K for UV. c) Zoom on normalized UV and Deep-UV spectra to $^{28}Si^{2+}$ peak.

height, the trend reverses, with UV analysis exhibiting shorter right-hand tails, showing better resolution then Deep-UV (61 UV, 33 Deep-UV).

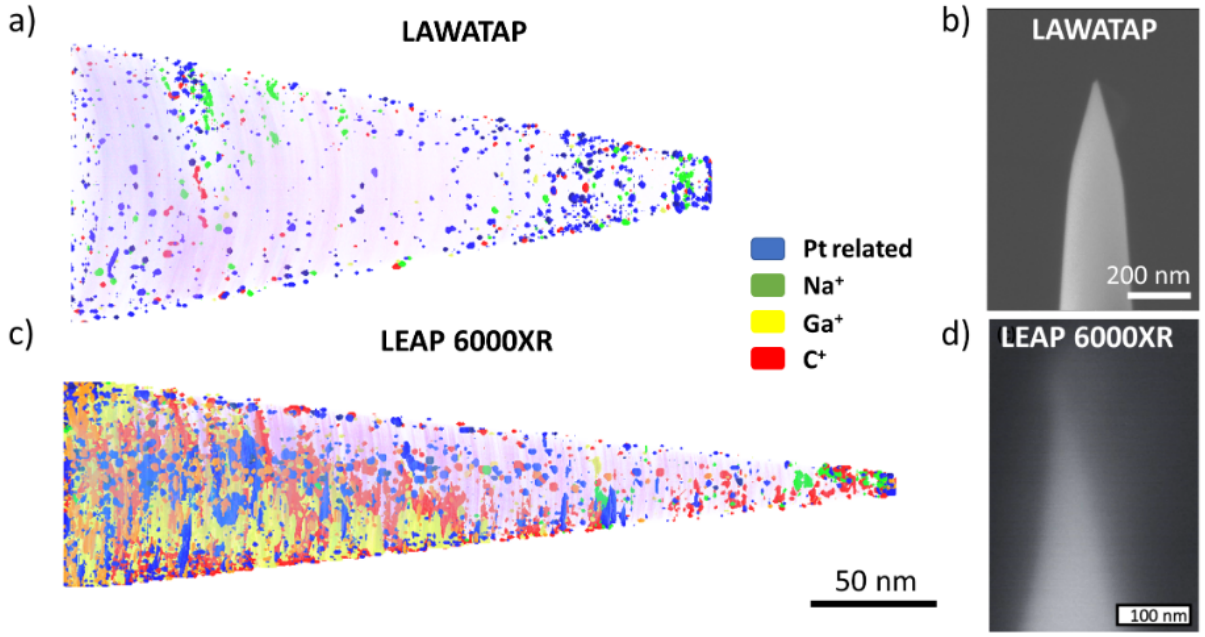

Figure 3.11: 3D reconstructions obtained by (a) LAWATAP and (c) LEAP 6000XR analyses performed on GPM3D software with cone angle method (Deep-UV: Radius = 10 nm, cone angle = 6.5°; UV: Radius = 15 nm, cone angle = 15°). Si and O are in light blue transparent dots background, while isosurfaces thresholds are set for Pt related species, Na, Ga and C respectively at 25%, 12%, 45%, 18% . SEM images of the respective tips are shown for LAWATAP (b) and LEAP (d).

Fig. 3.11(a,c) shows deep-UV and UV reconstructions with parameters chosen to align as much as possible with their respective SEM images, in Fig. 3.11(b,d) . Clusters of carbon and platinum are consistently observed across the analysis depth. While Pt–C from GIS protection/welding is expected at entry/exit, its pervasive presence suggests that the precursor mixture can fill sol-gel silica micropores during sample preparation, probably *via* precursor diffusion during flat-top post welding. Na is detected throughout (consistent with synthesis) and shows slightly higher concentration at the beginning. A similar redistribution has been reported for lithium in related films under electrostatic field [270], therefore Na migration through the porous network must also be considered as a possibility. Diffusion of Pt, Ga, and C is visibly more pronounced in deep-UV, presumably due to stronger laser heating (and, in small silica volumes, potential direct heating of the weld if the spot overlaps).

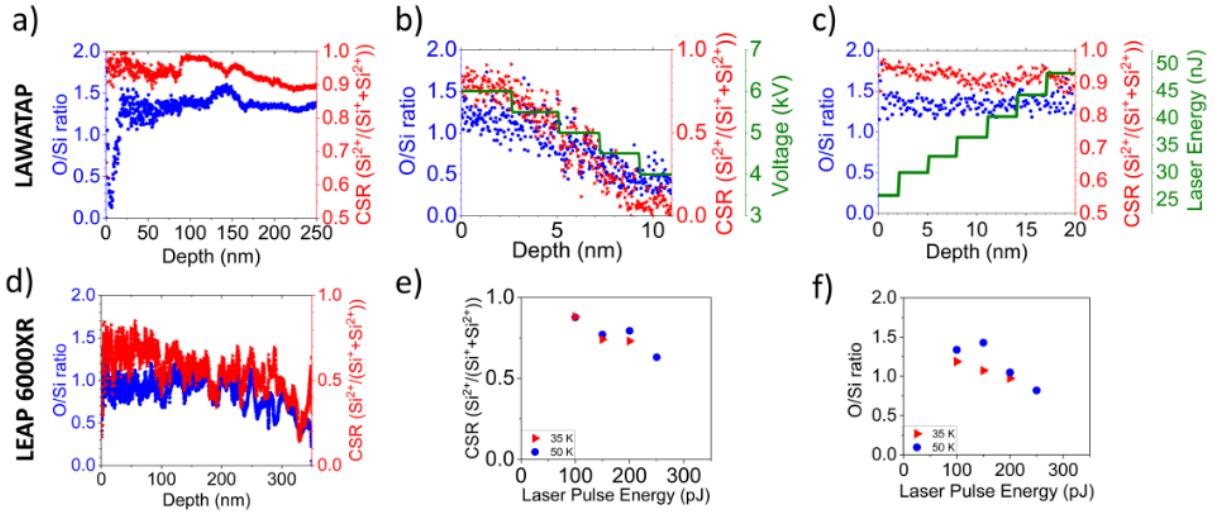

Figure 3.12: O/Si atomic ratio (blue line) and charge–state ratio (CSR, red line) versus analysis depth in silica samples under UV (a) and deep-UV (d) illumination. UV depth profiles with stepwise parameter changes: panels (c) and (b) show O/Si (blue dots) and CSR (red dots), where the green trace indicates the stepped DC voltage in (b) and the stepped laser energy in (c). Dependence on *laser energy* for deep-UV: CSR (e) and O/Si (f) at 30 K (red dots) and 50 K (blue dots).

3.2.1 Compositional analysis

To estimate the mean field during each analysis, we computed the silicon charge–state ratio (CSR), $Si^{2+}/(Si^{+}+Si^{2+})$. The mean CSR is 0.88 for UV and 0.48 for deep-UV , corresponding to mean fields of 21.6 and 19.9 $V\,nm^{-1}$, respectively, calculated using (2.4) [231]. The temporal evolution of CSR (and thus the field) is shown in Fig. 3.12(a) for UV and in Fig. 3.12(d) for deep-UV. The detection rates, though not identical, are similar in scale: approximately 0.005 atoms/pulse for deep-UV and 0.025 atoms/pulse for UV. APT detection rates can vary widely, influenced by analysis parameters like voltage and laser energy, leading to potential fluctuations. Transitioning from deep-UV to UV requires lower specimen temperatures and higher electric fields to maintain similar detection rates, suggesting different levels of sample heating by the two light sources, with deep-UV causing more heat. This implies a higher absorption of deep-UV by the material, affecting not only the evaporation process but also the mechanical stress and background noise levels. The energy densities are comparable (80 vs. 70 $J\,m^{-2}$), which implies a higher absorption coefficient for deep-UV in silica.

Tests show optical absorption of a thin silica slice (Fig. 3.13) is negligible in the green, rises modestly below $\sim$ 400 nm, and increases strongly below $\sim$ 300 nm, consistent with the enhanced experimental performance under UV and deep-UV illumination. Operating at a lower static

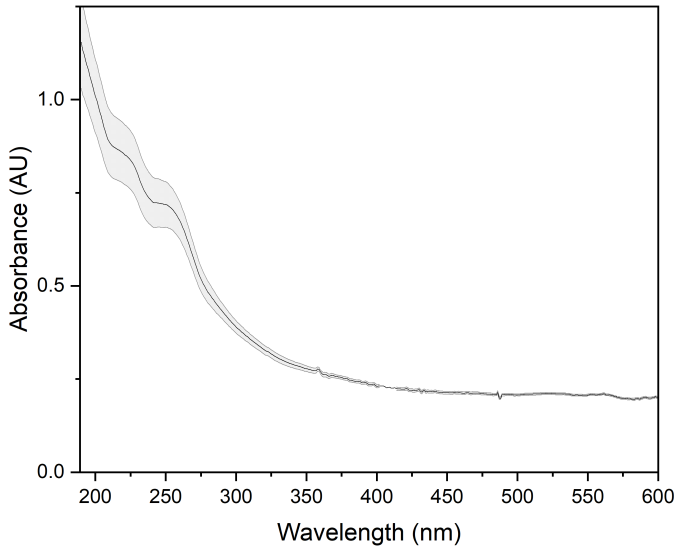

Figure 3.13: Absorption spectrum of a 0.6 mm thick silica sample that has been blanked against air. The standard de*via*tion is shown in grey. [29].

field with deep-UV also reduces fracture risk from electrostatic stress and lowers background (Fig. 3.10), since at fixed base temperature ($T_0 = 50\,\mathrm{K}$) inter-pulse evaporation is field-dependent and is reduced when the field is lowered [7].

Figures 3.12(a) and (d) (datasets as in Fig. 3.10) show O/Si and CSR versus analysis depth for UV and deep-UV, respectively. In the UV case (Fig. 3.12a)), both field and composition are quasi-constant, with O/Si ∼1.4. In deep-UV (Fig. 3.12d)), O/Si varies between ∼1.2 and 0.5; the field is generally lower and decreases when Ga, Pt, and C occur, and O/Si closely follows the field, consistent with other wide-gap materials. Oxide composition in APT depends on field [267]; CSR traces relative field changes.

The dependence on the laser energy was examined for both modalities. For UV (Figs. 3.12(b,c)), energy and voltage were varied independently: increasing energy from 12 to 48 nJ raises O/Si by ∼10%, whereas increasing voltage (CSR from 0.08 to 0.8) boosts O/Si by a factor of ∼3 (0.4→1.2), clearly showing the stronger field driven behavior. For deep-UV under constant detection-rate regulation (Figs. 3.12(e,f)), increasing laser energy is accompanied by a decrease in applied voltage (and thus field); O/Si and CSR decrease with energy with nearly identical slopes, indicating that the direct effect of laser energy is negligible compared with the field. In

both modalities, the measured composition deviates from the nominal O/Si = 2 at low field but approaches it at higher CSR.

The O/Si ratio was evaluated by integrating the corresponding mass-to-charge intervals in the mass spectrum, using fixed peak windows for oxygen- and silicon-containing ions. No explicit background subtraction was applied prior to integration. This choice is justified because the analysis focuses on relative composition trends as a function of field and laser energy under otherwise identical acquisition conditions, such that any residual background contribution is expected to be comparable across the datasets. In addition, the dominant oxygen signal arises from well-defined oxide-related molecular ions (e.g. O^+, O_2^+, SiO_x^+), for which the signal-to-background ratio remains high in the regimes considered.

3.2.2 Thermal response

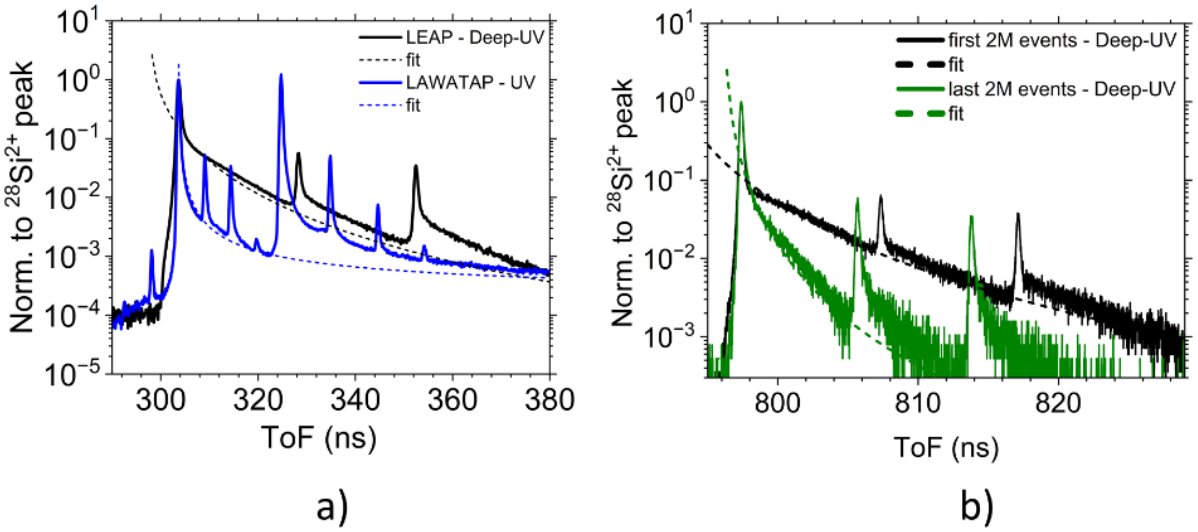

Figure 3.14: Time-of-Flight spectra magnifications of the regions around $^{28}Si^{2+}$ peak. (a) Comparison between UV (blue continuous curve) and Deep-UV (black continuous curve) ToF spectra. Cooling times after fitting with eq. (3.1) are 7.35 and 0.5 ns respectively for Deep-UV and UV analyses. (b) Fitting of the first and the last 2 million events of Deep-UV analysis with Eq. (3.1). Parameters: first 2 millions: $Q = 0.14\,\text{eV}$, $\Delta T_{\max} = 250\,\text{K}$, $\tau = 6\,\text{ns}$; last 2 millions: $Q = 0.13\,\text{eV}$, $\Delta T_{\max} = 250\,\text{K}$, $\tau = 1.5\,\text{ns}$.

Peak tails in mass spectra arise from post-pulse thermal emission and cooling [12, 271]. The time-of-flight (ToF) spectra for UV and Deep-UV (aligned on the reference peak of $^{28}Si^{2+}$ of the UV spectrum) analyses are shown in Fig. 3.14(a). They explain this thermal response and for this reason were fitted with the time-dependent evaporation-rate model (Eq. (1.8)) with the temperature expressed as in (1.11), written in the following form [29]:

$$\Phi(t) = A_0 \cdot \exp\left(-\frac{Q}{k_{\mathrm{B}}\left(T_0 + \frac{T_{rise}}{\sqrt{1+\frac{t-t_0}{\tau}}}\right)}\right), \tag{3.1}$$

where k_{B} represents the Boltzmann constant, $A_0 = 0.1 \cdot \exp\left(\frac{Q}{k_B(T_0+T_{rise})}\right)$ serves as a normalization factor, and T_0 denotes the initial temperature of the tip prior to laser exposure, which is constant at 50 K. The variable T_{rise} indicates the maximum increase in temperature following laser exposure. The beginning of the tip's cooling phase is marked at $t = t_0$, identified as the moment when the Si^{2+} peak intensity declines to 10% of its maximum value. Here, τ represents the cooling duration, and $Q \approx Q_0(1 - \frac{E}{E_{\mathrm{evap}}})$.

Such fits yielded cooling times of 7.35 ns for deep-UV and 0.5 ns for UV analyses. Prior studies relate τ to the heated area, thermal diffusivity, and specimen geometry (cone angle) [131, 271]. The heated area is $< 1\,\mu$m for both modalities (UV corrected for apex diffraction [12]); thus, the markedly different τ values primarily reflect geometry: SEM images show average cone angles of ∼6.5° (deep-UV) and ∼15° (UV). A ∼3× increase in angle can yield >10× reduction in τ *via* heat transport [131].

The Si^{2+} thermal tails (Fig. 3.14(a)) were fitted locally within a ∼100 ns window after the peak maximum, avoiding overlap from subsequent peaks. Both spectra were normalized to unity at the Si^{2+} peak and temporally aligned so that the onset of thermal decay (t_0) overlapped (defined at 10% of the peak maximum). Initial estimates and bounds were physically motivated: Q varied around 0.1 eV (CSR-derived fields); $\Delta T_{\max}$ ranged from 65 to 250 K; τ was constrained between 0.5 and 10 ns, consistent with [12, 271]. Fits yielded $Q_{\text{deep-UV}} = 0.12$ eV and $Q_{\mathrm{UV}} = 0.06$ eV, reflecting the higher field used for UV analyses (21.5 V nm^{-1}) versus deep-UV (19.7 V nm^{-1}). Extracted $\Delta T_{\max}$ values were 250 K for deep-UV and 65 K for UV.

Analyzing the evolution of the specimen geometry during deep-UV runs reveals noticeable variations in the cone angle along the tip, as evident from the accompanying SEM image 3.11(d). These variations influence the thermal response. A dataset of approximately 16 million ions was divided into two smaller sets, each containing the initial and final 2 million events. The corre-

sponding Si^{2+} ToF spectra (Fig. 3.14(b)) were normalized, aligned, and individually fitted with the cooling equation (3.1). Results from the initial phase were $Q = 0.14\,\text{eV}$, $\Delta T_{\text{max}} = 250\,\text{K}$, $\tau = 6\,\text{ns}$, while the later phase yielded $Q = 0.13\,\text{eV}$, $\Delta T_{\text{max}} = 250\,\text{K}$, $\tau = 1.5\,\text{ns}$. The significant decrease in τ suggests an increase in the cone angle during the analysis. Constant illumination conditions support the stable ΔT_{max} and nearly unchanged Q.

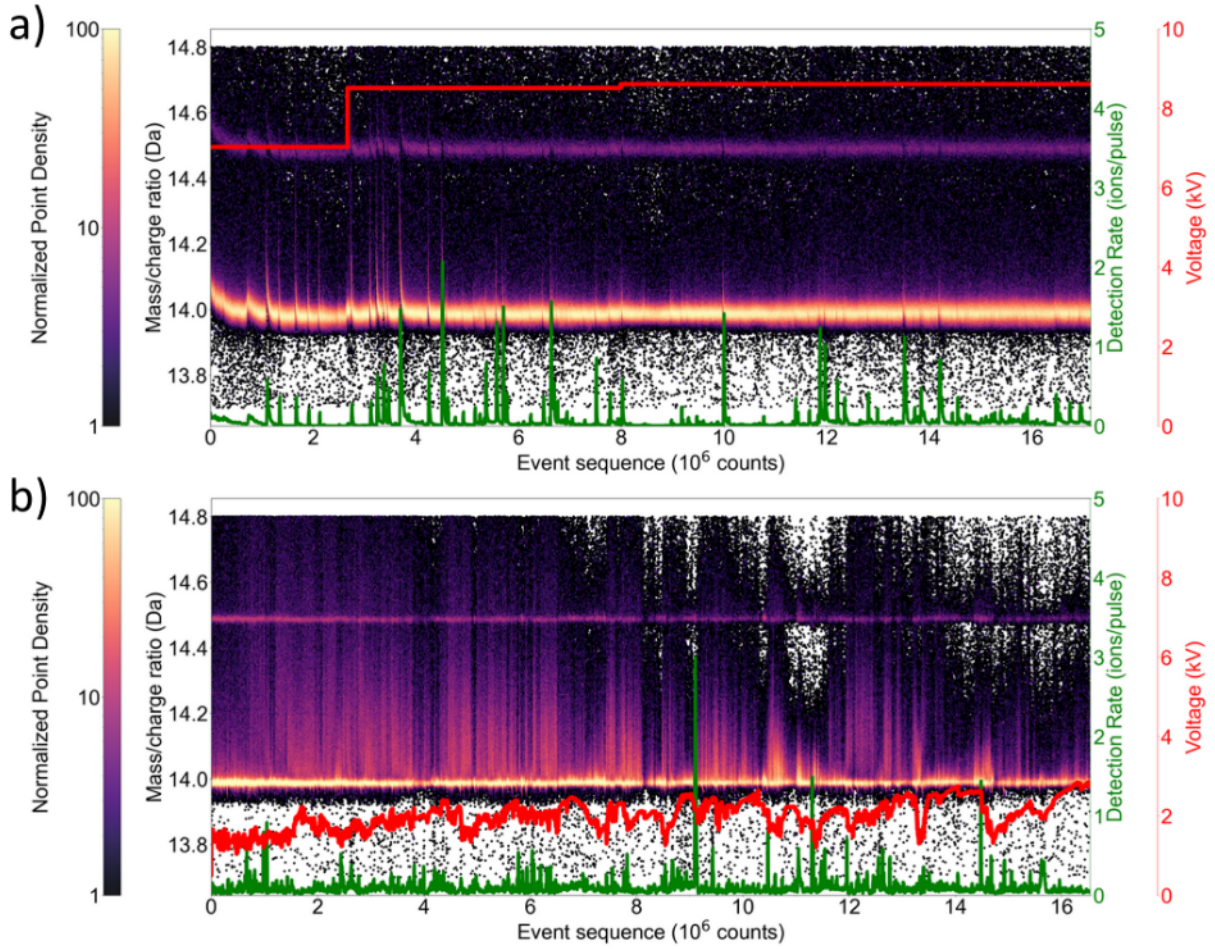

Figure 3.15: Mass-history diagrams for (a) UV and (b) Deep-UV datasets. The dot density plots are presented in a logarithmic color scale from 1 to 100 for the range [13.7-14.8] Da. In red are the applied voltage and in green the detection rate evolution plots.

Fluctuations in the detection rate were consistently noted in both the UV and Deep-UV analyses (Fig. 3.15(a,b)). These fluctuations are linked to micro-fractures caused by stress, where small fragments detach, leading to a surge of ion impacts. In addition, microporosity contributes; if a pore exists, the local effective radius decreases and the adjacent surface undergoes an increased field, causing rapid evaporation events. Simultaneously, the Si^{2+} peak appears at higher apparent m/n in the mass-history plots (Fig. 3.15(a-b)). This phenomenon is more evident in UV

conditions. The observed m/n shift correlated with evaporation rates is well-documented for wide-bandgap, low-conductivity materials such as MgO, SiO_2, and diamond [14, 272–274]. This occurrence is due to high resistivity: as emission current increases, the internal voltage drop also rises, causing ions to gain lower energy ($\frac{1}{2}mv^2 = nV = n(V_{DC} - V_{drop})$) and resulting in an upward m/n shift. The resistive behavior observed under both illumination conditions suggests that photo-generated carriers are not sufficient to notably enhance conductivity in silica.

3.3 Conclusion

Across all datasets, it emerges that the electrostatic field determines data quality in UV–assisted APT of sol–gel silica, while UV/deep–UV illumination plays a role in stabilizing the APT analysis conditions. The results on thin film samples showed that in the low–field regime spectra are dominated by molecular ions with strong H background and Xe residuals from PFIB; the 3D maps are inhomogeneous, and mass resolving power is insufficient for reliable composition or ferritin–specific interpretation. By contrast, in the high–field regime the pre–fracture segment exhibits cleaner spectra with abundant high charge states, higher CSR, and O/Si trending toward stoichiometry; yet fracture events are frequent and the porous matrix favors migration/diffusion. In neither dataset of thin-film specimens could we identify clear Fe isotopic peaks or clusters that can be ascribed to ferritin. Additionally, the potential overlap of $^{56}Fe^{2+}$ around 28 Da with Si^+, CO^+, and N_2^+ compounds further complicates the determination. While a workable approach for using UV has been established, the frequent issue of samples fracturing early limits their success. This challenge consequently encourages a shift to more durable and stable sample geometries to improve the reliability and success rate of the experiments.

Within that broader context, laser–assisted APT on sol–gel silica is affected by defect–assisted sub–bandgap absorption at UV and deep–UV wavelengths. Shorter wavelengths interact more effectively with the defective amorphous structure of sol-gel silica compared to longer wavelengths, like green light, enhancing the number of excited carriers and reducing the static field needed for evaporation, which stabilizes the process. However, the use of deep-UV light, while beneficial, also causes stronger thermal effects, leading to migration of elements like gallium, platinum, and carbon into the material's pores, necessitating careful experimental management.

Despite the increased photon energy, silica maintains high resistance. Normally, added energy

boosts conductivity, but silica's conductivity remains largely unchanged. This is shown by ongoing bursty evaporation and field-dependent drifts in silicon atoms. The photoexcited carriers, electrons, and holes from photon absorption, fail to significantly reduce the voltage drop across insulating regions on the tips. This indicates that silica's inherent electrical resistance, as a wide-band-gap material, persists even with attempts to modify it using higher photon energies.

Compositionally, silica behaves similarly to other materials with a wide band-gap, where the oxygen to silicon (O/Si) ratio is influenced by the strength of the electric field through a mechanism called charge state redistribution (CSR). At higher electric fields, the O/Si ratio approaches theoretical expectations, while lower fields reduce this ratio due to molecular crowding. Specific defects such as oxygen vacancies, carbon defects, and gallium concentrations affect deep-UV absorption. Strong static fields have minimal impact on the optical properties of amorphous silica. Reliable data in silica analysis is obtained using focused UV or deep-UV beams with careful monitoring of CSR and O/Si ratio, excluding data after tip fractures. UV and deep-UV illumination prove more effective than green light due to challenges like resistivity, porosity, and contamination from material preparation.

Future advancements in materials science and laser technology may be achieved by optimizing defect management near critical areas, improving interface performance with enhanced coatings, and refining laser-pulse protocols to reduce thermal diffusion. Incorporating advanced theoretical models like the Bethe–Salpeter equation into experimental studies will improve the understanding of defect impacts on absorption properties. These strategies aim to enhance overall performance by addressing defects and their interactions with external factors [29].

CHAPTER 4

Low repetition rate Tera-SAT - Analysis of sol-gel silica samples

This chapter addresses the central objective of the thesis: assessing the efficiency and physical mechanisms of terahertz (THz)-assisted field evaporation in amorphous sol–gel silica, and benchmarking this approach against near-infrared (NIR) and ultraviolet (UV) laser-assisted evaporation. The emphasis is placed on understanding how THz excitation modifies the evaporation regime, particularly in insulating materials where thermal effects and charging typically limit atom probe performance.

Two THz-assisted atom probe platforms were employed, as described in Chapter 2. The first system (Tera-SAT, 1 kHz) produces single-cycle THz pulses via a two-color plasma source and offers full control over waveform and polarity, enabling systematic investigations of polarity-dependent evaporation. A second, high-repetition-rate platform (100 kHz), introduced later in the project, provides access to higher throughput measurements with reversible polarity but more limited pulse-shape control. In the present work, both systems are used as experimental tools to probe evaporation physics; their core development was carried out by the host laboratories, while my contribution primarily concerns their application to atom probe measurements and the interpretation of the resulting data.

The initial ambition of the project was to directly identify and localize biological macromolecules embedded in sol–gel silica. In practice, the complexity of the evaporation behaviour of insulating silica, combined with charging effects and background contributions, made it clear that a detailed understanding of the matrix response itself was a prerequisite. The strategy of this thesis therefore evolved toward a stepwise approach, beginning with a systematic characterization of the evaporation behaviour of *empty* (protein-free) sol–gel silica under different excitation modalities. This intermediate step proved essential to disentangle matrix-driven effects from genuine biomolecular signatures and to establish reliable operating conditions.

With hindsight, several routes could be envisaged to better approach the original biological objective, including thicker or more conductive encapsulation layers, alternative isotopic labelling strategies, or earlier implementation of high-repetition-rate THz excitation to improve statistics at lower fields. A related and critical aspect concerns the stability of biomolecules within the sol–gel silica matrix. On experimental timescales prior to analysis (hours to days), the silica network is expected to provide substantial chemical and mechanical stabilization, strongly limiting spontaneous degradation or diffusion of embedded proteins.

By contrast, the degradation most relevant to atom probe measurements is not a slow ageing process but an ultrafast, field- and temperature-driven fragmentation occurring locally during evaporation, on sub-nanosecond timescales. In laser-assisted APT, this degradation is exacerbated by transient heating and prolonged evaporation windows, whereas THz-assisted excitation aims to confine evaporation to short, field-dominated time intervals with minimal thermal input. The matrix-focused investigation presented in this chapter therefore establishes the physical constraints under which biomolecular integrity can be preserved long enough for detection, and delineates the regimes in which degradation is expected to occur during analysis rather than prior to it.

At first, in section 4.1, using the low-rep. rate Tera-SAT system, we designed experiments that comparet positive vs. negative THz polarity and discuss the evaporation mechanisms they promote, and secondly compare THz operation NIR (λ = 800 nm) pulsing and UV pulsing (λ = 343 nm). Lastly, we delve into a more detailed exploration of evaporation processes that are supported by electron emission in the presence of THz negative polarity.

Building on those initial results, in section 4.2 we subsequently employed surface engineering techniques designed to improve THz field enhancement on sol-gel silica tips: chromium coatings applied *via* PECS sputtering and graphene encapsulation achieved through the wet-transfer method.

To conclude, section 4.3 outlines our preliminary experiments with the *high-repetition* Tera-SAT, employing both coated and uncoated silica. This section emphasizes the difficulties we faced and proposes some improvements.

4.1 Low repetition rate Tera-SAT: THz-assisted analysis of sol–gel silica specimens

4.1.1 Negative vs. positive–polarity THz pulses

In this study, we investigated THz triggering on an protein–free sol–gel silica tip using the low–repetition–rate Tera–SAT system at $T = 50\,\mathrm{K}$. Opposite waveform polarities were compared, and representative spectra are shown in Fig. 4.1(a,b); these results have been published in the Physical Review B journal [30].

Under negative polarity, a THz peak field of $0.02\ \mathrm{V\,nm^{-1}}$ was applied while the DC bias was set in automatic mode, in order to mantain a stable detection rate of 0.13 ions/pulse on average (see green line in Fig. 4.2), yielding $\sim 2.3 \times 10^5$ ions.

The mass spectrum (Fig. 4.1(a)) displays the expected silicon charge states: Si^{2+} in the range 14–15 Da and Si^+ in the range 28–30 Da, together with species associated with sol–gel processing and residual FIB preparation contamination (C^{2+}/C^+ at 6/12 Da, O^+ at 16 Da, Na^+ at 23 Da, OH^+/H_2O^+ at 17–18 Da and Pt^{2+} in the range 95-99 Da). Silica related molecular ions are also present (SiO^+ at 44 Da, SiO_2^+ at 60 Da, and minor 2+ peaks at 22 Da). In Figs. 4.1(b,c) are represented magnified regions of the spectrum around the Si^{2+} (13.5–14.5 Da) and Si^+ (27.5–28.5 Da) peaks, in order to better visualize their quality in terms of mass resolution and signal-to-noise ratio. The calculated values are summed up in Table 4.1 and, at least in the case of lighter species, like Si^{2+}, are comparable to UV–assisted analyses performed on oxides [271, 275]. An estimation of the field can be obtained by using the CSR (Si^{2+}/Si^{1+}) using the relation (2.4) and is found to be 20.93 V/nm. As a matter of fact, right–hand tails indicate a mi-

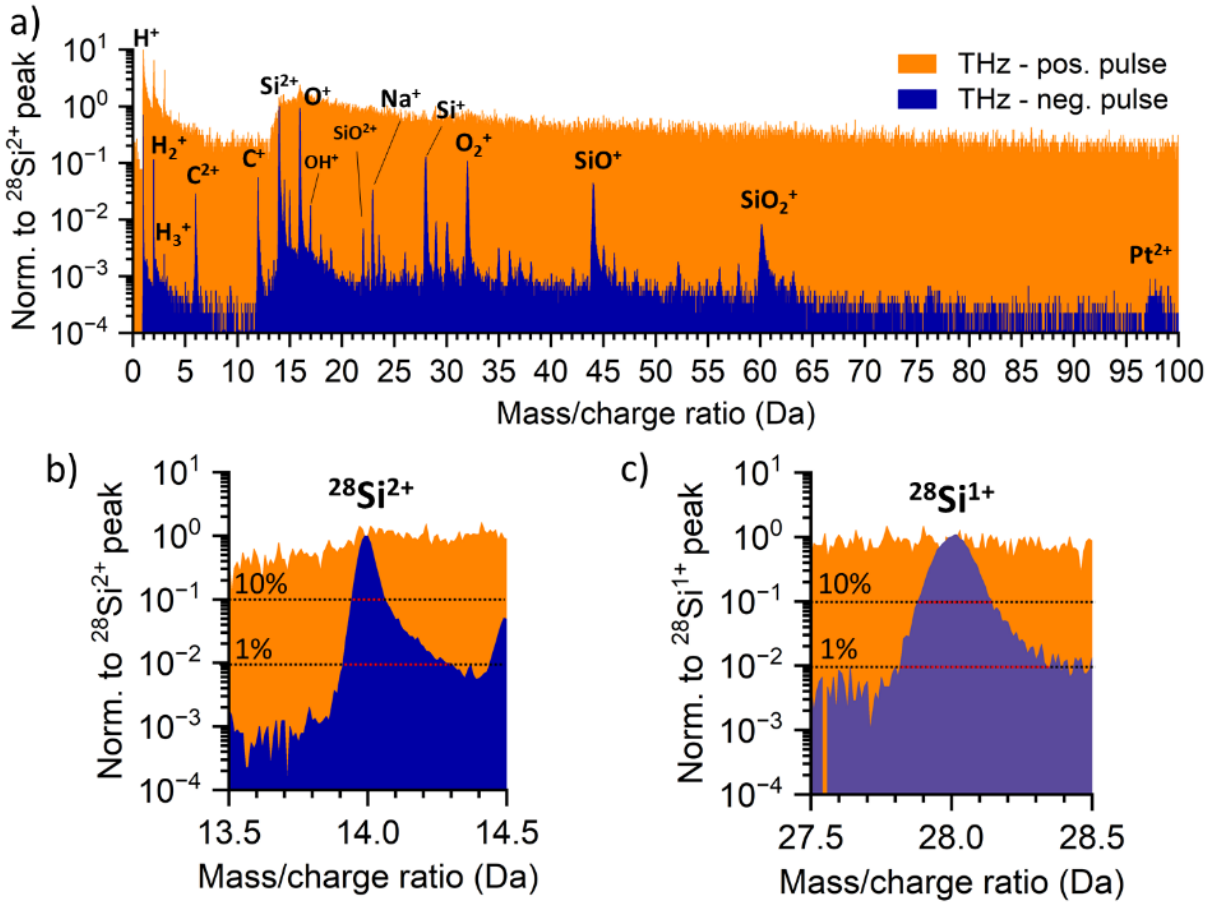

Figure 4.1: (a) THz–assisted mass spectra from sol–gel silica under negative (blue) and positive (orange) pulse polarities. Each spectrum contains about $2{\cdot}10^5$ events and is normalized to the 14 Da peak. (b) and (c) magnify the $^{28}Si^{2+}$ (13.5–14.5 Da) and the $^{28}Si^{+}$ regions (27.5–28.5 Da), each normalized to the correspondent peak. Dashed lines mark the 10% and the 1% value of the peak maximum to help visualization.

	$\mathbf{Si^{2+}}$ (14 Da)	$\mathbf{Si^{1+}}$ (28 Da)
SNR	$> 10^3$	$> 10^2$
$\frac{\Delta M}{M}$ @ 10% max	122	108
$\frac{\Delta M}{M}$ @ 1% max	39	54

Table 4.1: Signal-to-noise ratio and mass resolving power ($M/\Delta M$ at 1% and 10% peak max) values for the Si^{1+} and Si^{2+} peaks, for the THz negative polarity analysis.

nor thermal contribution, yet the overall response is field–evaporation–dominated and suitable for quantitative interpretation.

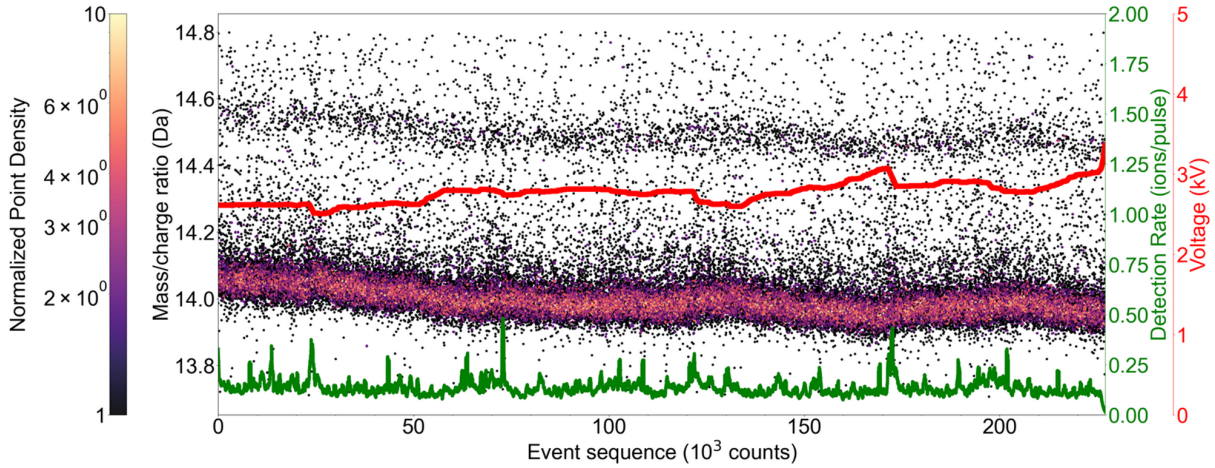

Figure 4.2: Mass history diagram for the THz negative polarity analysis (range 13.7-14.8 Da). The point density is normalized on a logarithmic scale. Th DC voltage curve evolution is in red, while the detection rate is in green.

As previously observed for UV and deep-UV analyses (Figs. 3.15(a,b)), THz-assisted measurements also exhibit mass-to-charge drifts in the mass history, in particular in correspondence with flux bursts (Fig. 4.2). However, the phenomenology differs from the UV case: here the dominant feature is a global shift of essentially the entire spectrum towards lower m/n (shorter times of flight), rather than a selective peak broadening and thermal tailing.

Such a global shift towards lower m/n values is most naturally attributed to transient changes in the effective extraction/acceleration conditions, i.e. variations in the effective voltage $V_{\text{eff}}(t)$ and/or in the local electrostatic potential at the apex during bursts. Since the time of flight scales approximately as $t \propto 1/\sqrt{V_{\text{eff}}}$, even small burst-correlated changes in V_{eff} (e.g. due to current-driven HV response, transient charging/discharging of the insulating silica, or variations of the local potential distribution) can produce a coherent shift of all peaks to lower apparent

m/n. In contrast, UV-induced heating primarily modifies the evaporation time window and produces peak reshaping with thermal tails, which does not necessarily translate into a rigid shift of the full spectrum.

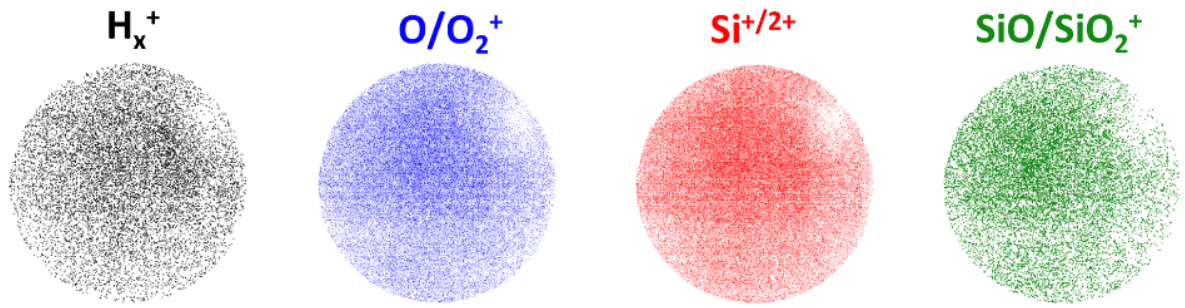

Figure 4.3: Detector hit-maps for negative–polarity THz analysis represented for $H^+/H_2^+/H_3^+$ (black), O^+/O_2^+ (blue), Si^+/Si^{2+} (red), and $SiO^{+/2+}/SiO_2^+$ (green), showing homogeneous distribution

In Fig. 4.3, the detector hit-maps show uniform distribution for $H^+/H_2^+/H_3^+$,O^+/O_2^+, Si^+/Si^{2+}, and SiO_x^+/SiO_x^{2+}, no signatures of localized damage, features that corroborate the field–driven character inferred from the spectra. The lower density observed in the top-right corner of the detector map arises from the geometric configuration of the experiment. The THz (or laser) beam impinges on the specimen at a finite angle with respect to the atom-probe axis, such that the detector plane is not perpendicular to the effective emission direction. As a consequence, ions emitted toward one side of the detector experience a reduced collection efficiency due to the inclination of the microchannel plate (MCP) assembly relative to the tip axis, leading to an apparent density gradient across the detector. This effect is purely geometric and does not reflect an intrinsic anisotropy of the evaporation process.

During the analysis with THz positive polarity, the THz field was still operated at its maximum amplitude of ~ 0.020 V nm^{-1} while the DC bias could sustain only a much lower steady rate of 0.003 ions/pulse; attempts to increase the bias led to inter–pulse evaporation and were therefore avoided. The corresponding spectrum (Fig. 4.1(a), in orange) is dominated by hydrogenic species and a broad feature near 14 Da, with enlarged views revealing an elevated baseline that masks weaker Si/O peaks. The broadened maxima and persistent background are consistent with apex heating/cooling cycles, indicative of thermally assisted emission. Under such conditions, peaks lack the sharpness and contrast required for reliable composition.

4.1.2 Comparative analysis: THz vs. NIR vs. UV assisted APT on sol–gel silica

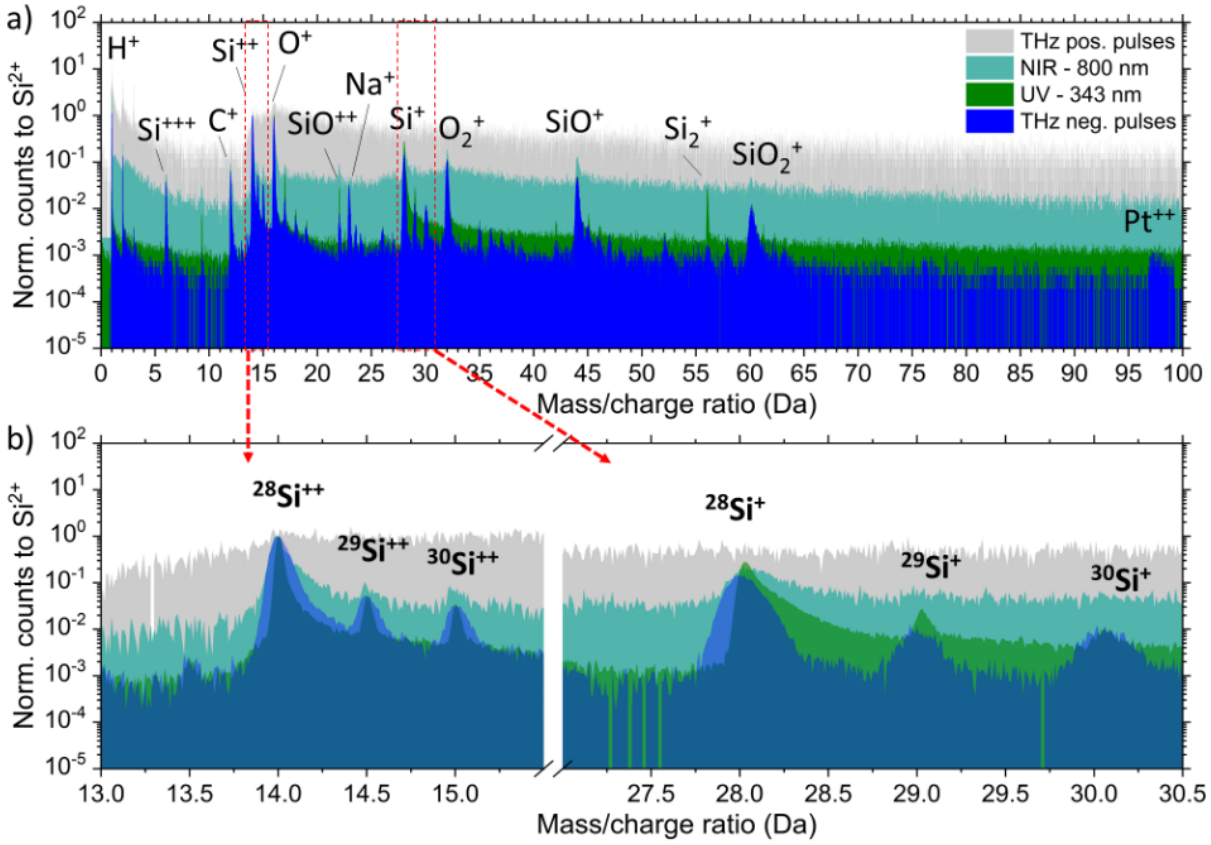

Figure 4.4: (a) Mass–spectrum comparison for THz (positive polarity, gray; det. rate = 0.003 ions/pulse, V_{DC} = 9 kV), THz (negative polarity, blue; field $F = 21.04\,\mathrm{V\,nm^{-1}}$, det. rate = 0.08 ions/pulse, V_{DC} = 2.5–3 kV), UV–assisted APT (green; $F = 20.87\,\mathrm{V\,nm^{-1}}$, det. rate = 0.002 ions/pulse, V_{DC} = 6.8–7.4 kV), and NIR–assisted APT (turquoise; $F = 20.93\,\mathrm{V\,nm^{-1}}$, det. rate = 0.03 ions/pulse, V_{DC} = 9 kV). All at $T = 50$ K. Counts are normalized to the $^{28}Si^{2+}$ peak at 14 Da. (b) Zoom on 13–15.5 Da and 27.5–30.5 Da.

To place THz–assisted APT in context, we compared spectra acquired on the same sol–gel silica material under four excitation modes: THz pulses with *positive* polarity, THz pulses with *negative* polarity, NIR laser pulsing ($\lambda = 800$ nm) delivered by the same platform, and UV laser pulsing on LAWATAP ($\lambda = 343$ nm). We selected analyses conducted under very similar near surface fields with the aim to assess mass–spectral quality (mass resolving power and SNR) and compositional fidelity (O/Si).

For each dataset, the near surface field was estimated from the charge–state ratio CSR = Si^{2+}/Si^{+} using Eq. (2.4) [231]. For the THz (positive) spectrum, the Si^{+}/Si^{2+} peaks are poorly resolved, so a reliable CSR could not be extracted. A mass spectra comparison is shown in Fig. 4.4(a,b), with a zoom on the regions including the $^{28}Si^{1+/2+}$ peaks.

Under positive polarity THz pulses, the spectrum is mostly characterized by hydrogen peaks (H^+, H_2^+, H_3^+), and a significant peak appears near 14 Da. Almost all peaks are heavily obscured, and the baseline is expanded with vague features over extensive m/n ranges. This is typical of non-localized, *thermally assisted* emissions: the apex experiences cycles of heating and cooling between pulses, which result in significant noise and broadened peaks, making accurate field or composition measurement impossible.

In the **NIR laser–assisted** configuration ($\lambda = 800\,\text{nm}$), the spectrum shows distinct Si peaks together with pronounced H peaks. Thermal activation is evident: lineshapes are broader and the SNR at 14 Da is of order 10^2. This is consistent with the larger optical penetration depth and less confined energy deposition at 800 nm, which increases the contribution of thermal processes relative to field-driven evaporation. The calculated field is F = 20.61 V/nm.

In **UV laser–assisted** APT ($\lambda = 343\,\text{nm}$), the beam's tight focus ensures energy is deposited into a smaller area at the tip, while sol-gel silica exhibits well-improved absorption at this wavelength. The spectrum exhibits SNR exceeding 10^3 at 14 Da and a mass resolution $\text{MRP}_{10\%}$ of 156 for $^{28}Si^{2+}$. Thermal tails are minimized relative to NIR and to THz positive polarity, placing UV at the top of the spectral-quality ranking, with THz negative polarity close behind, NIR further down, and THz positive polarity last due to its dominant thermal background. The calculated field for this analysis is F = 20.52 V/nm.

With **THz pulses of negative polarity**, clear Si^{2+} peaks appear at 14–15 Da and Si^+ at 28–30 Da, accompanied by O^+ at 16 Da, Na^+ at 23 Da (sample preparation residue), and molecular ions from the SiO/SiO_2 series (44/60 Da, with weaker 22/30 Da in the 2^+ state). Hydrogen remains visible, as expected at low repetition rate, yet the overall noise level is significantly lower than for positive polarity.

Hydrogen remains visible, as expected at low repetition rate, yet the overall noise level is significantly lower than for positive polarity, because negative THz pulses efficiently drive ultrafast electron emission from the apex, transiently enhancing the local electric field and thereby promoting field-driven ion evaporation.

The zoomed regions highlight substantially higher SNR and narrower Si peaks than in the positive-polarity case; nevertheless, the mass resolving power at 10% peak height for $^{28}Si^{2+}$ is

lower than in UV (e.g., $MRP_{10\%} \sim 67$ vs. 156), and a right-hand tail persists, a residual thermal component. The calculated field for this analysis is F = 20.87 V/nm.

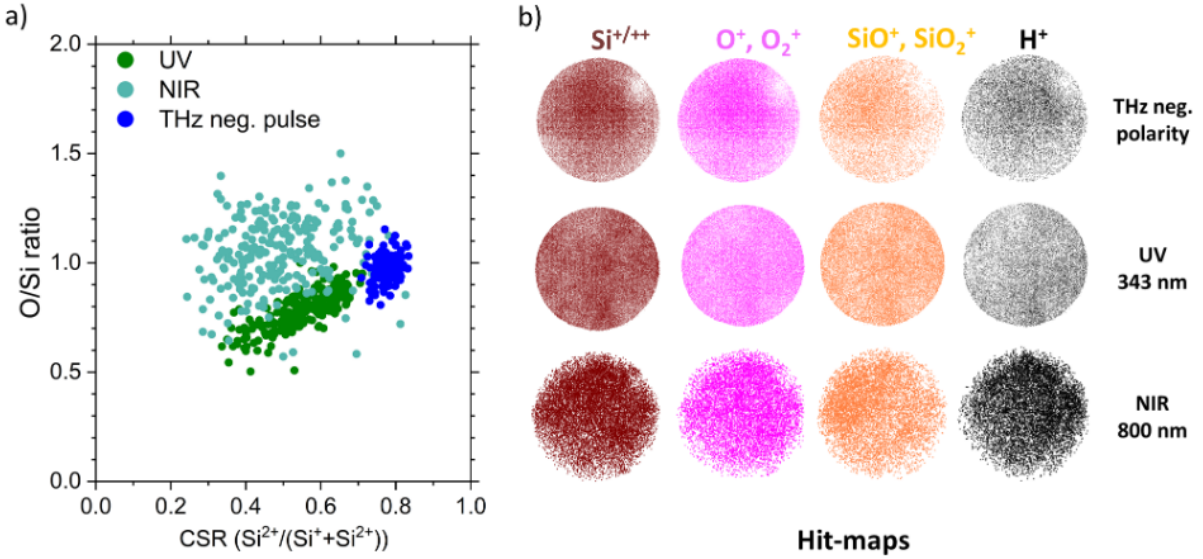

Figure 4.5: (a) Oxygen-to-silicon ratio (O/Si) vs. CSR for THz (negative), UV, and NIR runs. (b) Detector hit–maps ($2{\cdot}10^5$ ions each) illustrating spatial homogeneity of the dominant species under each modality.

In Fig. 4.5(a), the relationship between O/Si and CSR is depicted, revealing a consistent pattern across THz (negative), UV, and NIR: At a similar CSR range (approximately 0.6–0.8, calculated in this case as $\frac{Si^{2+}}{Si^{2+}+Si^{+}}$, which corresponds to $F \sim 20.5$ V/nm), the observed O/Si values cluster around ~ 1 (equating to roughly 50 at.% O and 50 at.% Si), indicating a deficit below the nominal SiO_2 O/Si ratio of 2. This deficit aligns with field-dependent neutral loss or dissociation (such as undetected O_2) under the applied fields, already seen in the previous Chapter 3 in UV analyses. While increasing the CSR/field raises the O/Si ratio, stoichiometry is not achieved within the parameters studied.

The spatial homogeneity is illustrated in Fig. 4.5(b), where two-dimensional hit-maps compiled from 200k detected ions per condition demonstrate uniform distribution across the detector plane for Si, O, SiO_x, and H in all three modalities (THz negative, NIR, UV). Due to limited statistics, full 3D reconstructions were not pursued; the visible low-count area in the upper-right quadrant results from the MCP/detector tilt, rather than sample inhomogeneity.

In conclusion, at comparable apex fields, UV pulsing delivers the best mass–spectral resolving power $MRP_{10\%}$, while negative–polarity THz analysis shows the best SNR. NIR remains more

thermally activated; and positive–polarity THz is dominated by thermal noise and static–evaporation constraints. Compositionally, all three useful modalities (THz negative polarity, NIR, UV) show similar O/Si versus CSR behavior, supporting the interpretation that the electric field and the neutral oxygen loss are again correlated [267], as previously seen in the case of UV analyses on thin film and bulk sol-gel silica samples 3.1.2, 3.2.1.

4.1.3 Evaporation mechanisms under THz negative polarity

When a small positive bias is applied, THz pulses (in both polarities) emit electrons that reach the detector; increasing V_{DC} reduces the electrons' detected rate until it falls to background, defining a threshold that we refer to as "stopping voltage" V_{stop}. As shown in ref. [30], to relate V_{stop} to the THz amplitude, it is possible to simulate electron trajectories (using the commercial software LORENTZ-2E V10.2) in an axially symmetric APT geometry: a conical tip with a semispherical apex (radius 70 nm, half-angle 87°), a grounded micro-channel plate at $L = 9$ cm (active height 4 cm), and a grounded hemispherical shield (radius 15 cm). Fields are obtained *via* a quasi-transient boundary element method (BEM), *i.e.* stationary snapshots over the monocycle $V_{\mathrm{THz}}(t)$ [276]. Trajectories are integrated with adaptive RK5 for the total field from $V_{\mathrm{DC}} + V_{\mathrm{THz}}(t)$, allowing emission only when the surface potential becomes negative.

The THz amplitude is then calibrated by *electron blocking*: for fixed V_{DC} (e.g., 2 kV), V_{THz} is reduced from a level yielding full electron detection until the signal vanishes, giving V_{stop}. Repeating versus V_{DC} yields:

$$A_{\mathrm{THz}}(\mathrm{kV}) = \alpha\, V_{\mathrm{stop}}(\mathrm{kV}), \tag{4.1}$$

with $\alpha \approx 3.3$ (negative polarity) and $\alpha \approx 7.8$ (positive).

The THz analyses with different pulse polarities, shown in Fig. 4.4, were performed on two different sol-gel silica specimens of the same type, but with different geometry and static field conditions. The experimental values found are:

- THz negative polarity: $V_{\mathrm{stop}} = 0.9$ kV, $F_{\mathrm{evap}} = 20.87$ V/nm, $V_{\mathrm{DC}} = 3$ kV, $\beta R =$

$V_{DC}/F_{evap} \simeq 1.44 \cdot 10^2$ nm. The THz field amplitude will be given by: $F_{THz}^{neg} = \frac{A_{THz}^{neg}}{\beta R} = \frac{3.3 \cdot 0.9 \cdot 10^3 V}{1.44 \cdot 10^2 nm} \sim 20$ V/nm.

- THz positive polarity: $V_{\text{stop}} = 0.4$ kV, $F_{\text{evap}} \sim 20$ V/nm (estimation), $V_{\text{DC}} = 7.5$ kV, $\beta R = V_{DC}/F_{evap} \simeq 3.75 \cdot 10^2$ nm. As before, $A_{THz}^{pos} = 7.8 \cdot 0.4$ kV $= 3.12$ kV and $F_{THz}^{pos} = \frac{A_{THz}^{pos}}{\beta R} = \frac{7.8 \cdot 0.4 \cdot 10^3 V}{3.75 \cdot 10^2 nm} \sim 8$ V/nm.

From this, by applying the respective values found for the two polarities, we finally know that $F_{\text{THz}} = A_{\text{THz}}/(\beta R)$ gives ≈ 20.6 V nm^{-1} (negative polarity, also consistent with the CSR-calculated value of 20.87 V/nm) and ≈ 8 V nm^{-1} (positive polarity). Referenced to the incident free-space field of ~ 80 V/μm the corresponding near-field gains are ~ 260 and ~ 100. The larger gain for negative pulses (factor 2.5 compared to positive pulses) justifies their higher efficiency on insulating silica.

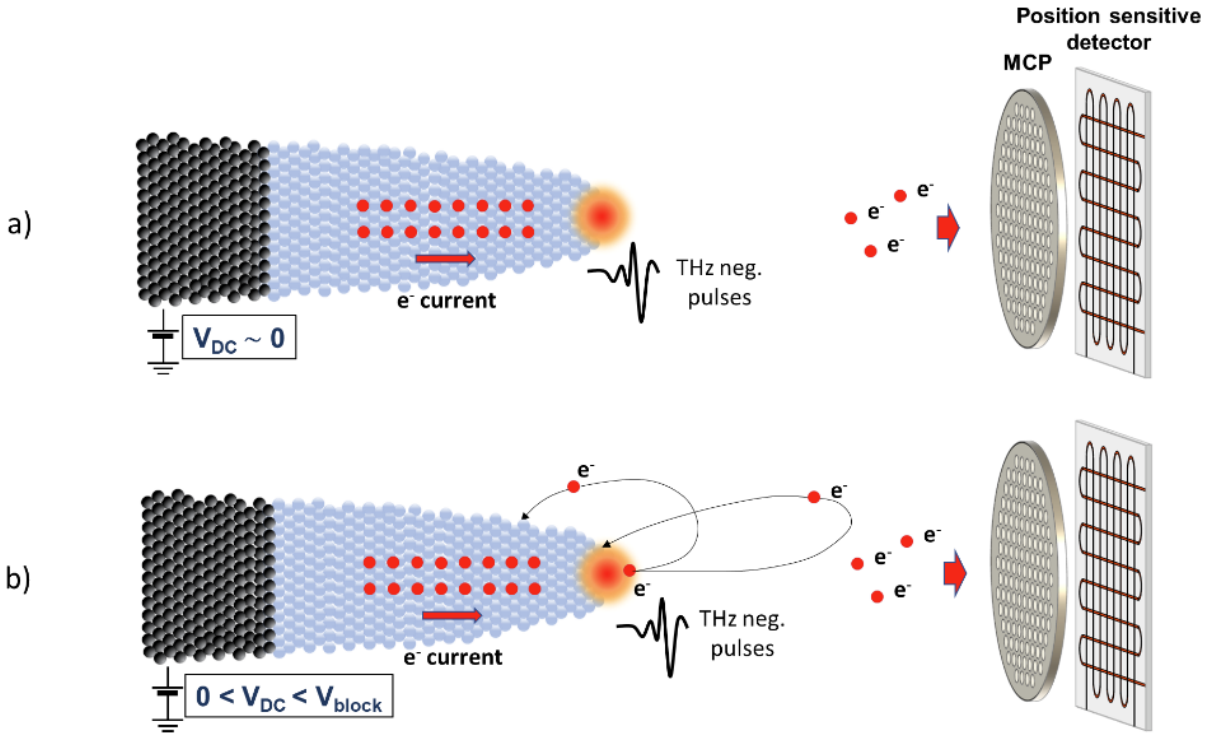

Figure 4.6: Electron–assisted mechanism under negative THz polarity. (a) with $V_{\text{DC}} \approx 0$, THz pulses emit electrons that reach the detector; the ion rate is negligible. (b) with $0 < V_{\text{DC}} < V_{\text{stop}}$, a fraction of the electrons are turned back and redeposited near the apex, creating localized heating that assists ion evaporation.

Comparing UV and THz–negative polarity datasets on sol–gel silica, we observe similar thermal tails and background levels in the mass spectra. This suggests that, as in UV La–APT, the emission under THz drive must have a thermal component as well. As shown in Fig. 4.6(a),

when subjected to negative THz polarity, the single-cycle waveform releases electrons from the apex, which have a kinetic energy influenced by the THz amplitude of its negative peak and the angle of emission from the tip surface. In a resistive tip the THz–emitted electrons heat the apex by *Joule heating*. The heat power P scales with the **square** of the electron current I,

$$P \;=\; I^2 R \qquad \text{(equivalently, per volume } q = J^2\rho\text{)},$$

The resulting steady temperature rise is, to first order,

$$\Delta T \;\approx\; \frac{P}{G_{\mathrm{th}}} \;=\; \frac{I^2 R}{G_{\mathrm{th}}},$$

where R is the electrical resistance of the heated region and G_{th} is its thermal conductance to the base (a constant set by geometry and material). Thus, higher electron current implies a larger ΔT, which elevates the probability of ions overcoming the energy barrier.

Moreover, for a small positive bias such that $0 < V_{\mathrm{DC}} < V_{\mathrm{stop}}$, two heating channels act simultaneously: (i) the through–tip electron current that dissipates Joule heat, and (ii) a sizeable fraction of the THz–emitted electrons that are decelerated by the positive bias and redirected back to the apex (Fig. 4.6(b)), where they deposit their kinetic energy on impact. This back-acceleration concentrates power in a nanometric region and creates additional local thermal gradients. Electron trajectories are influenced by both the emission angle and the departure time within the THz pulse cycle. Empirically, the ion rate often peaks as $V_{DC} < V_{stop}$ (when the returning-electron fraction is largest) and then decreases for $V_{DC} \sim V_{stop}$, where electron emission into free space is suppressed and the electron-assisted heating stops.

Experimental test: blocking electron emission

A direct way to test whether electrons assist the evaporation is to *scan* V_{DC} and track, pulse–by–pulse, the rates in two non–overlapping m/n windows: the Si^{2+} peak (ion proxy) and the detector's electron window (electron proxy). The key observable is the stopping voltage V_{stop} at which the detected electron rate falls to background. We ran an experiment on a different tip from the same sample (empty sol–gel silica) and the mass-history diagram in Fig. 4.7 shows the following trend:

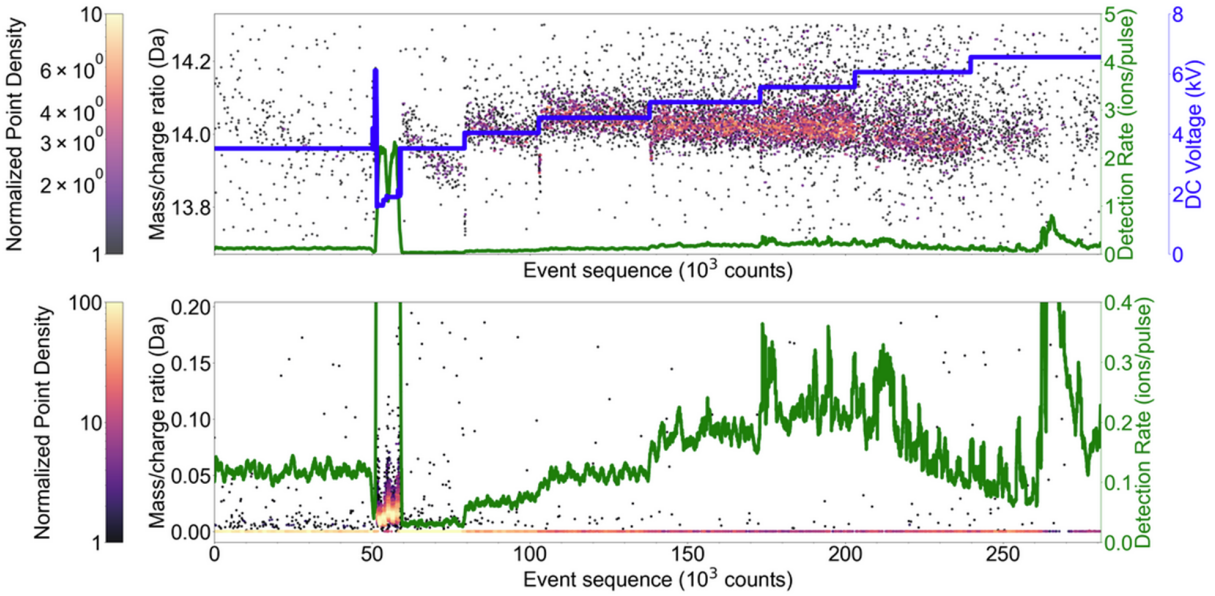

Figure 4.7: Top: Mass–history diagram for negative THz polarityanalysis around the Si^{2+} region (13.7-14.3 Da) V_{DC} (blue) and smoothed detection rate (green). Bottom: electron window (0-0.2 Da) and magnification on the detection rate curve (green).

1. For small positive V_{DC}, the electron rate is high and the total detection rate is dominated by electrons with almost no ion being detected.

2. As V_{DC} increases, the detected electron rate decreases (more electrons are turned back) and the *ion* rate rises, consistent with electron–assisted heating (Joule and/or back–impact) aiding evaporation.

3. Once $V_{DC} \gtrsim V_{threshold}$, the *ion* rate drops continues to decline with further increases in V_{DC}, until either the tip fractures or continuous DC evaporation starts.

Since the time-of-flight is proportional to the acceleration potential at the apex (V_{apex}), the peak positions change with V_{DC}: an increase in V_{apex} results in higher ion energy and a *downward* shift in m/n, whereas a decrease in V_{apex} causes an *upward* shift. In insulating sol–gel silica, V_{apex} differs from V_{DC} due to a resistive drop along the tip, which is influenced by the instantaneous emission current, as shown in previous Chapter in section 3.2.2.

In particular, as visible in Fig. 4.7, after initially decreasing V_{DC} to a point where only electrons are emitted, the subsequent three incremental increases (reaching approximately $\sim$4 kV) display a shift *upward* of the m/n bands. This can be explained by the fact that the resistive drop within the tip rises with increasing emission rate, resulting in a reduced V_{apex} with each step.

The gradual change in electron emission or charge transport decreases the internal voltage drop while the plateau persists.

When exceeding approximately 4 kV, increasing V_{DC} causes downward shifts in m/n, due to the increase of the emission rate. Around ~ 7 kV, the tip undergoes a transition into continuous, DC-driven evaporation, probably due to fracture, as there is no longer point density in the region around 14 Da and this corresponds in the mass history diagram (Fig. 4.7) to an evident detection rate burst after $2.5 \cdot 10^5$ collected events.

4.2 Coating Strategies for THz-field enhancement on sol-gel silica specimens

As mentioned in the previous sections, sol–gel silica is an insulating material, thus it does not experience THz-field enhancement nor behave like a metal antenna under THz pulsed irradiation. In our tip geometry the silica apex is bonded to a tungsten pre-tip, forming a Schottky contact that responds asymmetrically to the single-cycle field: a negative THz pulse forward-biases the junction and pushes surface charge to the apex, strongly amplifying the local field. A THz pulse of opposite polarity reverse-biases the junction, suppresses the antenna current and yields a lower field amplification. Since positive and negative polarity measurements are performed on the same tip without changes in apex geometry, this reduction cannot be attributed to geometric field-factor variations, so the apex field often falls short of the evaporation threshold and spectra become dominated by thermally assisted background when the DC voltage must be increased to sustain the flux, leading to continuous evaporation. [30]. To recover metal-like coupling for positive THz pulses configuration, in order to drive evaporation by field rather than heat, we therefore applied ultrathin conductive coatings that cover and connect the silica–tungsten junction: a conformal chromium (Cr) film deposited ex situ by broad-beam ion sputtering (Gatan PECS), and monolayer graphene encapsulation, techniques already described in chapter 2. Both paths electrically link the apex to the mount, thereby allowing significant apex field amplification during a positive pulse.

4.2.1 Chromium-coated sol–gel silica under THz pulsing

To quantify the effect of chromium metallization and isolate polarity effects, we carried out two complementary comparisons. First, in similar field conditions ($\sim$ 20.6 V/nm for all analyses, calculated using Eq. (2.4)), we compared four spectra:

- uncoated sol-gel silica under THz-negative pulses
- uncoated sol-gel silica under UV (343 nm wavelength) laser-assisted APT
- Cr-coated sol-gel silica under THz-positive pulses
- Cr-coated sol-gel silica under THz-negative pulses

selecting datasets of $1.6 \cdot 10^5$ events, excluding the hydrogen related peaks (H^+, H_2^+) and then normalized to the $^{28}Si^{2+}$ peak at 14 Da (Fig. 4.8(a,b)). Removing the dominant hydrogen counts (especially present in the THz positive pulses analysis) before fixing the total statistics yields a fairer SNR comparison under a common normalization. Relative to the UV uncoated case, the Cr-coated spectrum shows reduced thermal tails and improved signal-to-noise ratio compared to both uncoated samples analyzed with UV and THz, and an overall mass resolving power trending toward the values found for UV-assisted analysis on the uncoated sample. Those values are collected in Table 4.2. Cr and Cr-oxide species appear, proving the presence of the coating layer.

In a direct comparison analysis (Fig. 4.8(b)), we evaluated THz-negative and THz-positive pulse analyses. Peaks are sharper in the positive than in the negative-polarity case, with substantially reduced thermal tails and improvement in SNR of a factor 5. The expected silica- and chromium-related ions (Si, O, SiO, SiO_2, Cr^+, Cr^{2+}, $Cr_xO_x^{+/2+}$) are present under both polarities, indicating coating presence; Na^+ at 23 Da is observed in both as it comes from the sol-gel preparation steps. Hydrogen species (H^+, H_2^+, H_3^+) are present in both analyses, with considerable concentration (roughly 60% of the total volume) under THz-positive pulses, where their accumulation between pulses results more significant.

In order to assess peak shape improvements, Fig. 4.9(a,b) magnifies the 13.5–15.5 Da region (normalized to 14 Da, Si^{2+}) and the 27.5–30.5 Da region (normalized to 28 Da, Si^+). The Cr-coated THz spectra achieve SNR $> 10^4$ at the silicon peaks, a gain of at least 1 order of magnitude and

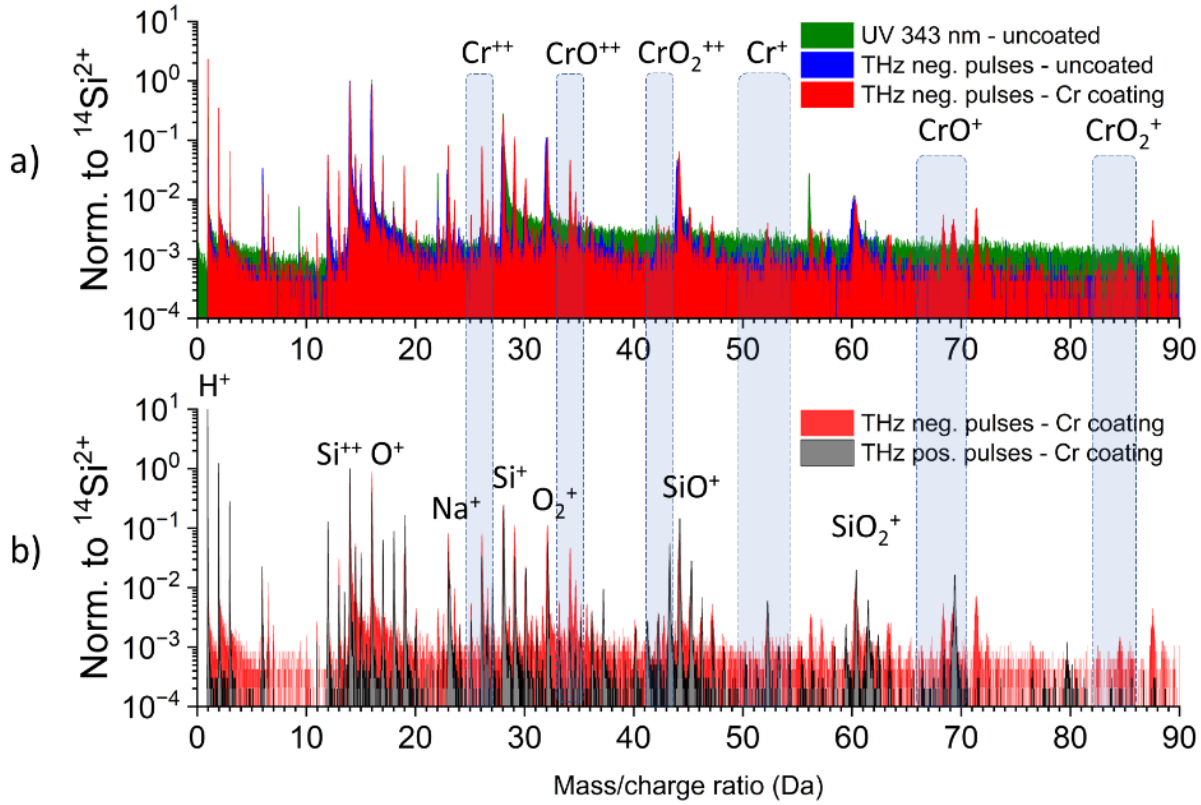

Figure 4.8: (a) Mass spectrum of uncoated silica sample with THz negative pulse (blue), Cr-coated silica sample with THz negative pulse (red), and uncoated silica sample with UV laser-assisted APT (green). All spectra 160k atoms, excluding H^+ and H_2^+ peaks and are normalized to the 14 Da Si^{2+} peak. Cr- and Cr-oxide-related species are highlighted in transparency. (b) Comparison of Cr-coated silica APT analyses using THz negative (red) and THz positive (dark gray) pulses. Similar field conditions were applied: F=20.5 V/nm, det. rate = 0.025 ions/pulse, for THz negative pulses; F = 20.5 V/nm, det. rate=0.003 ions/pulse, for THz positive pulses. T = 50 K for all analyses.

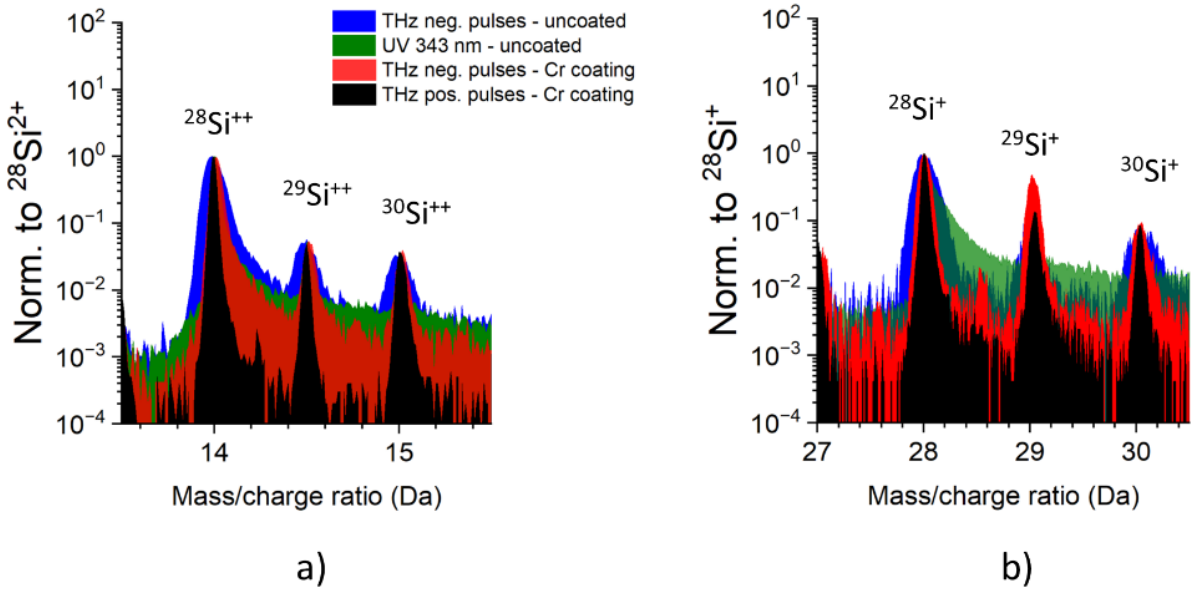

Figure 4.9: (a) Magnified mass spectra comparison of uncoated silica with UV laser-assisted APT (green) and THz negative pulse uncoated (blue), Cr-coated silica sample with THz negative pulse (red) and THz positive pulse (black) in the 13.5–15.5 Da range. The spectra are normalized to the 14 Da Si^{2+} peak. (b) Magnified mass spectra comparison of the same four analyses in (a) for the 27.5–30.5 Da range, normalized to the 28 Da Si^{1+} peak.

over uncoated THz-negative and UV uncoated cases, with a clear appreciation of a significant reduction of thermal tails when using positive THz pulses. Table 4.2 reports signal-to-noise ratio, $M/\Delta M$ at 1% and 10% of peak height values for 14 and 28 Da peaks. In conclusion, Cr metallization sharpens peaks and suppresses background, with the best performance realized operating with THz-positive pulses.

Peak at 14 Da (Si^{2+})	**UV**	**Uncoated THz−**	**Cr THz−**	**Cr THz+**
SNR	$\sim 10^3$	$\sim 10^3$	$\sim 10^4$	$\sim 10^4$
$\frac{\Delta M}{M}$ @ 1% max	37	27	47	121
$\frac{\Delta M}{M}$ @ 10% max	159	66	121	215
Peak at 28 Da (Si^{+})	**UV**	**Uncoated THz−**	**Cr THz−**	**Cr THz+**
SNR	$\sim 10^2$	$\sim 10^2$	$\sim 10^3$	$> 10^3$
$\frac{\Delta M}{M}$ @ 1% max	/	/	74	109
$\frac{\Delta M}{M}$ @ 10% max	79	71	132	225

Table 4.2: Summary of signal-to-noise ratio and mass resolving power ($M/\Delta M$ at 1% and 10% peak max) values for the Cr coated and uncoated samples under UV laser and THz positive/negative pulsing.

Two extended runs were performed on different tips from the same sample were reconstructed

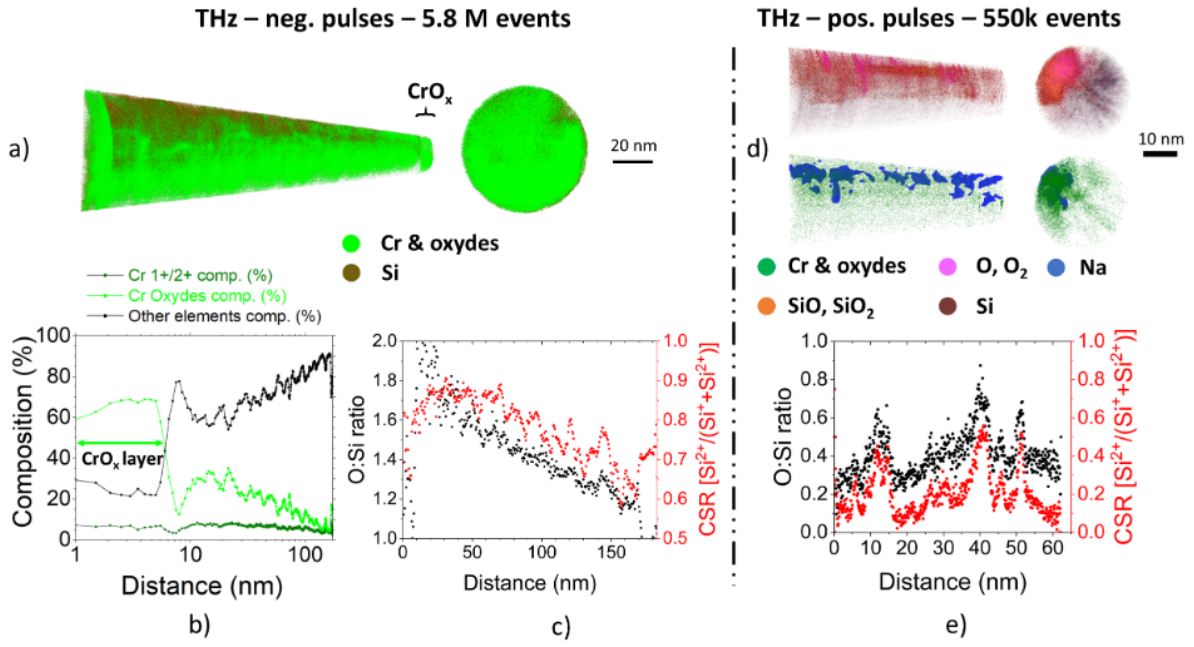

Figure 4.10: (a) 3D reconstruction of the Cr-coated tip analyzed with THz negative pulses (5.8M detected ions) with the top-down 2D projection. (b) Compositional profile of Cr species along depth. (c) O/Si ratio and charge state ratio (CSR) as a function of depth for THz negative pulses. (d) 3D reconstruction of the Cr-coated tip analyzed with THz positive pulses (550k detected ions) and the top-down 2D projection. (e) O/Si ratio and CSR trends for THz positive pulses.

to examine spatial homogeneity and composition as a function of depth (Fig. 4.10(a-e)): THz-negative ($5.8{\cdot}10^6$ ions, 0.10 ions/pulse, $F = 20.7$ V nm^{-1}) and THz-positive ($5.5{\cdot}10^5$ ions, 0.004 ions/pulse, $F = 19.2$ V nm^{-1}). Under THz-negative pulses, chromium and silica ions are distributed more uniformly across the detector (Fig. 4.10(a)), and the depth profile shows an initial ~ 10 nm region enriched in Cr-oxides that quickly relaxes to a stable mixture where elemental Cr (Cr^+, Cr^{2+}) reaches a level comparable to Cr-oxides (Fig. 4.10(b)). Under THz-positive excitation, species maps reveal a pronounced lateral inhomogeneity, with silica- and chromium-related ions preferentially concentrated on one side of the reconstruction, whereas hydrogen appears more uniformly distributed (Fig. 4.10(d)). This asymmetry is attributed to a non-uniform near-field coupling at the tip apex under positive-polarity THz illumination: because the THz beam impinges at a finite angle and interacts with a partially conductive chromium coating, the local field enhancement is stronger on one side of the apex, leading to a higher evaporation probability for field-sensitive species such as SiO_x^+ and Cr^{n+}. In contrast, hydrogen—characterized by high mobility and low activation fields under low-repetition-rate conditions—does not directly reflect these local field variations and therefore appears laterally homogeneous. Similarly, Na^+

is observed to redistribute across the porous sol–gel matrix, consistent with diffusion-driven transport rather than localized field-controlled evaporation.

The oxygen-to-silicon ratio (O/Si) tracks the local field along the analyses, which we probe *via* charge-state ratio calculated as $\frac{Si^{2+}}{Si^{2+}+Si^{+}}$ (Figs. 4.10(c,e)).

In the THz-negative run, O/Si climbs to $\approx$ 1.8 where CSR $\approx$ 9.9, *i.e.*, in the higher static voltage, approaching the stoichiometric value of 2 for SiO_2. Under THz-positive conditions, O/Si remains below $\approx$ 0.7 when CSR $\approx$ 0.7, indicating reduced oxygen recovery at lower field. This behavior is consistent with neutral evaporation of O_2 when the field is insufficient, which biases the measured composition toward lower O content [267].

4.2.2 Graphene-coated sol–gel silica under THz pulsing

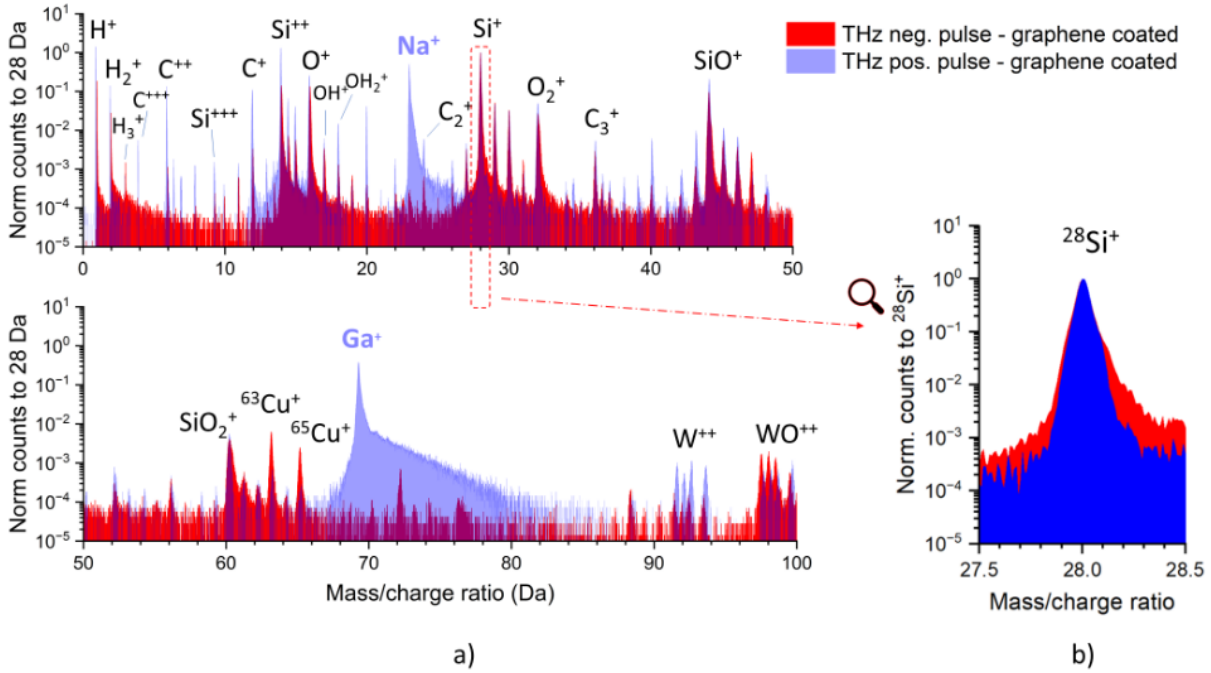

Figure 4.11: (a) Mass spectra of graphene-coated sol-gel silica tips analyzed using THz negative pulses (red) and THz positive pulses (blue transparency). The spectra are normalized to the Si^{1+} peak at 28 Da and each dataset contains about 1 million events. Different analysis conditions were applied (F= 18.2 V/nm, det. rate=0.08-0.10 ions/pulse, V_{DC} = 8.5 kV for THz negative pulses; F=19.3 V/nm, det. rate=0.144 ions/pulse, V_{DC}=5.5 kV for THz positive pulses, T = 50 K). (b) Magnified view of the mass spectra in the 27.5–28.5 Da range.

A polarity-controlled comparison was performed on graphene-coated tips with matched statistics (each dataset contains $\sim 10^6$ detected ions). The THz-positive run operated at $F = 19.3\ \mathrm{V\,nm^{-1}}$ (detection rate = 0.144 ions/pulse), while the THz-negative run used $F = 18.2\ \mathrm{V\,nm^{-1}}$ (detec-

tion rate = 0.08–0.10 ions/pulse), both at $T = 50$ K. Spectra were normalized to the Si^+ peak at 28 Da to compare peak shape and noise under a common reference (Fig. 4.11(a)). The mass resolving power at 1% height for Si^{2+} (14 Da) is $\sim$ 117 for THz-positive vs. $\sim$ 85 for THz-negative, and the 28 Da peak is visibly narrower in the THz-positive case. Background remains low for both polarities, with THz-positive consistently yielding higher SNR in the 14 and 28 Da windows (see zoom in Fig. 4.11(b)).

Beyond the silicon ranges, the THz-positive spectrum also reveals the presence of Na^+ (23 Da) and Ga^+ (69 Da), observed when Ga-FIB was used (and the cleaning steps were ineffective). Na^+ amd Ga^+ diffuse and reach the tip's surface in high quantity due to the porosity of the sol-gel silica sample. When the tip is prepared using the Xenon Plasma-FIB, as in the case on the onse analyzed with THz negative pulses, no Ga^+ peak is observed in the spectrum. The missing Na^+ peak under negative THz pulses can be attributed to the sampled region: sodium residues from the sol–gel synthesis are spatially heterogeneous, so detectability depends on the lift-out site.

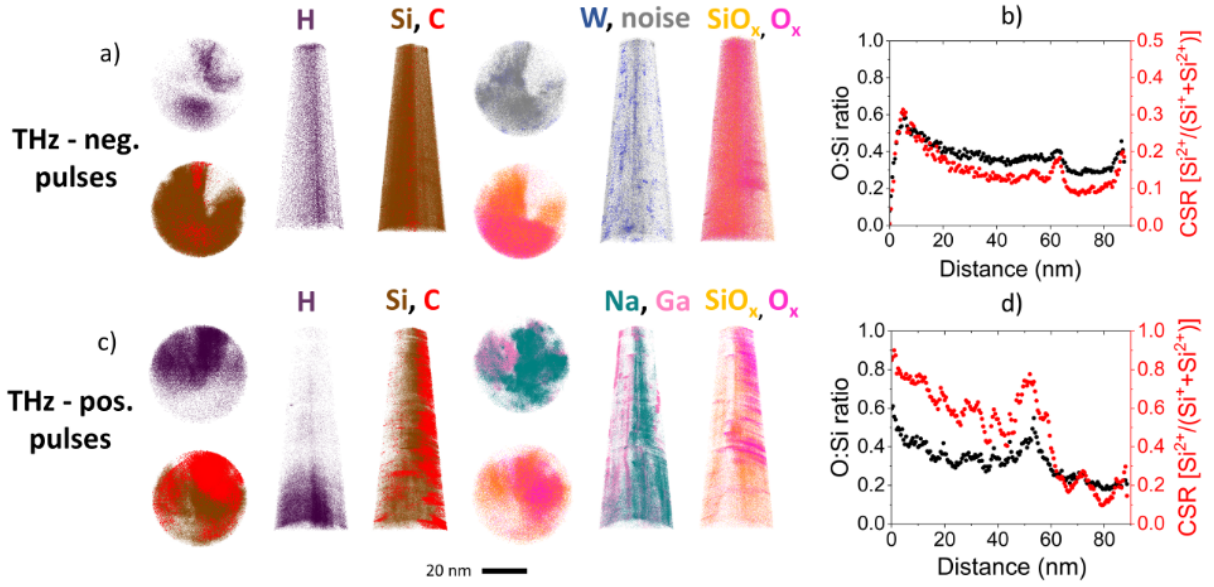

Figure 4.12: (a) 3D reconstruction of the graphene coated tip analyzed with THz negative pulses and (c) with positive THz pulses, together with the respective top-down 2D projections (1M detected ions). (b) O/Si ratio and charge state ratio (CSR) trends as a function of depth for the THz negative pulse analysis and (d) positive showing oscillations correlated with field variations along the tip.

Three-dimensional reconstructions (1 M ions each) show that both polarities can exhibit species inhomogeneity at the detector scale; under THz-positive, the carbon distribution appears less homogeneous compared with THz-negative, even though the overall conductive coating remains

intact over the analysis. This behaviour is attributed to a less stable and more thermally assisted evaporation regime under positive polarity, which enhances local fluctuations in evaporation sequence and ion trajectories, leading to apparent compositional inhomogeneities. (Fig. 4.12(a,c)). Depth profiles of O/Si and the Si charge-state ratio (CSR) display oscillations that correlate with field variations along the shank (Fig. 4.12(b,d)), in line with the field-dependent evaporation dynamics of oxygen-related species established for Cr-coated tips.

4.2.3 Comparative analyses under THz-Positive pulses: Graphene vs. Chromium coating

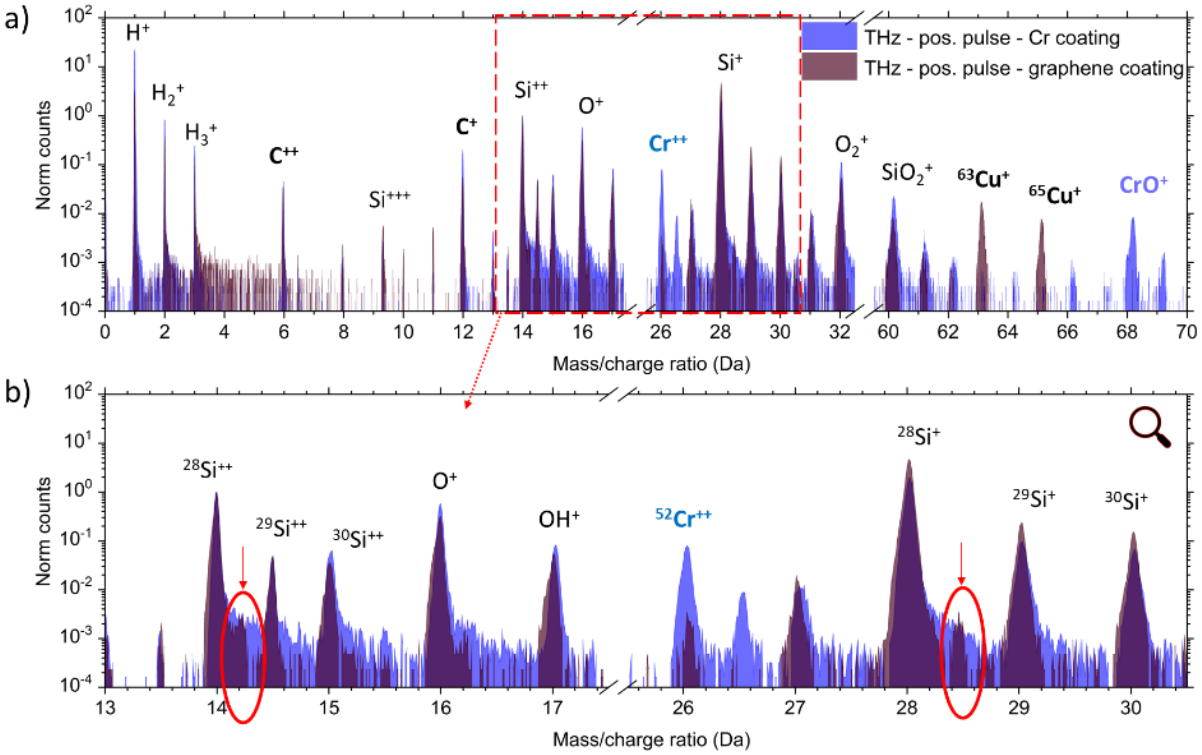

Figure 4.13: (a) Mass spectra of graphene coated sol-gel silica tips (black, det. rate=0.013 ions/pulse, V_{DC}=5 kV) and chromium coated sol-gel silica tips (blue, det. rate=0.011 ions/pulse, V_{DC}=9.5 kV), both analyzed using positive THz pulses. The spectra are normalized to the 14 Da Si^{2+} peak. (b) Zoomed-in view of the spectral regions 13–17.5 Da and 25.5–30.5 Da.

First comparison A comparison of mass spectra of graphene coated and chromium coated silica tips under positive THz pulses is illustrated in Fig.4.13(a). The analyses, consisting of two dataset of 300k events each, are performed under slightly different peak field conditions (18.2 V/nm for graphene coated – 19.3 V/nm for chromium coated) and very similar detection rate (0.013 at/pulse for graphene coated - 0.011 at/pulse for chromium coated).

Peak at 14 Da (Si^{2+})	**Chromium coating, THz+**	**Graphene coating, THz+**
SNR	$< 10^3$	$\mathbf{10^4}$
$\frac{\Delta M}{M}$ @ 1% max	**114**	100
$\frac{\Delta M}{M}$ @ 10% max	**210**	162
Peak at 28 Da (Si^{+})	**Chromium coating, THz+**	**Graphene coating, THz+**
SNR	$< 10^4$	$\mathbf{5 \times 10^4}$
$\frac{\Delta M}{M}$ @ 1% max	**114**	100
$\frac{\Delta M}{M}$ @ 10% max	224	**241**

Table 4.3: Summary of signal-to-noise ratio and mass resolving power ($M/\Delta M$ at 1% and 10% peak max) values for the graphene coated and Cr coated samples.

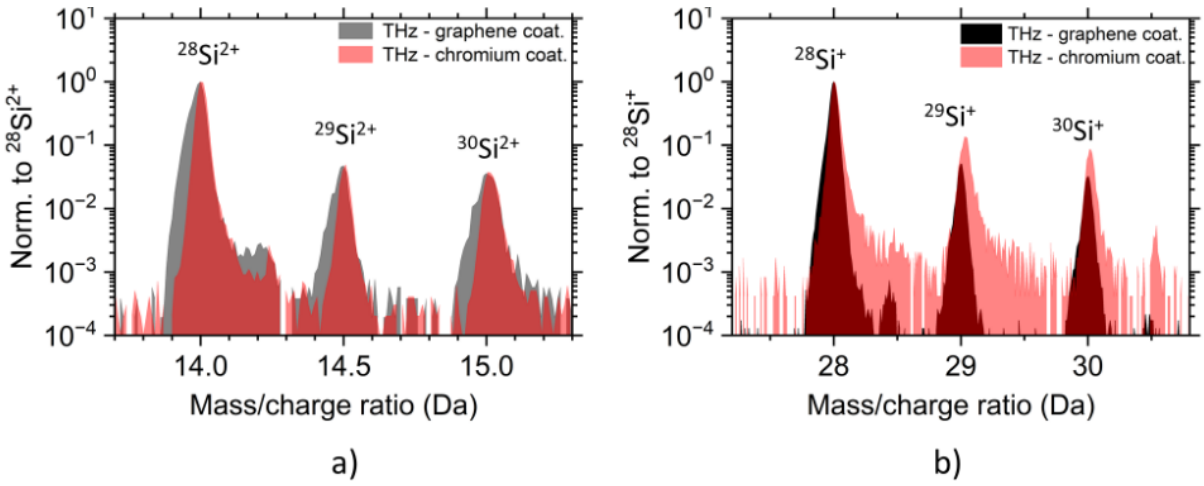

Figure 4.14: (a) Zoomed-in view of the spectral regions a) 13.5–15.5 Da, normalized to the 14 Da Si^{2+} peak, and b) 27–31 Da, normalized to the 28 Da Si^{+} peak for graphene coated sol-gel silica tips (black, det. rate=0.013 ions/pulse, V_{DC}=5 kV) and chromium coated sol-gel silica tips (red, det. rate=0.003 ions/pulse, V_{DC}=10 kV), both analyzed using positive THz pulses. Both dataset consist of 300k events.

The graphene coated sample exhibits sharper peaks, highlighting reduced thermal broadening. The zoomed-in view in Fig.4.13(b) focuses on the 13–17.5 Da and 25.5–30.5 Da ranges, where two red arrows indicate the 28.5 Da and 14.25 Da peaks, which are clearly resolved in the graphene coated sample but completely masked by thermal noise in the chromium coated sample. The accompanying Table 4.3 summarizes the SNR and mass resolving power ($M/\Delta M$ at 1% peak max) for both coatings, where graphene encapsulation looks advantaged over chromium in terms of minimizing thermal effects (consistently higher SNR compared to chromium coating) and enhancing spectral resolution for higher m/n species, but underperforms in terms of mass resolving power at lower m/n.

Second comparison We also compared the same graphene-coated sol–gel silica (THz positive) with a *second* chromium-coated sol–gel silica dataset acquired under THz-positive pulsing, again using $3{\cdot}10^5$ events. In this second case the chromium analysis was performed at a higher peak field of 20.5 V/nm and a different detection rate of 0.003 ions/pulse. This experimental conditions corresponds to a lower THz field contribution to the total field compared to the one used for graphene coated samples.

The magnified mass spectra, in Fig. 4.14 show only the two windows: (a) 13–15.5 Da and (b) 27–30.5 Da, normalized at 14 Da and 28 Da, respectively, to compare the Si^{2+} and Si^{+} isotope regions on the same scale. Contrary to the previous comparison, the chromium-coated tip now exhibits a higher mass resolving power than graphene at 14 Da—both at 1% and 10% of peak height—allowing the 14.25 Da feature to be resolved with a clarity comparable to the graphene spectrum. At higher masses, however, chromium still underperforms: at 28 Da a pronounced thermal tail remains visible, whereas graphene maintains a sharper, more symmetric peak. Lower m/n ions (e.g., Si^{2+}) exhibit greater peak broadening at higher THz fields because the pulse induces additional ion–energy dispersion [28]. Consequently, a lower $M/\Delta M$ is achieved with the graphene-coated sample for low-m/n species, reflecting the stronger THz-field contribution during this analysis compared with the chromium-coated case. Table 4.4 summarize the mass resolving power trends for the two m/n ranges.

14 Da (Si^{2+})	**THz–Cr coat.**	**THz–Graphene coat.**
$M/\Delta M$ @ 1% max	**116**	86
$M/\Delta M$ @ 10% max	**206**	166
28 Da (Si^{+})	**THz–Cr coat.**	**THz–Graphene coat.**
$M/\Delta M$ @ 1% max	107	**116**
$M/\Delta M$ @ 10% max	233	**240**

Table 4.4: Mass resolving power ($M/\Delta M$) at the silicon peaks for THz positive pulse analysis with chromium coating, graphene coating. Values are extracted from the zoomed spectra in Fig. 4.14.

4.3 Preliminary results on the high–repetition–rate Tera-SAT (100 kHz)

We performed a late-campaign test on *empty* sol–gel silica tips using the new high–repetition–rate Tera-SAT, characterized by a repetition rate of 100 kHz. Here THz generation is achieved by optical rectification in $LiNbO_3$. As on the low–repetition rate system, this new platform allows both THz drive (single-cycle pulses, selectable polarity, although non tunable pulse shape) and IR operation atλ = 1035 nm. However, for this new setup the amplitude of the THz field is of 170 kV/cm, about five times weaker than the 800 kV/cm delivered by the two color plasma THz source of the low repetition rate setup (see Chapter 2 for more details).

4.3.1 First experiment: THz negative pulses vs IR on empty sol-gel silica sample

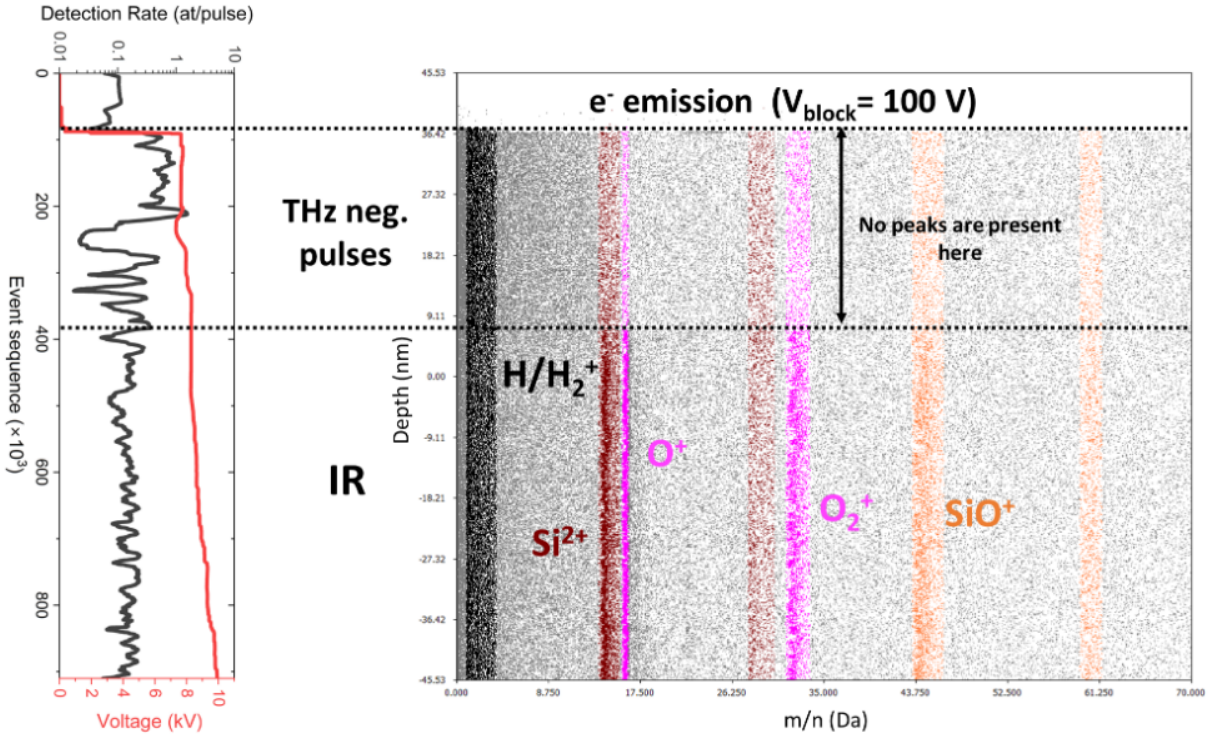

Figure 4.15: Mass history diagram on high–repetition rate THz negative polarity and IR run on empty sol–gel silica tip. Left: Detection rate and V_{DC} vs. event index. Right: mass–history diagram; the dashed band marks the THz segment ($V_{stop} \approx 100$ V for electron blocking) followed by the IR segment. The main slecies are indicated above withe corresponding colors.

A single tip was acquired for $\sim 9 \cdot 10^5$ events. We began with THz *negative* polarity to replicate the 1 kHz results and, after $\sim 4 \cdot 10^5$ events, switched to IR while keeping the detection rate as

similar as possible to the one of the previous phase (Fig. 4.15). In the THz segment we observed clear electron emission at low bias and determined a blocking voltage $V_{\text{stop}} \approx 100$ V (annotated in the figure). For the 1 kHz plasma–THz system, we measured $V_{\text{stop}} \approx 0.9$ kV. The much lower V_{stop} on the 100 kHz setup is consistent with the substantially smaller THz field provided from the $LiNbO_3$ source , as the THz amplitude is linked linearly to it through the relation (4.1), at page 118.

Being V_{stop} is so small, the electron current was not intense enough to assist evaporation. To evaporate ions we had to increase the bias up to $V_{\text{DC}} \sim 8$ kV, which eventually led to *continuous* DC-driven evaporation with thermal noise, meaning that the THz pulses were effectively non-effective as a trigger for field evaporation. This behavior mirrors what we previously observed under *positive* THz polarity: the ion emission is governed by the static field rather than by pulsed THz excitation. In this phase the detection rate curve shows important fluctuations and the automatic detection rate was unable to provide a constant evaporation.

After $\sim 4{\cdot}10^5$ events we switched to IR at 1035 nm and enabled automatic detection rate. The flux exhibited frequent bursts, forcing continuous voltage adjustments, but was more stable than under THz pulses; small m/n shifts are visible on Si^{2+} and O^+ bands in the mass history during these regulation steps. A spectral comparison between the two illumination conditions was then made by extracting $2{\cdot}10^5$–events subsets from the THz and IR portions and normalizing to equal area under the curves, as shown in (Fig. 4.16).

These preliminary tests indicate that, with the present 100 kHz configuration, the available THz field at the apex is too weak to enable the electron–assisted, pulse-gated mechanism that was effective at 1 kHz. Practically, operation devolves to DC-driven evaporation (thermal noise) in the THz segment, whereas the IR segment produces identifiable peaks but with pronounced thermal tails.

Several upgrades could restore THz efficacy on this platform and will be targeted in future work: (i) increasing the THz amplitude (reduce losses through the optical path, tighter focusing, or even using a more instense source); (ii) improving near-field coupling at the apex (conductive coatings or graphene encapsulation); and (iii) using electron-blocking bias and rate-matched protocols to re-test whether pulse-gated THz emission can be recovered at high repetition rate.

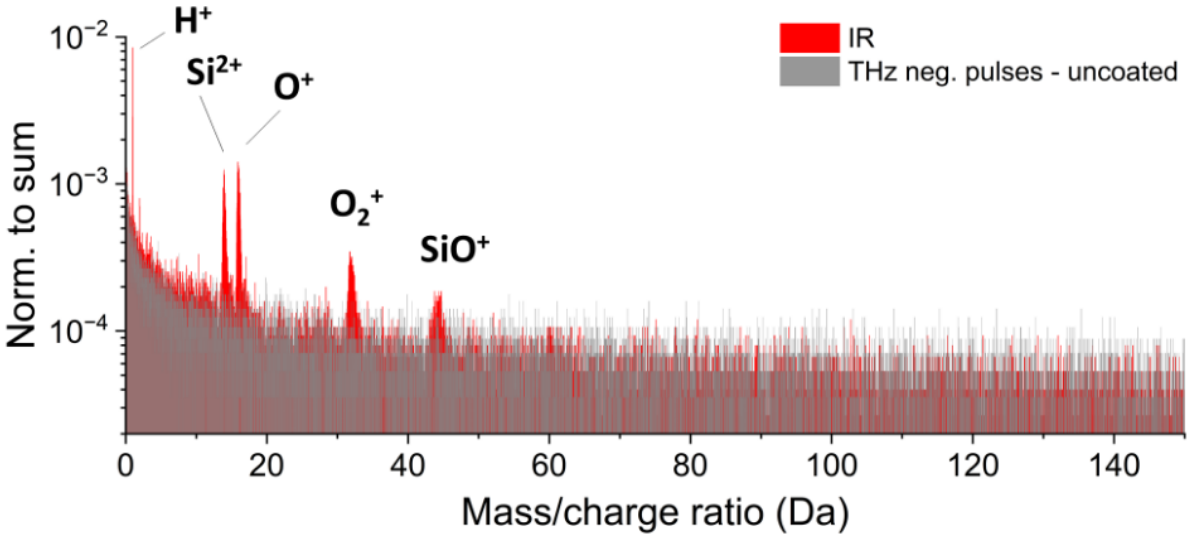

Figure 4.16: Spectral comparison ($2 \cdot 10^5$ events per spectrum, normalized to the area below the curves). IR spectrum (red) shows visible Si^{2+} (14 Da), O^+ (16 Da), O_2^+ (32 Da) and SiO^+ (44 Da), with thermal tails. THe THz negative subset (transparent grey) from the 100 kHz system is dominated by broadband thermal background with no distinguishable species.

4.3.2 Second experiment: THz positive pulses analysis on Cr–coated silica

Motivated by the necessity to enhance the near–apex THz field on the 100 kHz platform, we repeated the test on *Cr–coated* sol–gel silica tips. A $\sim$ 10 nm chromium film was deposited by PECS sputtering using the procedure in section 2.7.1. In this run, we chose a *positive* single-cycle THz polarity to reduce the impact of heating driven by electron emission.

A single run was acquired for $\sim$ 200 k events, in automatic mode. The flux fluctuates around the value of 0.1 at/pulse and is more stable than for non coated sample previously analyzed with negative THz pulses, while the voltage trace (Fig. 4.17) shows that ion emission starts already at $V_{DC} \approx 2$ kV, but the early spectrum is initially dominated by molecular species or charge state elements (OX_x^+, $x = 1-3$, at 17–19 Da; SiO^+ at 44 Da; Si^+ at 28 Da). Upon increasing V_{DC} toward $\sim$ 3 kV, elemental chromium and chromium oxides peaks becomes evident, with a prominent CrO^{2+} peak at 34 Da and its isotopes.

As the bias increases toward approximately $V_{DC} \sim$ 4 kV, the tip fractures around $\sim$ 200 k detected ions (indicated by the arrow in Fig. 4.17). Following this, the spectrum becomes dominated by Ga^+ at 69 Da (due to Ga-FIB preparation) and C^+ at 12 Da, while peaks associated with chromium disappear. This is consistent with the partial detachment of the ultra-thin Cr film during the fracture and the consequent abrupt decline in the apex field enhancement.

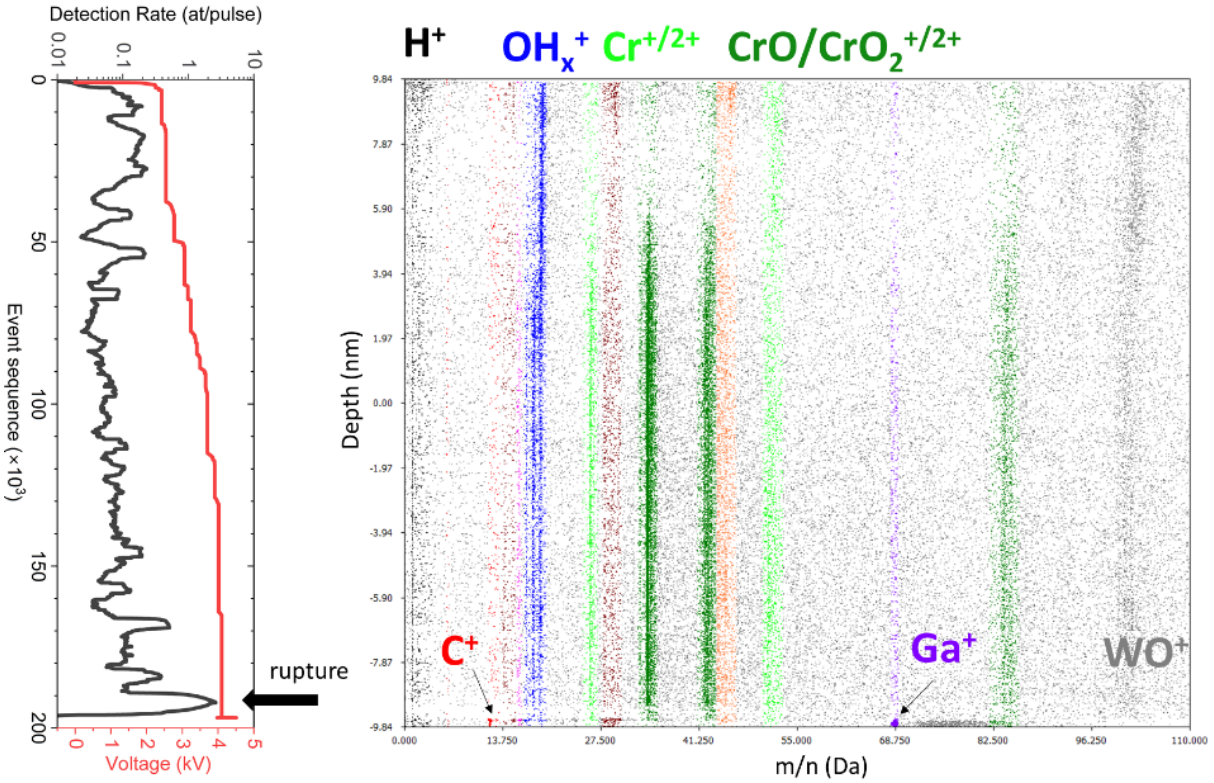

Figure 4.17: Mass history diagram for Cr–coated silica at 100 kHz, THz positive polarity. Left: Detection rate in logscale and V_{DC} vs. event index (fracture around $\sim 2 \cdot 10^5$ events). Right: mass–history diagram highlighting species with colors. In green $\mathrm{Cr/CrO/CrO_2}$ signatures can be noticed.

Species–resolved 3D reconstructions, performed using the E_β method (Fig. 4.18) corroborate the spectral picture. Hydroxyl-related ions (OH_x^+) are predominantly located at the start of the dataset, while Cr-oxide ions (CrO^+/CrO_2^+) are densely located further from the center, consistent with a thin, uniform coating. Silicon-containing ions are scattered though relatively uniform throughout the volume. Ga and C become concentrated at the conclusion of the run, coinciding with the fracture event.

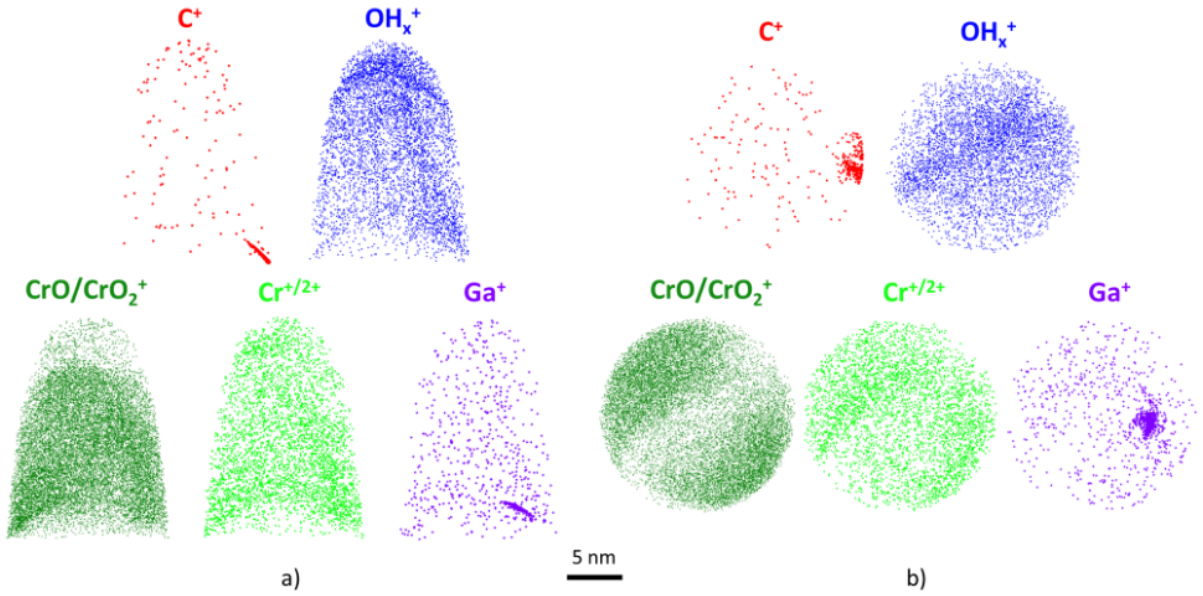

Figure 4.18: 3D reconstructions (E_β method) for Cr–coated silica analyzed with high-repetition rate THz positive pulses, a) side and b) top view. Species are indicated above in correspondent colors.

Spectral comparison with uncoated sample To evaluate how coating and polarity affect spectral quality at high repetition rates, Fig. 4.19 presents a comparison of two area-normalized spectra with $2{\cdot}10^5$ events: one analyzing *uncoated* silica with THz *negative* pulses, and the other analyzing *Cr-coated* silica with THz *positive* pulses. The coated tip shows a cleaner low m/n region, in which it is possible to identify elemental Cr peaks, around 26 Da, and Cr-oxide peaks, such as $CrO^{+/2+}$ at 34 and 68 Da, CrO_2^{2+} at 42 Da, CrO_2^+) at 84 Da, suggesting better coupling of the THz field at the tip's apex than in the case of the application of negative THz pulses on uncoated samples. Despite this, the overall thermal background remains significant, and the coating does not endure sufficiently long for extended high-quality runs, as the tip fractured around $2{\cdot}10^5$ events collected and the detection rate decreased dramatically.

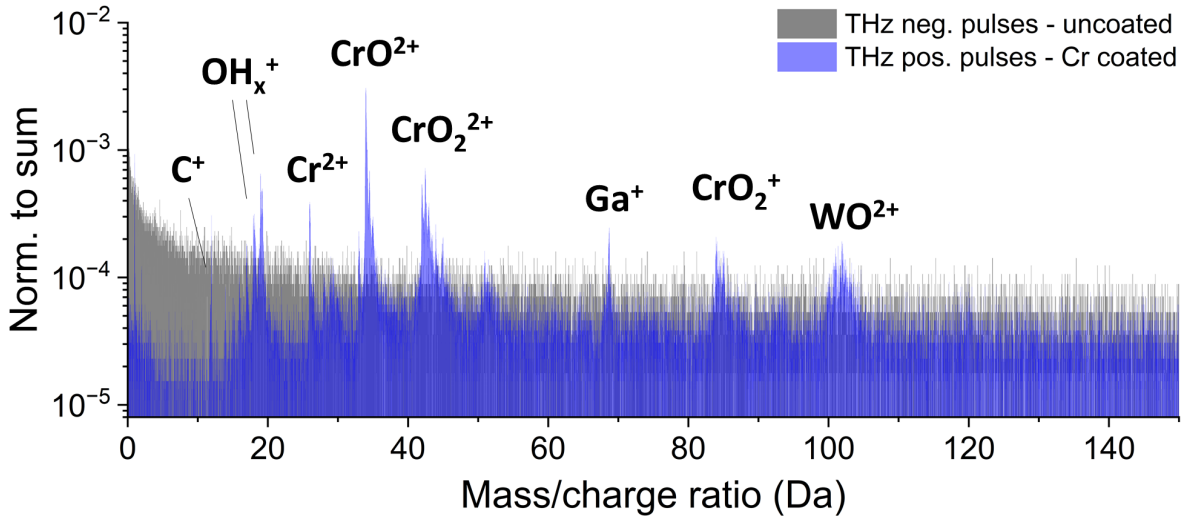

Figure 4.19: Area–normalized spectra (200k events) at 100 kHz. Black: uncoated silica, THz negative polarity—featureless thermal background. Blue: Cr–coated silica, THz positive polarity—improved low–mass SNR and clear chromium/oxide peaks, but persistent thermal tails; coating fails near the end of the run.

4.4 Conclusion

We studied the impact of THz pulse polarity on sol-gel silica using both low and high repetition rate setups, comparing these results to IR and UV -assisted analyses. Negative-polarity THz pulses deliver high signal-to-noise ratios and distinct peaks with minimal tails, aiding quantitative field assessment. They are associated with electron-assisted Joule heating, raising local lattice temperatures while maintaining field-induced evaporation, and ensuring consistent field-correlated oxygen loss trends, consistent with UV analysis. Conversely, positive polarity fails to enhance the THz field at the apex, leading to a mass spectrum largely influenced by continuous evaporation from static field and thermal background. While UV pulses exhibit superior mass resolution, NIR pulses show higher thermal activation.

We demonstrated effectiveness in optimizing field evaporation using metallic and graphene-based coatings to enhance THz-field coupling, using both THz instruments. In the case of low repetition rate THz-APT, Cr coating *via* PECS deposition notably enhanced mass resolution, reduced thermal tails, and facilitated field evaporation with positive THz pulses. Graphene encapsulation further improved peak sharpness, reduced background noise, and enhanced spectral clarity. Compositional profiling indicated oxygen loss due to neutral O evaporation, with O/Si ratios of 1.8 under negative THz pulses but below 0.7 with positive pulses. While analyses using

negative THz pulses yielded homogeneous reconstructions due to thermal diffusion, positive pulses resulted in inhomogeneous ion distributions, suggesting local field gradients and species segregation within the tip volume, attributed to diffusion and H-assisted evaporation at low fields.

The chromium coating, under high repetition conditions, improves the evaporation, in particular the signal-to-noise ratio for low-mass applications, and exhibits expected chromium/oxide characteristics. However, thermal effects significantly impact the performance, and the 10 nm coating is prone to ruptures under sustained fields. When the coating fails, THz enhancement is lost, reverting the process to DC-driven evaporation.

A quantitative comparison between excitation modalities further clarifies the regimes in which THz-assisted APT provides a tangible advantage. In the present experiments on sol–gel silica, NIR-assisted evaporation required significant transient heating, with estimated temperature excursions of several hundred kelvin, resulting in pronounced thermal tails and mass resolving power typically below $m/\Delta m \sim 600$. UV and deep-UV excitation reduced thermal broadening and enabled higher mass resolving power ($m/\Delta m \sim 800$–1500), but still relied on thermal activation and required elevated DC fields, leading to increased mechanical stress and background contributions.

By contrast, THz-assisted excitation operated in a field-dominated regime, with surface fields inferred from charge–state ratios in the range of $\sim$15–25 V nm^{-1}, while maintaining low effective thermal load. Under negative-polarity THz pulses, thermal tails contributed less than a few percent to peak areas and the measured O/Si ratio approached the nominal value of 2 at sufficiently high field. In this regime, detection rates of $(2\text{–}5) \times 10^{-3}$ ions per pulse were achieved with stable evaporation and improved signal-to-noise ratio. Conversely, positive-polarity THz excitation failed to provide sufficient near-field enhancement, resulting in low effective fields, compositional deviations (O/Si < 0.7), and inhomogeneous reconstructions dominated by charging and diffusion effects.

Taken together, these results indicate that THz-assisted APT outperforms NIR excitation whenever thermal effects limit compositional fidelity, and complements UV-assisted APT by enabling access to a low-thermal-load, field-controlled evaporation regime in insulating materials, pro-

vided that near-field coupling and coating stability are adequately ensured.

Consequently, future research will aim to enhance the THz field at the apex (optimizing the beamline for $LiNbO_3$, achieving tighter focusing, and adjusting polarization and pulse-front-tilt), increase the resilience and uniformity of conductive coatings (by using thicker Cr, multi-layer structures, or graphene encapsulation), and investigate polarity/energy maps to determine conditions that maintain coating stability while ensuring effective THz field enhancement.

CHAPTER 5

High-repetition-rate Tera-SAT: Results and discussion on NS8 nickel-based superalloy

5.1 Introduction

As anticipated in the previous chapter, the new high–repetition–rate Terahertz-assisted atom probe instrument delivers a terahertz (THz) field amplitude that is lower than that of the earlier used low–repetition–rate setup. Consequently, when operated without conductive coatings, the field enhancement provided by the antenna effect was insufficient to trigger field evaporation in insulating samples, even under negative–polarity THz pulses. In the light of this limitation, we decided to take a step back and validate the performance of the new instrument on conductive systems, which inherently exploit the antenna effect more efficiently than complex insulating materials such coated sol–gel amorphous silica.

Initial tests were successfully carried out on pure metals, including pure aluminium and pure nickel tips (results not presented in this thesis). Building on these initial results, we then turned our attention to conductive materials with a more complex micro or nano-structure which can allow to assess the capabilities of the high repetition–rate THz–assisted atom probe tomography

setup, in terms of fidelity of three–dimensional reconstructions and the accuracy of spectral and compositional analysis across chemically heterogeneous regions.

Possible interesting candidate materials can be nickel-based superalloys, as their microstructure follows the canonical γ/γ' architecture: a FCC Ni-rich γ matrix (substitutional solid solution) and crystalline γ' precipitates with $L1_2$ structure, nominally $Ni_3(Al, Ti)$. Earlier literature likewise reports nanometric intracrystalline particles in Ni superalloys, *e.g.* Merrick on IN738 [277], Oblak on related Ni–base alloys [278], and Miller on secondary γ precipitates ($\sim$5–10 nm) forming within γ' after specific heat treatments in PWA1480 [279]. In E. Cadel's doctoral thesis [280], an analysis conducted on the Nickel based superalloy N18 (Astroloy) reported the presence of such secondary γ precipitates, addressing them as θ-type clusters, characterized by no order signature, and lower field evaporation compared to the γ' phase in APT analysis, that locally modify the lattice parameter.

For our THz-APT study, we chose to analyze the nickel–based *NS8* superalloy, previously introduced in section 2.5.2. As a reminder, NS8 is a Ni-based superalloy derived from the N18/Astroloy family but formulated *without* B or Zr. Its nominal chemistry is Ni-rich ($\sim$53 at.%) with substantial Cr, Co, Al, Ti and Mo (plus controlled ppm-level C, S, O). In addition to the γ/γ' contrast, NS8 exhibits the presence θ-type nano-scale clusters within γ' phase precipitates.

For quantitative comparison, the reference values we use are reported from E. Cadel's doctoral thesis [280]: (i) the nominal NS8 composition (Table 5.1) and (ii) the phase compositions of γ and γ' measured by 1D APT (table 5.2). The standard deviations on the composition values are calculated according to the relation (2.6). These tabulated values serve as the reference bands against which we compare our THz–APT datasets. E. Cadel [280] does *not* report, in his thesis, the study of a region containing such θ clusters for NS8.

	Ni	Cr	Al	Ti	Mo	Co	C	S	O
at. %	53.3	15.7	8.239	4.41	2.78	15.47		—	
ppm							920	20	78

Table 5.1: Nominal composition of the NS8 superalloy [280].

For **spectral analysis**, we quantify the mass resolving power as $M/\Delta M$ at 10 % of peak height (we choose by default the peak of Ni^{2+} at 29 Da) and the signal-to-noise ratio (SNR) as the

	Ni (at.%)	Cr (at.%)	Al (at.%)	Ti (at.%)	Mo (at.%)	Co (at.%)	C (at.%)
γ phase (39 333 ions)	36.75	30.23	2.22	0.46	6.03	24.32	0.00
$\pm 2\sigma$	0.49	0.46	0.15	0.07	0.24	0.43	0.01
γ' phase (41 885 ions)	67.23	2.05	12.97	8.54	1.56	7.65	0.00
$\pm 2\sigma$	0.46	0.14	0.33	0.27	0.12	0.26	0.00

Table 5.2: Phase compositions (at.%) with standard de*via*tion $\pm 2\sigma$ of γ and γ' phases in NS8 for 1D APT analysis in electric mode, as presented in [280]. Note that results are indicative, given the limited statistics for both phases.

difference between the maximum intensity of the highest peak and the average background level measured in a nearby, line-free m/n window. When comparing spectra across modes, intensities are normalized to a common reference peak. The Ni^{2+}/Ni^{+} charge-state ratio is always reported as a near tip field estimation.

In the case of **3D reconstruction**, we conducted our analyses employing the automatic detection rate mode. The voltage curves displayed consistent smoothness, enabling us to always select the E_β reconstruction method across all analyses, as this method relies on the progression of the voltage. The precision of volume reconstruction scaling was confirmed by detecting crystallographic poles within the detector hit maps and calculating interplanar spacings using plane-counting profiles. The reconstruction scale was verified by exploiting known lattice parameters and spacings in crystalline areas, where poles could be discerned.

For **compositional analysis**, we report elemental atomic percentages for Ni, Cr, Al, Ti, Mo, Co, using regions of interest (ROIs) defined in the γ matrix phase with γ' phase precipitate regions, and occasional θ-type nodes/clusters.

In order to evaluate the quality of THz performances, comparative analyses were carried out using the same material on the CAMECA LEAP 5000XS, an instrument which has the same flight path geometry of the THz-assisted setup, both in laser pulsing mode (al λ=355 nm) and in voltage pulsing mode, under controlled and matched experimental conditions.

In the following, we present THz-assisted APT analyses using both positive- and negative-polarity pulses and assess them against IR/UV laser pulsing and high-voltage (electrical) pulsing, thereby covering the main evaporation modes for this material.

5.2 High repetition rate Tera-SAT - analysis of the γ phase region

5.2.1 Negative THz pulses vs IR-assisted analyses

The goal of this experiment is to compare **THz (negative polarity)** with **IR** ($\lambda = 1030\,\text{nm}$) under matched detection–rate conditions. The tip was prepared in Plasma-FIB with a radius below 30 nm. The acquisition workflow is summarized in Fig. 5.1, where it is possible to appreciate the evolution in voltage curve and detection rate accompanied by a mass history diagram.

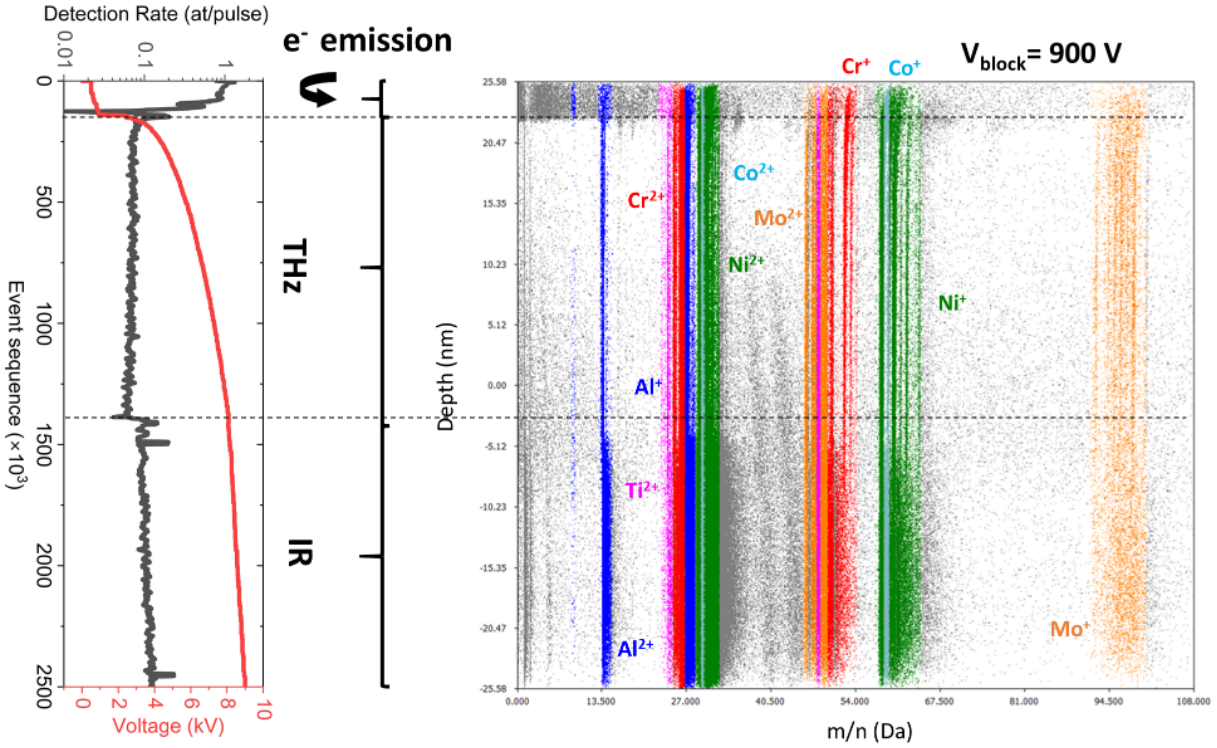

Figure 5.1: THz negative pulses vs IR analyses: a THz–negative segment followed by IR on the *same* NS8 tip, separated by a dashed black line. Left: detection rate (gray) and V_{DC} (red). Right: mass–history map with main species labeled. The stopping voltage for electron emission is $V_{stop} = 900$ V.

After an initial beam alignment onto the tip apex, the static bias was raised to ∼0.9 kV to suppress electron emission (see section 4.1.3 for details about the stopping voltage); the run then proceeded in *THz negative* polarity with the instrument in automatic rate control at ∼0.07 at/pulse. After collecting about $\sim 1.35 \times 10^6$ events, illumination was switched to IR. The IR pulse energy was adjusted in order to maintain a comparable flux (∼0.10 at/pulse). The THz → IR transition is visible in the mass–history panel of, as a broadened point distribu-

tion with less sharply resolved bands, consistent with increased thermal contributions under IR illumination.

The overlaid mass spectra for the two segments are shown in Fig. 5.2(a). Spectra are normalized to $^{59}Co^{2+}$, the main peak, and plotted on a logarithmic scale. THz-negative pulsing yields sharper peaks, a lower baseline, and reduced thermal tails, which minimizes overlaps and enables easier range selection. In contrast, the IR spectrum exhibits broader thermal tails with extensive peak overlap that prevents reliable deconvolution of neighboring species. The prominence of $^{52}Cr^{2+}$ (∼26 Da) and $^{59}Co^{2+}$ (∼29.5 Da) in both spectra indicates that this dataset samples predominantly the γ matrix (high Cr and Co, low Ti and Al concentrations). The charge–state ratio CSR = Ni^{2+}/Ni^{+} is ≈ 5.48 for THz negative polarity. For IR, a precise CSR cannot be extracted because the $^{58,60,62,64}Ni^{2+}$ peaks are blended by thermal tails; nevertheless, given the comparable flux and V_{DC} at the THz → IR transition and the stronger thermal effects under IR, the effective field (and thus CSR) is expected to be comparable or, most probably lower than in the THz case.

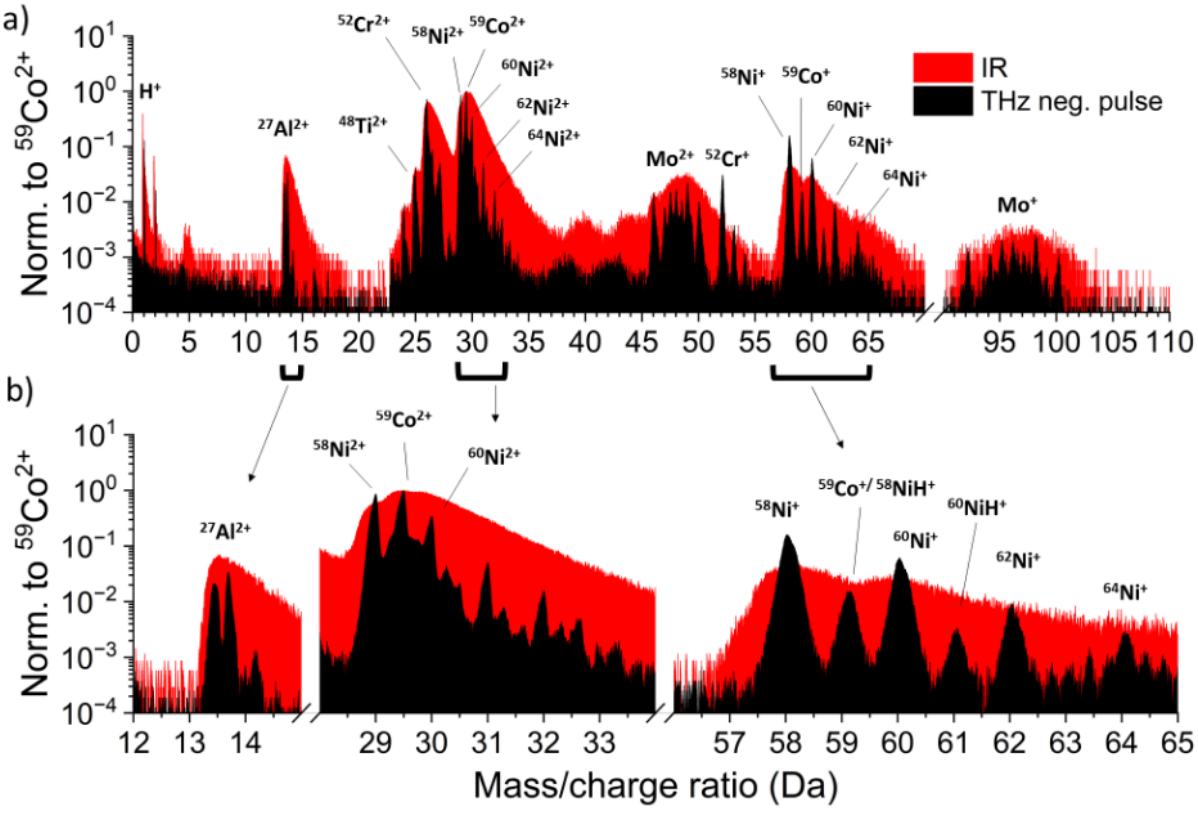

Figure 5.2: Mass–spectral comparison in the γ matrix, THz–negative (black) vs IR (red), normalized to $^{59}Co^{2+}$. (a) Full range on a log scale. (b) Zooms around Al^{2+}, Ni^{2+}, and Ni^{+} regions.

Fig. 5.2(b) zooms around three windows (Al^{2+}, Ni^{2+}, Ni^{+}). Under THz negative polarity, *lighter* ions exhibit a *double-peak* structure (most evident for Al^{2+}), whereas *heavier* species show a weaker splitting. This behavior is consistent with the single-cycle THz negative polarity waveform (see 2.10(c)): the negative half-cycle presents two local maxima separated in time by a minimum, so ions emitted near each maximum emerge at two distinct instants and experience a different acceleration by the THz pulse. The larger responsiveness (shorter inertia) of lighter ions accentuates the temporal separation and produces two resolvable peaks; heavier ions react more slowly, leading to a smaller energy/time spread and therefore a less pronounced or unresolved peak separation.

	Ni (at.% $\pm 2\sigma$)	Cr (at.% $\pm 2\sigma$)	Al (at.% $\pm 2\sigma$)	Ti (at.% $\pm 2\sigma$)	Mo (at.% $\pm 2\sigma$)	Co (at.% $\pm 2\sigma$)
γ **phase** (1D APT [280]) (39 333 ions)	36.75 ± 0.49	30.23 ± 0.46	2.22 ± 0.15	0.46 ± 0.07	6.03 ± 0.24	24.32 ± 0.43
γ **phase** (THz-neg.) (1 104 787 ions)	39.32 ± 0.09	29.55 ± 0.09	2.19 ± 0.03	0.33 ± 0.01	4.47 ± 0.04	24.14 ± 0.08

Table 5.3: NS8 γ-phase compositions with uncertainties shown as at.% $\pm 2\sigma$ comparing the data of [280] (1D APT) with this work's analysis (THz negative pulses).

The 3D reconstructions conducted using the E_β method (see Fig. 5.3) validate that both acquisition sections explore the identical γ-matrix area. As previously highlighted, due to significant overlaps and thermal tails, a raliable peak assignment in the IR segment is compromised. Thus, we present composition values exclusively for the THz-negative segment of the study, provided in table 5.3. These values are indicative of a Cr and Co-rich γ phase, with a reduction in Al and Ti, and they generally align with the γ-phase reference composition values found with 1D APT measurements, as shown in table 5.2. However, they exceed the typical de*via*tions of $\pm 2\sigma$ when assessed with Eq. (2.6). It is also significant that the dataset size for THz negative pulses is substantially larger compared to 1D APT.

5.2.2 Positive THz pulses - impact of THz beam energy variation

This section presents follow-up to the *THz-negative* pulses assisted analysis in the γ region (Sec. 5.2.1), now using *THz-positive* pulsing on a different NS8 tip from the one used for the previous analysis. After a prior run that removed $\sim 8 \times 10^6$ atoms, the tip was necessarily

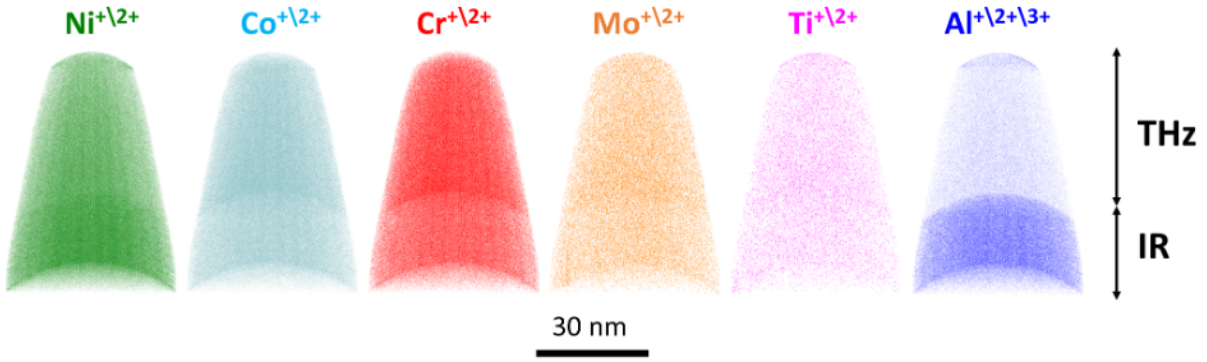

Figure 5.3: 3D reconstruction of the second dataset (E_{beta} reconstruction method, γ matrix). The THz→IR switch is visible as a change in point density/contrast.

operated at higher DC voltages (blunter apex), and the THz-energy series was acquired under near-constant detection-rate conditions. In this larger-volume experiment we systematically vary the THz pulse energy and quantify its impact on mass resolving power (MRP), signal-to-noise ratio (SNR), and the effective peak field estimated from the Ni^{2+}/Ni^{+} charge-state ratio (CSR); in parallel, we monitor how these spectral changes propagate to phase compositions in γ.

The acquisition timeline and experimental parameters for the THz-energy series are summarized in Fig. 5.4. Within a single run on the same NS8 tip, we varied the laser pump energy across three levels (120, 360, and 600 μJ), collecting several millions of events for each condition, while keeping the automatic detection-rate control active. As the THz energy was increased, the control loop reduced the DC voltage to maintain a nearly constant flux (around 0.06–0.07 at/pulse). The voltage trace and mass-history map mark the transition points clearly, and the background visibly decreases with increasing THz energy.

In Fig. 5.5, the overlaid mass spectra show that the signal–to–noise ratio increases from $\sim 10^3$ at 120 μJ to $\sim 10^4$ at 360 μJ and remains close to 10^4 at 600 μJ, whereas the mass resolving power, $M/\Delta M$ at 10% of the $^{58}Ni^{2+}$ peak (29 Da), decreases as the THz energy is raised. The corresponding values are listed in Table 5.4, showing that the analysis providing the best compromise in terms of both SNR and mass resolving power is the one performed at a laser energy of 360 μJ. This one is chosen to be compared afterwards (5.4) with LEAP analyses.

This SNR evolution follows the DC bias needed to keep a fixed detection rate: at low THz energy a higher V_{DC} is required, bringing the apex field nearer to the evaporation threshold and promoting inter-pulse evaporation that appears as elevated spectral background; at higher THz

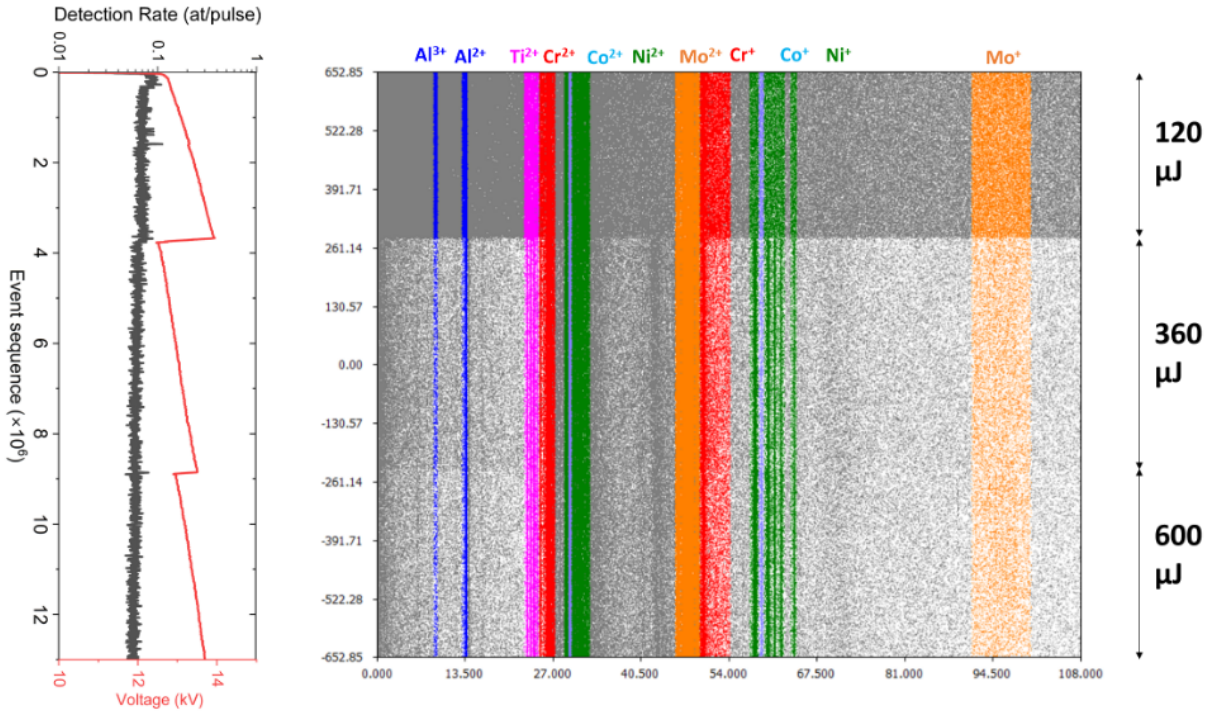

Figure 5.4: Acquisition history and operating traces for the laser pump energy energy-variation run (120, 360, 600 μJ at 100 kHz). Energy transitions are marked .

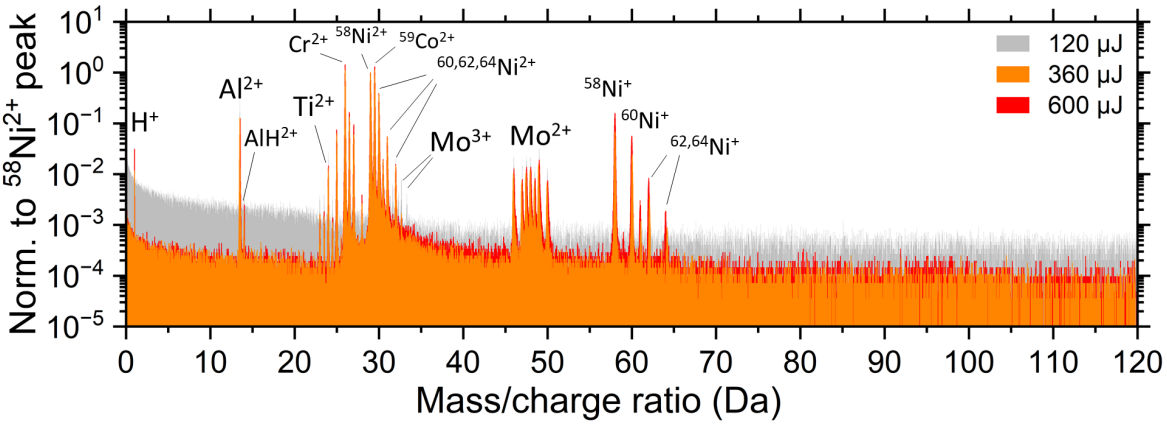

Figure 5.5: THz (positive) energy sweep in γ phase: overlaid mass spectra at 120 µJ, 360 µJ and 600 µJ (grey, orange, red), all normalized to the $^{58}Ni^{2+}$ peak and plotted on a logarithmic intensity scale. The main species are indicated for reference.

THz (+) energy per pulse	$M/\Delta M$ @ 10% (Ni^{2+}, 29 Da)	SNR
120 μJ	286.8	$\sim 10^3$
360 μJ	207.6	$\sim 10^4$
600 μJ	169.5	$\sim 10^4$

Table 5.4: Effect of positive THz pulse energy (100 kHz) on mass resolving power and SNR for NS8.

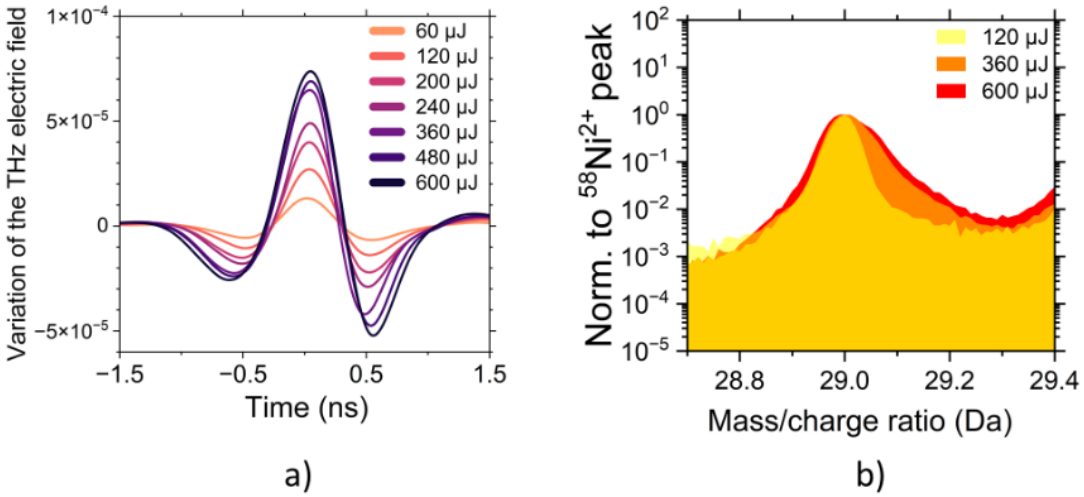

Figure 5.6: a) THz positive pulses amplitude variation with laser pump energy. b) Effect of energy dispersion induced by THz pulse amplitude on peak resolution (here $^{58}Ni^{2+}$) is shown for laser pump energies of 120, 360 and 600 μJ.

energy the required V_{DC} is reduced, evaporation is concentrated at the THz field maxima, the continuous (and thermal) component is suppressed, and the background drops.

A consistent explanation for the observed *decrease* in mass resolving power with growing THz amplitude is the increase of energy dispersion, as shown in Figs. 5.6(a,b). As the THz cycle amplitude rises, ions experience a larger variation of instantaneous accelerating field during their residence in the high-field region; this broadens their time–of–flight distribution and, for suitable waveform phases, can split emission into multiple emission instants separated in time. Both effects enlarge peak widths and reduce $M/\Delta M$. This peak broadening scaling with THz amplitude and the emergence of double features for appropriate polarity has been established numerically and experimentally in THz-driven field evaporation studies, which show (i) an approximately linear increase of $\Delta\mathrm{ToF}/\mathrm{ToF}_{\max}$ with THz amplitude for fixed V_{DC}, and (ii) bipolar waveforms (or negative pulses) producing two emission windows and hence double peaks with a separation that grows with THz cycle amplitude. These behaviors directly tie larger THz amplitudes to increased kinetic-energy spread and degraded resolving power [28].

For a direct spectral comparison of pulsing schemes (Fig. 5.7(a,b)), we extracted two γ-matrix ROIs: one from the present THz-positive run and one from the THz-negative run of Sec. 5.2.1. Both were acquired at a pump energy of 600 μJ, contain $\sim 1.2 \times 10^6$ ions, and were matched in operating field ($Ni^{2+}/Ni^{+} \approx 5$). The THz-negative spectrum exhibits the expected double-

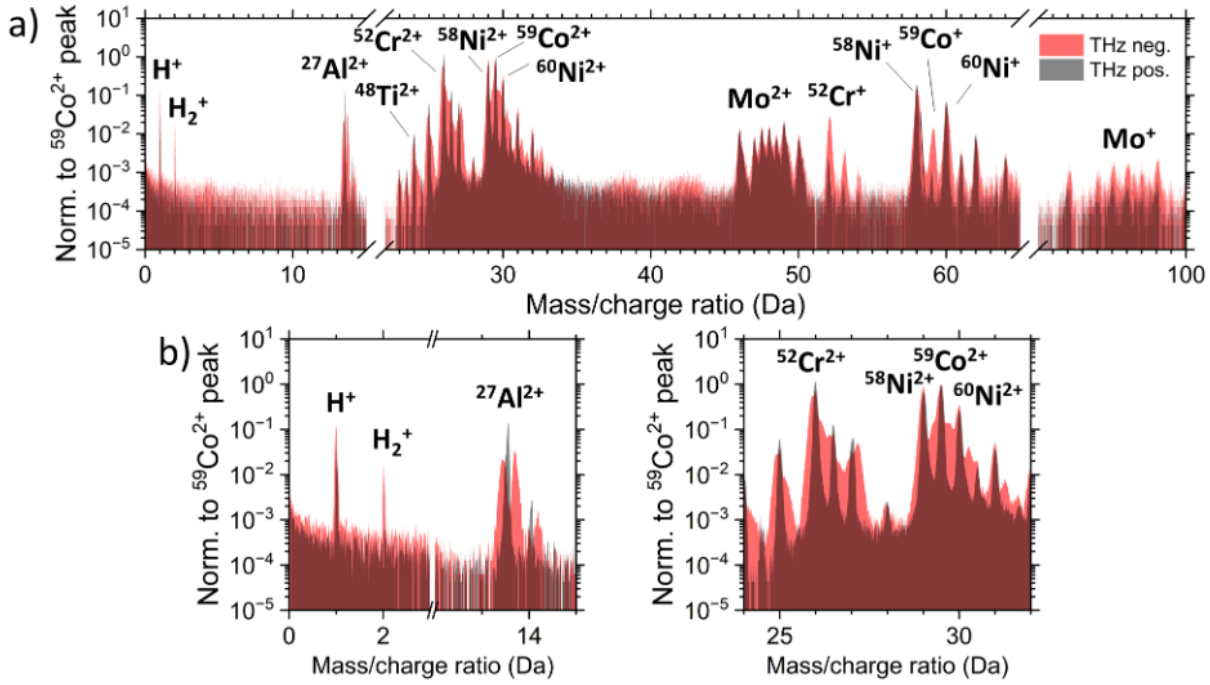

Figure 5.7: Overlaid mass spectra for γ-matrix. Both datasets count $1.2 \cdot 10^6$ events. a) THz-negative (red) vs THz-positive (black) (normalized to ^{59}Co2+ peak). b) Magnified x-axis ranges below: 0-15 and 24-32 Da.

window emission: clear double peaks for lighter species at low m/n, broadened ranges, and more ambiguous peak selection. In contrast, the THz-positive ROI shows single, narrower peaks, slightly higher SNR, and reduced H_2, yielding a higher effective resolving power and more robust peak assignment. The absence of double peaks under THz-positive pulsing, together with their presence under THz-negative pulsing, indicates that in this case the tip was positioned on the intended side of the Gouy-phase crossing. Consequently, quantitative composition derived from the THz-positive spectrum is less ambiguous and therefore more reliable than from the THz-negative case. Table 5.5 presents a summary and comparison of the derived compositions.

	Ni (at.% $\pm 2\sigma$)	Cr (at.% $\pm 2\sigma$)	Al (at.% $\pm 2\sigma$)	Ti (at.% $\pm 2\sigma$)	Mo (at.% $\pm 2\sigma$)	Co (at.% $\pm 2\sigma$)
γ **phase** THz **pos.** pulses (2 467 127 ions)	39.43 ± 0.06	27.23 ± 0.06	3.82 ± 0.02	0.42 ± 0.01	5.10 ± 0.03	24.00 ± 0.05
γ **phase** THz **neg.** pulses (1 104 787 ions)	39.32 ± 0.09	29.55 ± 0.09	2.19 ± 0.03	0.33 ± 0.01	4.47 ± 0.04	24.14 ± 0.08

Table 5.5: NS8 γ-phase compositions (at.% $\pm 2\sigma$) comparing THz *positive* and THz *negative* pulsing conditions.

5.3 High repetition rate Tera-SAT - analyses of the γ' phase and θ-type clusters region

The analyses in this section were carried out on two distinct tips from the same NS8 material, prepared with the same PFIB protocol and exhibiting similar apex radii (< 30 nm). Nevertheless, local geometric differences and alignment conditions can vary: in particular, the two tips may not have been positioned at the same location relative to the THz beam focus/waist, which could influence the effective waveform and evaporation response. Here we present two analyses:

- **Analysis 1 — THz$^-$ → IR in γ' phase:** a run conducted with *THz negative* pulses that, at the end, is switched to *IR* ($\lambda = 1030$ nm) for a direct comparison. The probed volume lies in the ordered, crystalline γ' phase and is particularly interesting to test because it contains nanoscale θ–type (Cr/Co–rich) clusters.
- **Analysis 2 — THz$^+$ in γ' phase:** a second run, on a different tip, under *THz positive* pulses, that happens to sample again the γ' matrix, collecting a large volume containing again θ–type clusters. An evaluation will be presented, drawing comparisons with analysis 1 in relation to mass spectrum, 3D reconstruction, and composition.

5.3.1 Analysis 1: THz$^-$ and IR-assisted APT in γ' phase with θ-type clusters

All data in this section originate from a single run acquired on the same NS8 tip at 100 kHz. The THz-assisted analysis was conducted using the negative polarity and a total of $\sim 4.7 \times 10^6$ ions were collected. Fig. 5.8 shows the voltage and the detection rate curves evolution (left) together with the mass history diagram (right), where the THz-negative pulses were used for Regions 1–2 and IR pulses for Region 3. We first determined the blocking voltage V_{stop} and for this tip a value $V_{\text{stop}} = 880$ V was found.

The mass history diagram in Fig. 5.8 for Regions 1–2 does not show major differences in the transition between Region 1 and 2. However, in Region 1 we operated in automatic detection rate mode at a flux of 0.02 at./pulse, adjusting the DC level to keep the rate within the target window. Between Regions 1 and 2 a small drop in voltage appears. This corresponds to an overnight stop and restart: upon re-enabling the THz beam the first seconds tend to be slightly more intense before stabilizing, so the automatic detection rate loop briefly reduces the DC

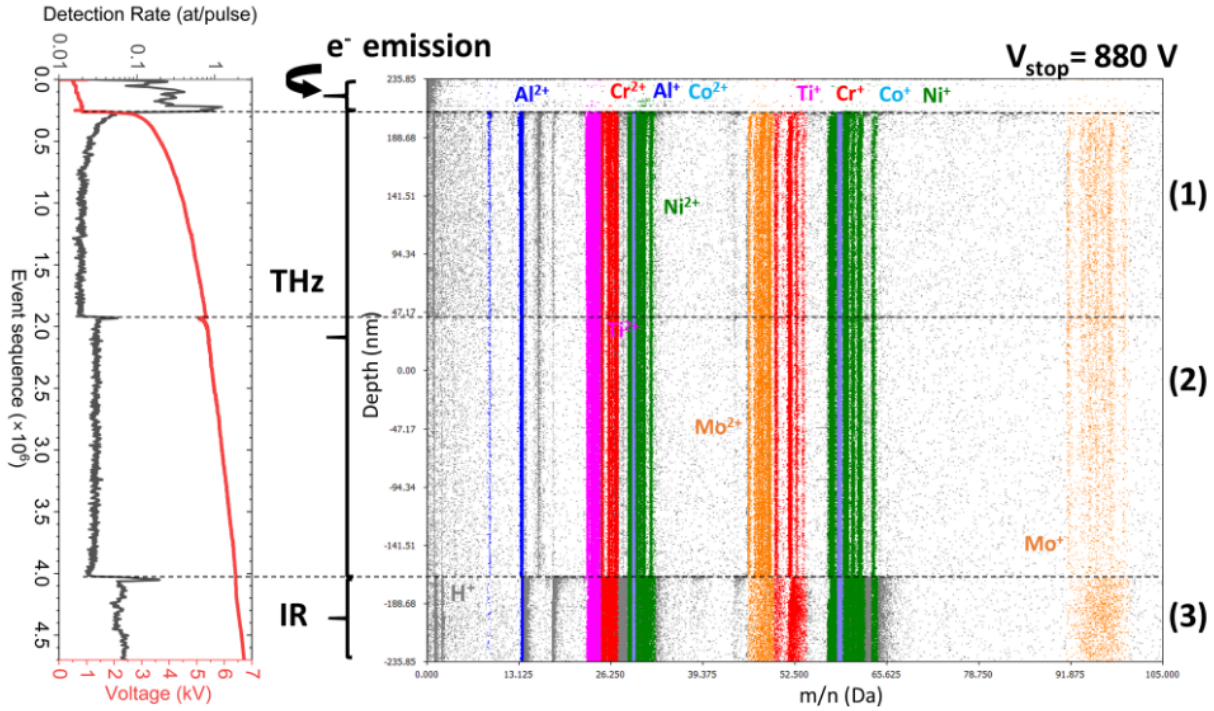

Figure 5.8: THz-negative and IR (λ=1030 nm) run on NS8 sample. Left) Detection rate (black curve) and voltage (red curve) evolution; right) mass-history map. The dataset counts ($\sim 4.7 \times 10^6$ events), divided into Regions 1-2 (analyzed with THz negative pulses) and 3 (analyzed with IR pulses), delimited by dashed black lines.

voltage and then raises it again as the source settles. In Region 2 we stabilized the analysis at a flux of 0.03 at./pulse and collected additional $\sim 1.8 \times 10^6$ atoms. In Region 3, the transition to IR pulsing is noticeable: in the detection rate curve we notice an initial burst at the moment of the switch, which then comes back to a stable constant value, slightly higher than the one with THz analysis (now 0.05 at/pulse), as the laser energy has been tuned to try to obtain a similar flux. This change complicates the ability to differentiate between the various peaks in the diagram, in contrast to the higher clarity achieved under THz negative pulsing.

For a direct spectral comparison, we extracted 5.5×10^5 events from **Region 2** (THz, negative polarity) and **Region 3** (IR), acquired in similar flux conditions and V_{DC}, and overlaid the spectra normalized to $^{58}Ni^+$ (Fig. 5.9(a)). Under THz excitation the charge–state ratio CSR = $Ni^{2+}/Ni^+ = 4.45$ is larger; as for the previous analysis, for IR analysis a reliable CSR cannot be extracted because thermal tails broaden peaks and induce overlaps that contaminate the $^{58}Ni^+$ window. Even so, with the same normalization, the $^{58}Ni^{2+}$ peak is clearly higher for THz, indicating a higher effective near–apex field. As a result, THz yields sharper, better–separated

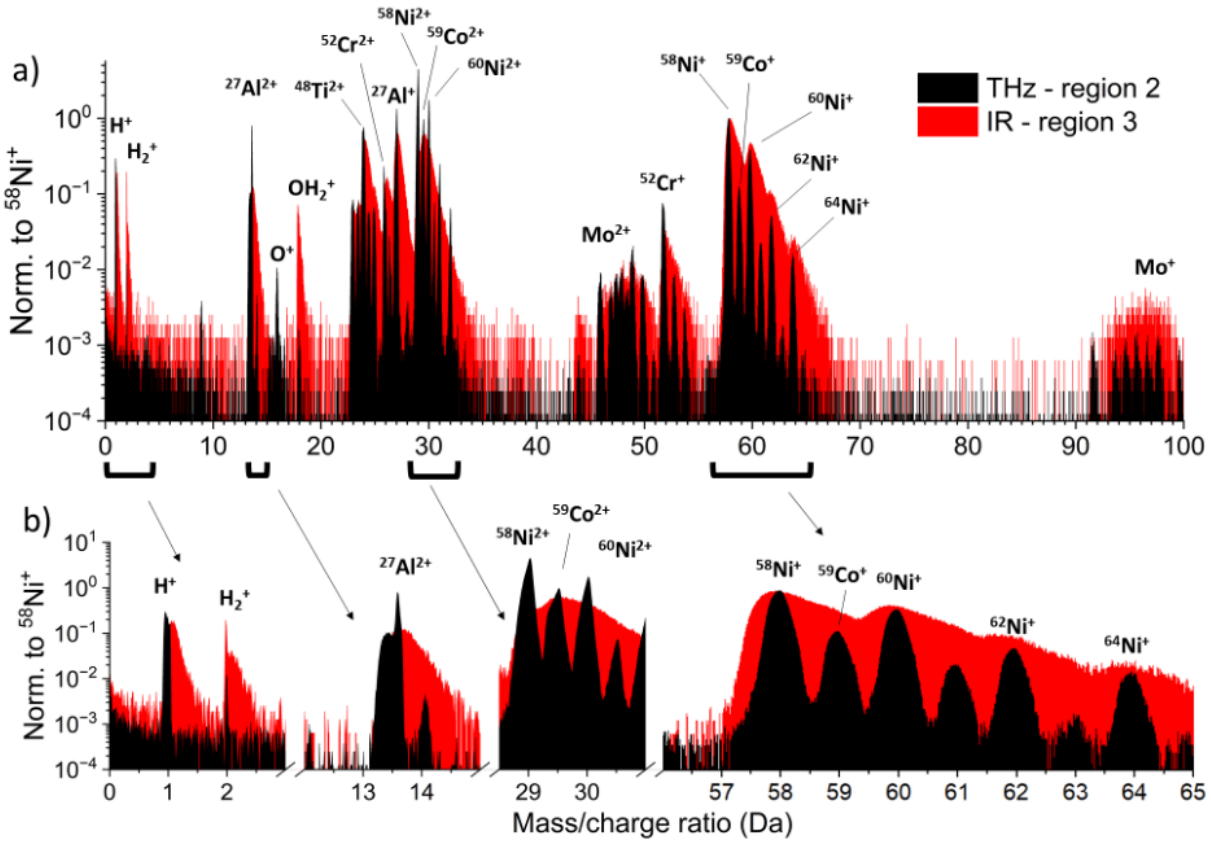

Figure 5.9: (a) Mass-spectra comparison for the γ' phase. positive THz pulse analysis of region 2 (black) vs IR analysis of region 3 (red), both counting $\approx 5.5 \times 10^5$ events. b) Magnification of the ranges delimited by black brackets in a).

peaks with lower background, which simplifies peak ranging for composition calculations. These trends are highlighted in the zoomed windows of Fig. 5.9(b). The presence of prominent $Al^{+/2+}$ and Ti^{2+} suggests peaks that the analyzed volume is a γ' phase. For the THz–negative analysis, as for the previous THz–negative analysis of the γ phase region (5.2.1), overlapping double peaks are observed, most pronounced for lighter m/n species (*e.g.*, Al^{2+}) and scarcely visible for heavier ions, such as the group beyond Ni^{+}.

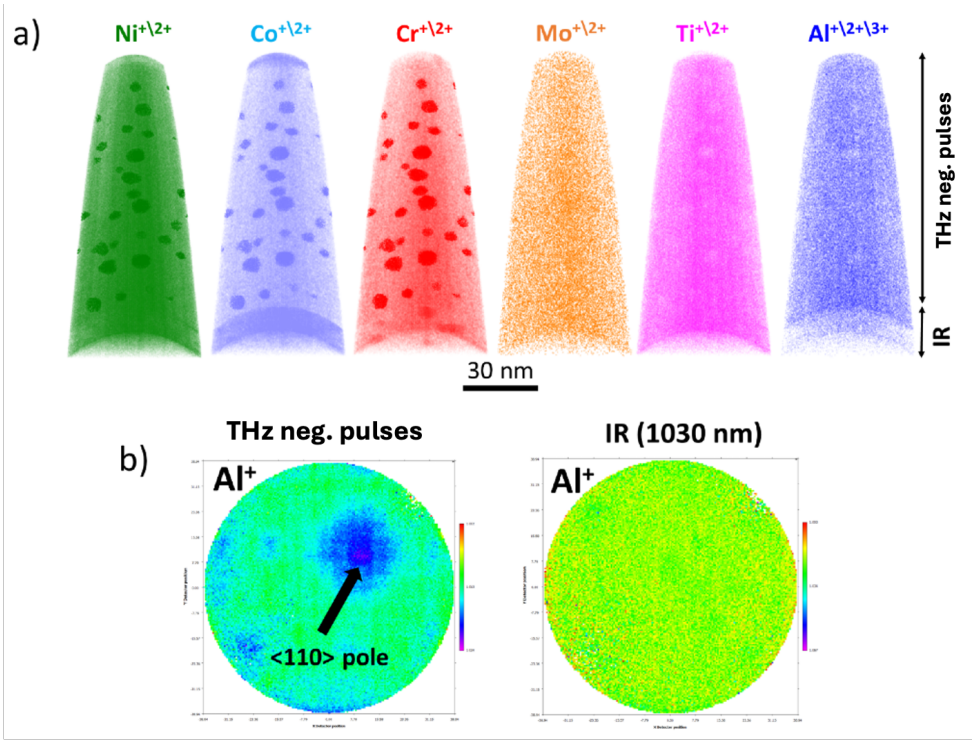

Figure 5.10: (a) Three–dimensional reconstruction of the acquisition with THz (negative polarity) followed by IR ($\sim 4.7 \times 10^6$ detected ions). The volume is colour–segmented by species (Ni, Co, Cr, Mo, Ti, Al); θ–type clustering was quantified for Cr, Co, and Ni. The transition from THz^{+} to IR is marked and visible as a loss of contrast and poorer or no cluster definition. (b) Two–dimensional detector hit–density maps for Al^{+}, under THz negative polarity (left) a clear crystallographic feature is resolved ($\langle 110 \rangle$ pole), whereas the IR map (right) shows no crystallographic signature.

The element–separated 3D reconstructions are shown in Fig. 5.10(a). Clear clusters are visible for **Cr**, **Co** and **Ni**; the enriched regions, present in Ni, Co and Cr volumes are highlighted after clustering to aid visualization. Conversely, **Ti** and **Al** exhibit local density deficits at the cluster sites, consistent with θ–type chemistry (closer to the γ matrix and therefore poorer in Al and Ti). A distinct change of contrast appears at the THz $\rightarrow$ IR switch: under IR the clusters are no longer well resolved, which we attribute to stronger thermally driven broadening that degrades spatial resolution, in constrast with its preservation under THz illumination. Figure 5.10(b)

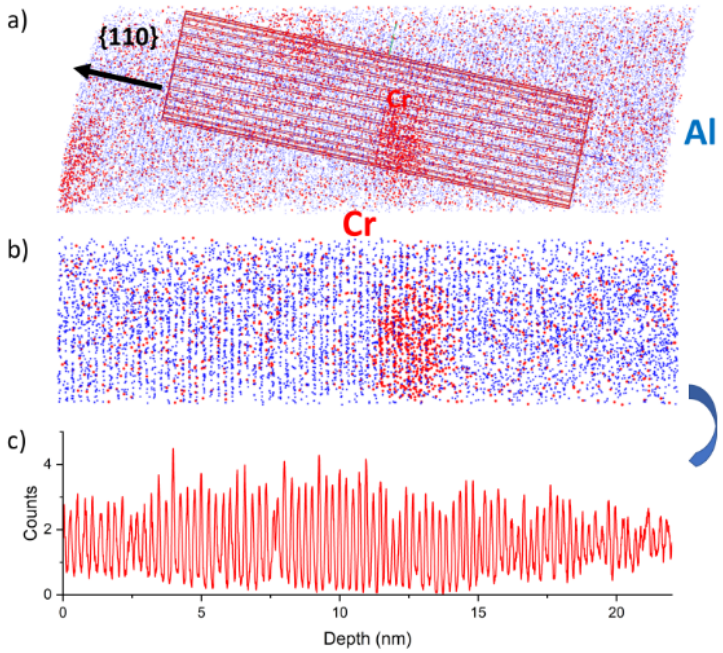

Figure 5.11: a) Cylindric 3D selection for the $< 110 >$ pole region gives evidence of crystallographic planes for Al. The magnification b) showing planes seperation and a detail on a Cr-enriched theta cluster, is c) profiled over depth to have a measure of the average interplanar space.

reports 2D detector hit maps for Al^+: with *THz negative* pulses a signature of the $\langle 110 \rangle$ pole is observed, whereas none is discernible in the IR-related hit-map.

Based on these findings, a 3D selection was made in the volume enclosing the Al pole visible in Fig. 5.10(b) in order to reveal lattice planes (Fig. 5.11(a); although shown for Al, analogous planes are also visible for Ni and Ti. A sub-selection normal to the planes (Fig. 5.11(b)) enables profiling of the regularity of the interplanar spacing for Al, as reported in Fig. 5.11(c), whose order is kept even in the region occupied by the θ cluster enriched in Cr. Using the theoretical ordered FCC structure of γ' (Ni_3Al, $a = 3.56$ Å), the expected spacing is $d_{110} = a/\sqrt{2} \approx 2.52$ Å. Guided by this value, we set the reconstruction *via* the E_β method in 3DGPM and verified that the peak-to-peak distance in the plane-counting profile along the pole is consistent with d_{110}, validating both reconstruction parameters and absolute scale.

Moreover, this analysis consents to assess how effectively THz pulses, compared to IR pulses, resolve θ clusters' species enrichment. For this purpose, cluster computation employed both the *iso-position* method and the *atomic-distance* approach, as detailed in Section 1.3. Specifically, we compared composition histograms from the *real* data with those from a randomized distribution of identical counts; the high-composition tail that departs from the random baseline (red in

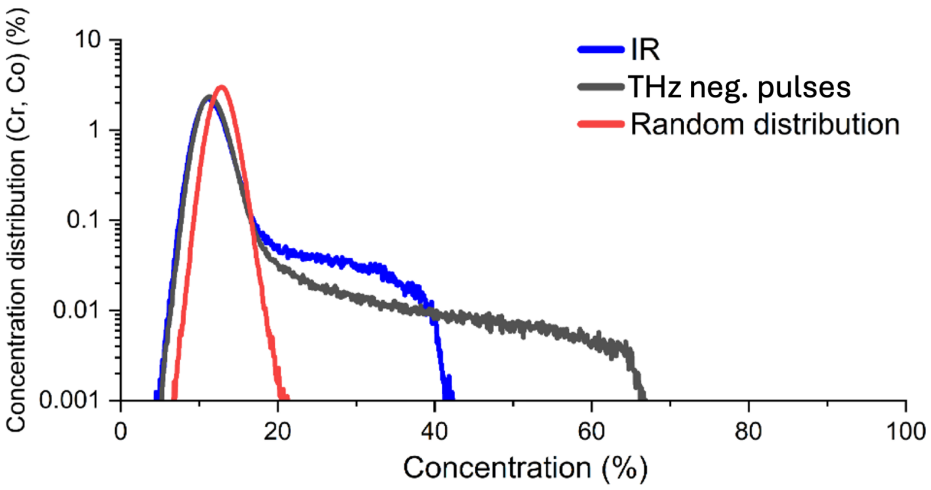

Figure 5.12: Clustering composition distributions for THz negative pulse and IR analyses. The tails in the real-data curve (blue) shows a more pronounced asymmetry in the case of THz-neg. pulses (black curve) with respect to the randomized baseline (red curve) than in the case of IR pulses (blue curve).

Fig. 5.12) defines the clustering threshold. Because θ clusters in this alloy are predominantly enriched in Cr and Co, the calculation was carried out considering these two species, using the real–vs–random divergence to set the cut-off and avoid over-counting random fluctuations. The outcomes are shown in Fig. 5.12, where THz and IR regions were chosen to have similar total Cr+Co content (as indicated by the random distribution, same for both THz and IR analyses). THz pulses allow to resolve Cr+Co enrichments up to $\sim$ 66%, whereas IR detects combined enrichment only up to $\sim$ 42%. This demonstrates that THz pulsing provides superior spatial and chemical resolution of nanometric features relative to IR.

Concerning compositional analysis, as in the previous section we do not report compositions for the IR–pulsed part of the run because peak-range assignment (and in some cases peak identification) is unreliable under the extensive overlaps produced by thermal tails. We therefore restrict compositional reporting to the THz–negative segment and compare them to the reference 1D APT datasets [280]. After performing the clustering procedure, we separated the ions from the surrounding γ' matrix ($\sim 3.5 \times 10^6$ events) from those belonging to the clusters only ($\sim 1.0 \times 10^5$ events) and evaluated their compositions independently. The resulting values are summarized in Table 5.6. Because E. Cadel's dataset [280] and ours differ significantly in statistics, the comparison is qualitative; nonetheless, the trends are consistent, with the THz analysis yielding a γ' matrix that shows relatively higher Ti and Co (and lower Cr) than the 1D-APT reference. The θ clusters, in contrast, are enriched in Cr and Co, depleted in Ni relative to

the surrounding γ', and contain lower Ti and Al. We emphasize that the quantitative accuracy of these values remains sensitive to peak-range definition and, consequently, to the degree of spectral overlap.

	Ni (at.% $\pm 2\sigma$)	Cr (at.% $\pm 2\sigma$)	Al (at.% $\pm 2\sigma$)	Ti (at.% $\pm 2\sigma$)	Mo (at.% $\pm 2\sigma$)	Co (at.% $\pm 2\sigma$)
γ' phase (1D APT [280]) (41 885 ions)	67.23±0.46	2.05 ± 0.14	12.97±0.33	8.54 ± 0.27	1.56 ± 0.12	7.65 ± 0.26
γ' phase (THz neg.) (3 499 853 ions)	62.06±0.05	2.49 ± 0.02	12.71±0.04	12.18±0.04	0.98 ± 0.01	9.58 ± 0.03
θ clusters (THz neg.) (99 036 ions)	38.25±0.31	25.36±0.28	4.82 ± 0.14	3.32 ± 0.11	1.90 ± 0.09	26.35±0.28

Table 5.6: NS8 compositions (at.% $\pm 2\sigma$) rounded to two decimals. First row: γ' phase from Cadel [280]. Second row: γ' phase measured in this work under THz negative pulsing. Third row: composition of θ–type clusters from this work.

5.3.2 Analysis 2: THz$^+$-assisted APT in γ' phase with θ-type clusters

As stated at the beginning, this analysis was carried out on a separate tip and on a different day, meaning the THz pulse conditions should not be assumed to match those of the previous analysis.

We first carried out a long acquisition with THz-positive pulses on NS8, whose evolution is shown in Fig 5.13, reaching $\sim$5.8 M events at a constant detection rate of 0.03 at/pulse. The blocking voltage was $V_{\text{block}} = 330$ V, consistent with a less pronounced negative minimum in the positive-polarity THz waveform (reduced energy for the emitted electrons). The voltage trace is smooth, with no signatures of fractures or instabilities, indicating that THz-positive pulsing can evaporate this alloy while preserving tip integrity. Similarly to the previous analysis done with THz negative pulses, here we sampled the γ' phase as well.

To compare the performance of THz negative and positive pulses on NS8, Fig. 5.14(a) shows the corresponding spectra, each normalized to the Ni^{2+} peak and matched in statistics ($\sim 3.74 \times 10^6$ events). The operating fields differ slightly: the charge–state ratio (CSR) is $Ni^{2+}/Ni^{+} = 4.45$ for THz negative and ~ 2 for THz positive. Overall, the SNR is higher under THz negative pulsing. The magnified windows in Fig. 5.14(b) reveal a double–peak structure for both polarities, more

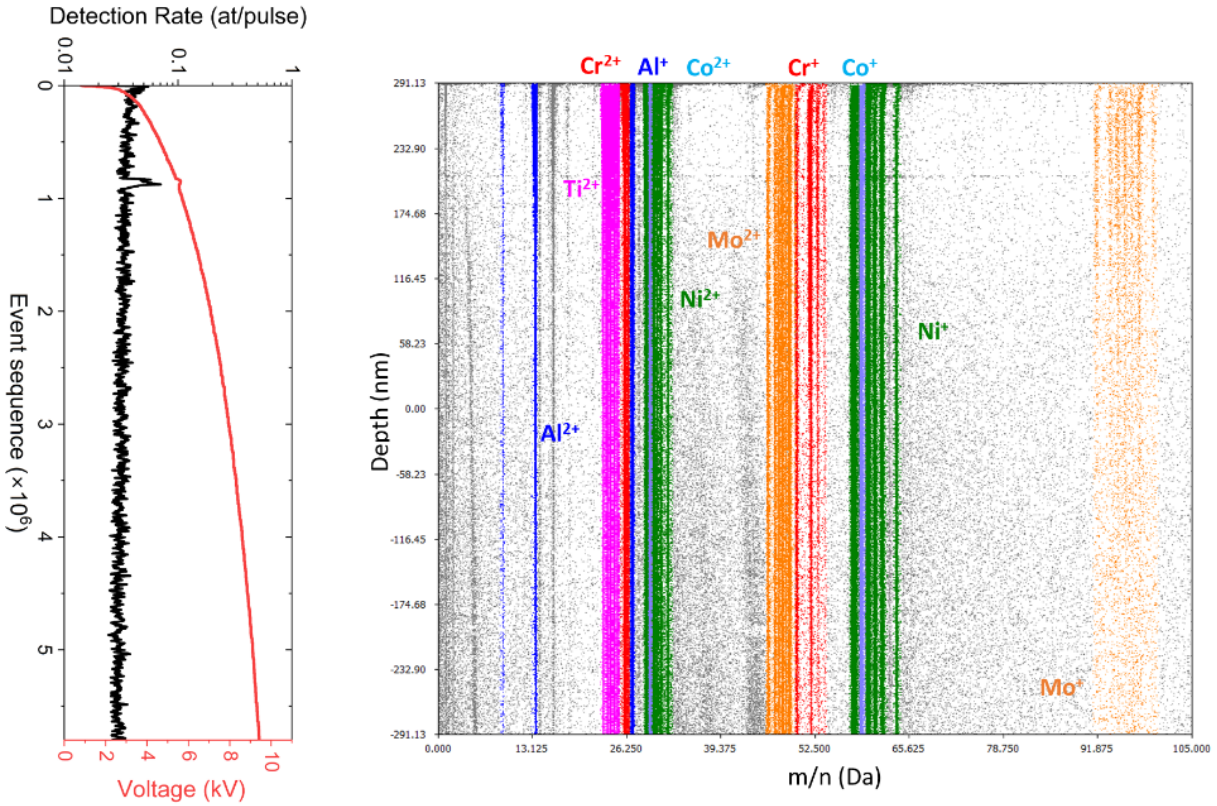

Figure 5.13: Acquisition workflow for the first study: THz-positive long run: 5.8M dataset, voltage curve and mass history.

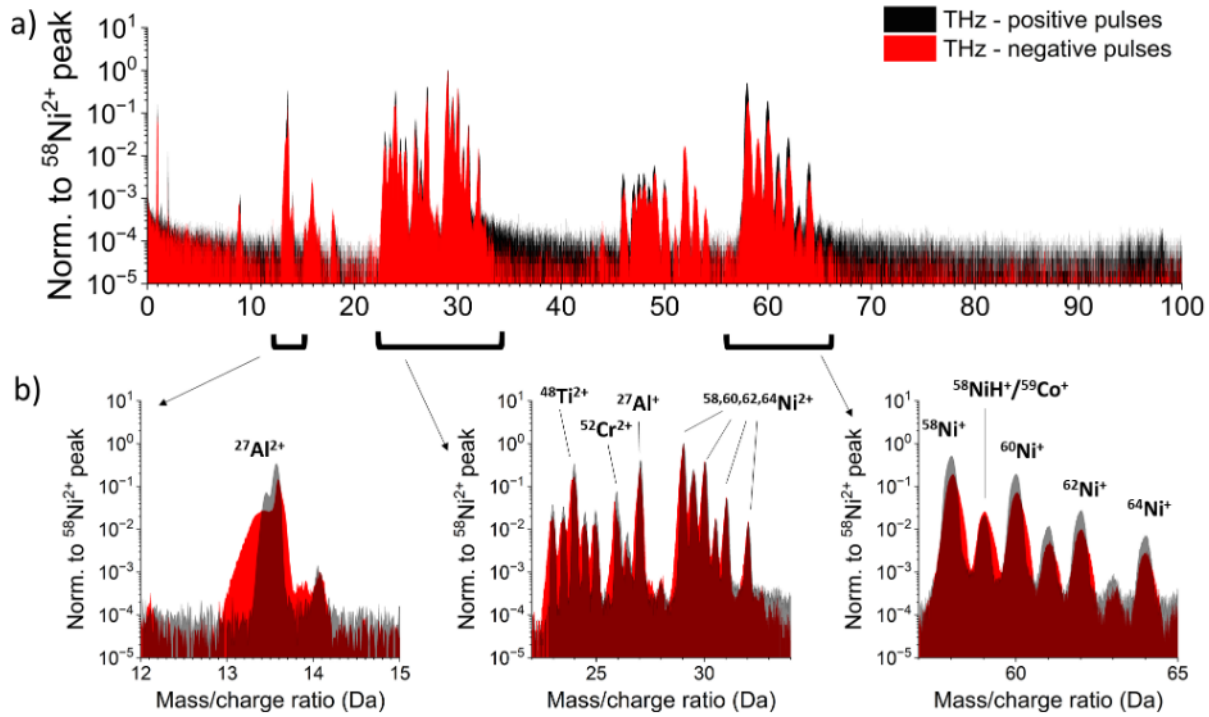

Figure 5.14: (a) Mass-spectra comparison for the γ' phase. positive THz pulse analysis (black) vs negative THz pulse analysis (red), both counting $\approx 3.74 \times 10^6$ events. (b) Magnification of the ranges delimited by black brackets in a).

pronounced at lower m/n. For the $^{58}Ni^{2+}$ peak, the mass resolving power at 10% height is 95 (THz negative) versus 100 (THz positive)—a marginal difference. In practice, the two spectra are strikingly similar.

A plausible reason for this similarity is that the datasets were acquired on different tips, likely at slightly different axial positions relative to the THz focus, so the local waveform experienced at the apex could have been comparably "intermediate" in shape despite the nominal polarity.

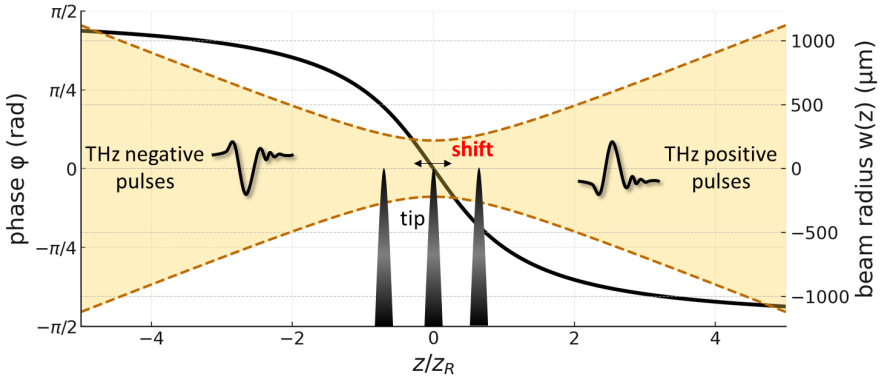

Figure 5.15: Apex polarity vs. axial position in a focused THz beam. The black curve is the Gouy phase $\phi_{Gouy} = -\arctan(z/z_R)$; the yellow wedge indicates the beam radius $w(z)$. Small axial shifts of the tip near $z = 0$ can flip the effective pulse polarity (negative on the left, positive on the right), whereas motions far from the phase crossing leave the polarity unchanged. The figure is inspired by [281].

In the schematic in Fig. 5.15 we depict the tip immersed in the THz beam and translated vertically along the optical axis z. Because the waveform at the apex follows the Gouy–phase evolution, a small displacement near the phase–inversion region can flip the effective polarity from "negative" to "positive" THz pulses. With $w_0 = 0.220$ mm and $\lambda_{\mathrm{THz}} = 300$ μm, the Rayleigh range is $z_R = \pi w_0^2/\lambda \simeq 507$ μm. Thus, when the tip is well inside either side of the phase curve, the usual repositioning performed in the APT chamber (usually the shift is less than 50 μm around the position that maximizes the detection rate) does not change the polarity. However, if the tip lies close to the phase crossing, even a small z-shift can place it in a region where the THz waveform changes appreciably. This provides a plausible reason why spectra recorded nominally under negative and positive THz pulses may appear similar: different tips were reinserted and realigned between runs, so a tip could inadvertently be positioned where the local waveform is intermediate (more bipolar) between the two polarities. Such an intermediate drive can yield the observed double–peak features, though with smaller splitting than the clearer separation observed for the γ-phase THz analysis in Section 5.2.1.

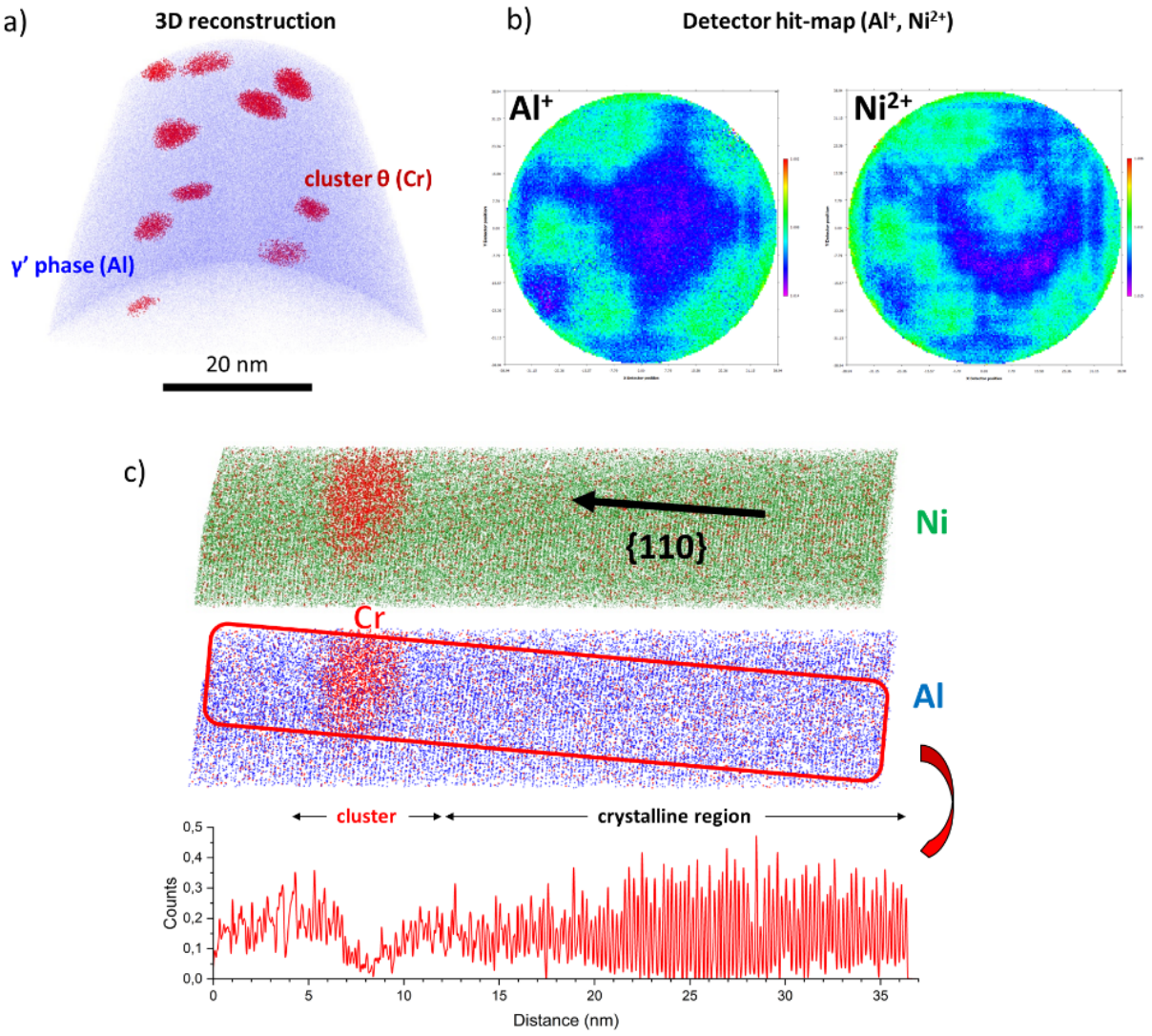

Figure 5.16: (a) Reconstruction from the THz-positive long run showing a γ' precipitate with embedded θ clusters. (b) Detector hit-map for Al^+ species. (c) Cylindric 3D selection for the $< 110 >$ pole region gives evidence of crystallographic planes for Ni and Al, profiled over depth to have a measure of the average interplanar space.

The reconstruction in Fig. 5.16(a) shows a γ' precipitate containing θ clusters homogeneously distributed throughout the volume. Al^{1+} and Ni^{2+} hit-maps—computed with the same threshold used for the THz–negative dataset—exhibit a pronounced crystallographic pole (Fig. 5.16(b)). By symmetry it seems consistent with $\langle 110 \rangle$, although the absence of clearly identifiable neighboring poles prevents a definitive assignment. A vertical slice through this pole resolves atomic planes, as shown in fig. 5.16(c). For ordered FCC γ' (Ni_3Al, $a = 3.56$ Å), the expected interplanar spacing is $d_{110} = a/\sqrt{2} \approx 2.52$ Å. We used this reference to refine the reconstruction using the E_β technique within 3DGPM and corroborated through plane counting that the peak-to-peak distance along the pole matches d_{110}, thus validating both the reconstruction parameters and the absolute scale.

Finally, we compare the compositions obtained under the two THz polarities (Table 5.7); the event statistics are of the same order, so the comparison is meaningful, and the values are broadly consistent, as THz-positive pulsing reproduces the concentration trends observed with THz-negative pulsing for both the γ' matrix and the θ clusters, though several entries still fall outside the quoted 2σ intervals, a divergence that is plausibly explained by analysis choices in the clustering workflow (*e.g.*, the degree of cluster "erosion" applied to exclude interfacial matrix atoms), which can shift the measured compositions by emphasizing core vs. boundary contributions.

	Ni (at.% $\pm 2\sigma$)	Cr (at.% $\pm 2\sigma$)	Al (at.% $\pm 2\sigma$)	Ti (at.% $\pm 2\sigma$)	Mo (at.% $\pm 2\sigma$)	Co (at.% $\pm 2\sigma$)
γ' **phase** — THz **neg.** (3 499 853 ions)	62.06 ± 0.05	2.49±0.02	12.71 ± 0.04	12.18 ± 0.04	0.98±0.01	9.58±0.03
γ' **phase** — THz **pos.** ((3 597 671 ions)	64.85 ± 0.05	2.24±0.02	13.30 ± 0.04	10.31 ± 0.04	1.00±0.02	8.29±0.03
θ **clusters** — THz **neg.** (99 036 ions)	38.25 ± 0.31	25.36 ± 0.28	4.82±0.14	3.32±0.11	1.90±0.09	26.35 ± 0.28
θ **clusters** — THz **pos.** (87 616 ions)	35.81 ± 0.32	29.75 ± 0.31	3.43±0.12	2.17±0.09	1.91±0.09	26.92 ± 0.30

Table 5.7: NS8 compositions (at.% $\pm 2\sigma$) for γ' and θ regions under THz excitation. Both negative- and positive-polarity datasets are reported with the corresponding ion counts.

5.4 Comparison THz-assisted APT vs LEAP 5000 XS (laser and electric mode) - γ and γ' phases

From the laser pump energy variation, the optimal value was identified as **THz-positive** pulsing at $\sim$360 μJ per pulse, which provides the best compromise between higher mass resolving power and low background. We benchmarked this setting against measurements on the same NS8 specimen, but on a new tip, with a LEAP 5000 XS operated (i) in laser mode at 355 nm and (ii) in high-voltage (HV) pulsing with a 20% pulse fraction. The repetition rate was 100 kHz for all three conditions analyzed with THz pulses, and the base temperature was 50 K. For both LEAP modes, the detection rate was held at 0.07 at/pulse. In laser mode, the instrument automatically adjusted V_{DC} and the laser energy to meet simultaneously the target flux and charge-state ratio $\mathrm{Ni}^{2+}/\mathrm{Ni}^{+} = 5$ (chosen to match the THz analyses); under these constraints, the laser energy varied between 25 and 30 pJ. In HV mode, the detection rate of 0.07 at/pulse was maintained by automatic V_{DC} control while keeping the pulse fraction fixed at 20% of the applied DC voltage. Charge-state ratio $\mathrm{Ni}^{2+}/\mathrm{Ni}^{+}$ was not set to a value of 5 in this case, as there is no Ni^{1+} peak in the mass spectrum.

Figure 5.17 compares spectra from LEAP laser mode, LEAP electric mode, and THz-positive pulsing at 360 μJ. For this comparison selections of datasets with similar statistical significance have been performed considering *uniquely* portions of volumes inside γ phase region. Laser pulsing shows its typical thermal signatures: elevated background, thermal tails, and peak broadening (pronounced $\mathrm{H}^{+}/\mathrm{H}_2^{+}$; tailing near 26 Da for Cr^{2+}, around 29/58 Da for $\mathrm{Ni}^{2+}/\mathrm{Ni}^{+}$, and between 46–50 Da for Mo^{2+}). Mo also appears prominently as Mo^{+} in laser mode, consistent with a lower average field during ion emission and enhanced thermal contribution.

For electric pulsing, the background drops, peaks sharpen, and the effective field increases, evidenced by the emergence of higher charge states (*e.g.*, Mo^{3+}). The 58 Da block associated with Ni^{+} isotopes and Co^{+} is essentially absent, with only their 2+ counterparts remaining; accordingly, the charge–state ratio $\mathrm{Ni}^{2+}/\mathrm{Ni}^{+}$ is on the order of 10^4.

THz-positive pulsing at 360 μJ yields the cleanest spectra of the three. Peaks are systematically narrower than in the LEAP electric mode, the background is slightly lower, and hydrogen is reduced. A notable difference concerns charge states: electric pulsing uses a longer pulse width

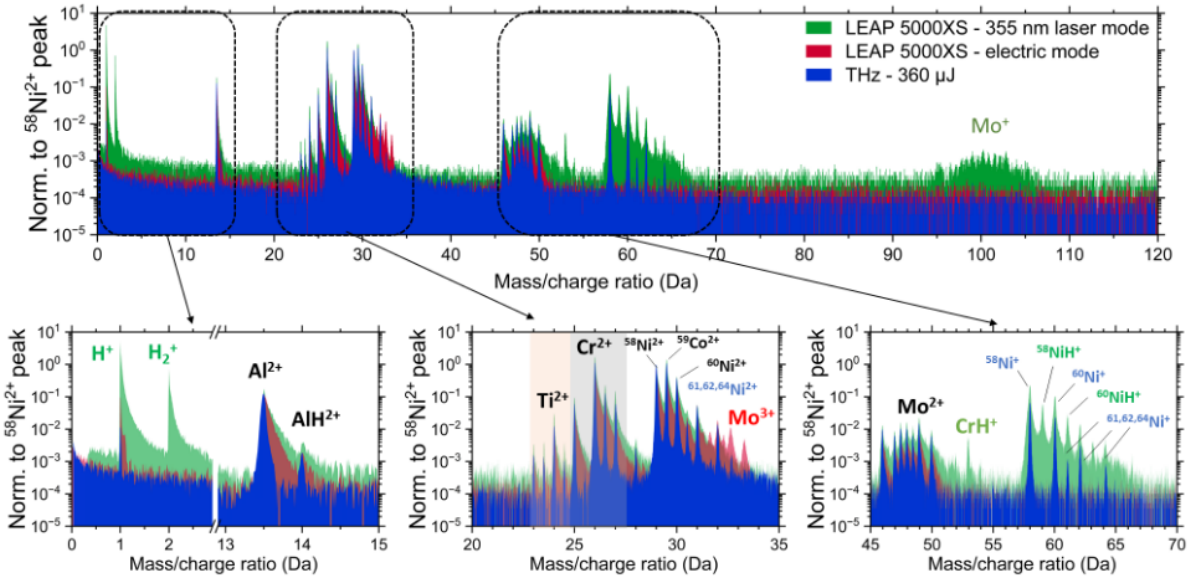

Figure 5.17: Overlaid spectra ($1.2 \cdot 10^6$ events datasets) of the γ phase, acquired under three conditions: LEAP laser mode (λ=355 nm), LEAP electric mode (20% pulse fraction), and THz-positive pulsing at 360 μJ. Selected regions (H, Cr, Ni, Mo) illustrate background level, tailing, and charge-state distribution.

(ns-scale), while THz pulses are picosecond in duration. The peak field is comparable to electric pulsing (hence similar SNR), but the shorter interaction time reduces post-ionization probability, particularly for high mass charge ratio ions ($m/n > 15$ Da), so singly charged species (*e.g.*, Ni^+, Co^+, Al^+) remain visible alongside doubly charged ions. This combination—high field with minimal post-ionization—explains the simultaneous improvement in resolving power and the persistence of lower charge states in the THz spectrum.

The LEAP datasets include ∼15 M events for the analysis performed in laser mode and ∼2 M events for the one conducted in electric mode. Reconstructions for both modes show γ' precipitates embedded in the γ matrix (Fig. 5.18(a,b)). In a γ' precipitate from both the laser and the electric mode datasets, crystallographic planes are visible and were used to refine the reconstruction parameters, providing an internal check on the absolute scale, as done for the previous study with THz-positive drive. By performing spatial resolution calculations using a Fourier-based analysis of the reconstructed atomic volumes (see details in section 1.1) on the software MoDaT, we found that THz positive pulses deliver the best performances in terms of in-depth resolution, while the best lateral resolution values are obtained in electric mode on the with the LEAP 5000XS. The comparison between the values are reported in Table 5.8.

The compositional histograms in Fig. 5.19 compare γ-phase regions acquired with LEAP laser

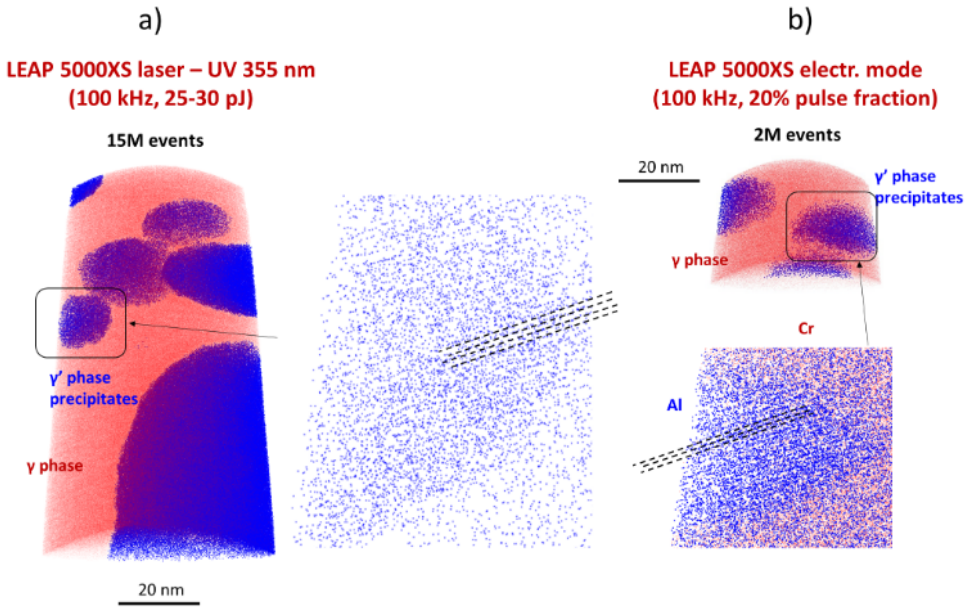

Figure 5.18: LEAP 5000 XS reconstructions of the same NS8 specimen: (a) laser mode (λ=355 nm, $\sim 15 \cdot 10^6$ ions) and (b) electric mode (20% pulse fraction, $\sim 2 \cdot 10^6$ ions). In both cases, γ' precipitates are embedded in a γ matrix; lattice planes are visible in a γ' precipitate for both dataset and were used to calibrate reconstruction parameters.

Condition	**In-depth resolution [Å]**	**Lateral resolution [Å]**
THz (positive pulses)	0.54 ± 0.08	4.04 ± 0.30
THz (negative pulses)	0.74 ± 0.10	8.00 ± 0.60
LEAP 5000XS — Electric (20% PF)	0.99 ± 0.07	1.87 ± 0.20
LEAP 5000XS — Laser (355 nm)	1.12 ± 0.10	4.42 ± 0.35

Table 5.8: Calculations for in-depth and lateral resolution for the γ' phase with all illumination conditions: THz in both polarities (Tera-SAT); UV, electric mode (LEAP 5000XS).

mode, LEAP electric mode, and THz-positive pulsing (360 μJ laser pump energy). Within the measurement uncertainties, the THz-derived compositions agree with those from both LEAP modes for the major elements (Ni, Cr, Al, Ti, Mo, Co). This indicates that the improved spectral quality from THz pulsing translates into reliable elemental analysis consistent with a commercial instrument of the same flight-path architecture.

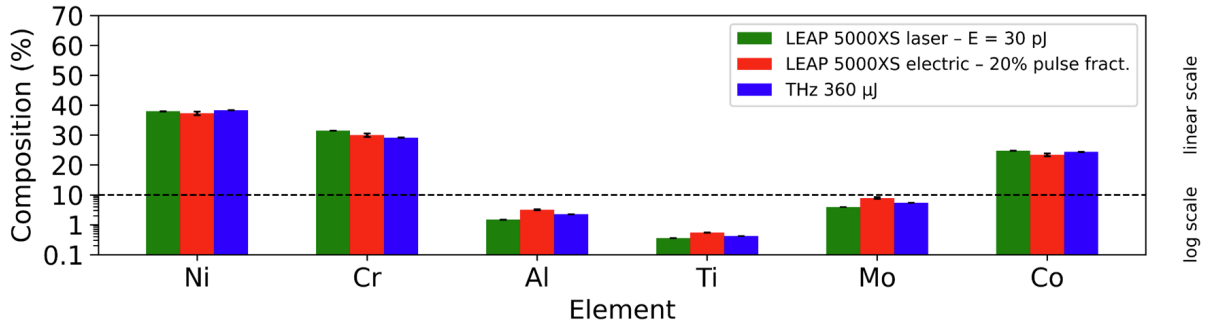

Figure 5.19: γ-phase compositions (at.%) for the same specimen acquired with LEAP laser mode, LEAP electric mode, and THz-positive pulsing at 360 μJ. Error bars indicate standard de*via*tions $\pm 2\sigma$.

5.5 Conclusion

In summary, the high–repetition–rate THz–assisted APT demonstrates field-driven evaporation with excellent spectral quality on the conductive, multiphase NS8 alloy, outperforming IR under matched detection–rate conditions and enabling reliable γ and γ' composition analysis together with the resolution of nanoscale, Cr/Co-enriched θ clusters inside γ'. In γ phase the THz mass spectrum shows sharper peaks, lower background and weaker thermal tails than IR, while in γ' the THz datasets (both polarities) recover crystallographic planes and resolve higher Cr+Co enrichments than IR, evidencing superior spatial/chemical resolution at the nanometric scale.

The spectral differences between negative and positive terahertz (THz) pulses and their dependence on the tip's position relative to the Gouy-phase crossing were examined. When positioned on the positive side, the spectral peaks are narrower and have a higher signal-to-noise ratio (SNR), while near the crossing, negative and positive polarities may result in similar, bipolar spectra.

We highlighted that increasing the THz pulse amplitude improves SNR but reduces mass resolving power due to energy dispersion and temporally separated emission windows, with 360 J identified as the optimal pump energy for a balance between these factors.

Benchmarking against the LEAP 5000 XS demonstrates THz's superior spectral clarity, in-depth resolution, and comparable compositions to LEAP's laser and electric modes, although LEAP's electric mode offers better lateral resolution, even though the values can be affected, in the case of THz analysis, by the actual temperature during the analysis in the APT chamber, which may have been higher than the planned 50 Kelvin.

General conclusion

The initial motivation of this thesis was to address one of the fundamental limitations of Atom Probe Tomography (APT): its restricted applicability to bio-materials so that APT could serve as a *complementary* technique alongside established biomaterials imaging microscopy techniques, adding at the same time quantitative, subnanometric 3D spatial and chemical information. However, the reliance of APT on voltage or laser pulsing poses challenges for low conductivity or composite organic–inorganic architectures, as in the case of insulating matrices embedding bio-molecules.

In particular, the analysis of proteins embedded in an amorphous matrix poses a two-fold challenge: preserving the native chemical state of bio-molecules during field evaporation and stabilizing the surrounding matrix to achieve reproducible, highquality spectra. To face these challenges, this thesis proposed two complementary strategies:

- the adoption of THz-assisted pulsing as an alternative activation mechanism capable of triggering evaporation in an athermal, field-driven regime—thereby reducing thermal effects and spectral broadening;
- use of sol–gel silica matrices prepared following the water glass route for protein encapsulation, combined with targeted surface engineering, such as metallic coatings and graphene encapsulation to enhance THz-field coupling with the sample, stabilize evaporation, thus

extend THz-assisted analysis beyond solely metallic samples.

The thesis opens with a systematic characterization of sol–gel silica under conventional UV- and deep-UV–assisted APT. This clarified both its potential and its limitations: wavelength-dependent absorption accentuates porosity- and defect-mediated instabilities that undermine run stability and spectral fidelity, while the applied field governs composition, yielding a measurable, field-dependent variation in the O:Si ratio.

Building on this foundation, the first experiments using a low-repetition-rate (1 kHz) THz-assisted system demonstrated that sol–gel silica could indeed be evaporated under THz drive. By systematically varying the polarity of the THz waveform, we identified distinct evaporation mechanisms: 1) positive pulses, whose efficiency is linked to the sample's ability to amplify the THz pulse and 2) negative pulses interacting through electron emission and local heating effects. This dual behavior clarified the role of THz polarity in governing ion emission, and confirmed the possibility of successfully using THz fields on insulating samples.

In parallel, surface engineering strategies were tested to improve THz-field coupling in the case of positive polarity. Both thin chromium coatings and graphene encapsulation established a more conductive interface at the apex, favoring sharper peaks with reduced background noise. Such coated sol-gel silica samples were tested under both THz polarities: graphene encapsulation, in particular, offered superior coupling under positive THz drive, while chromium coatings ensured overall higher success rate in the preparation steps.

The high-repetition-rate (100 kHz) THz-assisted system, finally demonstrated the successful acquisition of much larger volumes. Experiments on both coated and uncoated sol-gel silica and conductive metallic systems, such as Nickel-based superalloy NS8, demonstrated that THz pulsing can be used to analyze complex metallic and coated insulating structures, yielding excellent mass spectral quality and better spatial resolution compared to near-infrared or UV pulsing, while preserving compositional fidelity.

In perspective, further refining sol–gel synthesis and protein encapsulation is essential to obtain reproducible, stable tips that preserve bio-molecular integrity; reducing porosity, controlling surface chemistry, and improving coating attachment will be decisive to achieve a better THz-field coupling with the samples. Equally, more uniform nanoscale coatings, such as in-situ

deposition techniques, and improved graphene transfer are needed to fully exploit positive THz pulses while maintaining geometric sharpness.

A deeper investigation on electron emission under THz negative pulses is required to understand the origin of thermal contributions and stabilize field-driven regimes; tighter alignment, focusing, and phase control at the apex, together with in-situ waveform diagnostics and, if necessary, a more powerful and tunable THz source, would extend the accessible parameter space and enhance reproducibility.

Finally, we are also planning to explore cryogenic APT of bio-molecules, which demands rapid vitrification to form amorphous ice, thereby avoiding crystallization that could denature native structures—and strictly controlled cryogenic transfer into the APT chamber. Accordingly, upgrades of the THz-assisted APT platform are planned to accommodate cryogenic samples.

Overall, the main goal remains to achieve atomic-level (spatial and chemical) analysis of bio-molecules with APT while avoiding denaturation from thermal effects; the results obtained with THz-assisted APT indicate that we are on the right track, having demonstrated the possibility of analyzing and characterizing amorphous sol–gel silica using this wavelength for the first time, providing a concrete scientific breakthrough in the Atom Probe Tomography community. The remaining milestone is the unambiguous detection of the bio-molecular signature inside the matrix and further investigations on this issue are ongoing.

Appendix

1.1 Fourier-based estimate of spatial resolution in APT.

Following the approach in [7], the spatial resolution of reconstructed atom-probe volumes can be quantified from the Fourier content orthogonal to crystallographic planes. Let z be the real-space coordinate normal to a family of planes and $f(z)$ the corresponding one-dimensional atomic density in a selected sub-volume. The Fourier transform

$$F(\xi) = \int f(z)\, e^{i2\pi\xi z}\, dz$$

yields the Fourier intensity $I(\xi) = F(\xi)F^*(\xi) = |F(\xi)|^2$. For perfectly periodic planes, $I(\xi)$ exhibits harmonics regularly spaced along ξ (the reciprocal direction normal to the planes); in real data, peak amplitudes decay with increasing spatial frequency. Assuming atomic positions suffer random errors described by a Gaussian blur

$$G(z) = \exp\left(-\frac{z^2}{2\sigma^2}\right),$$

the regular sequence of plane-related peaks is convolved by G, so each Fourier peak has a finite width whose full width at half maximum (FWHM) is

$$\Delta = 2\sqrt{2\ln 2}\,\sigma,$$

taken as a direct measure of the resolution *perpendicular* to the planes. Practically, cubic subvolumes ($\sim 2 \times 2 \times 2$ nm^3) are extracted around crystallographic poles, and Δ is evaluated as a function of the take-off angle θ between an atom and the pole center. The observed broadening combines two contributions: lateral precision (Δ_L) in the detector plane and depth precision (Δ_ρ) along the analysis direction. Approximating the local surface by a plane, the angular dependence of the apparent resolution is

$$\Delta^2(\theta) = \underbrace{(\Delta_L \sin\theta)^2}_{\text{lateral contribution}} + \underbrace{(\Delta_\rho \cos\theta)^2}_{\text{depth contribution}} .$$

Fitting the measured $\Delta(\theta)$ with this form (least squares) provides separate estimates of Δ_L and Δ_ρ, thereby delivering a quantitative, direction-resolved assessment of spatial resolution in atom probe tomography.

1.2 Artefacts, biases, and quality control in 3D reconstruction

Several effects can bias either the spectrum or the reconstructed geometry and are therefore handled, or at least monitored, during reconstruction. Hydrogen uptake can lead to hydride formation and peak shifts, which is particularly problematic in crowded spectra (e.g. bio-related systems) [6]. Local variations of evaporation field (e.g. at precipitates or second phases) transiently reshape the emitting surface and the electrostatic field, producing trajectory aberrations (*local magnification*) that distort true shapes. In some materials, field-driven surface migration displaces atoms over the surface before evaporation, degrading lateral fidelity in the point cloud [100]. A timing issue, *wrap-around*, occurs when an ion's ToF exceeds the pulse period and the ion is recorded in the subsequent detection window; this produces a broad low-m/n feature and information loss. Lower repetition rates mitigate wrap-around but tend to raise the baseline noise.

Across this thesis, lateral and depth scales were cross-checked against external constraints (SEM/TEM images, crystallographic poles/planes [238]) and by internal consistency (stoichiometry, density with Q). Where minor species were added to the ranging post hoc, reconstructions were re-run so those ions contributed correctly to the final 3D maps [220].

1.3 Clusters and precipitates

Clusters and precipitates are 3D solute–rich features revealed by composition contrast in the reconstruction. In classical nucleation theory [282], the free-enthalpy change $\Delta G(r)$ for a spherical particle exhibits a barrier ΔG^* at the critical radius r^*; sub-critical embryos ($r < r^*$) are unstable (Fig. 1.1). In APT we refer to *clusters* as the earliest, matrix-like solute aggregates (often lacking a sharp interface), and to *precipitates* as compositionally defined particles with a discernible interface. Canonical sequences (e.g. GP zones in age-hardenable Al alloys) illustrate the continuum between the two [283–286]. Interfaces (grain or phase boundaries) are 2D defects and are analysed with similar tools, using composition steps to localise the boundary.

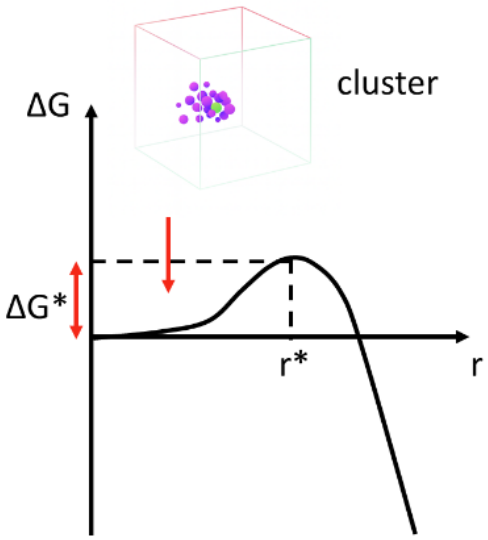

Figure 1.1: Classical nucleation sketch: $\Delta G(r)$ with barrier ΔG^* at r^* for a spherical particle [282], adapted from [7].

Detection strategy. Throughout this thesis we identify clusters as local solute enrichments using a two-step pipeline in the *3D GPM* software: (i) a *local-composition pre-selection* (Iso Position) to keep atoms from enriched regions, followed by (ii) *distance-based grouping* via the maximum–separation rule [287, 288]. For step (i), 3D *Real* and *Random* composition grids

are computed on the current subset (*Atom memory*); for each atom, the local Real/Random compositions at (x, y, z) are obtained by linear interpolation. Atoms are retained if their Real composition exceeds a user threshold (or, in `Randomized` mode, if the Random composition does); the threshold is chosen from an area-normalised, log-scaled histogram of per-atom Real (blue) and Random (grey) values (Fig. 1.2(a)), typically above the Random tail (0.1–0.01% percentiles) to suppress false positives.

For step (ii), two solute atoms p, q belong to the same cluster if

$$d(p, q) \leq d_{\max}, \tag{1.1}$$

with linking length $d_{\max}$. Here $d_{i,j} = \|\mathbf{r}_i - \mathbf{r}_j\|$ denotes the Euclidean distance in reconstructed space between atoms i and j; $d_{i,k}$ is the *nearest–neighbour* distance from i to its closest atom k; and $d_{i,m}$ illustrates distances from i to atoms m in another group (typically $d_{i,m} > d_{\max}$). Operationally, atoms within $d_{\max}$ are linked and transitive closure forms clusters, after which a size filter $N_{\min}$ removes noise-like aggregates (Fig. 1.2b). The test uses 1NN-scale distances, which makes it sensitive to local density variations and APT positional limits (trajectory aberrations, local magnification, crystallographic artefacts) [287, 288]. There is no universal $d_{\max}$; in practice we calibrate it by (i) matching against a randomised solution of the same global chemistry [289] with lattice/efficiency corrections [290], and/or (ii) taking the first local minimum of the total cluster-count curve [291]. For sparse datasets ($< 10^6$ ions), mass-to-charge vs. detection-sequence maps (with voltage) help relate clustering to run segments.

After grouping, we compute cluster metrics (size, composition, radius of gyration, number density). Because both Iso Position and $d_{\max}$ respond to local density, we check stability against small parameter changes and sub-sampling; where possible, we cross-check with isoconcentration/isodensity isosurfaces on the same volume and compare cluster chemistry to the matrix ranging to exclude artefacts.

Isosurfaces. Isosurfaces highlight regions where a scalar field equals a target value, typically a local composition (*isoconcentration*) or atomic number density (*isodensity*). The data are voxelised; the field is computed per voxel; voxels near the target level are merged into a closed surface. Isosurfaces conveniently reveal segregation, second phases, precipitates, interface

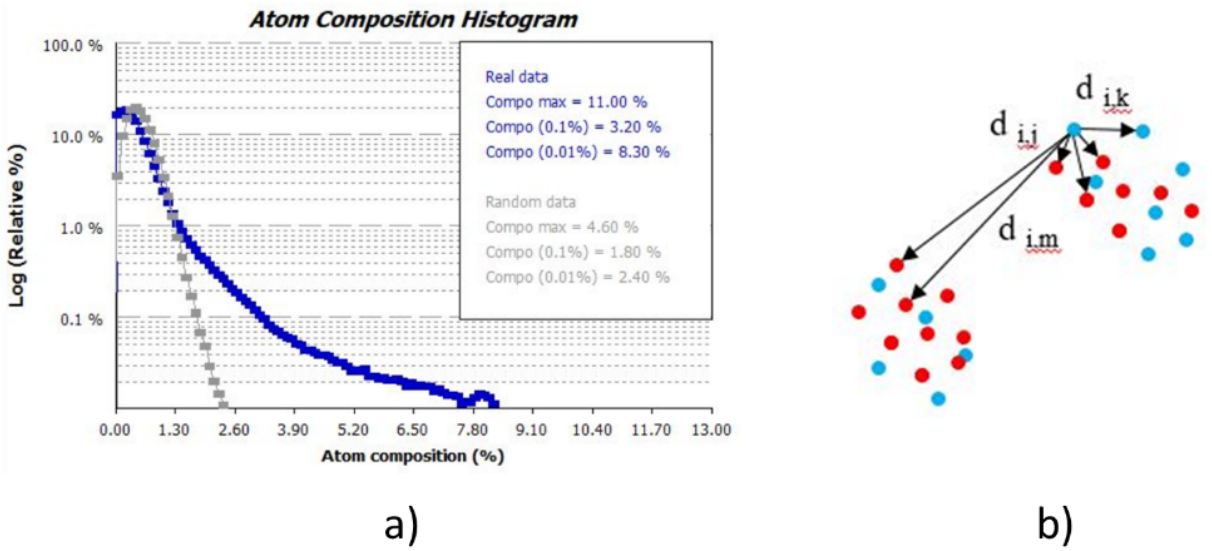

Figure 1.2: (a) Iso Position (local composition): area-normalised, log-scaled histograms of per-atom *Real* (blue) and *Random* (grey) local compositions; the threshold is set above the Random tail (e.g. 0.01%). (b) Maximum–separation clustering: schematic of pairwise Euclidean distances $d_{i,j} = \|\mathbf{r}_i - \mathbf{r}_j\|$ from a reference atom i to neighbours j. The nearest-neighbour distance $d_{i,k}$ is tested against $d_{\max}$; if $d_{i,k} \leq d_{\max}$ a link is created. Distances $d_{i,m}$ to atoms in another group typically exceed $d_{\max}$ and do not link. Transitive closure of all links yields clusters.

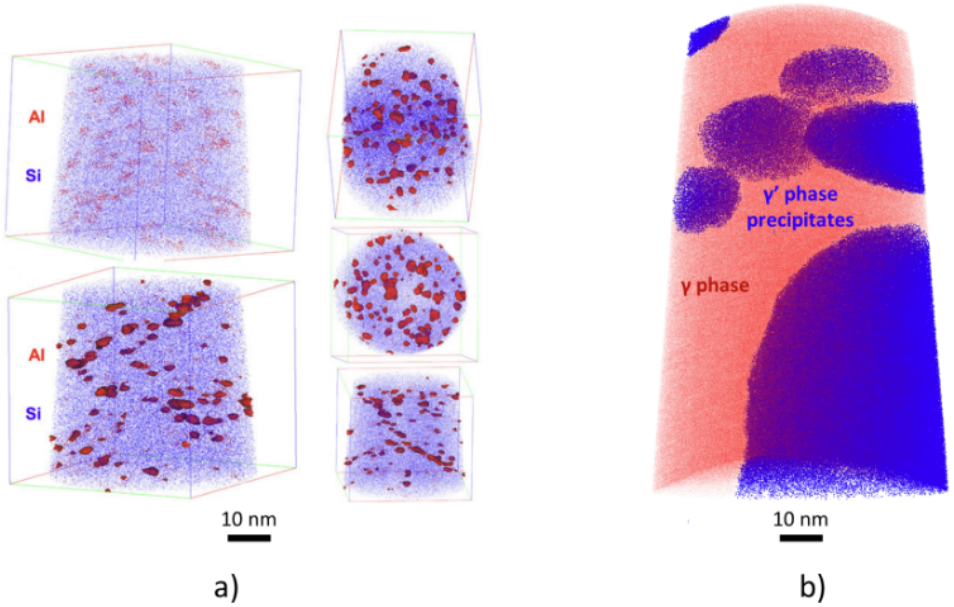

Figure 1.3: Tomographic APT maps. (a) UV-LEAP map of Al-doped Si: 1.8% of Si atoms (blue) in a $77 \times 74 \times 65$ nm^3 volume ($\sim 6.2 \times 10^6$ atoms); 2 at.% Al isoconcentration surfaces (red). Adapted from [292]. (b) UV-LEAP 5000XS ($\lambda = 355$ nm) reconstruction of a Ni-based superalloy (NS8) showing γ' precipitates (Al) in a γ matrix (Cr).

enrichment, and density variations, while suppressing background points; however, their appearance depends on voxel size, threshold/tolerance, smoothing, and connectivity filters, which must be reported. We therefore pair isosurfaces with quantitative tools (frequency distributions, proxigrams, and the clustering workflow above) to link visual features to composition and size statistics. Examples of data visualization are shown in Fig. 1.3, where clustering techniques and isoconcentration surfaces help both 3D visualization and quantitative compositional analysis.

Bibliography

[1] C. Bonnaud et al. "Cryo-TEM and ET of Liposome–Nanoparticle Hybrids for Drug Delivery". In: *ACS Nano* 8.4 (2014), pp. 3451–3460. DOI: 10.1021/nn500061y.

[2] J.-P. Renaud et al. "Cryo-EM in drug discovery: achievements, limitations and prospects". In: *Nature Reviews Drug Discovery* 17.7 (2018), pp. 471–492. DOI: 10.1038/nrd.2018.77.

[3] Peter Ercius et al. "Electron Tomography: A Three-Dimensional Analytic Tool for Nanostructures". In: *Advanced Materials* 27.38 (2015), pp. 5638–5663. DOI: 10.1002/adma.201501015.

[4] S. G. Wolf and et al. "Three-Dimensional Imaging of Mitochondrial Calcium-Rich Granules in Whole Cells by Cryo Electron Tomography". In: *eLife* 6 (2017), e29929. DOI: 10.7554/eLife.29929.

[5] M. A. Herzik and et al. "High-resolution structure determination of biomolecules by cryo-EM: opportunities and challenges". In: *Nature Communications* 10 (2019), p. 1032. DOI: 10.1038/s41467-019-08968-2.

[6] Baptiste Gault et al. *Atom Probe Microscopy*. Vol. 160. Springer Series in Materials Science. New York, Heidelberg, Dordrecht, London: Springer, 2012. ISBN: 978-1-4614-3435-1. DOI: 10.1007/978-1-4614-3436-8.

[7] Williams Lefebvre, François Vurpillot, and Xavier Sauvage, eds. *Atom Probe Tomography: Put Theory Into Practice*. Academic Press (Elsevier), 2016. ISBN: 978-0-12-804647-0. DOI: 10.1016/B978-0-12-804647-0.

[8] B. Gault et al. "Atom Probe Tomography". In: *Nature Reviews Materials* 6 (2021).

[9] D Blavette et al. "Three-dimensional atomic-scale imaging of impurity segregation to line defects". In: *Science* 286.5448 (1999), pp. 2317–2319.

[10] Michael K. Miller and Richard G. Forbes. *Atom-Probe Tomography: The Local Electrode Atom Probe*. New York, NY: Springer, 2014. ISBN: 978-1-4899-7429-7. DOI: 10.1007/978-1-4899-7430-3.

[11] B. Gault et al. "Design of a femtosecond laser-assisted tomographic atom probe". In: *Review of Scientific Instruments* 77.4 (2006), p. 043705. DOI: 10.1063/1.2194089.

[12] A Vella. "On the interaction of an ultra-fast laser with a nanometric tip by laser assisted atom probe tomography: A review". In: *Ultramicroscopy* 132 (2013), pp. 5–18.

[13] T. T. Tsong. *Atom-Probe Field-Ion Microscopy*. Cambridge, UK, New York, NY: Cambridge University Press, 1990. DOI: 10.1017/CBO9780511599842.

[14] L Arnoldi et al. "Role of the resistivity of insulating field emitters on the energy of field-ionised and field-evaporated atoms". In: *Ultramicroscopy* 159 (2015), pp. 139–146.

[15] Thomas F. Kelly and Michael K. Miller. "Invited Review Article: Atom-probe tomography". In: *Review of Scientific Instruments* 78.3 (2007), p. 031101. DOI: 10.1063/1.2709758.

[16] L. M. Gordon et al. "Three-Dimensional Chemical Mapping of Enamel at the Nanoscale". In: *ACS Nano* 6.12 (2012), pp. 10667–10675. DOI: 10.1021/nn303299e.

[17] Brian Langelier, Xiaoyue Wang, and Kathryn Grandfield. "Atomic Scale Chemical Tomography of Human Bone". In: *Scientific Reports* 7.1 (2017), p. 39958. DOI: 10.1038/s41598-017-00126-1.

[18] Gustav Sundell et al. "Atom Probe Tomography for 3D Structural and Chemical Analysis of Individual Proteins". In: *Small* 15.24 (2019), p. 1900316. DOI: 10.1002/smll.201900316.

[19] Daniel E. Perea et al. "Atom Probe Tomographic Mapping Directly Reveals the Atomic Distribution of Phosphorus in Resin-Embedded Ferritin". In: *Scientific Reports* 6 (2016), p. 22321. DOI: 10.1038/srep22321.

[20] Thomas F. Kelly et al. “Prospects for Nanobiology with Atom-Probe Tomography”. In: *MRS Bulletin* 34.10 (2009), pp. 744–749. DOI: 10.1557/mrs2009.207.

[21] Ian E. McCarroll et al. “New Frontiers in Atom Probe Tomography: A Review of Research Enabled by Cryo and/or Vacuum Transfer Systems”. In: *Materials Today Advances* 7 (2020), p. 100090. DOI: 10.1016/j.mtadv.2020.100090.

[22] Lara Wimmer et al. “Terahertz control of nanotip photoemission”. In: *Nature Physics* 10.6 (2014), pp. 432–436.

[23] Sha Li and RR Jones. “High-energy electron emission from metallic nano-tips driven by intense single-cycle terahertz pulses”. In: *Nature communications* 7.1 (2016), p. 13405.

[24] Angela Vella et al. “High-Resolution Terahertz-Driven Atom Probe Tomography”. In: *Science Advances* 7.7 (2021), eabd7259. DOI: 10.1126/sciadv.abd7259.

[25] Vedran Jelic et al. “Ultrafast terahertz control of extreme tunnel currents through single atoms on a silicon surface”. In: *Nature Physics* 13.6 (2017), pp. 591–598.

[26] Shoji Yoshida et al. “Subcycle transient scanning tunneling spectroscopy with visualization of enhanced terahertz near field”. In: *ACS Photonics* 6.6 (2019), pp. 1356–1364.

[27] Jonathan Houard et al. “Nanotip response to monocycle terahertz pulses”. In: *Applied Physics Letters* 117.15 (2020), p. 151105. DOI: 10.1063/5.0022182.

[28] Michella Karam et al. “THz-driven field emission: energy and time-of-flight spectra of ions”. In: *New Journal of Physics* 25 (2023). DOI: 10.1088/1367-2630/ad0855.

[29] Gustav Eriksson et al. “Role of Defects in Atom Probe Analysis of Sol–Gel Silica”. In: *ACS Omega* 10.30 (2025), pp. 33741–33754. DOI: 10.1021/acsomega.5c04733. eprint: https://doi.org/10.1021/acsomega.5c04733. URL: https://doi.org/10.1021/acsomega.5c04733.

[30] M. De Tullio et al. “Evaporation of cations from nonconductive nanosamples using single-cycle terahertz pulses: An experimental and theoretical study”. In: *Physical Review B* 111.4 (Jan. 2025), p. 045428. DOI: 10.1103/PhysRevB.111.045428.

[31] Eugene Y. D. Chua et al. “Better, Faster, Cheaper: Recent Advances in Cryo–Electron Microscopy”. In: *Annual Review of Biochemistry* 91 (2022), pp. 1–32. DOI: 10.1146/annurev-biochem-032620-110705.

[32] Mengyu Wu, Gabriel C. Lander, and Michael A. Herzik Jr. "Sub-2 Å Resolution Structure Determination Using Single-Particle Cryo-EM at 200 keV". In: *Journal of Structural Biology: X* 4 (2020), p. 100020. DOI: 10.1016/j.yjsbx.2020.100020.

[33] M. A. Aronova and R. D. Leapman. "Development of Electron Energy-Loss Spectroscopy in the Biological Sciences". In: *MRS Bulletin* 37.1 (2012), pp. 53–62. DOI: 10.1557/mrs.2011.329.

[34] R. F. Egerton. *Electron Energy-Loss Spectroscopy in the Electron Microscope*. 3rd ed. New York: Springer, 2011. DOI: 10.1007/978-1-4419-9583-4.

[35] Mengyu Wu, Gabriel C. Lander, and Jr. Herzik Michael A. "Sub-2 Å resolution structure determination using single-particle cryo-EM at 200 keV". In: *Journal of Structural Biology: X* 4 (Feb. 2020), p. 100020. DOI: 10.1016/j.yjsbx.2020.100020.

[36] R. F. Egerton. "Radiation Damage to Organic and Inorganic Specimens in the TEM". In: *Micron* 119 (2019), pp. 72–87. DOI: 10.1016/j.micron.2019.01.005.

[37] Yong Zi Tan et al. "Addressing Preferred Specimen Orientation in Single-Particle Cryo-EM Through Tilting". In: *Nature Methods* 14.8 (2017), pp. 793–796. DOI: 10.1038/nmeth.4347.

[38] Daniel J. Müller and Yves F. Dufrêne. "Atomic Force Microscopy as a Multifunctional Molecular Toolbox in Nanobiotechnology". In: *Nature Nanotechnology* 3.5 (2008), pp. 261–269. DOI: 10.1038/nnano.2008.100.

[39] Daniel J. Müller and Yves F. Dufrêne. "Atomic Force Microscopy: A Nanoscopic Window on the Cell Surface". In: *Trends in Cell Biology* 21.8 (2011), pp. 461–469. DOI: 10.1016/j.tcb.2011.04.008.

[40] Alexander X. Cartagena-Rivera et al. "Fast, Multi-Frequency and Quantitative Nanomechanical Mapping of Live Cells Using the AFM". In: *Scientific Reports* 5 (2015), p. 11692. DOI: 10.1038/srep11692.

[41] Umesh Gawas, Vinod Mandrekar, and Mahesh Majik. *Structural analysis of proteins using X-ray diffraction technique*. Book chapter. 2019. DOI: 10.1016/B978-0-12-817497-5.00005-7.

[42] D. R. Smyth et al. "Crystal structures of proteins: A guide to understanding protein function". In: *QJM: An International Journal of Medicine* 93.8 (2000), pp. 509–514. DOI: 10.1093/qjmed/93.8.509.

[43] N. E. Chayen. “Turning protein crystallisation from an art into a science”. In: *Acta Crystallographica Section D: Biological Crystallography* 59.7 (2003), pp. 1336–1342. DOI: 10.1107/S0907444903009986.

[44] A. A. Kermani. “An overview of membrane protein crystallization in lipidic mesophases”. In: *The FEBS Journal* 288.6 (2021), pp. 1748–1764. DOI: 10.1111/febs.15648.

[45] E. Eyal et al. “The limit of accuracy of protein modeling: Influence of crystal packing on protein structure”. In: *Journal of Molecular Biology* 351.2 (2005), pp. 431–442. DOI: 10.1016/j.jmb.2005.05.067.

[46] G. Brändén and R. Neutze. “Time-resolved structural biology at X-ray free-electron lasers”. In: *Science* 373.6554 (2021), eaba0954. DOI: 10.1126/science.aba0954.

[47] Paul Schanda and Matthias Ernst. “Studying Dynamics by Magic-Angle Spinning Solid-State NMR Spectroscopy: Principles and Applications to Biomolecules”. In: *Progress in Nuclear Magnetic Resonance Spectroscopy* 96 (2016), pp. 1–46. DOI: 10.1016/j.pnmrs.2016.02.001.

[48] Benoıt̂ Plainchont et al. “Dynamic Nuclear Polarization Opens New Perspectives for NMR Spectroscopy in Analytical Chemistry”. In: *Analytical Chemistry* 90.1 (2018), pp. 363–381. DOI: 10.1021/acs.analchem.7b05236.

[49] Baptiste Gault et al. “Atom Probe Tomography”. In: *Nature Reviews Methods Primers* 1.51 (2021), pp. 1–38. DOI: 10.1038/s43586-021-00047-w.

[50] Frédéric De Geuser and Baptiste Gault. “Metrology of Small Particles and Solute Clusters by Atom Probe Tomography”. In: *Acta Materialia* 188 (2020), pp. 406–415. DOI: 10.1016/j.actamat.2020.02.012.

[51] Y.-S. Chen et al. “Atom Probe Tomography for the Observation of Hydrogen in Materials: A Review”. In: *Microscopy and Microanalysis* 29.1 (2023), pp. 1–28. DOI: 10.1093/micro/miaa120.

[52] J. A. Panitz. “My Life With Erwin: The Beginning of an Atom-Probe Legacy”. In: *Microscopy and Microanalysis* 25.2 (2019), pp. 274–279. DOI: 10.1017/S1431927619000049.

[53] T. F. Kelly et al. “On the many advantages of local-electrode atom probes”. In: *Ultramicroscopy* 62.1-2 (1996), pp. 29–42. DOI: 10.1016/0304-3991(95)00152-2.

[54] D. J. Larson et al. *Local Electrode Atom Probe Tomography*. New York, NY, USA: Springer, 2013.

[55] James Keeler. *Understanding NMR Spectroscopy*. 2nd. Wiley, 2010.

[56] *Sample Preparation for Solution NMR*. University College London NMR Facility. Accessed 2025. URL: https://www.ucl.ac.uk/mathematical-physical-sciences/nmr/sample-preparation.

[57] S. E. Ashbrook and S. Sneddon. "New methods and applications in solid-state NMR spectroscopy". In: *Journal of the American Chemical Society* 136.44 (2014), pp. 15440–15456. DOI: 10.1021/ja508349x.

[58] A. A. El-Zoka et al. "Enabling Near-Atomic–Scale Analysis of Frozen Water". In: *Science Advances* 6.51 (2020), eabd6324. DOI: 10.1126/sciadv.abd6324.

[59] Shi Qiu et al. "Direct Imaging of Liquid–Nanoparticle Interfaces with Atom Probe Tomography". In: *The Journal of Physical Chemistry C* 124.44 (2020), pp. 24163–24172. DOI: 10.1021/acs.jpcc.0c05504.

[60] Vahid R. Adineh et al. "Near-Atomic Three-Dimensional Mapping for Site-Specific Chemistry of 'Superbugs'". In: *Nano Letters* 16.11 (2016), pp. 7113–7120. DOI: 10.1021/acs.nanolett.6b03409.

[61] Robert Gomer and Robert Gomer. *Field emission and field ionization*. Vol. 34. Springer, 1961.

[62] Toshio Sakurai and Erwin W Müller. "Field calibration using the energy distribution of a free-space field ionization". In: *Journal of Applied Physics* 48.6 (1977), pp. 2618–2625.

[63] François Vurpillot et al. "Pragmatic reconstruction methods in atom probe tomography". In: *Ultramicroscopy* 111.8 (2011), pp. 1286–1294.

[64] F Vurpillot. "Field ion emission mechanisms". In: *Atom probe tomography*. Elsevier, 2016, pp. 17–72.

[65] Shyeh Tjing Loi et al. "Electrostatic simulations of a local electrode atom probe: The dependence of tomographic reconstruction parameters on specimen and microscope geometry". In: *Ultramicroscopy* 132 (2013), pp. 107–113.

[66] Cristelle Pareige et al. "Time-of-flight mass spectrometry and composition measurements". In: *Atom probe tomography*. Elsevier, 2016, pp. 123–154.

[67] Michael K Miller. *Atom probe tomography: analysis at the atomic level*. Springer Science & Business Media, 2012.

[68] Ty J Prosa and David J Larson. "Modern focused-ion-beam-based site-specific specimen preparation for atom probe tomography". In: *Microscopy and Microanalysis* 23.2 (2017), pp. 194–209.

[69] Gérald Da Costa. "Atom Probe Tomography: Detector Issues and Technology". In: *Atom probe tomography*. Elsevier, 2016, pp. 155–181.

[70] P. Bas et al. In: *Applied Surface Science* 87–88 (1995), pp. 298–304.

[71] E. W. Müller. In: *Phys. Rev.* 102.3 (1956), pp. 618–624.

[72] R. Gomer. In: *J. Chem. Phys.* 31 (1959), p. 341.

[73] R. Gomer and L. W. Swanson. In: *J. Chem. Phys.* 38 (1963), p. 1613.

[74] R. K. Biswas and R. G. Forbes. In: *J. Phys. D: Appl. Phys.* 15.7 (1982), pp. 1323–1338.

[75] R. G. Forbes. In: *J. Phys. D: Appl. Phys.* 15.11 (1982), pp. L149–L152.

[76] K. Chibane and R. G. Forbes. In: *Surf. Sci.* 122.2 (1982), pp. 191–215.

[77] R. Haydock and D. R. Kingham. In: *Phys. Rev. Lett.* 44 (1980), pp. 1520–1523.

[78] G. L. Kellogg. "Determining the field emitter temperature during laser irradiation in the pulsed laser atom probe". In: *Journal of Applied Physics* 52 (1981), pp. 5320–5328.

[79] D. R. Kingham. "The post-ionization of field-evaporated ions: A theoretical explanation of multiple charge states". In: *Surface Science* 116.2 (1982), pp. 273–301. DOI: 10.1016/0039-6028(82)90434-4.

[80] K. Hirose and M. Tsukada. In: *Phys. Rev. Lett.* 73.1 (1994), p. 150.

[81] H. J. Kreuzer, L. C. Wang, and N. D. Lang. In: *Phys. Rev. B* 45.20 (1992), pp. 12050–12055.

[82] N. D. Lang. In: *Solid State Commun.* 84.1–2 (1992), pp. 155–158.

[83] N. D. Lang. In: *Phys. Rev. B* 45.23 (1992), p. 13599.

[84] N. D. Lang. In: *Phys. Rev. B* 49.3 (1994), p. 2067.

[85] Y. Suchorski et al. In: *Prog. Surf. Sci.* 53.2–4 (1996), pp. 135–153.

[86] Y. Suchorski et al. In: *Prog. Surf. Sci.* 48.1–4 (1995), pp. 121–134.

[87] C. G. Sanchez, A. Y. Lozovoi, and A. Alavi. In: *Mol. Phys.* 102.9–10 (2004), pp. 1045–1055.

[88] T. T. Tsong and C. S. Chang. "Field Evaporation and Post-Ionization: A Critical Reappraisal". In: *Japanese Journal of Applied Physics* 34.6B (1995), pp. 3309–3318. ISSN: 1347-4065.

[89] G. L. Kellogg. "Measurement of activation energies for field evaporation of tungsten ions as a function of electric field". In: *Physical Review B* 29.8 (1984), pp. 4304–4312. ISSN: 2469-9969. DOI: 10.1103/PhysRevB.29.4304.

[90] M. Wada. "On the thermally activated field evaporation of surface atoms". In: *Surface Science* 145.2–3 (1984), pp. 451–465. ISSN: 0039-6028.

[91] A. Menand and D. Blavette. In: *Journal de Physique* 47.C7 (1986), pp. 17–20.

[92] A. Menand and D. R. Kingham. In: *Journal of Physics D: Applied Physics* 17 (1984), pp. 203–208.

[93] A. Menand and D. R. Kingham. In: *Journal of Physics C: Solid State Physics* 18 (1985), pp. 4539–4547.

[94] F. Vurpillot et al. "Estimation of the cooling times for a metallic tip under laser illumination". In: *Applied Physics Letters* 88.9 (2006), p. 094105.

[95] G. L. Kellogg and T. T. Tsong. "Pulsed-laser atom-probe field-ion microscopy". In: *Journal of Applied Physics* 51.2 (1980), pp. 1184–1193.

[96] T. T. Tsong. *Atom-Probe Field Ion Microscopy*. Cambridge University Press, 1988.

[97] M. K. Miller and G. D. W. Smith. *Atom Probe Microanalysis: Principles and Applications to Materials Problems*. Materials Research Society, 2000.

[98] B. Gault et al. In: *Ultramicroscopy* 111.6 (2011), pp. 448–457.

[99] P. J. Felfer et al. In: *Microscopy and Microanalysis* 18 (2012), pp. 359–364.

[100] B. Gault et al. "Impact of directional walk on atom probe microanalysis". In: *Ultramicroscopy* 113 (2012), pp. 182–191.

[101] T. T. Tsong et al. In: *The Journal of Chemical Physics* 65.6 (1976), pp. 2469–2470.

[102] B. Viswanathan et al. In: *The Journal of Chemical Physics* 70 (1979), p. 2582.

[103] S Nishigaki, W Drachsel, and JH Block. "Photon-induced field ionization mass spectrometry of ethylene on silver". In: *Surface Science* 87.2 (1979), pp. 389–409.

[104] G. L. Kellogg and T. T. Tsong. In: *Ultramicroscopy* 5.2 (1980), pp. 259–260.

[105] W. Drachsel, S. Nishigaki, and J. H. Block. In: *International Journal of Mass Spectrometry and Ion Physics* 32.4 (1980), pp. 333–343.

[106] T. T. Tsong, S. B. McLane, and T. Kinkus. In: *Review of Scientific Instruments* 53.9 (1982), pp. 1442–1448.

[107] P. Stender et al. In: *Ultramicroscopy* 107.9 (2007), pp. 726–733.

[108] J. H. Bunton et al. In: *Microscopy and Microanalysis* 13 (2007), pp. 418–427.

[109] A. Cerezo, G. D. W. Smith, and P. H. Clifton. In: *Applied Physics Letters* 88.15 (2006), p. 154103.

[110] T. T. Tsong. "Pulsed-laser-stimulated field ion emission from metal and semiconductor surfaces: A time-of-flight study of the formation of atomic, molecular, and cluster ions". In: *Physical Review B* 30.9 (1984), pp. 4946–4958. DOI: 10.1103/PhysRevB.30.4946.

[111] A. Cerezo, C. R. M. Grovenor, and G. D. W. Smith. "Pulsed laser atom probe analysis of semiconductor materials". In: *Journal of Microscopy* 141 (2 1986), pp. 155–170.

[112] A Grenier et al. "Atomic-scale study of tbco2. 5/fe multilayers by laser-assisted tomographic atom probe". In: *Journal of applied physics* 102.3 (2007).

[113] J. G. Fujimoto et al. In: *Physical Review Letters* 53 (1984), p. 1837.

[114] S. D. Brorson et al. In: *Physical Review Letters* 64 (1990), p. 2172.

[115] R. H. M. Groeneveld, R. Sprik, and A. Lagendijk. In: *Physical Review B* 51 (1995), pp. 11443–11445.

[116] C. Voisin et al. In: *Physical Review Letters* 85.10 (2000), pp. 2200–2203.

[117] C. Voisin et al. In: *Physical Review B* 69 (2004), p. 195416.

[118] O. P. Varnavski et al. In: *Physical Review B* 72 (2005), p. 235405.

[119] S. Link et al. In: *Physical Review B* 61.9 (2000), pp. 6086–6090.

[120] M. Bass et al. "Optical Rectification". In: *Physical Review Letters* 9.11 (1962), pp. 446–448. DOI: 10.1103/PhysRevLett.9.446.

[121] TT Tsong and TJ Kinkus. "Energy distributions of pulsed-laser field-desorbed gaseous ions and field-evaporated metal ions: a direct time-of-flight measurement". In: *Physical Review B* 29.2 (1984), p. 529.

[122] TT Tsong. "Field penetration and band bending near semiconductor surfaces in high electric fields". In: *Surface Science* 81.1 (1979), pp. 28–42.

[123] Baishaki Mazumder et al. "Reneutralization time of surface silicon ions on a field emitter". In: *New Journal of Physics* 12.11 (2010), p. 113029.

[124] M. A. Fortes and B. Ralph. "[Title to be confirmed]". In: *Philosophical Magazine* 18.154 (1968), pp. 787–805.

[125] K. D. Rendulic and E. W. Müller. "[Title to be confirmed]". In: *Journal of Applied Physics* 37.7 (1966), pp. 2593–2596.

[126] M. Gilbert et al. "[Title to be confirmed]". In: *Ultramicroscopy* 107.9 (2007), pp. 767–772.

[127] MJG Lee et al. "Thermally enhanced field emission from a laser-illuminated tungsten tip: temperature rise of tip". In: *Journal of Applied Physics* 51.9 (1980), pp. 4996–5006.

[128] J Hohlfeld et al. "Electron and lattice dynamics following optical excitation of metals". In: *Chemical physics* 251.1-3 (2000), pp. 237–258.

[129] J. Houard et al. In: *Physical Review B* 81.12 (2010), p. 125411.

[130] G Sha, A Cerezo, and GDW Smith. "Field evaporation behavior during irradiation with picosecond laser pulses". In: *Applied Physics Letters* 92.4 (2008).

[131] F. Vurpillot et al. In: *Journal of Physics D: Applied Physics* 42.12 (2009), p. 125502.

[132] J Houard et al. "Three-dimensional thermal response of a metal subwavelength tip under femtosecond laser illumination". In: *Physical Review B—Condensed Matter and Materials Physics* 84.3 (2011), p. 033405.

[133] EP Silaeva et al. "Do dielectric nanostructures turn metallic in high-electric dc fields?" In: *Nano letters* 14.11 (2014), pp. 6066–6072.

[134] Janusz Bogdanowicz et al. "Laser-assisted atom probe tomography of semiconductors: The impact of the focused-ion beam specimen preparation". In: *Ultramicroscopy* 188 (2018), pp. 19–23.

[135] A. R. Anway. "Field Ionization of Water". In: *The Journal of Chemical Physics* 50.5 (Mar. 1969), pp. 2012–2021.

[136] J. A. Panitz. "Point-projection imaging of macromolecular contours". In: *Journal of Microscopy* 125.1 (1982), pp. 3–23.

[137] J. A. Panitz. "Direct visualization of unstained nucleic acids on a metal substrate". In: *Ultramicroscopy* 11.2 (Jan. 1983), pp. 161–166.

[138] J. A. Panitz and I. Giaever. "Ferritin deposition on field-emitter tips". In: *Ultramicroscopy* 6.1 (Jan. 1981), pp. 3–6.

[139] Kathryn Grandfield et al. "Atom Probe Tomography for Biomaterials and Biomineralization". In: *Acta Biomaterialia* 148 (2022), pp. 44–60. DOI: 10.1016/j.actbio.2022.05.042.

[140] Gustav Sundell et al. "Nanoscale Chemistry at the Ti–Bone Interface Revealed by Atom Probe Tomography". In: *Acta Biomaterialia* 48 (2017), pp. 443–453. DOI: 10.1016/j.actbio.2016.11.058.

[141] F. Exertier et al. “Atom probe tomography analysis of the reference zircon GJ-1: An interlaboratory study”. In: *Chemical Geology* 495 (2018), pp. 27–35.

[142] J. W. Valley et al. “Hadean age for a post-magma-ocean zircon confirmed by atom-probe tomography”. In: *Nature Geoscience* 7 (2014), p. 219.

[143] J. W. Valley et al. “Nano- and micro-geochronology in Hadean and Archean zircons by atom-probe tomography and SIMS: New tools for old minerals”. In: *American Mineralogist* 100.7 (2015), pp. 1355–1377.

[144] D. Saxey et al. *Atomic worlds: Current state and future of atom probe tomography in geoscience*. Review/position paper. 2017.

[145] A. Devaraj et al. “Three-dimensional nanoscale characterisation of materials by atom probe tomography”. In: *International Materials Reviews* 63.2 (2018), pp. 68–101.

[146] L. Daly et al. “Solar wind contributions to Earth’s oceans”. In: *Nature Astronomy* 5.12 (2021), pp. 1275–1285.

[147] L. M. Gordon and D. Joester. “Nanoscale chemical tomography of buried organic–inorganic interfaces in the chiton tooth”. In: *Nature* 469 (2011), p. 194.

[148] Lyle M. Gordon et al. “Amorphous intergranular phases control the properties of rodent tooth enamel”. In: *Science* 347.6223 (2015), pp. 746–750. DOI: 10.1126/science.1258950. URL: https://www.science.org/doi/10.1126/science.1258950.

[149] L. M. Gordon, M. J. Cohen, and D. Joester. “Towards Atom Probe Tomography of Hybrid Organic-Inorganic Nanoparticles”. In: *Microscopy and Microanalysis* 19.S2 (2013), pp. 952–953.

[150] L. M. Gordon, L. Tran, and D. Joester. “Atom Probe Tomography of Apatites and Bone-Type Mineralized Tissues”. In: *ACS Nano* 6.12 (2012), pp. 10667–10675.

[151] L. M. Gordon and D. Joester. “Mapping residual organics and carbonate at grain boundaries and the amorphous interphase in mouse incisor enamel”. In: *Frontiers in Physiology* 6 (2015). Original Research, p. 57.

[152] A. La Fontaine et al. “Atomic-scale compositional mapping reveals Mg-rich amorphous calcium phosphate in human dental enamel”. In: *Science Advances* 2.9 (2016), e1601145.

[153] K. Eder et al. “A New Approach to Understand the Adsorption of Thiophene on Different Surfaces: An Atom Probe Investigation of Self-Assembled Monolayers”. In: *Langmuir* 33.38 (Sept. 2017), pp. 9573–9581.

[154] H. Solodenko, P. Stender, and G. Schmitz. "Atom Probe Study of 1-Octadecanethiol Self-Assembled Monolayers on Platinum (111) and (200) Surfaces". In: *Microscopy and Microanalysis* (2021), pp. 1–10.

[155] J. T. Bingham et al. "Understanding Fragmentation of Organic Small Molecules in Atom Probe Tomography". In: *The Journal of Physical Chemistry Letters* 12.42 (2021), pp. 10437–10443.

[156] A. P. Proudian et al. "Atom Probe Tomography of Molecular Organic Materials: Sub-Dalton Nanometer-Scale Quantification". In: *Chemistry of Materials* (2019).

[157] C. Barroo, A. J. Akey, and D. C. Bell. "Nanoscale Investigation of Belgian Chocolate by Atom Probe Tomography". In: *Microscopy and Microanalysis* 23.S1 (2017), pp. 708–709.

[158] L. Jacobs and C. Barroo. "Imaging chocolate at the nanoscale using field emission techniques". In: *Applied Surface Science* 535 (2021), p. 147747.

[159] T. D. Pinkerton et al. "Electric Field Effects in Ionization of Water—Ice Layers on Platinum". In: *Langmuir* 15.3 (1999), pp. 851–856.

[160] C. J. Rothfuss, V. K. Medvedev, and E. M. Stuve. "Temperature and field dependence of protonated water cluster emission from field adsorbed water layers on platinum". In: *Surface Science* 501.3 (2002), pp. 169–181.

[161] C. J. Rothfuss, V. K. Medvedev, and E. M. Stuve. "The influence of the surface electric field on water ionization: a two step dissociative ionization and desorption mechanism for water ion cluster emission from a platinum field emitter tip". In: *Journal of Electroanalytical Chemistry* 554-555 (Sept. 2003), pp. 133–143.

[162] A. Stintz and J. A. Panitz. "Isothermal ramped field-desorption of water from metal surfaces". In: *Journal of Applied Physics* 72.2 (July 1992), pp. 741–745.

[163] A. Stintz and J. A. Panitz. "Cluster ion formation in isothermal ramped field-desorption of amorphous water ice from metal surfaces". In: *Surface Science* 296.1 (Oct. 1993), pp. 75–86.

[164] Eric M. Stuve. "Ionization of water in interfacial electric fields: An electrochemical view". In: *Chemical Physics Letters* 519-520 (Jan. 2012), pp. 1–17.

[165] Shanshan Qiu et al. "Three-Dimensional Chemical Mapping of a Single Protein in the Hydrated State with Atom Probe Tomography". In: *Analytical Chemistry* 92.7 (2020), pp. 5168–5177. DOI: 10.1021/acs.analchem.9b05674.

[166] Shi Qiu et al. “Graphene encapsulation enabled high-throughput atom probe tomography of liquid specimens”. In: *Ultramicroscopy* 216 (2020), p. 113036. DOI: 10.1016/j.ultramic.2020.113036.

[167] Shuaizhong Qiu et al. “Direct Imaging of Liquid–Nanoparticle Interfaces with Atom Probe Tomography”. In: *The Journal of Physical Chemistry C* 124.35 (Sept. 2020), pp. 19389–19395.

[168] Leigh T. Stephenson et al. “The Laplace Project: An integrated suite for preparing and transferring atom probe samples under cryogenic and UHV conditions”. In: *PLOS ONE* 13.12 (2018), e0209211.

[169] Thomas M. Schwarz et al. “3D sub-nanometer analysis of glucose in an aqueous solution by cryo-atom probe tomography”. In: *Scientific Reports* 11.1 (2021), p. 11607.

[170] Daniel K. Schreiber et al. “A method for site-specific and cryogenic specimen fabrication of liquid/solid interfaces for atom probe tomography”. In: *Ultramicroscopy* 194 (Nov. 2018), pp. 89–99.

[171] Daniel E. Perea et al. “Tomographic mapping of the nanoscale water-filled pore structure in corroded borosilicate glass”. In: *npj Materials Degradation* 4.1 (Mar. 2020), p. 8.

[172] Amr A. El-Zoka et al. “Enabling near-atomic–scale analysis of frozen water”. In: *Science Advances* 6.49 (2020), eabd6324.

[173] Thomas M. Schwarz et al. “Field evaporation and atom probe tomography of pure water tips”. In: *Scientific Reports* 10.1 (2020), p. 20271.

[174] Philipp Stender et al. “Status and Direction of Atom Probe Analysis of Frozen Liquids”. In: *Microscopy and Microanalysis* 28.4 (2022), pp. 1150–1167.

[175] Vahid R. Adineh et al. “Pulsed-voltage atom probe tomography of low-conductivity and insulator materials by application of ultrathin metallic coating on nanoscale specimen geometry”. In: *Ultramicroscopy* 181 (2017), pp. 150–159. DOI: 10.1016/j.ultramic.2017.05.002.

[176] Tim M. Schwarz et al. “In Situ Metallic Coating of Atom Probe Specimen for Enhanced Yield, Performance, and Increased Field-of-View”. In: *Microscopy and Microanalysis* 30.6 (2024). DOI: 10.1093/mam/ozae006.

[177] Vahid R. Adineh et al. "Graphene-Enhanced 3D Chemical Mapping of Biological Specimens at Near-Atomic Resolution". In: *Advanced Functional Materials* 28.32 (2018). DOI: 10.1002/adfm.201801439.

[178] R. R. Nair et al. "Fine structure constant defines visual transparency of graphene". In: *Science* 320 (2008), p. 1308. DOI: 10.1126/science.1156965.

[179] A. A. Balandin. "Thermal properties of graphene and nanostructured carbon materials". In: *Nature Materials* 10 (2011), pp. 569–581. DOI: 10.1038/nmat3064.

[180] Shi Qiu et al. "Graphene encapsulation enables vitreous ice sample for atom probe tomography and near-atomic reconstruction of nanoparticle–liquid interfaces". In: *Microscopy and Microanalysis* 27.S1 (2021), p. 1270. DOI: 10.1017/S1431927621004761.

[181] E. L. Andreas. "New estimates for the sublimation rate for ice on the Moon". In: *Icarus* 186.1 (Jan. 2007), pp. 24–30. DOI: 10.1016/j.icarus.2006.08.024.

[182] R. S. Anderson and S. P. Anderson. *Geomorphology: The Mechanics and Chemistry of Landscapes*. Cambridge University Press, 2010, p. 187.

[183] J. Götze, Y. Pan, and A. Müller. "Mineralogy and mineral chemistry of quartz: A review". In: *Mineralogical Magazine* 85.5 (2021), pp. 639–664. DOI: 10.1180/mgm.2021.71.

[184] O. W. Flörke et al. "Silica". In: *Ullmann's Encyclopedia of Industrial Chemistry*. Wiley-VCH, 2008. DOI: 10.1002/14356007.o24_081.pub2.

[185] S. R. Elliott. "The structure of amorphous materials". In: *Properties and Applications of Amorphous Materials*. Dordrecht: Springer, 2001, pp. 1–11. DOI: 10.1007/978-94-010-0638-7_1.

[186] M. Sumper and E. Brunner. "Learning from diatoms: Nature's tools for the production of nanostructured silica". In: *Advanced Functional Materials* 16.1 (2006), pp. 17–26. DOI: 10.1002/adfm.200500616.

[187] N. Nassif and J. Livage. "From diatoms to silica-based biohybrids". In: *Chemical Society Reviews* 40.2 (2011), pp. 849–859. DOI: 10.1039/B906577F.

[188] R. Ravindra et al. "Protein encapsulation in mesoporous silicate: The effects of confinement on protein stability, hydration, and volumetric properties". In: *Journal of the American Chemical Society* 126.39 (2004), pp. 12224–12225. DOI: 10.1021/ja047031o.

[189] L. M. Ellerby et al. “Encapsulation of proteins in transparent porous silicate glasses prepared by the sol-gel method”. In: *Science* 255.5048 (1992), pp. 1113–1115. DOI: 10.1126/science.1312257.

[190] R. B. Bhatia et al. “Aqueous sol-gel process for protein encapsulation”. In: *Chemistry of Materials* 12.8 (2000), pp. 2434–2441. DOI: 10.1021/cm991186f.

[191] D. M. Liu and I. W. Chen. “Encapsulation of protein molecules in transparent porous silica matrices via an aqueous colloidal sol-gel process”. In: *Acta Materialia* 47.18 (1999), pp. 4535–4544. DOI: 10.1016/S1359-6454(99)00289-0.

[192] G. Novi Inverardi et al. *Silica In Silico: A Molecular Dynamics Characterization of the Early Stages of Protein*. TODO: add full title, journal, year, volume, pages, and DOI once available.

[193] Stephen Brunauer, Paul Hugh Emmett, and Edward Teller. “Adsorption of gases in multimolecular layers”. In: *Journal of the American chemical society* 60.2 (1938), pp. 309–319.

[194] Elliott P Barrett, Leslie G Joyner, and Paul P Halenda. “The determination of pore volume and area distributions in porous substances. I. Computations from nitrogen isotherms”. In: *Journal of the American Chemical society* 73.1 (1951), pp. 373–380.

[195] Géza Horváth and Kunitaro Kawazoe. “Method for the calculation of effective pore size distribution in molecular sieve carbon”. In: *Journal of Chemical Engineering of Japan* 16.6 (1983), pp. 470–475.

[196] W. Stöber, A. Fink, and E. Bohn. “Controlled Growth of Monodisperse Silica Spheres in the Micron Size Range”. In: *Journal of Colloid and Interface Science* 26.1 (1968), pp. 62–69. DOI: 10.1016/0021-9797(68)90272-5.

[197] G. H. Bogush, M. A. Tracy, and C. F. Zukoski. “Preparation of monodisperse silica particles: Control of size and mass fraction”. In: *Journal of Non-Crystalline Solids* 104.1 (1988), pp. 95–106. DOI: 10.1016/0022-3093(88)90078-5.

[198] S. Y. Chang and T. A. Ring. “Map of gel times for three-phase region tetraethoxysilane, ethanol and water”. In: *Journal of Non-Crystalline Solids* 147–148 (1992), pp. 56–61. DOI: 10.1016/S0022-3093(05)80615-5.

[199] D. J. Belton, O. Deschaume, and C. C. Perry. “An overview of the fundamentals of the chemistry of silica with relevance to biosilicification and technological advances”. In:

FEBS Journal 279.10 (2012), pp. 1710–1720. DOI: 10.1111/j.1742-4658.2012.08531.x.

[200] C. J. Brinker et al. "Review of sol-gel thin film formation". In: *Journal of Non-Crystalline Solids* 147–148 (1992), pp. 424–435. DOI: 10.1016/S0022-3093(05)80644-1.

[201] J. H. Lee and et al. "Study of vertical Si/SiO_2 interface using laser-assisted field evaporation". In: *Applied Physics Letters* 105.15 (2014), p. 153111. DOI: 10.1063/1.4900439.

[202] Xi-Cheng Zhang, Jingzhou Xu, et al. *Introduction to THz wave photonics*. Vol. 29. Springer, 2010.

[203] SW Smye et al. "The interaction between terahertz radiation and biological tissue". In: *Physics in Medicine & Biology* 46.9 (2001), R101.

[204] S Hunsche et al. "THz near-field imaging". In: *Optics communications* 150.1-6 (1998), pp. 22–26.

[205] S Mair, B Gompf, and M Dressel. "Spatial and spectral behavior of the optical near field studied by a terahertz near-field spectrometer". In: *Applied physics letters* 84.7 (2004), pp. 1219–1221.

[206] Q Chen et al. "Near-field terahertz imaging with a dynamic aperture". In: *Optics letters* 25.15 (2000), pp. 1122–1124.

[207] Zhenzhe Ma et al. "Optical generation of strong-field terahertz radiation and its application in nonlinear terahertz metasurfaces". In: *Nanophotonics* 11 (2022). DOI: 10.1515/nanoph-2021-0714.

[208] Angela Vella et al. "Femtosecond field ion emission by surface optical rectification". In: *Physical review letters* 99.4 (2007), p. 046103.

[209] M. Karam et al. "THz vs NIR laser-assisted atom probe tomography of LaB_6 samples". In: *APL Materials* 12.7 (2024), p. 071113. DOI: 10.1063/5.0209916.

[210] György Tóth, Gyula Polónyi, and János Hebling. "Tilted pulse front pumping techniques for efficient terahertz pulse generation". In: *Light: Science & Applications* 12.1 (Oct. 2023), p. 256. DOI: 10.1038/s41377-023-01293-1.

[211] L. Guiramand et al. "Near-optimal intense and powerful terahertz source by optical rectification in lithium niobate crystal". In: *Photonics Research* 10 (2022), pp. 340–346. DOI: 10.1364/PRJ.428418.

[212] C. Millon, S. Houver, and C. J. Saraceno. "400 kHz repetition rate THz-TDS with 24 mW of average power driven by a compact industrial Yb-laser". In: *Optics Express* 31.5 (2023), p. 7922. DOI: 10.1364/OE.476261.

[213] C. J. Brinker. "Hydrolysis and condensation of silicates: Effects on structure". In: *Journal of Non-Crystalline Solids* 100.1–3 (1988), pp. 31–50. DOI: 10.1016/0022-3093(88)90005-1.

[214] R. B. Bhatia et al. "Aqueous sol-gel process for protein encapsulation". In: *Chemistry of Materials* 12 (2000), pp. 2434–2441. DOI: 10.1021/cm000640d.

[215] Marco Fragai et al. "SSNMR of biosilica-entrapped enzymes permits an easy assessment of preservation of native conformation in atomic detail". In: *Chemical Communications* 50.4 (2014), pp. 421–423. DOI: 10.1039/C3CC46896H.

[216] F. Tang et al. In: *Ultramicroscopy* 110.7 (2010), pp. 836–843.

[217] L. Yao et al. In: *Philosophical Magazine Letters* 90.2 (2010), pp. 121–129.

[218] F. De Geuser et al. In: *Surface Science* 601.2 (2007), pp. 536–543.

[219] L. T. Stephenson et al. In: *Microscopy Research and Technique* 74.9 (2011), pp. 799–803.

[220] *IVAS™ 3.8 User Guide*. User manual. Cameca Instruments Inc. 2017.

[221] B. Gault et al. In: *Applied Physics Letters* 86 (2005), p. 094101.

[222] B. Gault et al. In: *Ultramicroscopy* 110.9 (2010), pp. 1215–1222.

[223] G. Da Costa et al. "Design of a Delay-Line Position-Sensitive Detector with Improved Performance". In: *Review of Scientific Instruments* 76 (2005).

[224] A. Cerezo et al. In: *Review of Scientific Instruments* 69.1 (1998), p. 49.

[225] P. Panayi et al. Presented at IVNC 2006/IFES 2006 (unpublished). 2006.

[226] E. Bemont et al. In: *Ultramicroscopy* 95.1–4 (2003), pp. 231–238.

[227] B. Deconihout et al. In: *Ultramicroscopy* 95.1–4 (2003), pp. 239–249.

[228] P. H. Clifton et al. In: *Microscopy and Microanalysis* 14.Suppl. 2 (2008), pp. 454–455.

[229] A. Cerezo et al. In: *Ultramicroscopy* 107.9 (2007), pp. 720–725.

[230] A. Bostel et al. WO/2009/047265. 2009.

[231] Levi Tegg, Leigh T Stephenson, and Julie M Cairney. "Estimation of the electric field in atom probe tomography experiments using charge state ratios". In: *Microscopy & Microanalysis* 30.3 (2024), pp. 466–475. DOI: 10.1093/mam/ozae047.

[232] H.-O. Andrén, A. Henjered, and D. R. Kingham. "On the charge state of tungsten ions in the pulsed-field atom probe". In: *Surface Science* 138.1 (1984), pp. 227–236. DOI: 10.1016/0039-6028(84)90508-9.

[233] S. C. Lam and R. J. Needs. "Calculations of ionization rate-constants for the field-ion microscope". In: *Surface Science* 277.3 (1992), pp. 359–369. DOI: 10.1016/0039-6028(92)90775-2.

[234] R. Cuduvally et al. "Post-field ionization of Si clusters in atom probe tomography: A joint theoretical and experimental study". In: *Journal of Applied Physics* 132.7 (2022). DOI: 10.1063/5.0106692.

[235] Derek K. Schreiber et al. "Applicability of post-ionization theory to laser-assisted field evaporation of magnetite". In: *Applied Physics Letters* 105.24 (2014), p. 244106. DOI: 10.1063/1.4904802.

[236] F. Danoix et al. In: *Ultramicroscopy* 107 (2007), pp. 734–738.

[237] F. Danoix et al. In: *Ultramicroscopy* 107 (2007), pp. 739–743.

[238] B. Gault et al. "Advances in the calibration of atom probe tomographic reconstruction". In: *Journal of Applied Physics* 105.3 (2009), p. 034913.

[239] Baptiste Gault et al. "Atom probe tomography". In: *Nature Reviews Methods Primers* 1.51 (2021), pp. 1–51. DOI: 10.1038/s43586-021-00047-w.

[240] L. Renaud et al. "The New Laser-Assisted Wide Angle Tomographic Atom Probe (LAWATAP)". In: *Microscopy and Microanalysis, Supplement 2 (Proceedings)*. Microsc. Microanal. **12** (Suppl. 2), 2006. Cambridge, UK: Cambridge University Press, 2006.

[241] B. Deconihout et al. "Improvement of the Detection Efficiency of Channel Plate Detectors for Field-Ion Microscopy and Atom Probe". In: *Applied Surface Science* 94–95 (1996).

[242] S. J. Sijbrandij, T. T. Tsong, and D. N. Seidman. "Characterization of Efficiency Enhancement in Microchannel-Plate Detectors". In: *Journal de Physique IV* 6 (1996).

[243] M. Thuvander et al. "Improving Compositional Accuracy in Atom Probe Tomography: Detector and Algorithmic Considerations". In: *Microscopy and Microanalysis* 25 (2019).

[244] Y. Zhang and coauthors. "LEAP reflectron vs. straight flight-path geometries: reported path lengths (382 mm vs. 100 mm)". English. In: *Microscopy and Microanalysis* (2023). Reports ∼382 mm reflectron path for 4000HR/5000XR and ∼100 mm straight path for 5000XS; accessed via Ovid.

[245] T Bartel et al. “Generation of single-cycle THz transients with high electric-field amplitudes”. In: *Optics Letters* 30.20 (2005), pp. 2805–2807.

[246] Anna Martinez et al. “Controlling the time shape of terahertz pulses from two-color plasma by combining wavelength dispersion and laser chirp”. In: *Applied Physics Letters* 124.2 (2024). Published 10 January 2024; Accepted 27 December 2023, p. 021105. DOI: 10.1063/5.0177262.

[247] K. Y. Kim et al. “Coherent control of terahertz supercontinuum generation in ultrafast laser–gas interactions”. In: *Physical Review Letters* 99 (2007), p. 073901. DOI: 10.1103/PhysRevLett.99.073901.

[248] Domenico Paparo et al. “THz Generation by Two-Color Plasma: Time Shaping and Ultra-Broadband Polarimetry”. In: *Sensors* 24.13 (2024), p. 4265. DOI: 10.3390/s24134265.

[249] Martin van Exter, Ch. Fattinger, and D. Grischkowsky. “Terahertz Time-Domain Spectroscopy of Water Vapor”. In: *Optics Letters* 14.20 (1989), pp. 1128–1130. DOI: 10.1364/OL.14.001128.

[250] Gustav Eriksson et al. “Silica-embedded Gold Nanoparticles Analyzed by Atom Probe Tomography”. In: *Microscopy and Microanalysis* 30.6 (Dec. 2024), pp. 1036–1046. DOI: 10.1093/mam/ozae024.

[251] S. Brunauer, P. H. Emmett, and E. Teller. “Adsorption of Gases in Multimolecular Layers”. In: *Journal of the American Chemical Society* 60.2 (1938), pp. 309–319. DOI: 10.1021/ja01269a023.

[252] G. Horvath and K. Kawazoe. “Method for calculation of effective pore size distribution in molecular sieve carbon”. In: *Journal of Chemical Engineering of Japan* 16.12 (1983), p. 470. DOI: 10.1252/jcej.16.470.

[253] E. P. Barrett, L. G. Joyner, and P. P. Halenda. “The Determination of Pore Volume and Area Distributions in Porous Substances. I. Computations from Nitrogen Isotherms”. In: *Journal of the American Chemical Society* 73.1 (1951), pp. 373–380. DOI: 10.1021/ja01145a126.

[254] Emily V. Woods, J. Smith, and coauthors. “Scalable Substrate Development for Aqueous Sample Preparation in Atom Probe Tomography”. In: *Microscopy and Microanalysis* 29.S1 (2023). Includes statement: “APT mapping directly reveals the atomic distribution of phosphorus in resin embedded ferritin.”. DOI: 10.1017/S143192762300XXX.

[255] Chiara Cappelli, Arun Devaraj, et al. “Atom Probe Tomography Analysis of Mica”. In: *Microscopy and Microanalysis* 28.4 (2022). Discusses Fe^{2+} (28 Da) overlap with Si^{+}, pp. 1207–1219. DOI: 10.1017/S1431927622000947.

[256] M. A. Hink, A. J. W. G. Visser, and J. W. Borst. “Structural Dynamics of Green Fluorescent Protein Alone and Fused with a Single Chain Fv Protein”. In: *Journal of Biological Chemistry* 275.24 (2000). Reports GFP cylinder 4.2 nm length, 2.4 nm diameter. DOI: 10.1074/jbc.M909028199.

[257] Roger Y. Tsien. “The Green Fluorescent Protein”. In: *Annual Review of Biochemistry* 67 (1998), pp. 509–544. DOI: 10.1146/annurev.biochem.67.1.509.

[258] A. M. Belu et al. “Enhanced ToF-SIMS Imaging of a Micropatterned Protein by Stable Isotope Protein Labeling”. In: *Analytical Chemistry* 73.2 (2001), pp. 143–150. DOI: 10.1021/ac0007711.

[259] Michael Kenneth Miller et al. *Atom probe field ion microscopy*. Oxford University Press, 1996.

[260] T. L. Burnett and et al. “Large volume serial section tomography by Xe Plasma FIB dual beam microscopy”. In: *Ultramicroscopy* 161 (Feb. 2016), pp. 119–129.

[261] K. Eder et al. “A multi-ion plasma FIB study: Determining ion implantation depths of Xe, N, O and Ar in tungsten via atom probe tomography”. In: *Ultramicroscopy* 228 (2021), p. 113334.

[262] J. Jiruse et al. “Combined plasma FIB-SEM”. In: *Microscopy and Microanalysis* 18.S2 (2012), pp. 652–653.

[263] Florant Exertier et al. “Nanoscale Analysis of Frozen Water by Atom Probe Tomography Using Graphene Encapsulation and Cryo-Workflows”. In: *Microscopy and Microanalysis* 30.6 (2025), pp. 1181–1194. DOI: 10.1093/mam/ozae054.

[264] Shi Qiu et al. “Graphene nanopipette enabled liquid delivery at zeptoliter precision”. In: *arXiv preprint arXiv:2008.08254* (2020). Preprint. DOI: 10.48550/arXiv.2008.08254. arXiv: 2008.08254 [physics.app-ph]. URL: https://arxiv.org/abs/2008.08254.

[265] Enrico Di Russo et al. “Field-Dependent Measurement of GaAs Composition by Atom Probe Tomography”. In: *Microscopy and Microanalysis* 23.6 (2017), pp. 1067–1075. DOI: 10.1017/S1431927617012582.

[266] Enrico Di Russo et al. “Compositional Accuracy of Atom Probe Tomography Measurements in GaN: Impact of Experimental Parameters and Multiple Evaporation Events”. In: *Ultramicroscopy* 187 (2018), pp. 126–134. DOI: 10.1016/j.ultramic.2018.02.001.

[267] Lorenzo Mancini et al. “Composition of Wide Bandgap Semiconductor Materials and Nanostructures Measured by Atom Probe Tomography and Its Dependence on the Surface Electric Field”. In: *The Journal of Physical Chemistry C* 118.41 (2014), pp. 24136–24151. DOI: 10.1021/jp5071264. URL: https://pubs.acs.org/doi/10.1021/jp5071264.

[268] Mukesh Bachhav et al. “Investigation of O-18 enriched hematite (α-Fe2O3) by laser assisted atom probe tomography”. In: *International Journal of Mass Spectrometry* 335 (2013), pp. 57–60.

[269] Ivan Blum et al. “Dissociation Dynamics of Molecular Ions in High dc Electric Field”. In: *The Journal of Physical Chemistry A* 120.20 (2016), pp. 3654–3662. DOI: 10.1021/acs.jpca.6b01791.

[270] Gerd-Hendrik Greiwe, Zoltan Balogh, and Guido Schmitz. “Atom probe tomography of lithium-doped network glasses”. In: *Ultramicroscopy* 141 (2014), pp. 51–55.

[271] A Vella et al. “Field evaporation mechanism of bulk oxides under ultra fast laser illumination”. In: *Journal of Applied Physics* 110.4 (2011).

[272] L Arnoldi et al. “Energy deficit of pulsed-laser field-ionized and field-emitted ions from non-metallic nano-tips”. In: *Journal of Applied Physics* 115.20 (2014).

[273] L Arnoldi et al. “Thermal diffusivity of diamond nanowires studied by laser assisted atom probe tomography”. In: *Applied Physics Letters* 112.14 (2018).

[274] Benjamin W Caplins et al. “An algorithm for correcting systematic energy deficits in the atom probe mass spectra of insulating samples”. In: *Ultramicroscopy* 213 (2020), p. 112995.

[275] Emmanuelle A. Marquis et al. “Probing the improbable: Imaging C atoms in alumina”. In: *Materials Today* 13.10 (2010), pp. 34–36. DOI: 10.1016/S1369-7021(10)70184-X.

[276] C. Constanda, D. Doty, and W. Hamill. *Boundary Integral Equation Methods and Numerical Solutions: Thin Plates on an Elastic Foundation*. Vol. 35. Developments in Mathematics. Springer, 2016.

[277] H.F. Merrick. “The structure of the superalloy IN-738”. In: *Metallurgical Transactions* 4 (1973), pp. 885–887.

[278] J.M. Oblak et al. “On the precipitation of secondary phases in Ni-based superalloys”. In: *Metallurgical Transactions* 5 (1974), pp. 1252–1255.

[279] M.K. Miller, R. Jayaram, and L.S. Lin. “Secondary γ precipitation in the single-crystal nickel-base superalloy PWA1480”. In: *Applied Surface Science* 76/77 (1994), pp. 172–176.

[280] Emmanuel Cadel. “Étude de la ségrégation intra et intergranulaire de solutés par sonde atomique tomographique et microscopie électronique en transmission”. PhD thesis. Rouen, France: Université de Rouen, 2000. URL: https://theses.hal.science/tel-01131302.

[281] D. Hoff et al. “Tracing the phase of focused broadband laser pulses”. In: *Nature Physics* 13 (2017), pp. 947–951. DOI: 10.1038/nphys4185. URL: https://doi.org/10.1038/nphys4185.

[282] J. W. Christian. *The Theory of Transformations in Metals and Alloys*. Elsevier, 2002.

[283] I. J. Polmear. *Light Alloys*. Elsevier, 2005.

[284] A. Guinier. In: *Nature* 142 (1938), pp. 569–570.

[285] G. D. Preston. In: *Nature* 142 (1938), p. 570.

[286] Enrico Di Russo et al. “Order and disorder at the atomic scale: Microscopy applied to semiconductors”. In: *Reviews of Modern Physics* 97.2 (2025), p. 025006. DOI: 10.1103/RevModPhys.97.025006. URL: https://doi.org/10.1103/RevModPhys.97.025006.

[287] J. M. Hyde and C. A. English. In: *MRS 2000 Fall Meeting, Symposium R: Microstructural Processes in Irradiated Materials*. Ed. by R. G. E. Lucas et al. Vol. 650. Boston: Materials Research Society, 2000, R6.6.1–R6.6.12.

[288] M. K. Miller and E. A. Kenik. In: *Microscopy and Microanalysis* 10.3 (2004), pp. 336–341.

[289] A. Cerezo and L. Davin. In: *Surface and Interface Analysis* 39.2–3 (2007), pp. 184–188.

[290] L. T. Stephenson, M. P. Moody, and S. P. Ringer. In: *Philosophical Magazine* 91.17 (2011), pp. 2200–2215.

[291] R. P. Kolli and D. N. Seidman. In: *Microscopy and Microanalysis* 13.4 (2007), pp. 272–284.

[292] Oussama Moutanabbir et al. “Evidence of sub-10 nm aluminum-oxygen precipitates in silicon”. In: *Nanotechnology* 27.20 (2016), p. 205706. DOI: 10.1088/0957-4484/27/20/205706.